



LEXNET Low EMF Exposure Future Networks

D3.2 Wideband dosimeter design study & performances characterization

Contractual delivery date: M16

Actual delivery date: M17

Document Information

Version	V1.2	Dissemination level	PU
Editor	S. BORIES (CEA-L	ETI)	
Other authors	S.M. ANWAR (SA	T), M. LE HENAFF (SAT), Y.	TOUTAIN

PROPRIETARY RIGHTS STATEMENT

This document contains information, which is proprietary to the LEXNET Consortium. Neither this document nor the information contained herein shall be used, duplicated or communicated by any means to any third party, in whole or in parts, except with prior written consent of the LEXNET consortium.



	(SAT), Y. FERNANDEZ (TTI), A. SANCHEZ (TTI), D. DASSONVILLE (CEA), S. BORIES (CEA), T. SARREBOURSE (ORANGE) M. KOPRIVICA (TKS), A. NEŠKOVIĆ (TKS), M. POPOVIĆ (TKS), J. MILINKOVIĆ (TKS), S. NIKŠIĆ (TKS), M. MACKOWIAK, L. CORREIA (INOV), C. ROBLIN (TPT),
Abstract	The design studies of the LEXNET wearable wideband dosimeter components are reported with architecture choices and final simulation results. A validation campaign of these different parts is addressed with measured performances characterization. The impact of external parameters as the body shadowing, the polarization distribution, and the traffic load are also addressed in this deliverable.
Key words	Dosimeter, wideband, wearable, correction factor, uncertainty.

Project Information

Grant Agreement n°	318273
Dates	1 st November 2012 – 31th October 2015

Document approval

Name	Position in project	Organisation	Date	Visa
Joe Wiart	Coordinator	France Telecom	16/05/2014	ok

Document history

Version	Date	Modifications	Authors
V1.0	10/04/2014	revised version from review	S. Bories
V1.2	16/05/2014	Revised versión with figures numbering	S.Bories



Table of contents

1 IN	TRODUCTION	15
2 WI	EARABLE DOSIMETER: STATE OF THE ART	17
2.1 Sat	imo solution: EME SPY 140	17
2.2 MA	SCHEK solution: ESM140	18
2.3 Cor	nparison between EME-SPY and ESM 140	18
2.4 Lim	itations of existing dosimeters	19
3 LE	XNET WEARABLE DOSIMETER DESIGN	21
3.1 Ger	neral architecture and design	22
3.2 Tri-	axial probe	23
3.3 Tun	able filter	25
3.3.1	RF Filter technology overview	25
3.3.2	Tunable Filter Technology	26
3.3.3	Peregrine Digitally Tunable Capacitor choice and validation	28
3.3.4	Tunable Filter requirements	30
3.3.5	Tunable Filter simulation (791-960 MHz)	30
3.3.6	Tunable Filter simulation (1710-2690 MHz)	32
	iable gain LNA	
3.4.1	Design study	
3.4.2	Experimental characterization	35
	R block	
3.5.1	Wide band PLL-VCO: HMC833LP6GE	
3.5.2	Wide band mixer: ADL 5801	
3.5.3	Tunable low pass filter: HMC900LP5E	
3.5.4	RMS power detector: HMC1020LP4E	
3.5.5	DCR block measurements in CW	
3.5.6	DCR block measurements in real scenario	48
3.6 Mic	rocontroller	53
3.7 Me	mory block	53
3.8 Blu	etooth / USB connectivity block	53
3.9 Inte	egration proposal for the LEXNET dosimeter	54



3.10 Batte	ry design	55
3.11 Mech	nanical design proposal	56
	MINARY RESULTS ON WEARABLE DOSIMETER CHARACTER RONMENT IMPACT STUDY	
4.1 Goals ar	nd approach description	57
4.2 Prelimin	ary measurements	57
4.2.1 Iso	olated triaxial sensor	
4.2.1.1	Polarimetric approach	
4.2.1.2	Non polarimetric approach	
	nsor on whole body phantom	
4.2.2.1	Phantom characteristics	
4.2.2.2	Measurement setup	
4.2.2.3 4.2.2.4	Measurement results – Elementary approach and global view Polarimetric approach	
	ons	
4.3.1 Sir	nplified model of isolated sensor	
4.3.1.1	Polarimetric approach	88
4.3.1.2	Non polarimetric approach	
4.3.2 Re	alistic body model simulations	
4.3.2.1	Simulated body impact : dosimeter worn on the waist	
4.3.2.2	Simulated body impact analysis : dosimeter worn on the chest	
4.3.3 Int	termediate results summary tables	105
4.4 Strategi	es for body-worn field sensor correction	106
5 NETW	ORK ENVIRONMENT IMPACT STUDIES	107
5.1 Traffic L	oad impact	107
5.1.1 De	escription of the topic	107
5.1.2 Di	scussions and conclusions	108
5.2 Extrapo	ation from mono-axial to isotropic EMF measurements	109
	easurement system and methodology	
5.2.2 De	etermination of extrapolation factor	110
5.2.3 Ur	ncertainty caused by the usage of mono-axial probe - u(MA)	110
	scussions and conclusions	
6 CONCI	LUSIONS	112
7 REFER	RENCES	113
APPENDIX	1: INTERNAL REVIEW	116
ADDENINIV	2. CHADACTEDIZATION OF THE TDAFFIC IMPACT OF PAR	
	2: CHARACTERIZATION OF THE TRAFFIC IMPACT OF EMF MENTS	118
Version: V1.2		4

D3.2 Wideband dosimeter: design study & performances characterization

FP7 Contract n°318273



Long-term variability of EMF strength - Paris measurements
APPENDIX 3: GUIDELINES ON THE EXPRESSION OF UNCERTAINTY IN LEXNET DOSIMETER MEASUREMENTS
DOSIMETER MEASUREMENTS
DOSIMETER MEASUREMENTS
Uncertainity caused by Measurement device - u(Md)
Uncertainty of the calibration of the sensor - u(MS)
Uncertainty of the Antenna Factor Interpolation - u(FA)
Uncertainty of the anisotropy - u(A)
Uncertainty caused by the usage of monoaxial probe - u(MA)
Uncertainty caused by mismatching - u(VSWR)
Uncertainty caused by "electrical noise" - u(Noise)135
Uncertainty caused by drift in the transmitting powers, measurement equipment, temperature and
humidity - u(Drift)
Uncertainty caused by human bodies - u(Body)136
Uncertainty caused by small-scale fading - u(Fad)136
Uncertainty caused by telecommunication traffic and transmitter functionalities - u(Traff)
Total (combined) standard uncertainty
Expanded uncertainty



List of Acronyms

Abbreviations Meanings

ADC Analogue to Digital Convertor

AF Antenna Factor
AOA Angle of Arrival
AP Access Point

ASA Azimuth Spread of Arrival
ATF Antenna Transfer Function

BPF Band Pass Filter
BS Base Station

BST Barium-Strontium-Titanate

CMOS Complementary Metal Oxide Silicon

CDF Cumulative Distribution Function

DCR Direct Conversion Receiver

DC Direct Continuous

DET Detector
DL Down Link

DCS Digital Cellular System

DOA Direction of Arrival

DTC Digitally Tunable Capacitor

EC European Community

EEPROM Electrically Erasable Programmable ROM

EI Exposure Index
EM Electro-Magnetic

EMC Electro-Magnetic Compatibility

EMF Electro-Magnetic Field

ESA Elevation Spread of Arrival

FET Field Effect Transistor

FF Far Field

FOM Figure of Merit

Version: V1.2

D3.2 Wideband dosimeter: design study & performances characterization



FTBR Front to Back Ratio

GSM Global System for Mobile

IF Intermediate Frequency

I/O Inputs/Outputs
IL Insertion Loss

LEXNET Low EMF EXposure future Networks

LED Light Emitting Diode

LTE Long Term Evolution

LNA Low Noise Amplifier

LOS Local Oscillator
LOS Line of Sight
LPF Low Pass Filter

LTCC Low Temperature Co-fired Ceramics

MAA Mono-Axial Antenna

MEMS Micro ElectroMechanical Systems

MRG Mean Realized Gain
MIM Metal Insulator Metal
MPC Multi Path Component

NF Noise Figure

NLOS Non Line of Sight
O2I Outdoor to Indoor

OIP3 Output Third-Order Intercept Point

P1dB Compression Point at 1 dB

PC Personal Computer
PCB Printed Board Circuit

PL Path Loss

PLL Phase Locked Loop

RAT Radio Access Technology

RF Radio Frequency

Rx Received

RMS Root Mean Square

SAR Specific Absorption Rate

SAW Surface Acoustic Wave

Dissemination level: PU



SRF Self-Resonant Frequency

SOI Silicon On Insulator
SOS Silicon On Sapphire

SPI Serial Peripheral Interconnect

USB Universal Serial Bus

Tx Transmitted

TTL Transistor Transistor Logic
VGA Variable Gain Amplifier

UMTS Universal Mobile Telecommunication System

UL Up Link

UART Universal Asynchrobous

UMa Urban Macrocell

VCO Voltage Controlled Oscillator
WLAN Wireless Local Area Network

XPR Cross Polarization Ratio



List of figures

Figure 1 : EME Spy 140	. 17
Figure 2: Main characteristics of ESM 140 dosimeter	. 18
Figure 3 : Comparison between EMESPY 121 and ESM 140 [5]	. 19
Figure 4: Block diagram of the LEXNET wearable dosimeter	. 23
Figure 5: Tri-axial probe selected for the LEXNET dosimeter (a) simulation model, (b) prototype us	sec
in actual EME-SPY dosimeters	. 23
Figure 6: Comparison between measured and simulation results for the probe reflection coefficient	
dB)	
Figure 7 - RF filter selection with 4 way switches	
Figure 8 - Block diagram of Peregrine DTC – taken from Peregrine Application Note 29 (DTC The of Operation)	ory: 28
Figure 9 - Capacitance vs Tuning State of DTC – taken from Peregrine Application Note 29 (D	TC
Theory of Operation)	
Figure 10 - DTC linear equivalent model - taken from Peregrine Application Note 29 (DTC Theory	y of
Operation)	
Figure 11 - Simulation (red) vs Measurement (black) of an LC resonator transmission (dB) for stat	e 8
(top) and state 1 (bottom)	. 30
Figure 12 - Tuning filter 790-960 MHz	. 31
Figure 13 - Simulation Result for F1 Tuning filter (790-960 MHz) for different values of the DTC	. 31
Figure 14 - Simulation Result for F2 Tuning filter (1710-2690MHz) for different values of the DTC	
Figure 15: Two possible configurations for the variable gain LNA: option A (left) and option B (right)	35
Figure 16: Photograph of the VMMK-2303 evaluation board	. 36
Figure 17: HMC624LP4 functional diagram showing its control interfaces	. 37
Figure 18 : Photograph of the PGA-1021+ evaluation board	. 38
Figure 19 : Direct Conversion Receiver block diagram	
Figure 20 : PLL VCO HMC833LP6GE test bench for characterization	. 41
Figure 21 : Output of the PLL-VCO on the spectrum analyzer for (a) 900 MHz, and (b) for 2500 MHz	
Figure 22 : Mixer ADL5801 test bench for characterization	
Figure 23: Wide band mixer IF output for, (a) RF = 898 MHz @ -10 dBm; LO = 900 MHz @ 0 dB	3m
(b) RF = 898 MHz @ -85 dBm; LO = 900 MHz @ 0 dBm	
Figure 24 : Tunable low pass filter HMC900LP5E test bench for characterization	
Figure 25: Tunable low pass filter results from network analyzer, (a) datasheet, (b) measureme	ents
over narrow band, (c) measurements up to 6 GHz.	
Figure 26: RMS power detector HMC1020LP4E test bench for characterization	
Figure 27: RMS power detector results from (a) datasheet, (b) measurements	
Figure 28 : Test bench setup for two-tone RF input characterization of the DCR block	
Figure 29: Screen shots of the oscilloscope showing the output of the power detector for differ	
cases.	. 48
Figure 30: Test bench setup DCR block test with real scenario, (a) block diagram, (b) photograph	1 0
the test bench, (c) GSM frequency band distribution in France.	
Figure 31: Result from the reference measurement with the mobile calling a landline number after	
minute of measurements with max-hold	
Figure 32: Output of the DCR block on the oscilloscope with LO frequency locked to 895 MHz	
Figure 33: Measurement scenarios with the DCR block and LO frequency positions	
measurements.	
Figure 34: Electrical diagram of the RF front end of the dosimeter	
Figure 35 : Flat battery identified for the LEXNET dosimeter Figure 36 : Proposal for the mechanical structure for the LEXNET wearable dosimeter	
Figure 36 : Proposal for the mechanical structure for the LEXNET wearable dosimeter Figure 37 : Experimental setup for the measurement of the isolated sensor in anechoic chamber	. 50
Figure 38 : Reflection coefficient of each probe sensor	
Figure 39 : Realized gains per probe	
Figure 40 : Antenna Factor per probe.	



Figure 41 : Normalized realized gain patterns (averaged over each RAT band) of the "V"(z'Oz) probe and combined "H" probes (xOy) in the azimuthal plane, $\theta = 90^\circ$
Figure 43 : XPR levels (averaged for each RAT) of the isolated "V"(z'Oz) probe and combined "H" probes (xOy) in the azimuthal plane, $\theta = 90^{\circ}$
Figure 44: Influence of the incoming wave XPR level on the isotropy (for various RATs), (a-e)
received signal "patterns" in azimuth, (f) variance of the isotropy ($\theta = 90$ °)
Figure 46: Non polarimetric statistics (CDF) of isotropy deviation for 4 typical WINNER+ based 3D
channel environments. The field strength ei0 is normalized to 1 V/m
Figure 47: Non polarimetric statistics (CDF) of isotropy deviation for 4 typical WINNER+ based 3D channel environments. Normalized field expressed in dB
Figure 48: Non polarimetric statistics (CDF) of isotropy deviation and examples of statistical fits for an
NLOS and a LOS environments. 72
Figure 49: Whole body phantom ("Kevin") dielectric properties (from [17])
Figure 51 : Sensor positioning on the phantom: left chest, left hip and right back
Figure 52: Sensor/phantom spacing: ~ 0, 10 and 20 mm (not shown here)
Figure 53 : Sensor positioning details: left chest,. \sim 12.5 cm from the saggital plane and \sim 23.5 cm from the top of the shoulder
Figure 54: Left: Sensor positioning details on left hip,. ~10 cm from the saggital plane and ~ 81 cm
from the ground; Right: reference antenna positioning for the conical cut at an elevation of 20° abov e
horizon
ground
Figure 56: Reflection coefficient of each probe sensor and for all "scenarios" (compared to the isolated case)
isolated case)
Figure 58: Normalized (co-polar) realized gain patterns (averaged over each RAT band) of the
"V"(z'Oz) probe and combined "H" probes (xOy) in the azimuthal plane for the "Chest scenario", $\theta = 90^{\circ}$ and 70° , $\phi = 10$ mm
Figure 59: Normalized (co-polar) realized gain CDF (averaged over each RAT band) of the "V"(z'Oz)
probe and combined "H" probes (xOy) in the azimuthal plane for the "Chest scenario", all φ and θ 80
Figure 60: Normalized (co-polar) realized gain patterns (averaged over each RAT band) of the "V"(z 'Oz) probe and combined "H" probes (x Oy) in the azimuthal plane for each "scenario", all ϕ and
θ
Figure 61: Normalized (co-polar) realized gain patterns (averaged over each RAT band) of the
"V"(z'Oz) probe and combined "H" probes (xOy) in the azimuthal plane for the "Hip scenario", θ = 90°, δ = 10 mm
Figure 62: Normalized (co-polar) realized gain CDF (averaged over each RAT band) of the "V"(z'Oz)
probe and combined "H" probes (xOy) in the azimuthal plane for the "Hip scenario", all φ and θ 82
Figure 63 : XPR levels (averaged for each RAT) of the "V"(z'Oz) probe and combined "H" probes (xOy) in the azimuthal plane. Sensor on chest, $\delta = 10$ mm, $\theta = 90^{\circ}$
Figure 64: XPR levels CDF (averaged for each RAT) of the "V"(z'Oz) probe and combined "H" probes
(xOy) in the azimuthal plane. Sensor on chest, all θ and ϕ
(xOy) in the azimuthal plane. Sensor on hip, $\delta = 10$ mm, $\theta = 90^{\circ}$
Figure 66 : Sketch of the sensor simplified model (from Satimo)
Figure 67: Simulated reflection coefficient of each probe sensor.
Figure 68 : Simulated realized gains per probe
LTE 2600 and WiFi 5G) of the "V"(z'Oz) probe (top) and combined "H" probes (xOy) in the azimuthal
plane (bottom)
"V"(z 'Oz) probe and combined "H" probes (x Oy) in the azimuthal plane, $\theta = 90^{\circ}$ 88



Figure 71: Simulated normalized realized gain pattern standard deviation over azimuth (average over frequency for each RAT – yellow circles) of the "V"(z'Oz) probe and combined "H" probes (xOall θ (circles) and $\phi = 90^{\circ}$ (plain).	Ďу),
Figure 72: Influence of the incoming wave XPR level on the isotropy (for various RATs): stand	lard
deviation of the received non polarimetric signal. Figure 73: Influence of the incoming wave XPR level on the isotropy (for each RATs): stand	lard
deviation of the received non polarimetric signal	. 90
Figure 74: Non polarimetric statistics (CDF) of isotropy deviation and examples of statistical fits for NLOS and a LOS environments (n°1 & 2, based on WIN NER+ 3D channel models)	
Figure 75: S11 for the dosimeter's probes	
Figure 76: Radiation of the Isolated Dosimeter at 2.6 GHz	. 93
Figure 77: Radiation of the dosimeter on the Waist at 2.6 GHz	. 94
Figure 78: Realized Gain pattern difference distribution.	. 94
Figure 79: Realized Gain pattern difference vs. frequency (GHz	. 95
Figure 80 : (a) Sketch of the triaxial sensor placed on Eartha's phantom chest, (b) Example of realizing pattern (2.5 GHz, □-polarization)	
Figure 81 : Simulated reflection coefficient of each probe sensor – comparison between the worn a	and
isolated cases.	. 96
isolated cases	- 6
GHz (3D radiation patterns)	. 97
Figure 83: Relative (to isolated) realized gain patterns (averaged over each RAT band) of	the
"V"(z'Oz) probe and combined "H" probes (xOy) in the azimuthal plane for the sensor worn on earth	
chest scenario, $\theta = 90^\circ$. Co-polar (top) and cross-polar (bottom) Figure 84: Polarimetric "isotropy" (averaged over each RAT band) of the "V"(z'Oz) probe a	
combined "H" probes (xOy) for the sensor worn on Eartha's chest (relative to isolated), all φ	
Figure 85: Simulated realized gain pattern (relative to isolated) standard deviation over azim	
(averaged over frequency for each RAT – yellow circles) of the "V"(z'Oz) probe and combined	"H"
probes (xOy), all φ	. 99
Figure 86: Influence of the incoming wave XPR level on the isotropy (for various RATs), (a	
received signal in azimuth (relative to isolated sensor), (f) variance of the isotropy ($\theta = 90^{\circ}$)	
Figure 87: Influence of the incoming wave XPR level on the isotropy (for various RATs): stand	
deviation of the received non polarimetric signal (relative to isolated sensor)	
of the received non polarimetric signal (relative to isolated sensor), $\theta = 90^{\circ}$	
Figure 89 : Non polarimetric statistics (CDF) of isotropy deviation for an NLOS (left) and a LOS (rig	
environments. Sensor worn by Eartha (signal relative to isolated case).	103
Figure 90: Empirical CDF of the MRG for each sensor position and both polarizations, and rest	
combining two or all positions	
Figure 91: Frequency selective measurement system	
Figure 92 Example of the variation of the surface power density over 24 hours for the DCS	
Figure 94 Variability of the surface power density over 24h for DCS	
Figure 95 Variability of the surface power density over 24h for UMTS 2100	120
Figure 96 Time variability of electric field strength for GSM	123
Figure 97 Probability density function of electric field strength for "all days" - GSM	
Figure 98 Probability density function of electric field strength for "working days" - GSM	
Figure 99 Time variability of electric field strength for DCS	124
Figure 100 Probability density function of electric field strength for "working days" - DCS	
Figure 102 Time variability of electric field strength for UMTS	
Figure 103 Probability density function of electric field strength for "all days" - UMTS	
Figure 104 Probability density function of electric field strength for "working days" - UMTS	
Figure 105: Traffic uncertainty with regards to time averaging intervals for "all days" - GSM	
Figure 106: Traffic uncertainty with regards to time averaging intervals for "working days" - GSM 1	
Figure 107 Traffic uncertainty with regards to time averaging intervals for "all days" - DCS 1 Figure 108 Traffic uncertainty with regards to time averaging intervals for "working days" - DCS 1	
Figure 109 Traffic uncertainty with regards to time averaging intervals for "all days" - UMTS	
Version: V1.2	11

D3.2 Wideband dosimeter: design study & performances characterization

FP7 Contract n°318273



Figure	110 Traffic uncertainty with regards to time averaging intervals for "working days" – UMTS •	132
Figure	111 Electric field strength (mV/m) with regards to time for scenario 1	143
Figure	112 Extrapolation factors with regards to time for scenario 1	143
Figure	113 Electric field strength (mV/m) with regards to time for scenario 2	144
Figure	114 Electric field strength (mV/m) with regards to time for scenario 3	145

Version: V1.2



List of Tables

Table 1: Main features of the LEXNET dosimeter	21
Table 2 – Frequency bands requirements	22
Table 3: Isotropy of the tri-axial probe over the LEXNET frequency bandband	24
Table 4: Measured results for the probe antenna factor over the LEXNET frequency band	
Table 5 - Different RF Filter Technologies	
Table 6 - Different tunable RF Filter Technologies	
Table 7 : Estimated maximum and minimum input power at LNA	33
Table 8 : Variable gain LNA requirements from DCR block	
Table 9 : Variable gain LNA specifications	
Table 10 : VMMK-2303 measured features with 3.3 V supply	36
Table 11 : VMMK-2303 measured features with 1.8V supply	
Table 12 : PGA-1021+ measured features	
Table 13 : Evaluation of the variable gain LNA expected performance	
Table 14: Harmonic levels for the PLL-VCO from (a) datasheet, and (b) measurements	
Table 15: Results for two-tone RF input to the DCR block (a) integration time setting for the po	
detector from the datasheet, (b) RF and LO inputs, (c) summary of measured results	
Table 16: Output of the power detector for different LO frequency locks in the scenario studie	
Figure 30	
Table 17 : DL exposure target frequency bands (e.g. France spectrum) for the LEXNET dosimeter	
Table 18 : Power consumption, size, and time delay estimation for the LEXNET dosimeter	
Table 19 : Polarimetric isotropy statistics (over azimuth), in dB	
Table 20 : Polarimetric isotropy statistics (over azimuth), in dB	
Table 20 : Foldimetric sensor AFK statistics (over azimuth), in db.	63
Table 21 : Radio charmer parameters for the considered environments Table 22 : Non polarimetric sensor isotropy deviation statistics (over azimuth) for Env. n°1	67
Table 23 : Non polarimetric sensor isotropy deviation statistics (over azimuth) for Env. n°2	
Table 23 : Non polarimetric sensor isotropy deviation statistics (over azimuth) for Env. in 2 Table 24 : Non polarimetric sensor isotropy deviation statistics (over azimuth) for Env. n°3	
Table 25: Polarimetric isotropy statistics (over azimuth), Chest, all θ and φ (dB)	
Table 26 : Polarimetric isotropy statistics (over azimuth), Hip, all θ and φ (dB)	ഠാ
Table 27: Polarimetric sensor XPR statistics (over azimuth) – Sensor on Chest (all θ and ϕ)	84
Table 28: Virtual Population (ITIS' Foundation) anthropometric characteristics	
Table 29 : Polarimetric isotropy statistics (over azimuth and elevation), in dB	
Table 30: Non polarimetric sensor isotropy deviation statistics (over θ and φ) for Env. n°1	
Table 31: Non polarimetric sensor isotropy deviation statistics (over θ and ϕ) for Env. n°2	
Table 32 Realized gain pattern difference statistics for 2.6 GHz.	
Table 33 The average Realized Gain difference in [0.4, 6] GHz	95
Table 34: Polarimetric isotropy statistics (over φ and θ), Eartha's chest (dB)	99
Table 35 : Non polarimetric sensor isotropy deviation statistics (over θ and φ) for Env. n°1	
Table 36 : Non polarimetric sensor isotropy deviation statistics (over θ and φ) for Env. n°2	
Table 37: Measurement and simulation approaches summary: averages ("bias")	
Table 38: Measurement and simulation approaches summary: standard deviations	
Table 39Measured frequency bands	. 118
Table 40 Traffic uncertainty (%) with regards to time averaging intervals for GSM	. 128
Table 41 Traffic uncertainty (%) with regards to time averaging intervals for DCS	
Table 42 Traffic uncertainty (%) with regards to time averaging intervals for UMTS	
Table 43: Mean values, medians, standard deviations and uncertainties for scenario 1	
Table 44: Mean values, medians, standard deviations and uncertainties for scenario 2	
Table 45 Mean values, medians, standard deviations and uncertainties for scenario 3	
Table 46 Comparison of mean values, medians, standard deviations and uncertainties for all t	hree
scenarios	145



Executive Summary

The wearable dosimeter represents a key tool for the LEXNET project since this network-independent measurement device will be used by the other work packages. It is able to feedback measurements on the wireless network and to assess the Exposure Index from electrical field values directly measured at the position of the user who wears it. This information could be used by the service providers to manage the network configuration in order to reduce global exposure. Compared to the LEXNET simplified dosimeter, the wearable one allows to differentiate any telecom services within the 0.7-6 GHz and also to identify the service provider both in Up-Link and in Down-Link.

The design of the LEXNET wearable dosimeter has been initiated from a review of existing dosimeters and other available solutions. Regarding this state of the art, two major innovations on the RF front-end are implemented. The first one concerns the high selectivity of the selected frequency band which enables to isolate and measure a given network provider contribution to the overall experience EMF exposure. The second innovation brings the advantage of a large flexibility to assess existing and future telecom standards without changing the hardware thanks to a frequency reconfigurable RF architecture on the 0.7-6 GHz frequency band. Part of the design innovation consists to distribute the complexity and selectivity constraints on both the pre-filter and the Direct Conversion Receiver.

Another main achievement in LEXNET is the study of the parameters impacting the accuracy of the measured results and to propose solutions that decrease uncertainties. First, the shadowing due to the close proximity of obstacles as well as the human body results in an important bias that could be compensated for the down link exposure measurement. Moreover, the roles of long-term variability, averaging time window, and polarization distribution of the electrical field are analyzed. The objective is to embrace the trade-off between simplifying and fastening measurements on one side and improving the accuracy and reducing the uncertainties on the other side.

During the two first years of the LEXNET project, the wearable dosimeter has been specified, designed, and it will be prototyped at the end of the second year. During the third year, functional prototypes will be deployed during the validation demonstrations. This tight schedule is made possible by the collaboration and the coordination of the different involved partners, who have developed the dosimeter components by considering all together the sensitivity/selectivity trade-off (5 mV/m minimum level for 3 MHz bandwidth), the battery autonomy (more than a day), and the dimensions performances (smartphone form factor).



1 Introduction

The main objective of the Low EMF EXposure future Networks (LEXNET) project is twofold. First LEXNET has defined a global metric to assess human exposure to electromagnetic fields (EMF) radiated by radio frequency communications devices. This aims to quantify, compare, and predict the current and future trends (usage and technologies) in term of global EMF exposure. The second objective is to provide means of reducing exposure thanks to low EMF radio and networks technologies. The LEXNET metric assessment approach requires evaluating the exposure induced by different devices and standards with a representative spatial sampling. This can be done through modeling with assumptions, but also via real-life measurements. The wearable and fixed dosimeters developed in LEXNET fill up this last requirement. This D3.2 deliverable focuses on the wearable version which has high-performances thanks to a more complex design compared to the fixed one.

The user exposure is obtained from the assessment of the whole body SAR induced by EM sources. Although SAR evaluation is not practically easy, SAR is mainly related to the field strength and location of the source regarding the user body. This field level can be estimated in different ways: first, through the Network to which the user is connected, second, thanks to information collected by disseminated field sensors or personal dosimeters directly worn by user. Individual user device transmitted (Tx) and received (Rx) powers, Base Stations (BS) or Access Point (AP) Tx power and traffic load are assessed information from network providers, but usually not fully available from the user equipment.. Moreover this solution ignores emissions from other networks and is hence partial. Note that dosimeters can be deployed by the operators themselves or by independent external stakeholders such as regulatory agencies or local authorities (provinces, regions, cities, etc.).

The dissymmetry between Up-Link (UL) and Down-Link (DL) radio transmissions is retrieved in UL and DL user exposure evaluation challenges. On the one hand for the DL, the isotropy of the dosimeter is strongly affected by the user body. Fortunately the DL fields from far sources are at the end of the day statistically uniformly distributed over the azimuth directions and statistical model can compensate the bias. The DL challenge is addressed in this deliverable. On the other hand for the UL, sources are close to the body but dosimeter cannot estimate their location as regards the body neither the exact transmit power. Thus it is not possible to estimate UL user exposure (in term of SAR) from the field measured at the body-worn dosimeter location. The UL problem is not solved in LEXNET nevertheless the selected architecture will remain possible the use of multi probes for future studies.

This deliverable is organized as follow. The chapter 2 presents the state of the art of the existing wearable dosimeters or other solutions to estimate exposure and their limitations. The chapter 3 details the design and the performances of the isolated parts of the wearable dosimeter such as the antenna, the tunable band pass filter, the variable gain Low Noise Amplifier, and the Direct Conversion Receiver. A global evaluation is proposed by considering all together the sensitivity/selectivity trade-off,



the battery autonomy, and the dimensions performances. The preliminary results on the dosimeter characterization are addressed in chapter 4. First part deals with the body shadowing effect in the Down-Link exposure of body-worn scenario. A statistical approach proposes to model and compensate this bias. The second part evaluates the bias and uncertainty level when mono-axial probe is used instead of the isotropic one. At last the variability of band selective measurements with regards to network environment is considered in different cities during the full day.

At last the conclusion synthesizes the reached performances and suggests the way forward. As regards the DoW description, a two steps delivery has been requested and accepted to release this D3.2 in two versions. For the release 1, D3.2 details the parts with technical materials mainly concerning the dosimeter sub-components' prototypes that will be updated and added in the release 2 at M18.

Version: V1.2



2 WEARABLE DOSIMETER: STATE OF THE ART

The dosimeter is a device used to measure EMF value with good precision. They provide a low-end solution with reliable measurement certainty as compared to highend professional solutions such as wide band probes with spectrum analyzers.

In this section, two existing wearable and "frequency selective" dosimeters are presented. These are the only ones to the author's best knowledge available in the market with reliable EMF measurement capabilities. Other solutions called "broadband" (EME Guard from SATIMO [1] or Radman from Narda [2]) exist. But these are not relevant in the context of this study, because they give an indication of the total E-field over the whole frequency band without any frequency selectivity characteristics.

2.1 Satimo solution: EME SPY 140

EME Spy 140 [3] (Figure 1) is a light and portable RF safety dosimeter which performs continuous measurements of the human exposure level to electromagnetic fields (EMF) on 14 pre-defined frequency bands. This unique solution enables accurate selective measurements without incurring the costs of an integrated spectrum analyzer.



FREQUENCY RANGES	AXIAL IS	OTROPY
	Min - Max	Standard deviation
FM (88 – 108 MHz)	± 2.6 dB	± 1.7 dB
TV3 (174 – 223 MHz)	± 2.2 dB	± 1.3 dB
TETRA (380 - 390 MHz)	± 2.5 dB	± 1.2 dB
TV4&5 (470 – 830 MHz)	± 0.8 dB	± 0.4 dB
GSM Tx (880 – 915 MHz)	± 2.6 dB	± 1.6 dB
GSM Rx (925 – 960 MHz)	± 2.4 dB	± 1.5 dB
DCS Tx (1710 – 1785 MHz)	± 2.3 dB	± 1.3 dB
DCS Rx (1805 – 1880 MHz)	± 2.2 dB	± 1.4 dB
DECT (1880 – 1900 MHz)	± 1.2 dB	± 0.8 dB
UMTS Tx (1920 – 1980 MHz)	± 0.9 dB	± 0.5 dB
UMTS Rx (2110 – 2170 MHz)	± 1.3 dB	± 0.6 dB
WiFi 2G (2400 – 2500 MHz)	± 1.5 dB	± 0.8 dB
WiMAX (3400 – 3800 MHz)	± 2.9 dB	± 1.5 dB
WiFl 5G (5150 – 5850 MHz)	± 3.9 dB	± 2.0 dB

Figure 1: EME Spy 140

This dosimeter is able to discriminate upload and download link. This original specification is not only useful to assess the contribution of each transmitter, but also to avoid corruption of the results by phones emitting close to the dosimeter.

Measurements are done from a sensitivity of 5 mV/m up to 5 V/m (with a dynamic of 60 dB). The dimensions of this dosimeter are 168,5*79*49,7 mm (H*L*W) for a weight of 410 g. It is able to store around 80 000 measurements with 4 to 255 seconds between measurements.



There are two modes of operation:

- 1. The apparatus is operable in real time. In this case, the visualization can be done on a PC, tablet or smartphone. The data transfer can be done via an USB cable or directly via Bluetooth.
- 2. It is also possible to program a measurement cycle. The measurements are then stored in the device, and at the end of the cycle can be downloaded via an USB link to a PC.

2.2 MASCHEK solution: ESM140

The German Company MASCHEK has also developed a frequency selective dosimeter [4]. The main characteristics of this dosimeter are summarized below:

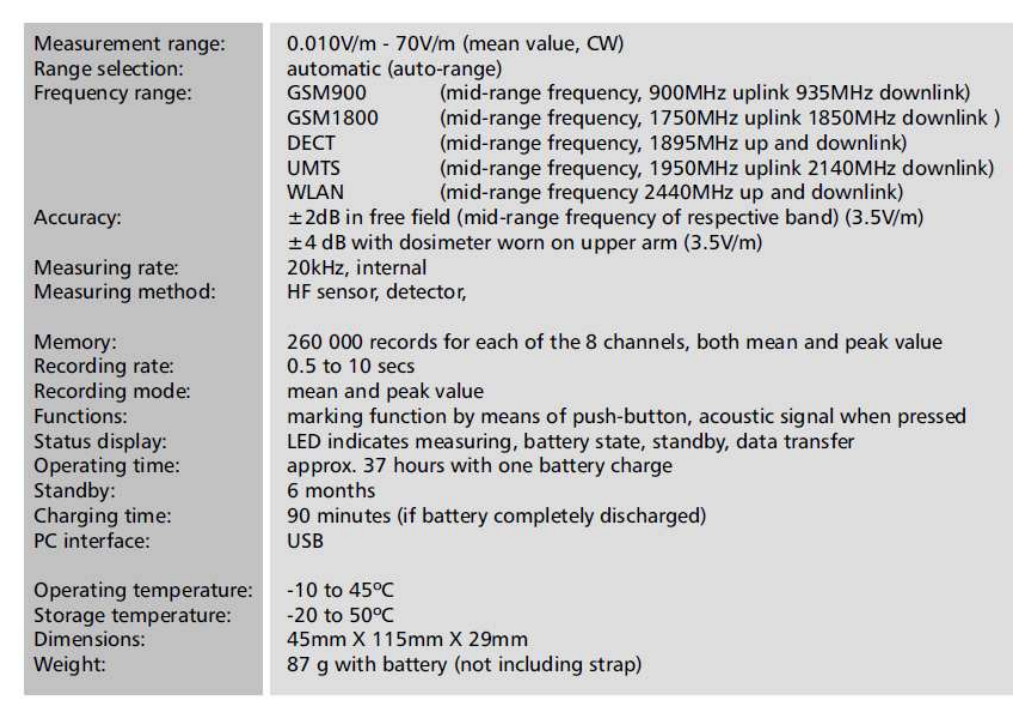


Figure 2 : Main characteristics of ESM 140 dosimeter

2.3 Comparison between EME-SPY and ESM 140

For 10 years, a lot of validations and comparisons of these dosimeters were performed. Among the most comprehensive studies, we can mention:

- Seawind project "Sound Exposure & Risk Assessment of Wireless Network Devices – Deliverable 1.1 - Literature review of exposure assessment and dosimetry of wireless networks" [5]
- Dominique PICARD, Luce FOUQUET, Sébastien CHAUVIN -"Characterization of four different Radio Frequency dosimeters [6]
- Georg Neubauer, Stefan Cecil, Wolfram Giczi, Benjamin Petric, Patrick Preiner, Jürg Fröhlich, Martin Röösli – Final Report on the project C2006-07: "Evaluation of the correlation between RF dosimeter reading and real human exposure" – 2008 [7]



Lots of these studies were realized with an old version of the SATIMO dosimeter (EME Spy 90/120/121), but they have the advantage to propose comparisons between both devices.

	Satimo EME Spy 121	Maschek ESM 140
Frequency bands		
FM	88-108 MHz	Not included
TV3	174–223 MHz	Not included
TETRA	380–400 MHz	Not included
TV 4&5	470–830 MHz	Not included
GSM900 Uplink	880–915 MHz	900 MHz
GSM900 Downlink	925–960 MHz	935 MHz
GSM1800 Uplink	1710–1785 MHz	1750 MHz
GSM1800 Downlink	1805–1880 MHz	1850 MHz
DECT	1880–1900 MHz	1895 MHz
UMTS Uplink	1920–1980 MHz	1950 MHz
UMTS Downlink	2110-2170 MHz	2140 MHz
WLAN	2400-2500 MHz	2440 MHz
Antennas	Isotropic three axis	Folded
Spectral analysis	Passive filters	Narrow band antennas
Measurement range	0.05-10 V/m	0.01-70 V/m
Logging interval	4-255 s	0.5–10 s
No of samples stored	12,540	260,000
Size	193 x 95.6 x 69.4 mm ³	100 x 45 x 20 mm
Weight	450 g	70 g

^aCenter frequency mentioned in the technical specifications

Figure 3: Comparison between EMESPY 121 and ESM 140 [5][8]

The term "folded" for the antenna type used for the Maschek ESM 140 dosimeter signifies the folded dipole antennas.

The principal interest of Maschek ESM 140 is its small dimension and its low weight. That is why it was sometimes preferred to the first one in studies involving children. Anyway, the others technical specifications (selectivity and isotropy) are lower than the specifications of the EME Spy.

2.4 Limitations of existing dosimeters

The current dosimeters allow to carry out frequency selective exposure measurements. However, there are two major limitations:

- i. Current dosimeters do not have the ability to distinguish between different service providers. This property would be useful in the case where one wishes to determine the exposure from a specific service provider in a given area. This capability will also be helpful in comparing / calibrating the exposure simulations, which provide the exposure maps for a single operator (single source).
- ii. Actual dosimeters do not take into account the error induced due to the immediate dosimeter environment (i.e. presence of the human body, or other

Dissemination level: PU

D3.2 Wideband dosimeter: design study & performances characterization FP7 Contract $n^{\circ}318273$



obstacles). This error is quite considerable especially when measuring the Up-Link (UL) exposure, due to the shadowing effect of the human body between the mobile device (emitting source) and the dosimeter position [5], [8], and [9]. However the compensation of the DL bias is addressed in chapter 4.

Version: V1.2



3 LEXNET WEARABLE DOSIMETER DESIGN

In this section, the global design of the wearable dosimeter designed under the LEXNET project, is detailed. First the proposed architecture is defined as a whole. The choice of each component of the architecture was finalized after detailed calculations and discussions. Then each of the sub-components of the dosimeter is presented with details regarding their design and experimental characterization. Finally, a preliminary mechanical design is presented for the integrated solution. The principal characteristics are presented in the Table 1 below.

Characteristics	Description
Measurement capabilities	 Able to contribute to the determination of the EMF exposure index (defined by LEXNET-WP2) Measurement differentiation by application (GSM, DCS, UMTS, LTE, WiFi etc.) and also by service provider Up-Link and Down-Link differentiation Log of measurements
User profile	 Service providers / operators Research organizations Regulatory bodies
Frequency bands	0.7 GHz – 6 GHz
Interface	Bluetooth (tablet / smartphone)USB
Product compliance	 Fully compliant with ICNIRP recommendations / guidelines (Or other references, IARC, WHO,etc.) EC marking compatibility (EMC, electrical safety) Mechanical and climatical certification
Probe sensitivity	• 5 mV/m
Dynamic range	• 60 dB (5 mV/m to 5 V/m)
Dimensions	Smartphone form factor
Weight	• < 400 g

Table 1: Main features of the LEXNET dosimeter

Version: V1.2



The dosimeter has to cover the frequency bands as described in Table 2.

	Start	Center	Stop	BW
LTE 20 - Uplink	791	806	821	30
LTE 20 - Downlink	832	847	862	30
GSM 900 - Uplink	880	897.5	915	35
GSM 900 - Downlink	925	942.5	960	35
DCS1800 - Uplink	1710	1747.5	1785	75
DCS 1800 - Downlink	1805	1842.5	1880	75
DECT	1880	1890	1900	20
UMTS - Uplink	1920	1950	1980	60
UMTS Downlink	2110	2140	2170	60
Wifi	2400	2441.75	2483.5	83.5
LTE band VII - Uplink	2500	2535	2570	70
LTE band VII - Downlink	2620	2655	2690	70
Wimax 3.6GHz	3300	3600	3900	600
Wifi 5 GHz	5150	5487.5	5825	675

Table 2 - Frequency bands requirements

3.1 General architecture and design

At first, two architectures were chosen and studied in parallel. One of them was a low level, simplistic solution with all the complexity focused on one component. The other was a high level, more complex solution with increased flexibility. After initial evaluation, it was decided to merge the two solutions and focus on a single architecture which would be suitable in terms of performance, design flexibility, power consumption, and cost.

The block diagram of the finalized architecture is presented in Figure 4. The main block, marked as "wearable dosimeter", is the actual dosimeter. The external RF block, marked as "optional external front end", is designed for more precise measurements with an external probe.

The first part of the dosimeter is the probe. A three axis probe has been selected for best isotropy. Next there is the band pass filter (BPF) which is a tunable filter for initial frequency selectivity. After that we have the variable gain low noise amplifier (LNA) block to amplify the received signal. This signal is then down-converted to base-band frequencies using the Direct Conversion Receiver (DCR) block. The base-band signal is then detected using a RMS power detector (part of the DCR block) and then sampled by the Analog to Digital Converter (ADC) present in the microcontroller. The measurements are stored in an internal memory block and can be transferred to a PC or a mobile device using the USB or Bluetooth connectivity modules. The



battery provides the power to the RF and digital blocks. The external RF block for increased precision and sensitivity can be connected directly to the internal DCR block via an RF switch connector.

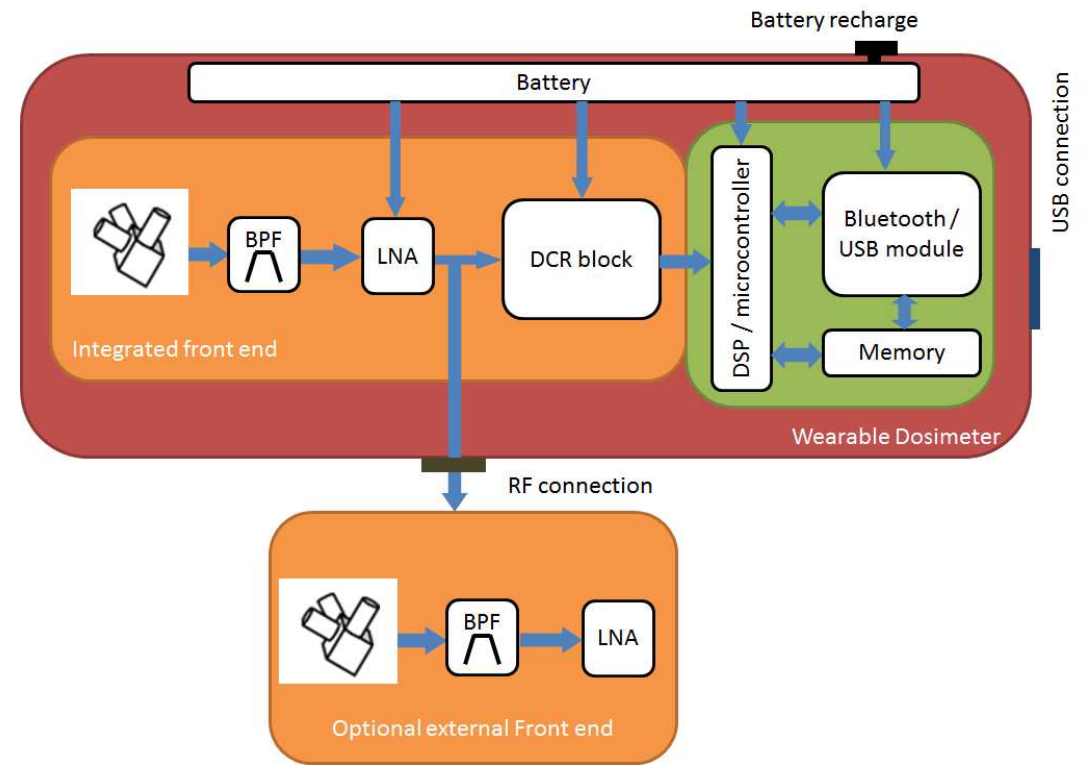


Figure 4: Block diagram of the LEXNET wearable dosimeter

Each of the dosimeter sub-components (blocks) identified in Figure 4 is presented in detail in the following.

3.2 Tri-axial probe

The antenna probe selected for the LEXNET wearable dosimeter is presented in Figure 5. It consists of three monopole ball shaped antennas.

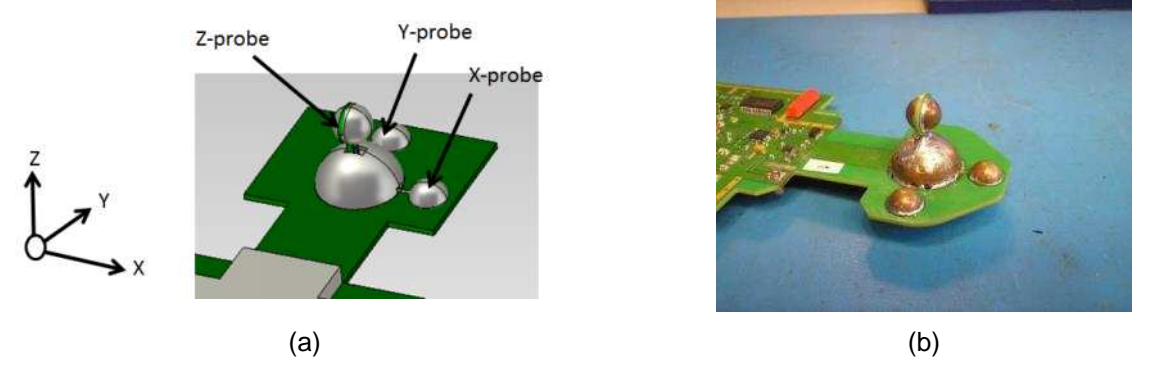


Figure 5 : Tri-axial probe selected for the LEXNET dosimeter (a) simulation model, (b) prototype used in actual EME-SPY dosimeters.



This probe is currently used in the EME-SPY dosimeters [3] for operation between 80 MHz up to 6 GHz. It represents excellent isotropy over the LEXNET frequency band as shown in Table 3 below.

FREQUENCY RANGES	AXIAL ISOTROPY		
	Min - Max	Standard Deviation	
GSM Tx (880 – 915 MHz)	± 2.6 dB	± 1.6 dB	
GSM Rx (925 – 960 MHz)	± 2.4 dB	± 1.5 dB	
DCS Tx (1710 - 1785 MHz)	± 2.3 dB	± 1.3 dB	
DCS Rx (1805 - 1880 MHz)	± 2.2 dB	± 1.4 dB	
UMTS Tx (1920 - 1980 MHz)	± 0.9 dB	$\pm 0.5 dB$	
UMTS Rx (2110 - 2170 MHz)	± 1.3 dB	± 0.6 dB	
WiFi 2G (2400 – 2500 MHz)	± 1.5 dB	$\pm~0.8~dB$	
WiMAX (3400 - 3800 MHz)	± 2.9 dB	± 1.5 dB	
WiFI 5G (5150 - 5850 MHz)	± 3.9 dB	± 2.0 dB	

Table 3: Isotropy of the tri-axial probe over the LEXNET frequency band

The simulation and measured reflection coefficient for the probe are presented in Figure 6 for the three axes. The measurements and simulations were carried out at Satimo industries, Brest, France.

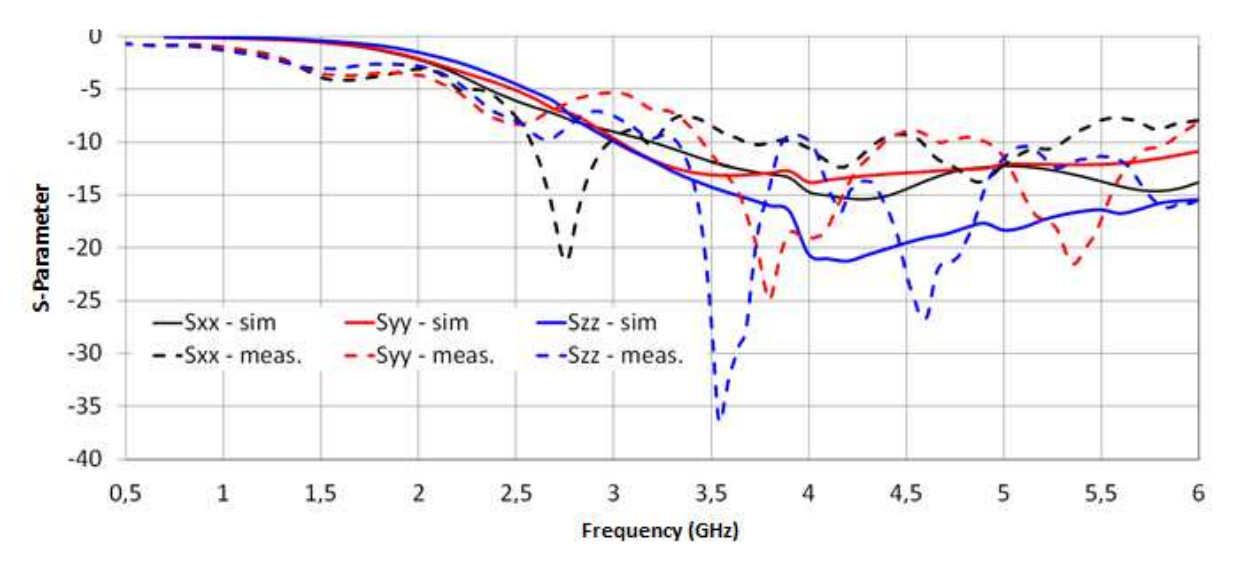


Figure 6 : Comparison between measured and simulation results for the probe reflection coefficient (in dB)



A good agreement in general is observed between the simulation and measurement results. The differences are principally due to the line losses and presence of connecting cables, which were not taken into account in the simulations.

The measured antenna factors for the dosimeter are presented in Table 4 for the different Telecommunication frequency standards present in the LEXNET frequency bandwidth. This measured data will be used in the calculations and determination of the whole system dynamic, sensitivity level, and the required gain ranges required for the low noise amplifier block. The external probe will be a similar one with better antenna factors (larger monopole size, and lower impact of immediate RF components, PCB, and battery) for increased sensitivity levels.

Standard	Centre freq. (MHz)	Antenna factor Probe X (dB)	Antenna factor Probe Y (dB)	Antenna factor Probe Z (dB)
LTE- XX DL	806	49	51	47
LTE -XX UL	847	49	49	46
GSM UL	895	48	49	46
GSM DL	947	47	48	46
DCS UL	1747	41	41	42
DCS DL	1842	41	42	42
UMTS UL	1950	41	43	41
UMTS DL	2140	39	43	41
Wifi	2450	41	43	41
LTE - VII UL	2535	42	42	40
LTE - VII DL	2650	43	43	43
WiMAX	3600	45	44	43
Wifi 5G	5500	48	47	47

Table 4: Measured results for the probe antenna factor over the LEXNET frequency band

3.3 Tunable filter

The tunable filter is the RF Band Pass Filter (BPF) placed just after the antenna and followed by the LNA. This filter provides the first RF selectivity for the whole dosimeter architecture. The design goals for this BPF are:

- RF selectivity
- Low loss
- Distorsion-less response
- Flexibility (ability to be used for different frequency band configurations)
- Small physical size

3.3.1 RF Filter technology overview

Several technologies are available for RF BPF. From a dosimeter designer perspective, the most interesting technologies are:

• Discrete inductor (L) and capacitor (C): discrete components soldered to a PCB.



- Distributed parameters: some components are implemented with sections of transmission lines or coupled transmission lines on a PCB, in a planar structure.
- LTCC (low temperature co-fired ceramics): this is a technology that allows the very compact realization of RF filters in the form of monolithic components, by integrating capacitors, inductors, and transformers.
- SAW (surface acoustic wave): the electrical waves are transformed into mechanical (pressure) waves and back, through the use of transducers that are designed to pass only certain frequencies.

Each option has its pros and cons, summarized in Table 5.

To reach the specification for the tunable filter, a mix of these technologies is used.

	RF Filter Technologies for PCB implementation						
Technology:	Discrete L and C	LTCC and SAW					
Selectivity	low	low	high				
Insertion Loss	high	medium	low				
Distortion	low	low	low				
Flexibility	high	high	low				
Size	medium	large, worse at lower frequencies	small				

Table 5 - Different RF Filter Technologies

3.3.2 Tunable Filter Technology

To be able to monitor different frequency bands, the dosimeter has to switch between different frequency bands. RF switches are used to select one among n filter (Figure 7). This approach has been used in previous designs. It is a simple way to split the specified band into several sub-bands, selecting one different RF filter for each sub-band.



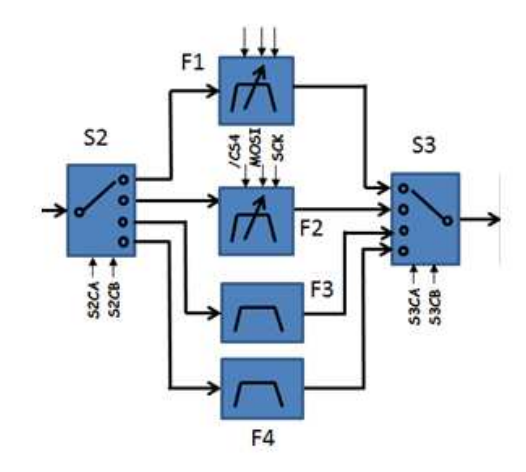


Figure 7 - RF filter selection with 4 way switches

Note that the RF switch brings insertion loss and non-linear distortion. Also this approach is limited by the space available for n way switches. It is desirable to have RF filters with inherent tunability, in order to cover future frequency bands. Such tunability can be obtained by several means:

- Varactor Diodes: these diodes exhibit a variable capacitance as a function of DC reverse bias.
- Integrated tunable capacitor: these are integrated RF switches and MIM (Metal Insulator Metal) capacitors. The capacitance is a function of the digital control word applied to the device.
- Ferroelectric device: these have a variable capacitance depending on the DC bias applied to a ferroelectric substrate, such as Barium-Strontium-Titanate (BST).
- Micro Electromechanical Systems (MEMS): in these devices, variable capacitances are realized with either mechanical switches, or with mechanically actuated membranes.

All these technologies have pros and cons, summarized in the following Table 6 - Different tunable RF Filter Technologies.

	Tunable parts for RF Filter				
Technology:	Varactor Diodes	Integrated BST Switched capacitors Capacitors		MEMS capacitors	
Q factor	Moderate	low	moderate	high	
Intercept Point	Low	low	moderate	high	
Tuning Ratio	Moderate	moderate	low	high	
Tuning Speed	Fast	fast	moderate	slow	
Commercial Availability	high	moderate	low	low	
Cost	low	moderate	moderate	moderate	

Table 6 - Different tunable RF Filter Technologies



3.3.3 Peregrine Digitally Tunable Capacitor choice and validation.

After a search for commercially available parts, it was decided to use Integrated switched capacitors made by Peregrine (Digitally Tunable Capacitor). These cover a large range of capacitance values and are readily available from part distributors.

In the Peregrine DTC, a serial interface is used to control Field Effect Transistor (FET) switches that connect or disconnect High-Q MIM (Metal Insulator Metal) capacitors. The technology employed for these DTC is Silicon on Insulator (SOI) and is characterized by a Figure of Merit (FOM) equal to the product of On state resistance (Ron) times Off state capacitance (Coff). A block diagram of the DTC is shown in Figure 8, and a graph of Capacitance vs. Tuning State is shown in Figure 9.

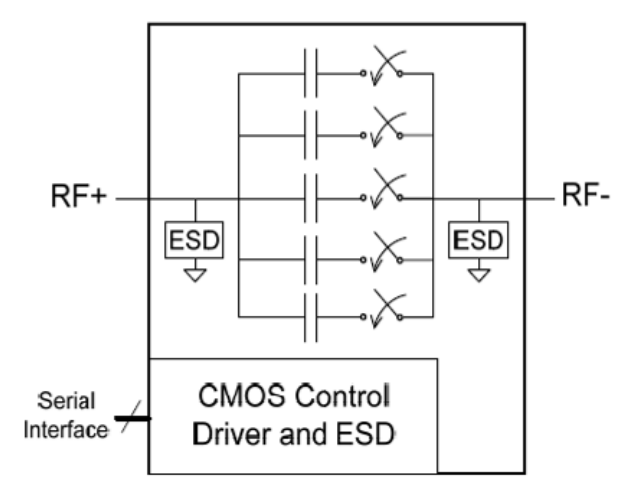


Figure 8 - Block diagram of Peregrine DTC - taken from Peregrine Application Note 29 (DTC Theory of Operation)

Version: V1.2



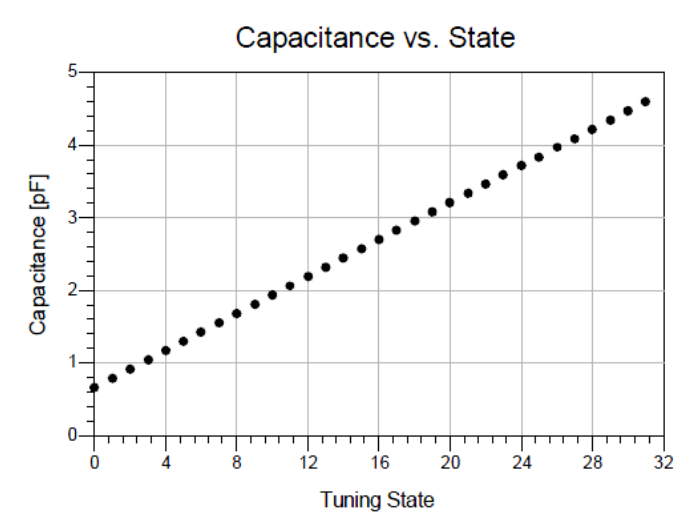


Figure 9 - Capacitance vs Tuning State of DTC – taken from Peregrine Application Note 29 (DTC Theory of Operation)

The Peregrine DTC comes in several part numbers, with different capacitance range and capacitance steps. A linear electrical model is supplied by Peregrine, that integrates the unwanted resistive, capacitive and inductive parasitics (Figure 10). Simulation of this model in Ansys Designer® and comparison with measurements have been performed in order to validate the accuracy of the model.

Figure 11 shows a comparison between measurement and simulation for an LC shunt resonator composed of an inductor and a DTC type PE64102, in two different tuning states.

A good fit can be seen between simulation and measurement.

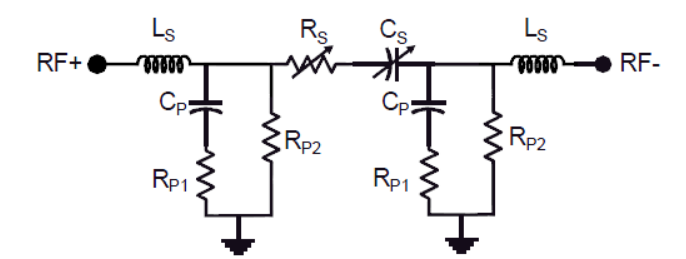


Figure 10 - DTC linear equivalent model - taken from Peregrine Application Note 29 (DTC Theory of Operation)

Version: V1.2



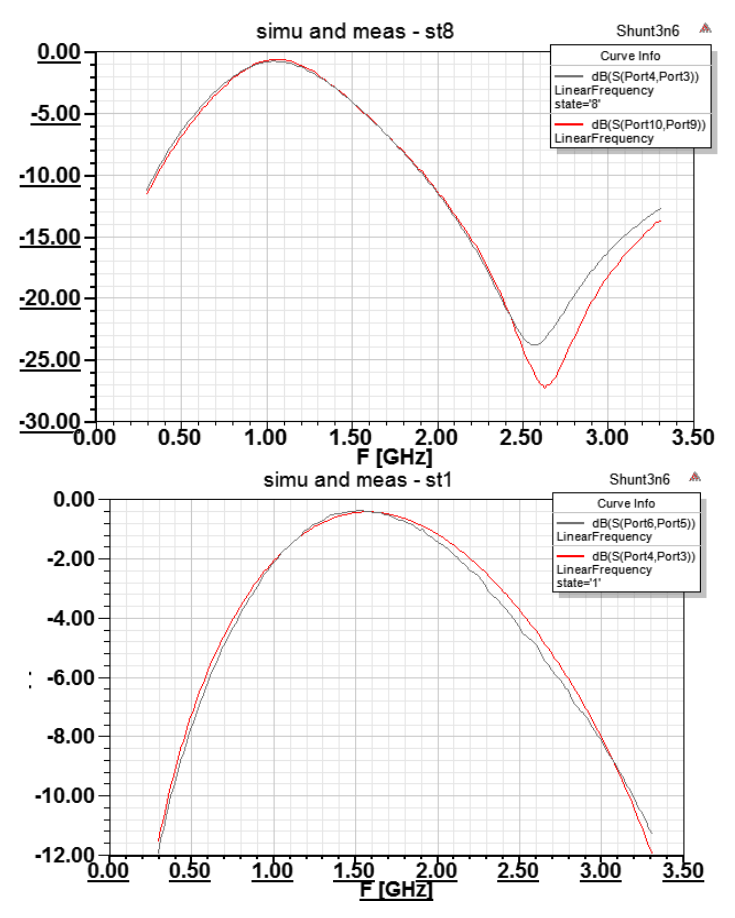


Figure 11 - Simulation (red) vs Measurement (black) of an LC resonator transmission (dB) for state 8 (top) and state 1 (bottom)

3.3.4 Tunable Filter requirements

Regarding the frequency bands to cover Table 2, the following scheme was decided, as a compromise between number of filters, tuning range and flexibility. The RF filter can be switched between 4 different RF filters F1 F2 F3 F4:

- F1: tuning filter for 791 to 960 MHz. (Fmax/Fmin = 1.21)
- F2: tuning filter for 1710 to 2690 MHz. (Fmax/Fmin = 1.57)
- F3: fixed filter for Wimax 3.5GHz.
- F4: fixed filter for Wifi 5.5GHz.

Refer to Figure 7 for RF filter block diagram.

3.3.5 Tunable Filter simulation (791-960 MHz)

The 791-960 MHz BPF has been simulated. The topology (See Figure 12 - Tuning filter 790-960 MHz) is an L coupled shunt resonator with an order 2. Each resonator is composed of:

a fixed inductor (discrete type),



- a fixed capacitor
- and a DTC in parallel.

The simulation result is in Figure 13, showing response for several tuning states.

By testing in simulation, it has been seen that most of the insertion loss is caused by the parasitics of the DTC. Also these parasitics cause a degradation of the rejection at higher frequencies (>3GHz). These can be mitigated by the adjunction of a notch filter (order 2, tuned at 1.9GHz), with still acceptable loss (between 1 and 4 dB IL). Also the filter bandwidth is not constant with tuning frequency: it is larger at higher frequencies, because only the resonators' frequencies are actuated, not the coupling coefficient (top coupling fixed inductor).

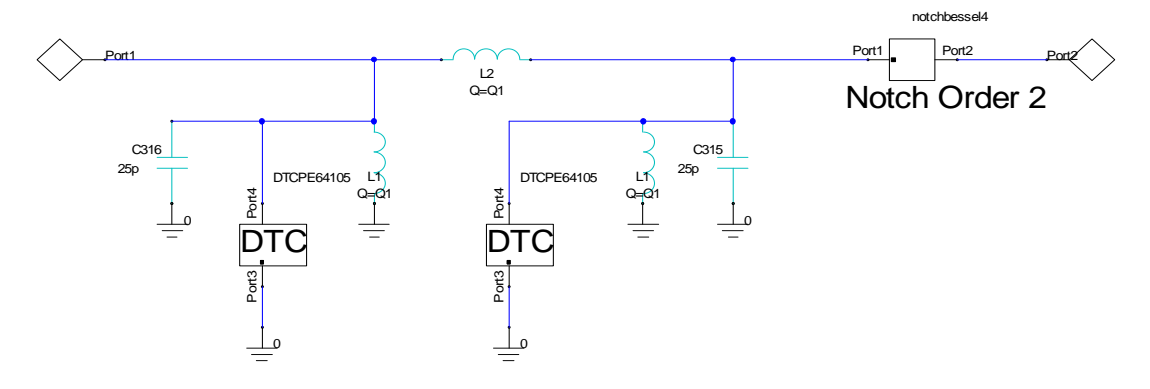


Figure 12 - Tuning filter 790-960 MHz

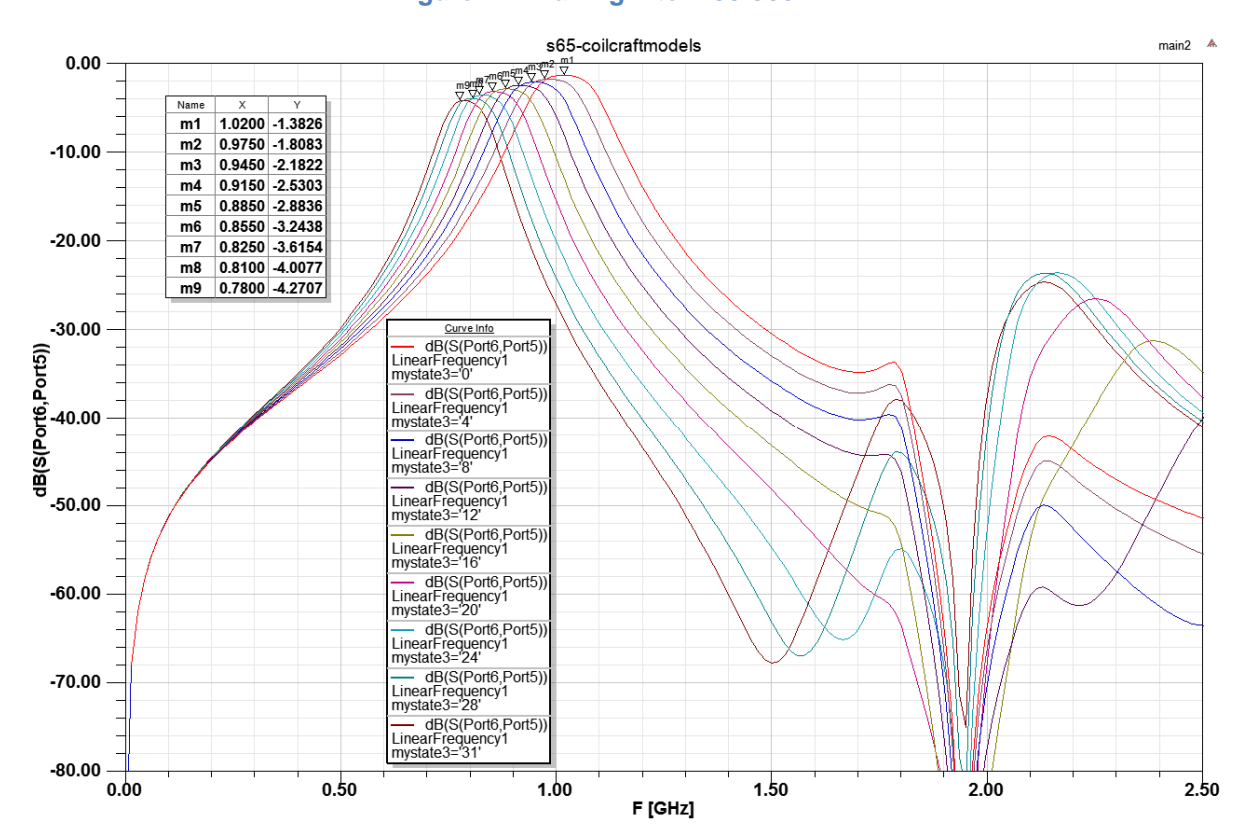


Figure 13 - Simulation Result for F1 Tuning filter (790-960 MHz) for different values of the DTC

Dissemination level: PU

Version: V1.2

31



3.3.6 Tunable Filter simulation (1710-2690 MHz)

The 1710–2690 MHz filter has been simulated. The topology is an L coupled shunt resonator, order 2. Each resonator is composed of a fixed inductor (discrete type), 2 DTC and a varactor diode in parallel. The varactor diode helps to get the tuning range, which is larger for this frequency band.

The DTC with the highest Self-Resonant Frequency (SRF) was chosen for the 1710-2690 MHz filter.

Simulation results for this configuration can be seen in Figure 14. Each filter (F1 and F2) fit within a 16*16mm space.

The realization of a prototype PCB for filter F2 is under progress.

The power consumption is limited to a maximum of 0.14 mA per DTC (typ). The total consumption for the filter bank is well within the DC power budget for the dosimeter.

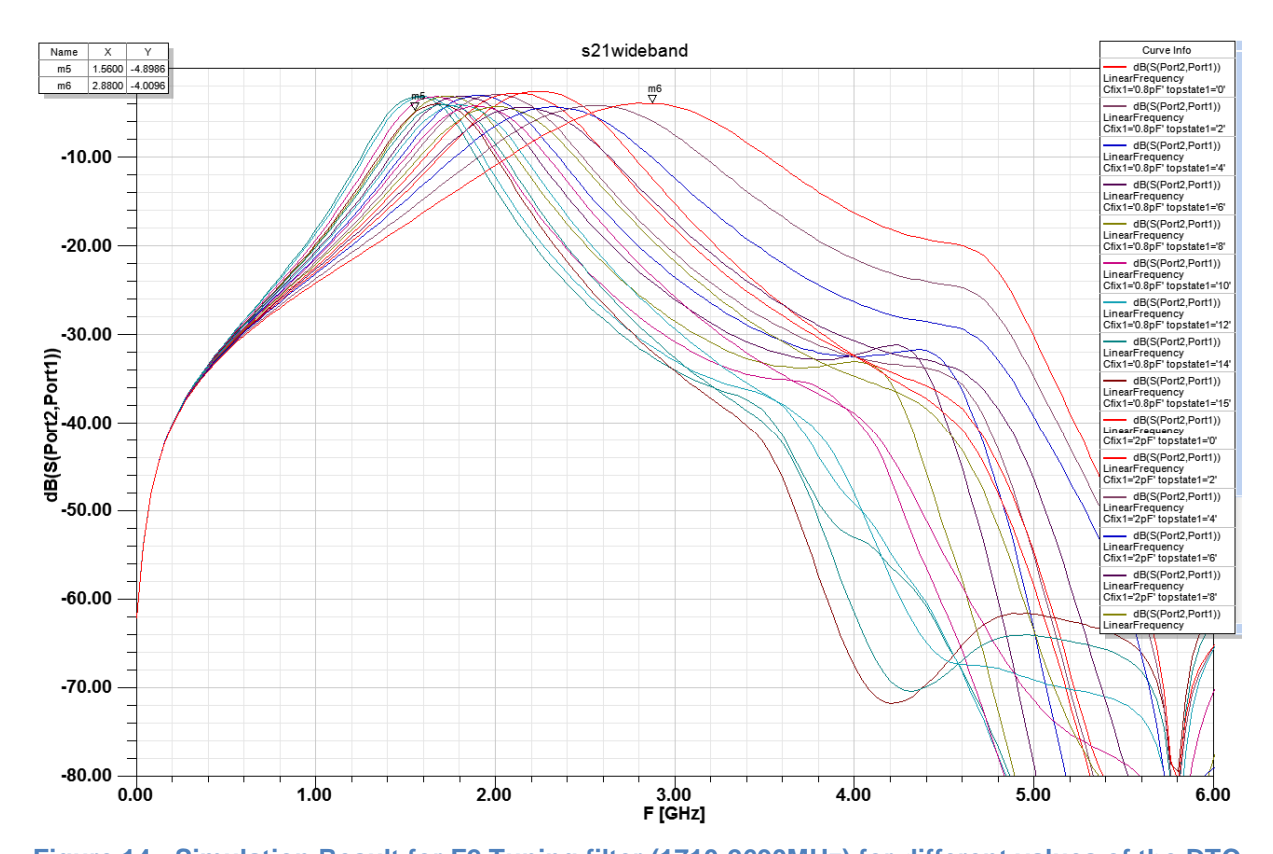


Figure 14 - Simulation Result for F2 Tuning filter (1710-2690MHz) for different values of the DTC

Version: V1.2



3.4 Variable gain LNA

The variable gain LNA is placed just after the tunable filters and followed by the down conversion receiver block. The aims of this stage are:

- to improve the dosimeter sensibility providing a good noise figure,
- to add gain to the RF chain and a dynamic gain control in order to accommodate the input signals to be properly detected,
- to offer enough P1dB and OIP3 to avoid intermodulation products when high interfering signals are wrapping the signal to be measured.

In this section, we will study the design of this variable gain LNA as well as carry out experimental characterization of the different parts.

3.4.1 Design study

The design of the variable gain LNA started with the definition of specifications based on the information from the previous and following blocks. After defining the requirements, we will discuss about the possible configurations to fulfil those specifications.

Some initial calculations were carried out analyzing the antenna factors and expected E-field values. Additionally, the expected losses in the reconfigurable filters were evaluated to estimate the maximum and minimum input power at variable gain LNA, Table 7.

	Values obtained from the antenna factors and expected E-field: min. 5mV/m (74dBµV/m) // max. 5V/m (134dBµV/m)						
Freq. (MHz)	Antenna Factor MAX (dB)	Antenna Factor MIN (dB)	Pant MAX (max. E- field) (dBm)	Pant MIN (min. E- field) (dBm)	Losses up to LNA (dB)	LNA max. Input Power (dBm)	LNA min. Input Power (dBm)
800	47	50	-20	-83	8.8	-28.8	-91.8
900	47	50	-20	-83	8.8	-28.8	-91.8
1900	39	41	-12	-74	9.8	-21.8	-83.8
2400	38	39	-11	-72	9.8	-20.8	-81.8
3600	36	39	-9	-72	8.8	-17.8	-80.8
5500	39	41	-12	-75	8.8	-20.8	-82.8

Table 7: Estimated maximum and minimum input power at LNA

Furthermore, other requirements come from the down conversion receiver block analysis; in this case in terms of P1dB and OIP3, Table 8. The LNA should ensure a free-of-intermodulation spectrum just before the down conversion mixer so we would be able to filter the selected baseband signal and detect its level accurately.

Version: V1.2 33



34

Values						
Frequency (MHz)	Mixer ADL5801 Input P1dB (dBm)	Mixer ADL5801 OIP3 (dBm)	Estimated DRC block gain (dB)			
800	13.3	28.5	11.			
900	13.3	28.5	11.8			
1900	13.3	27	11.8			
2400	14	24.5	11			
3600	12.5	23.5	10.9			
5500	11.5	23	10.8			
HMC1020LP4E power detector input range: -65 to 7dBm (72dB dynamic range)						

Table 8 : Variable gain LNA requirements from DCR block

The gain control feature is required to equalize the level at the final power detector. We must be able to map the range of E-fields values, in this case from 5 mV/m to 5 V/m, into the dynamic range of the power detector. A calibration process will be performed to apply a gain adjustment according to the frequency of E-field to be measured.

Preliminary specifications for the variable gain LNA are summarized in Table 9:

Variable Gain LNA specifications								
Frequency (MHz)	NF, typ (dB)	Gain, nominal (dB)	OIP3 (dBm)	P1dB (dBm)	Attenuation range (dB)			
800		24	28.5	13.3				
900		24	28.5	13.3				
1900	5	18	27	13.3	20			
2400	5	16	24.5	14	20			
3600		14	23.5	12.5				
5500		17	23	11.5				
Operating voltage		5V (or 3.3V) // O	perating current	75mA, typ (100r	nA, max)			

Table 9 : Variable gain LNA specifications

Two different RF configurations were proposed to fulfil all these requirements (Figure 15):

- Option A: LNA + variable gain amplifier solution
- Option B: LNA + digital attenuator + driver amplifier solution



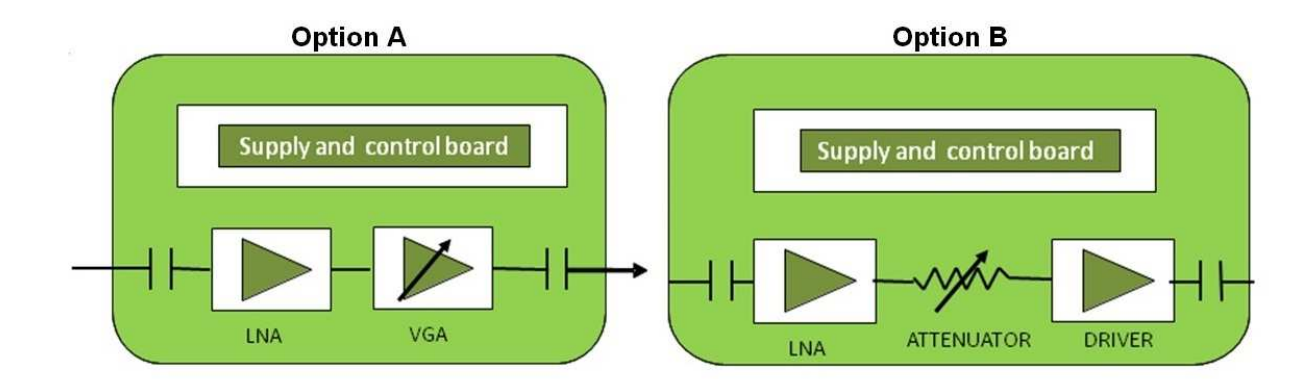


Figure 15 : Two possible configurations for the variable gain LNA: option A (left) and option B (right)

Based on these configurations, a component selection process was carried out:

Option A:

- VMMK-2303 LNA from Avago Technologies [10] was selected. It offers
 2 dB NF and 13-14 dB gain. P1dB and OIP3 are 9-10 dBm and 21 24 dBm respectively. It can works either with 3.3 V (24 mA) or 1.8 V (21mA).
- HMC625LP5 variable gain amplifier from Hittite [11] provides 20 dB maximum gain at 0.8 GHz and 9 dB at 5.5 GHz. P1dB values are 20 dBm and 13 dBm at these frequencies, and OIP3 goes from 35 to 26 dBm.

Option B:

- o VMMK-2303 LNA from Avago Technologies [10] was selected.
- HMC624LP4 digital attenuator from Hittite [11] has insertion losses lower than 4 dB at 6 GHz. It offers an attenuation range of 31.5 dB that can be set with a 6-bits resolution allowing steps of 0.5 dB.
- o 3 driver amplifiers were evaluated:
 - **GVA-83+** from Minicircuits [12]
 - *PGA-1021*+ from Minicircuits [12]
 - *NBB-400* from RFMD [13]

GVA-83+ presents higher OIP3 level (29-31 dBm) with higher power consumption (72 mA @ 5 V), while *PGA-1021*+ has lower OIP3 level (26.5-27 dBm) with lower power consumption (57 mA @ 3.3 V). Finally, *NBB-400* has an intermediate power consumption (50 mA @ 5 V) but lower P1dB (13-15 dBm) even having a good OIP3 performance (29 dBm).

3.4.2 Experimental characterization

Once the main specifications were clearly defined, and possible RF configurations were presented, some measurements on evaluation boards from individual parts



were carried out. As the final design should find a trade-off between power consumption and P1dB/OIP3 performance, option A was discarded and in option B, **PGA-1021+** was selected as the most promising part to fulfil RF requirements. Therefore only measured values from selected parts are presented.

Below test results from evaluation boards for selected parts for the variable gain LNA (*VMMK-2303 + HMC624LP4 + PGA-1021+*) are presented.

VMMK-2303 characterization:

LNA is suitable for the first stage of the variable gain LNA. It can work with 3.3 V or 1.8 V supply, having low current consumption, and few external components (an advantage in terms of board size and mounting ease).

After modifying some component values on the evaluation board (Figure 16) to improve its performance over the full operating band, we made some gain, P1dB and OIP3 measurements.



Figure 16: Photograph of the VMMK-2303 evaluation board

VMMK-2303 experimental characterization Vd = 3.3V ; Vc = 1.8V ; Id = 24mA							
Freq. (MHz)	S11 (dB)	S21 (dB)	S22 (dB)	S22 (dB)	P1dB (dBm)	G1dB (dB)	OIP3 (dBm)
650	-5.1	12.7	-20.9	-8.4	8.9	11.7	24.0
890	-7.1	13.6	-19.9	-10.1	10.1	12.6	24.0
950	-7.5	13.7	-20.0	-10.4	10.2	12.6	24.1
1750	-11.0	13.7	-19.8	-14.8	10.6	12.7	24.7
1840	-11.2	13.7	-19.8	-15.1	10.5	12.7	24.8
1890	-11.3	13.7	-19.9	-15.2	10.6	12.6	24.9
1950	-11.4	13.6	-20.0	-15.3	10.5	12.6	25.0
2140	-11.7	13.6	-20.1	-15.6	10.6	12.5	25.2
2450	-12.4	13.4	-20.2	-15.3	10.5	12.4	25.2
3600	-13.6	12.9	-21.3	-12.6	10.1	11.9	24.8
5500	-13.1	12.3	-25.7	-8.1	10.5	11.3	24.2

Table 10: VMMK-2303 measured features with 3.3 V supply



	VMMK-2303 experimental characterization Vd = 1.8V ; Vc = 1.8V ; Id = 21mA												
Freq. (MHz)	S11 (dB)	S21 (dB)	S22 (dB)	S22 (dB)	P1dB (dBm)	G1dB (dB)	OIP3 (dBm)						
650	-5.2	12.8	-21.0	-8.8	8.2	11.8	23.0						
890	-7.3	13.7	-20.1	-10.7	9.2	12.7	23.0						
950	-7.6	13.7	-20.0	-11.2	9.3	12.7	23.1						
1750	-11.2	13.7	-19.9	-17.1	9.7	12.8	23.7						
1840	-11.4	13.7	-19.9	-17.5	9.7	12.7	23.8						
1890	-11.6	13.7	-19.8	-17.7	9.7	12.7	23.9						
1950	-11.7	13.7	-20.0	-18.0	9.7	12.7	23.9						
2140	-12.0	13.6	-19.9	-18.5	9.7	12.6	24.1						
2450	-12.7	13.5	-20.0	-18.4	9.7	12.5	24.2						
3600	-13.9	13.0	-21.0	-15.0	9.5	12.0	24.1						
5500	-14.2	12.6	-24.4	-10.0	10.0	11.6	24.0						

Table 11: VMMK-2303 measured features with 1.8V supply

As we can see in Table 10 and Table 11, the LNA achieves good performance with both polarization points. Therefore, 1.8 V is the suitable bias point with an operating current of 21 mA. Furthermore, it provides around 2 dB wideband NF that allows a total NF lower than the specified 5 dB.

HMC624LP4 characterization:

The digital attenuator can work with 3.3 V or 5 V supply, and shows high OIP3. Its operating current is almost negligible, 2 mA. It offers a dual mode control interface which is CMOS/TTL compatible, and accepts either a three wire serial input or a 6 bits parallel word.

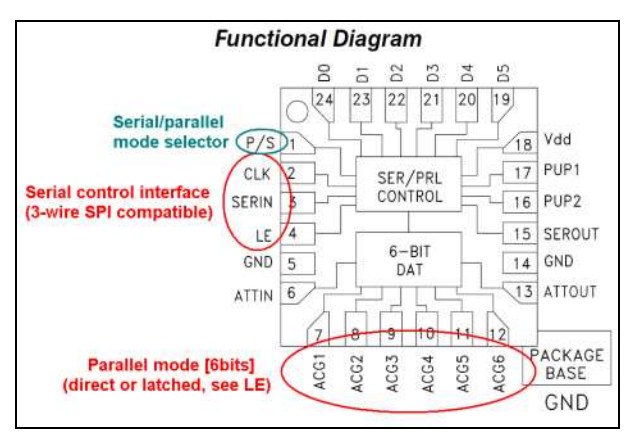


Figure 17: HMC624LP4 functional diagram showing its control interfaces

PGA-1021+ characterization:

Measurements from the evaluation board of the *PGA-1021+* (Figure 18) are shown in Table 12.



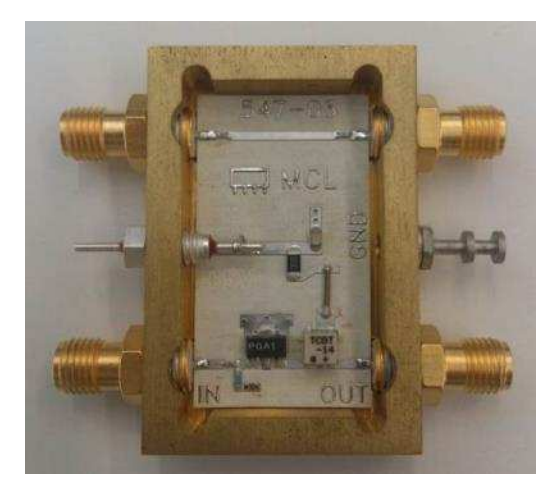


Figure 18: Photograph of the PGA-1021+ evaluation board

	PGA-1021+ experimental characterization Vcc = 3.3V ; Icc = 57mA												
Freq. (MHz)	Hz) S11 (dB) S21 (dB) S22 (dB) S22 (dB) P1dB (dBm) G1dB (dB) OIP3 (dBr												
650	-18.0	15.1	-21.2	-25.7	17.6	14.2	26.3						
890	-16.6	14.7	-21.3	-24.4	17.7	13.8	26.3						
950	-16.2	14.7	-21.2	-24.1	17.7	13.8	26.4						
1750	-12.3	13.3	-21.6	-18.3	17.8	12.5	26.7						
1840	-11.9	13.1	-21.6	-16.9	17.8	12.2	26.9						
1890	-11.5	12.6	-22.0	-14.7	17.4	11.7	27.0						
1950	-11.5	13.0	-21.7	-17.5	17.6	12.2	26.9						
2140	-11.1	12.8	-21.9	-17.6	18.0	11.9	26.5						
2450	-10.5	12.3	-21.9	-16.5	18.1	11.5	26.5						
3600	-9.5	11.1	-22.4	-14.9	18.1	10.2	26.8						
5500	-11.4	10.4	-22.0	-13.2	17.4	9.4	27.3						

Table 12 : PGA-1021+ measured features

Based on measured results from evaluation boards, a block diagram analysis at 4 different frequencies was performed in Table 13 to evaluate the expected variable gain LNA specifications, once these 3 stages will be merged in a single PCB prototype.

Version: V1.2 38



LNA + ATT	V + PGA-	1021+ @ 9	00MHz	LNA + ATT	/ + PGA-1	021+ @ 19	900MHz
Component P/N	VMMK-2303	HMC624LP4	PGA-1021+	Component P/N	VMMK-2303	HMC624LP4	PGA-1021+
Component type	LNA	Variable ATT	Driver	Component type	LNA	Variable ATT	Driver
NF (dB)	2.0	1.6	2.3	NF (dB)	2.0	1.9	2.4
Gain (dB)	13.7	-1.6	14.8	Gain (dB)	13.8	-1.9	12.6
OIP3 (dBm)	23.0	50.0	26.3	OIP3 (dBm)	23.9	50.0	27.0
P1dB (dBm)	9.3	30.0	17.7	P1dB (dBm)	9.8	30.0	17.4
Aggreg. values	VMMK-2303	HMC624LP4	PGA-1021+	Aggreg. values	VMMK-2303	HMC624LP4	PGA-1021+
NF (dB)	2.0	2.1	2.2	NF (dB)	2.0	2.1	2.2
Gain (dB)	13.7	12.1	26.9	Gain (dB)	13.8	11.9	24.5
OIP3 (dBm)	23.0	21.4	25.9	OIP3 (dBm)	23.9	22.0	26.3
P1dB (dBm)	9.3	7.6	16.4	P1dB (dBm)	9.8	7.8	15.7
LNA + ATT\	/ + PGA-1	021+ @ 23	300MHz	LNA + ATT	V + PGA-1	021+ @ 5	500MHz
Component P/N	VMMK-2303	HMC624LP4	PGA-1021+	Component P/N	VMMK-2303	HMC624LP4	PGA-1021+
Component type	LNA	Variable ATT	Driver	Component type	LNA	Variable ATT	Driver
NF (dB)	2.0	2.0	2.6	NF (dB)	2.0	4.5	3.6
Gain (dB)	13.5	-2.0	12.6	Gain (dB)	12.6	-4.5	10.4
OIP3 (dBm)	24.2	50.0	26.5	OIP3 (dBm)	24.0	50.0	27.3
P1dB (dBm)	9.7	30.0	18.1	P1dB (dBm)	10.0	30.0	17.5
Aggreg. values	VMMK-2303	HMC624LP4	PGA-1021+	Aggreg. values	VMMK-2303	HMC624LP4	PGA-1021+
Aggreg. values NF (dB)	VMMK-2303 2.0	HMC624LP4 2.1	PGA-1021+	Aggreg. values NF (dB)	VMMK-2303 2.0	HMC624LP4 2.3	PGA-1021+ 2.7

Table 13: Evaluation of the variable gain LNA expected performance

25.9

16.0

OIP3 (dBm)

P1dB (dBm)

24.0

10.0

19.5

5.5

13.6

The expected NF is pretty lower than the specified one, keeping suitable gain level which can be adjusted thanks to 31.5 dB attenuation range from the digital attenuator. Finally, the selected driver amplifier fits P1dB and OIP3 requirements.

The total power consumption is around 80 mA with 3.3 V supply voltage.

22.2

7.7

Next step will be to evaluate a single PCB prototype with 3 stages (*VMMK-2303* + *HMC624LP4* + *PGA-1021*+) to be finally integrated in the wearable dosimeter.

.

OIP3 (dBm)

P1dB (dBm)

24.2

Version: V1.2



3.5 DCR block

After the signal is amplified from the LNA block, the next step is the down-conversion. The proposed architecture for the DCR block is presented in Figure 19 with references for each of the sub-components.

The RF signal coming from the amplification block enters the wide band RF mixer. This mixer has an operating range from 10 MHz up to 6 GHz. The local oscillator (LO) signal for this mixer comes from a wide band controlled reference clock. The Phase Locked Loop - Voltage Controlled Oscillator (PLL-VCO) operating range is between 25 MHz up to 6 GHz. Next the intermediate frequency (IF) signal at the output of the wide band mixer goes to the IF base band tunable LPF. This filter has two paths (for the I and Q channels). In our case, only one of the two paths is used. The IF filter block includes two base-band variable gain amplifiers per path, to provide increased gain at baseband frequencies. The tuning frequency for the Low Pass Filter (LPF) can be set between 3.5 MHz and 50 MHz. Once the IF signal is amplified and filtered, it goes towards the RMS power detector. This detector has a wide dynamic range at base band frequencies (up to 70 dB) and it is the main limiting component in the dynamic range and sensitivity of the whole dosimeter. Once the base-band power is converted to a voltage level, it is then sampled easily by the ADC in the microcontroller. Using a lookup table, the digital voltage level is then converted to RMS power using the characteristic of the power detector. This power can then be converted to E-field (in V/m) using the RF chain characteristics (antenna factor and RF chain gain).

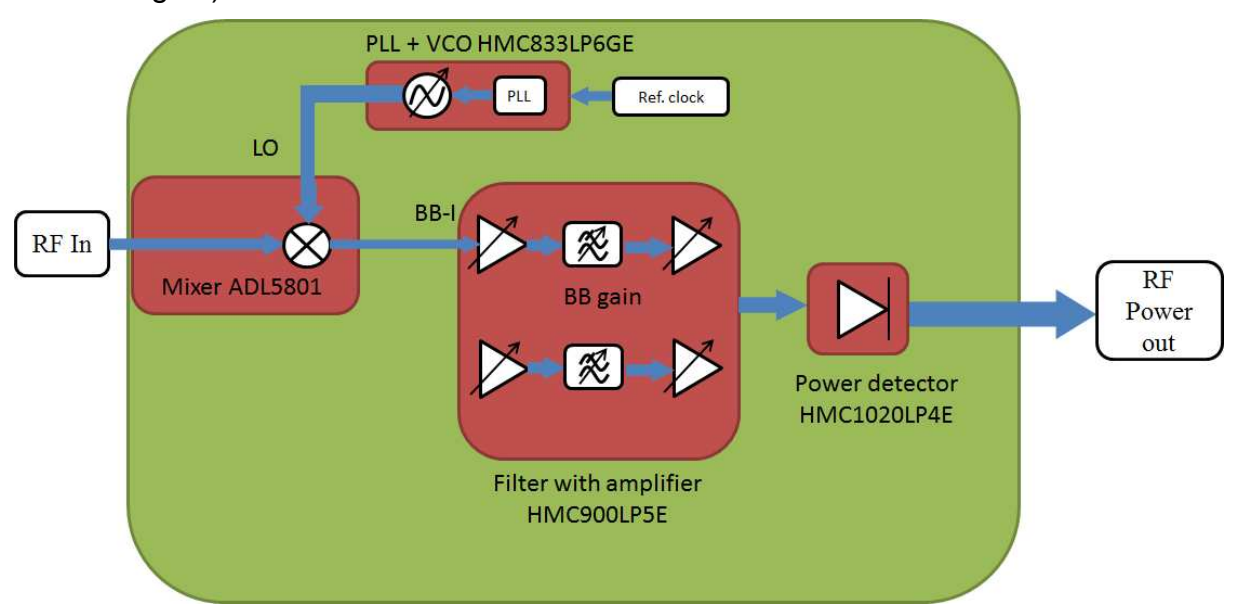


Figure 19: Direct Conversion Receiver block diagram

Individual experimental validation of each of sub-component and the complete DCR block test results are presented in the following.



3.5.1 Wide band PLL-VCO: HMC833LP6GE

The wide band PLL-VCO [14]**Erreur! Source du renvoi introuvable.** was tested separately at Satimo industries, Brest, France using a demo-board, a PC, and a spectrum analyzer. The test bench is presented in Figure 20 in the form of a block diagram and the actual setup.

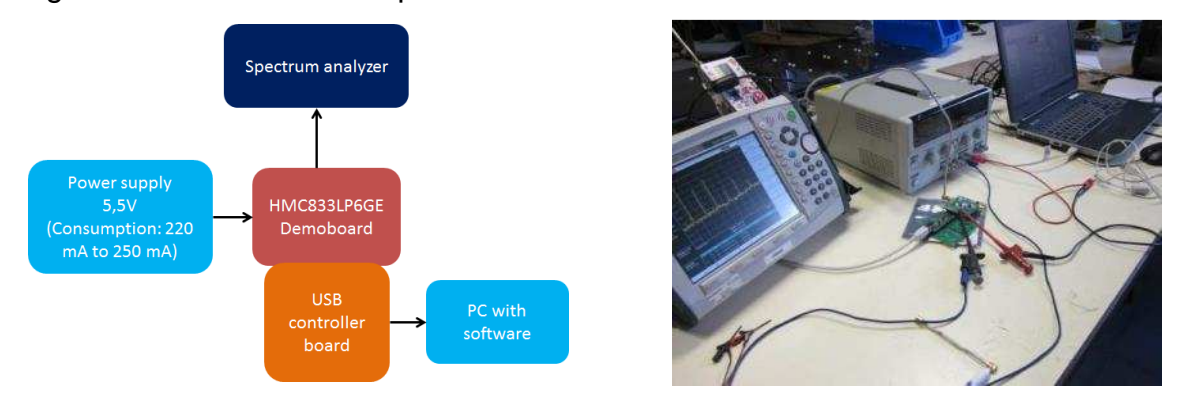
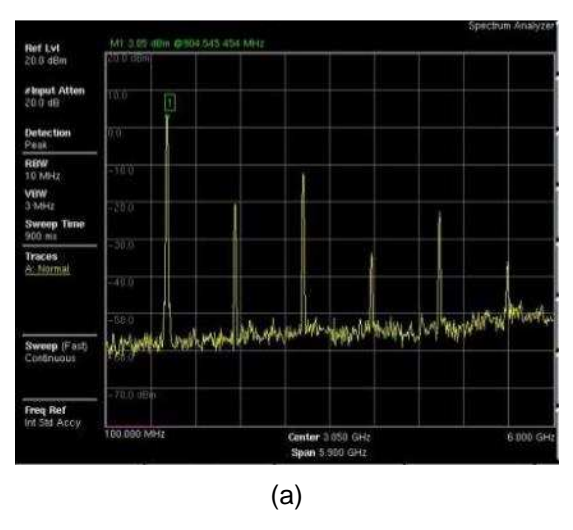
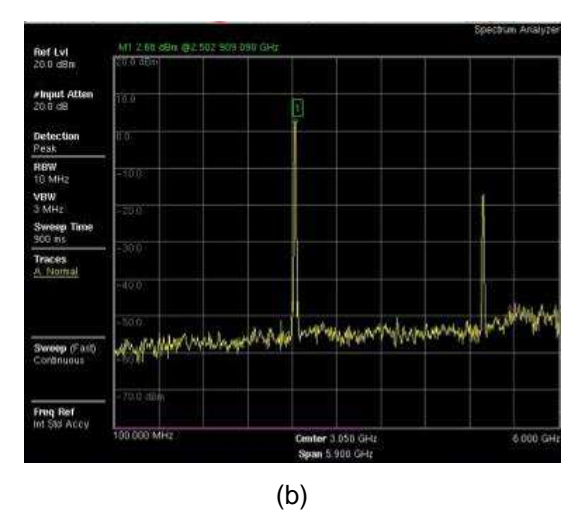


Figure 20: PLL VCO HMC833LP6GE test bench for characterization

To characterize this component, we programmed the PLL-VCO using the software provided with the demoboard at different frequencies and studied the spectral response on the spectrum analyzer over the whole LEXNET bandwidth (up to 6 GHz). The aim was to compare the accuracy of the LO signal frequency and the harmonic levels with those specified in the datasheet. As seen in the Table 17, the total consumption of this component is around 250 mA maximum which is quite significant. This component is the most power consuming one in the LEXNET dosimeter architecture.

In the Figure 21, we present some screen shots of the spectrum analyzer at different frequencies. We can see that when the PLL-VCO is programmed to 900 MHz, it has high level of harmonics which could disturb the output of the mixer when the incoming RF signal is composed of all frequencies. To avoid this phenomenon, the output of the PLL-VCO will be filtered to suppress the harmonic levels.





Version: V1.2



Figure 21 : Output of the PLL-VCO on the spectrum analyzer for (a) 900 MHz, and (b) for 2500 MHz

Comparing the measured performance with the one in the data sheet, the harmonic levels are in good agreement as shown in Table 14.

Parameter	Condition	Min.	Тур.	Max.	Units	
Harmonics for Fundamental Mode						
fo Mode at 2 GHz	2nd / 3rd / 4th		-20/-29/-45		dBc	
fo/2 Mode at 2GHz/2 = 1 GHz	2nd / 3rd / 4th		-23/-15/-35		dBc	
fo/30 Mode at 3 GHz/30 = 100 MHz	2nd / 3rd / 4th		-25/-10/-33		dBc	
fo/62 Mode at 1550 MHz/62 = 25 MHz	2nd / 3rd / 4th		-17/-8/-21		dBc	
Harmonics in Doubler Mode						
2fo Mode at 4 GHz	½ / 3rd / 4th/5th		-7/-23/-15/-40	-4/-15/-7/-28	dBc	

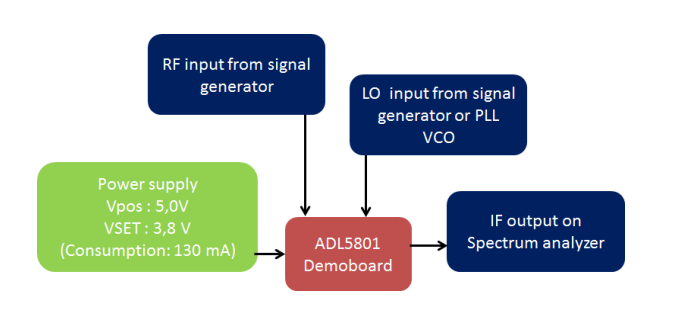
(a)

Fundamental frequency (MHz)	Fundamental mode power at o/p (dBm)	Harmonic levels up to 6GHz with reference to the fundamental mode (dBm) 2nd / 3rd / 4th
900 MHz	3.05	-24 / -16 / -37
1800 MHz	4.97	-19 / -20
2500 MHz	2.70	-20
	(b)	

Table 14: Harmonic levels for the PLL-VCO from (a) datasheet, and (b) measurements

3.5.2 Wide band mixer: ADL 5801

The wide band mixer demo board was used for its characterization. The test bench setup is shown in Figure 22. Two input RF sources were used. The RF input to the mixer comes from a wide band signal generator and the LO input from a signal generator at first and then from the PLL-VCO which was presented in the previous section. The mixer requires two power supply voltage levels. The 5 volt supply is the one which consumes 130 mA of current. The 3.8 V level can be applied using a resistive voltage divider circuit as it does not consume any current. The output of the mixer (IF frequency) was observed on a spectrum analyzer.



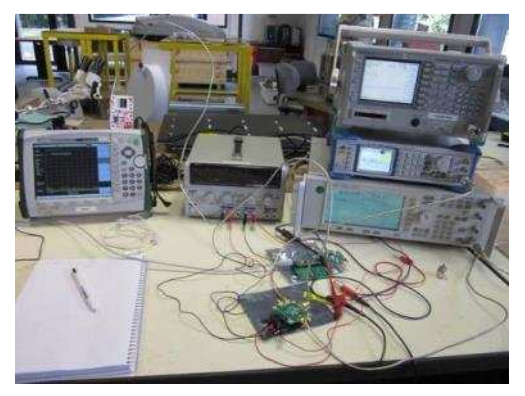


Figure 22: Mixer ADL5801 test bench for characterization

Version: V1.2



The ADL5801 is a high linearity, doubly balanced, active mixer with operating range between 10 MHz up to 6 GHz. The IF output can vary from DC up to 6000 MHz. To characterize this mixer, we provided several input frequencies at the RF input from the signal generator. Results from two extreme scenarios are shown in the Figure 23 below.

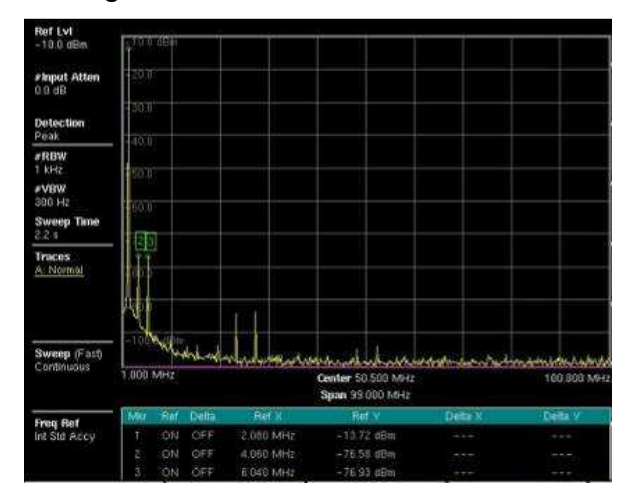




Figure 23 : Wide band mixer IF output for, (a) RF = 898 MHz @ -10 dBm; LO = 900 MHz @ 0 dBm, (b) RF = 898 MHz @ -85 dBm; LO = 900 MHz @ 0 dBm

The first case is with strong RF and LO input levels to see the harmonics at the IF output. The -10 dBm RF input level was chosen as it represents the worst case scenario for the LEXNET dosimeter. It corresponds to a maximum 5 V/m input at the dosimeter probe. The IF output (Figure 23a) shows a fundamental frequency at 2 MHz with 2nd and 3rd level harmonic levels around at -63 dB with respect to the fundamental frequency level. These values correspond to the ones announced in the datasheet.

Next a very low level RF input was used (-85 dBm), while the LO input levels remained the same as in the previous case. This RF level corresponds to the 5mV/m E-field at the dosimeter probe input (sensitivity level). The results (Figure 23b) show that the fundamental IF level is still at 2 MHz, with harmonics below the noise floor.

3.5.3 Tunable low pass filter: HMC900LP5E

The programmable LPF was evaluated using the demoboard and the software provided with it. The test bench setup is presented in Figure 24. This filter has two RF chains for use as I and Q channels. In our case, we need only one of the two filter chains. Hence, one of the RF chain was switched off. This reduces the current consumption by about 60 mA. The total consumption is thus 90 mA for this component.



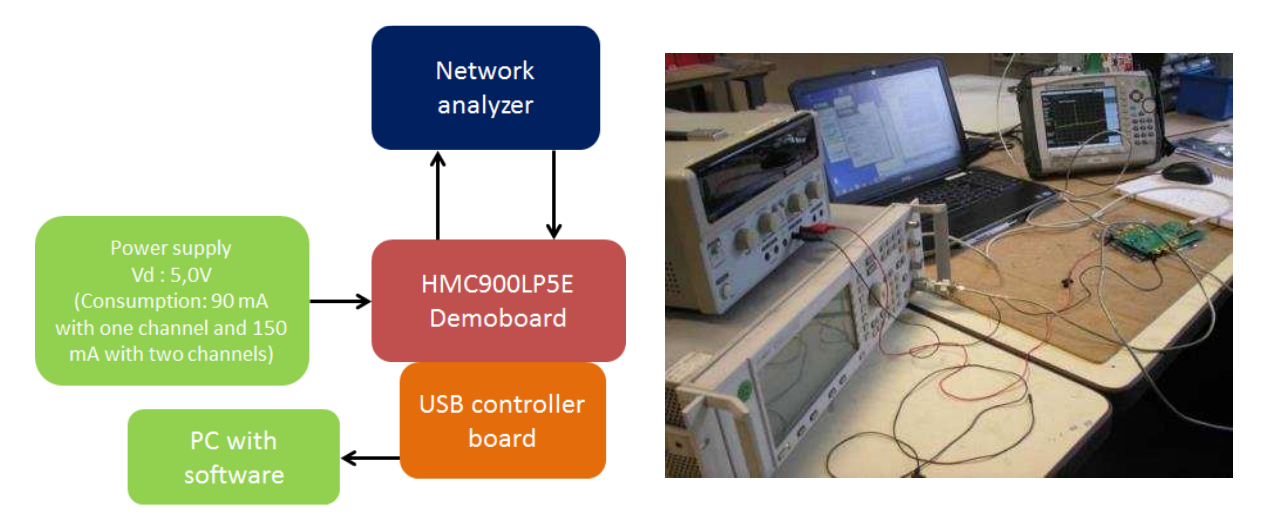


Figure 24: Tunable low pass filter HMC900LP5E test bench for characterization

To evaluate this programmable filter, it was connected to a network analyzer and the software was used to program different cut-off frequencies. The results are compared in the Figure 25 below.

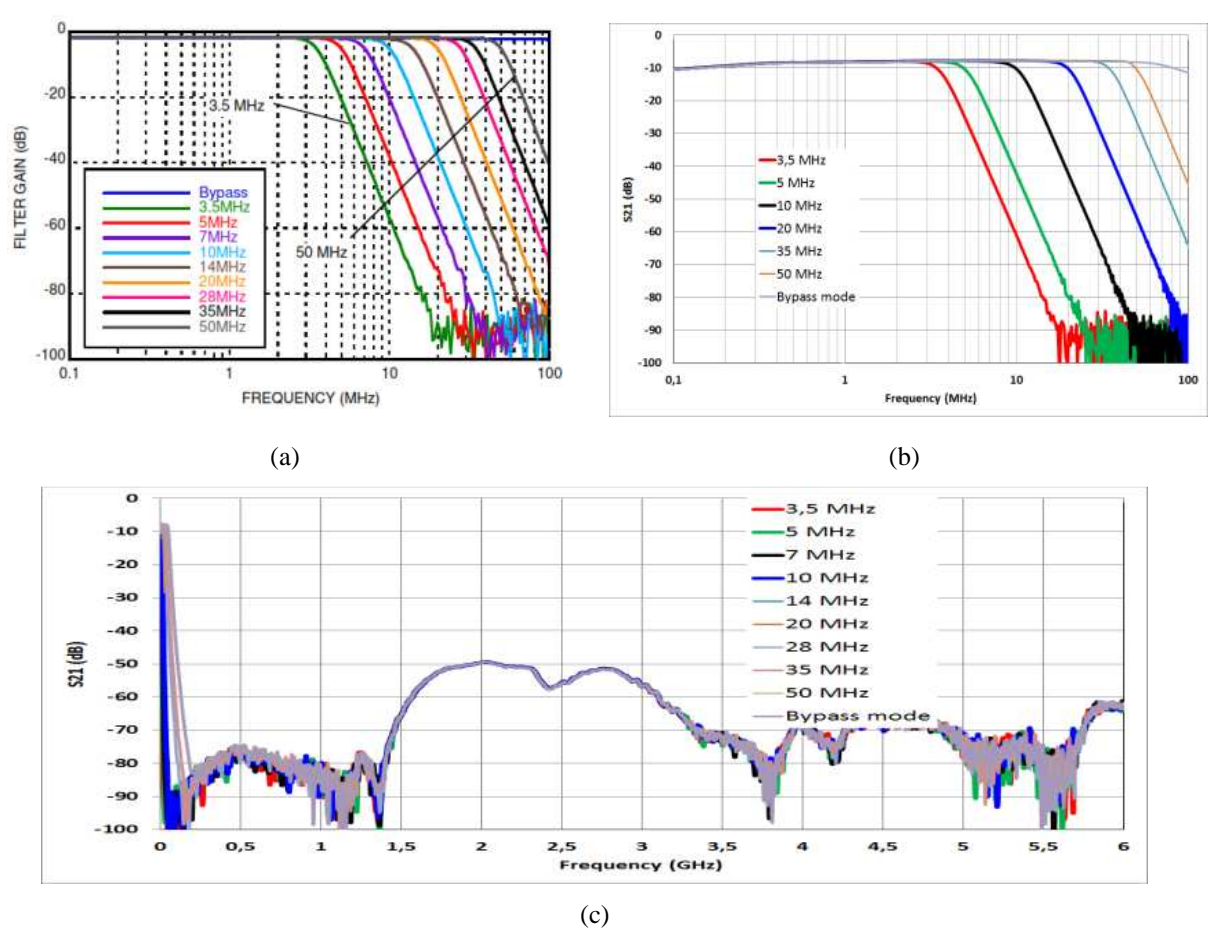


Figure 25 : Tunable low pass filter results from network analyzer, (a) datasheet, (b) measurements over narrow band, (c) measurements up to 6 GHz.

Version: V1.2



The results are in excellent agreement in terms of rejection levels. The loss of about -9 dB observed in the measurements is due to fact that there is an attenuator of -19.8 dB at the output of the low-pass filter demoboard (not taken into account for the results in the datasheet). And with the gain set at maximum of 10 dB, we find the -9dB value as observed in the measurements. The measurements up to 6 GHz are shown in Figure 25c which shows minimum attenuation levels of about 50 dB over the whole frequency band.

3.5.4 RMS power detector: HMC1020LP4E

The final component in the RF chain is the RMS power detector. The test bench for its characterization is presented in Figure 26. A 5v power supply is needed for the power detector with the consumption varying between 50 and 60 mA corresponding to the input power level. The input RF signal was generated using a signal generator. The output was observed on a voltmeter.

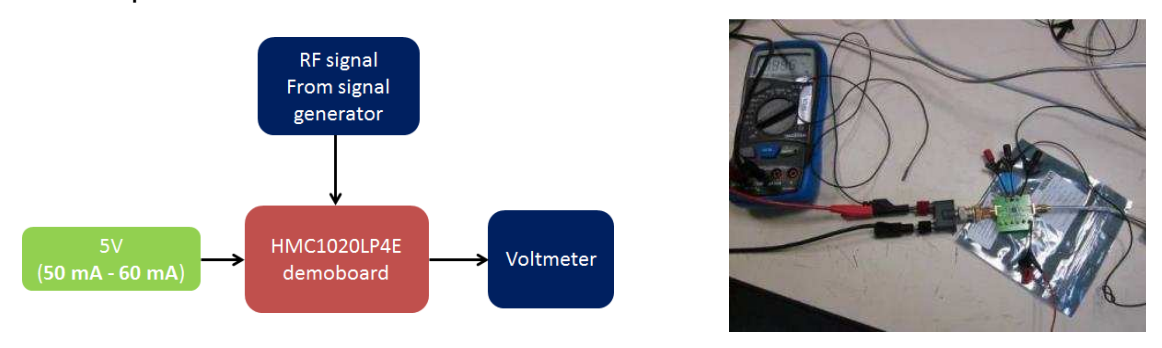


Figure 26: RMS power detector HMC1020LP4E test bench for characterization

To evaluate this component, the RF input signal was varied over the IF frequency band (up to 100 MHz). The power levels were varied for each test frequency between -70 dBm and +10 dBm. The datasheet had results starting from 100 MHz up to the 3.9 GHz limit. After exchange with the suppliers, we managed to acquire results for the power detector for frequencies below 100 MHz. For these frequencies, the DC coupling capacitors at the detector input were changed to 10 μ F (from 1 nF initially). The results are shown in Figure 27 below. Excellent agreement is observed with a measured dynamic range of more than 70 dB.

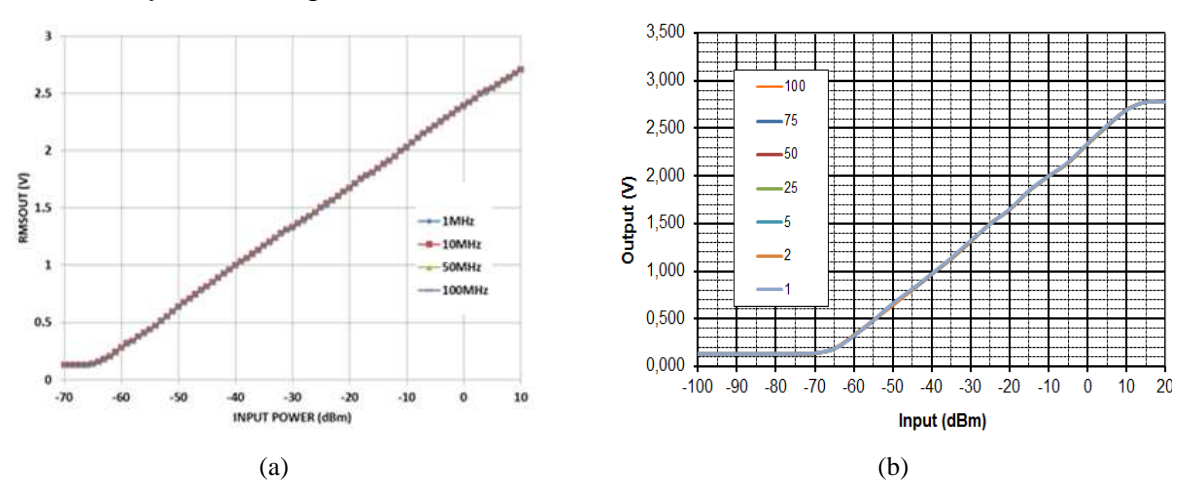


Figure 27: RMS power detector results from (a) datasheet, (b) measurements

Version: V1.2 45



3.5.5 DCR block measurements in CW

After validation of each of the individual components of the DCR block, several tests were carried out in cascading the whole DCR chain.

The first test was carried out with a two-tone RF input using two-signal generators (RF1 and RF2) and a power combiner circuit. The two-tone input signal was injected into the wide band RF mixer. The LO signal was provided through the programmable PLL-VCO. The output from the mixer (IF frequency) was connected to the tunable LPF. Finally the output of the filter was connected to the RMS power detector. The output of the power detector was observed on the oscilloscope. The test bench setup is presented in Figure 28 below.

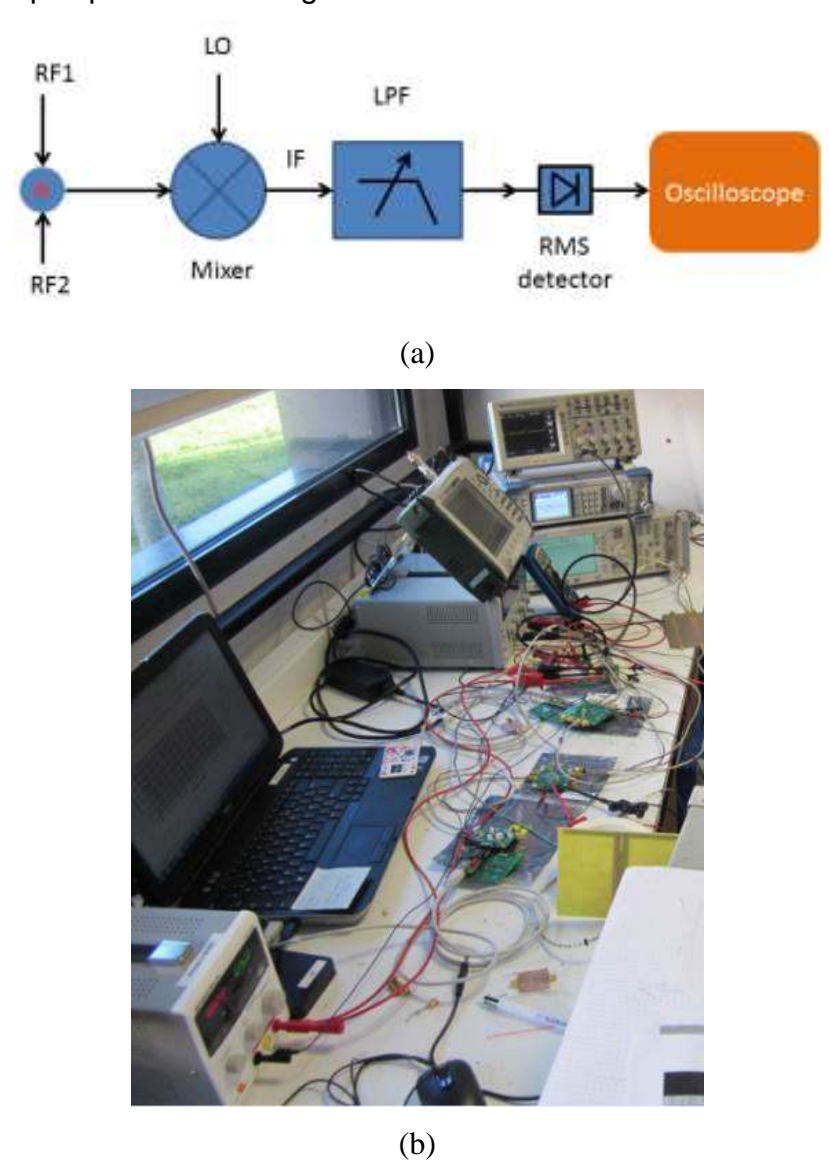


Figure 28: Test bench setup for two-tone RF input characterization of the DCR block

The total current consumption of the DCR block was around 470 mA with two voltage levels of 5 V and 3.8 V. The 3.8 V level did not draw any current.

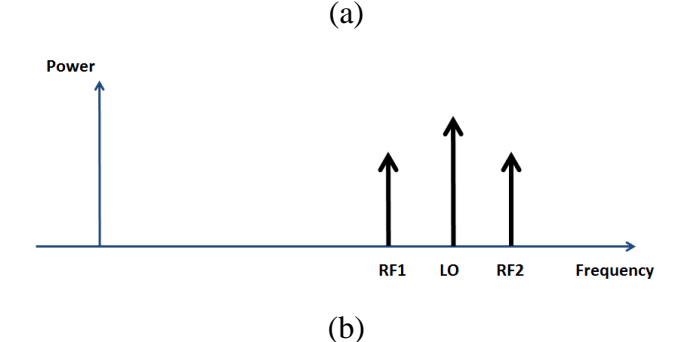
Version: V1.2 46



The RF1 frequency was set to 905 MHz and RF2 at 895 MHz. Both RF signal power levels were fixed at -50 dBm at first. The LO signal was fixed at 900 MHz at -10 dBm from the PLL-VCO. This corresponds to the worst case scenario, when the LO frequency is in the middle of two RF signals. Both signals when down-converted to baseband at the same frequency (IF = RF2 - LO = LO - RF1), generates a modulation which gives an incorrect reading of the total power. This problem can be avoided using an appropriate integration time for the RMS power detector. The power detector integration time was then varied using the 4bit-digital inputs from minimum (corresponding to 0000) to intermediate (1000) values. The LPF was programmed for a cut-off frequency of 5 MHz.

The RF1 and RF2 sources were switched ON and OFF and the behavior of the output voltage signal after the power detector was observed through an oscilloscope. The results are summarized in the Table 15 below.

	RMSOUT Ris	se-Time 10% ->	> 90% (µs) ^[3]	RMSOUT	Rise Settling 1	Γime (μs) ^[2]	RMSOUT Fall-time 100% -> 10% (μs) [4]			
SCI4,3,2,1	Pin = 0 dBm	Pin = -20 dBm	Pin = -40 dBm	Pin = 0 dBm	Pin = -20 dBm	Pin = -40 dBm	Pin = 0 dBm	Pin = -20 dBm	Pin = -40 dBm	
0000	0.0686	0.044	0.053	0.509	0.504	0.257	0.969	0.975	1	
0010	0.0684	0.05	0.093	0.54	0.524	0.6788	2.98	3.193	3.35	
0100	0.076	0.066	0.878	1.956	1.872	2.82	13.5	14.18	14.978	
0110	1.624	3.432	4.84	7.8	8.056	8.92	62.9	65.384	69.224	
1000	8.6	15.32	23.4	35.52	37.28	40.92	294.64	304.52	317.32	
1010	38.6	65.8	109.6	165.2	156	188	1379.4	1423.6	1477.6	
1100	186	325	509	802	770	831	6447	6640	6881	



RF1 (905 MHz, -50 dBm)	RF 2 (895 MHz, -50 dBm)	LO (900 MHz, -10 dBm)	LPF cut off (MHz)	Power detector integration time (SCI-4321)	Output at Oscilloscope (V)
ON	OFF	ON	5	1000	0,608 (Stable o/p)
OFF	ON	ON	5	1000	0,656 (Stable o/p)
ON	ON	ON	5	1000	0,732 (Stable o/p)
ON	ON	ON	5	0000	0,9 (modulated o/p)
ON	OFF	ON	5	0000	0,644 (modulated o/p)

(c)

Table 15: Results for two-tone RF input to the DCR block (a) integration time setting for the power detector from the datasheet, (b) RF and LO inputs, (c) summary of measured results.

Version: V1.2



It can be observed from the above results that as the integration time is increased the output of the power detector becomes more stable. The screenshot from the oscilloscope corresponding to four interesting cases are shown in the Figure 29 below.

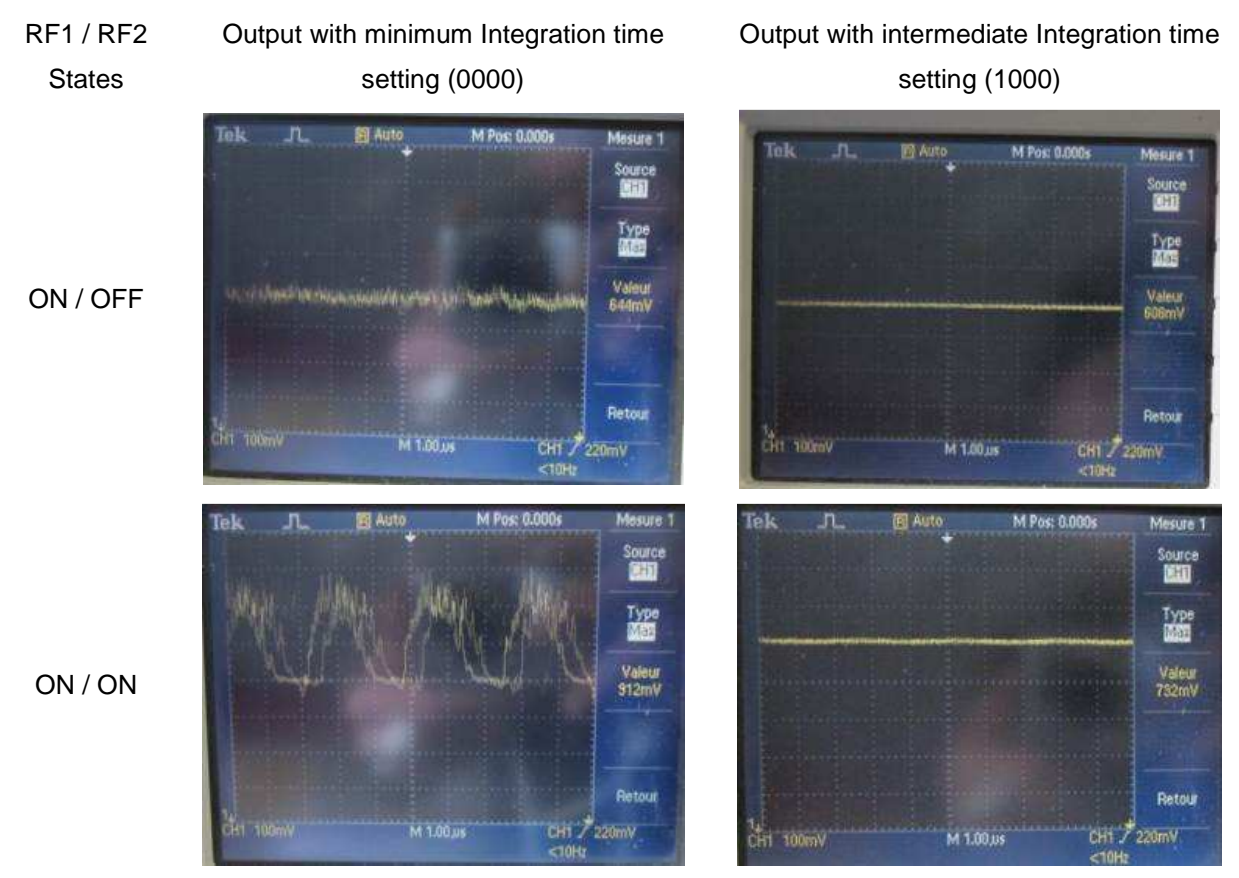


Figure 29 : Screen shots of the oscilloscope showing the output of the power detector for different cases.

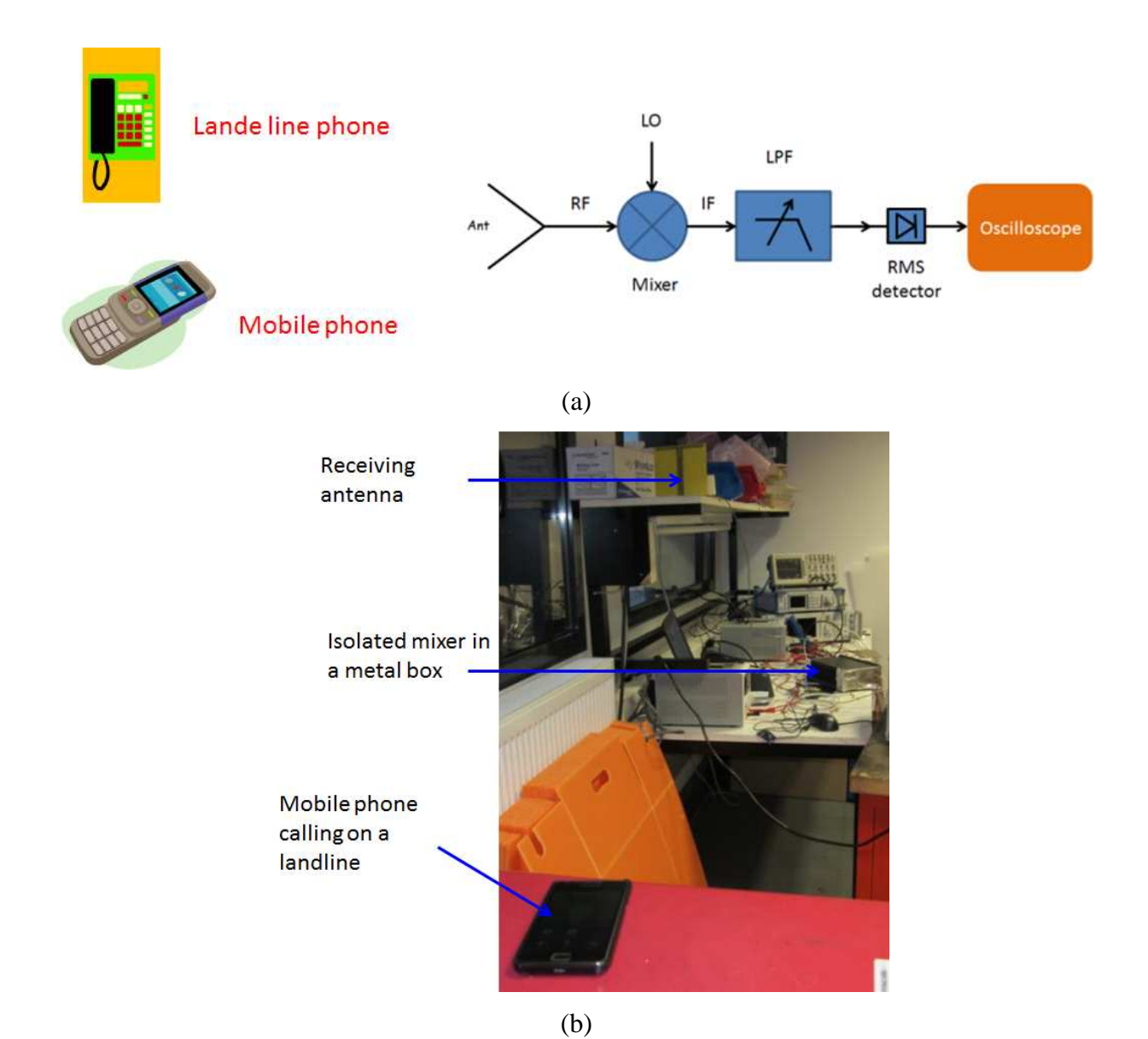
From the above results, the importance of selecting an appropriate integration time for the power detector is highlighted. Even for a single tone RF input, using a small integration time gives a noisy result. For a two-tone RF input, with the LO in between the two tones, the output is highly modulated. Using an appropriate integration time suppresses the modulated signal and gives us a correct reading. It can be observed that the difference between the output levels, when we have a single tone and two-tones with same input power, corresponds to 3 dB (as expected).

3.5.6 DCR block measurements in real scenario

To validate the proposed DCR block architecture in a real scenario, a test bench was setup as presented below in Figure 30. A mobile phone calling a landline number was placed at about 1.2 meters from a receiving GSM antenna. The antenna was connected directly to a spectrum analyzer at first to obtain reference signal level for comparison.

Version: V1.2 48





						Bouygues		Orange		Free			SFR			
	Center	Start	End	BW (MHz)	Start	End	BW (MHz)	Start	End	BW (MHz)	Start	End	BW (MHz)	Start	End	BW (MHz)
GSM 900 UL	895	880	915	35	880	890	10	890	900	10	900	905	5	905	915	10
GSM 900 DL	947	925	960	35	925	935	10	935	945	10	945	950	5	950	960	10

Figure 30: Test bench setup DCR block test with real scenario, (a) block diagram, (b) photograph of the test bench, (c) GSM frequency band distribution in France.

(c)

The screenshot for the reference measurement, when the mobile is calling a landline number is presented in Figure 31. These results were obtained using the max-hold capture option on the spectrum analyzer. The first peak occurs instantaneously while the second peak is captured a bit later. The peak signal observed from the reference measurement is about -20 dBm. The frequency band extends from 895 MHz up to 900 MHz for the two peaks.

The LO frequency was set in the middle of the operator band (verified from the reference measurements). The output was observed on the oscilloscope. The



objective was to detect successfully the GSM UL signal using the DCR block for the target operator. The GSM UL frequency range of the operator in question is between 890 – 900 MHz (Figure 30c). The LO was thus set to 895 MHz at first, and then varied to other center frequencies corresponding to other GSM UL operator frequencies. The rejection with other frequency bands could thus be evaluated in a real scenario.

The test in DL scenario could not be carried out using the complete DCR block, as the received signal strength was well below the power detector sensitivity levels, and a LNA would be required at the front end.

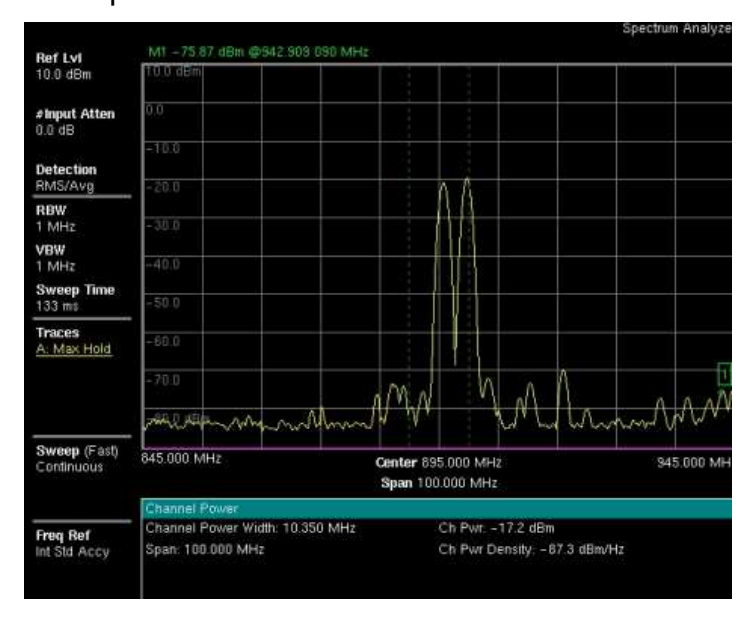


Figure 31 : Result from the reference measurement with the mobile calling a landline number after 1 minute of measurements with max-hold.

Next, the antenna is disconnected from the spectrum analyzer and is connected directly to the RF input of the DCR block (Figure 30a) while the mobile position is not changed and the call is not disconnected. The LO frequency is locked to 895 MHz (center frequency of the operator band from 890 MHz up to 900 MHz). The output on the oscilloscope is shown in Figure 32.



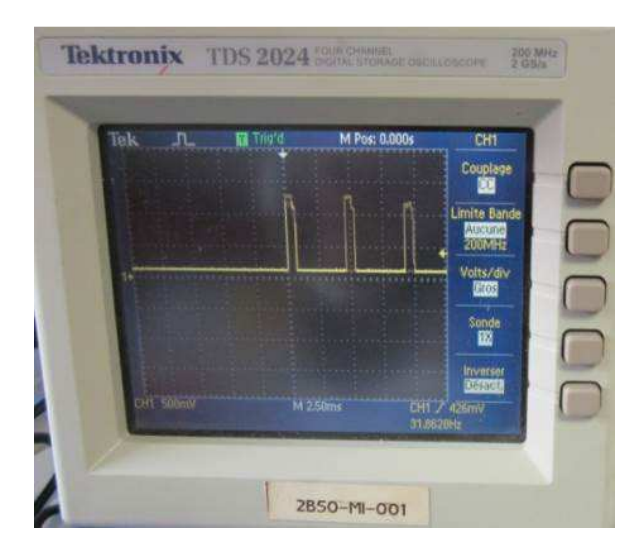


Figure 32: Output of the DCR block on the oscilloscope with LO frequency locked to 895 MHz.

From the output of the oscilloscope (Figure 32), a clean GSM time domain signal is detected. The peak level of this detected signal is 1.22 V. Using the reference curve for the power detector (Figure 27), the output power is about -33 dBm. Subtracting the RF path losses in the DCR block (measured to be around -13 dB at 900 MHz), we obtain an input power level of -20 dBm at the receiving antenna. This is the same as the reference measurement level (Figure 31). To determine the rejection in adjacent operator bands, the LO frequency is changed and the output of the power detector is measured. The results are summarized in the Table 16 below.

Mobile	Landline	LO (MHz)	LPF (MHz)	DET o/p (V)	Power (dBm) From detector curve	Powerat antenna output (dbm)
Calling	Receive	885	5	0	< 65	
Calling	Receive	890	5	0,9	-42	-29
Calling	Receive	895	5	1,22	-33	-20
Calling	Receive	900	5	1,14	-35	-22
Calling	Receive	905	5	1,2	-34	-21
Calling	Receive	910	5	0,11	< -65	
Calling	Receive	915	5	0	< -65	

Table 16: Output of the power detector for different LO frequency locks in the scenario studied in Figure 30.

Table 16 provides interesting results. As the LO is locked to center frequencies of different operators, the output of the power detector changes according to the rejection provided by the tunable low pass filter. The power at the antenna output (last column in the Table 14 above) is calculated by adding the 13 dB losses in the RF chain (from measurements at 900 MHz). These losses are due to the 19 dB attenuator present at the output of the low-pass filter.

When the LO frequency is locked to the center frequency of the first operator (at 885 MHz), the detector output is about 0 volt, which means there is no signal detected. When the LO moves to the center of the second operator frequency band Version: V1.2



(i.e. at 895 MHz), the signal is correctly detected (at -20 dBm). Moving 5 MHz below and 5MHz above this frequency, the signal still falls inside the low-pass filter bandwidth. That is why when the LO is locked to 905 MHz (third operator), we still detect a -21 dBm signal level, because the signal from the second operator is at 900 MHz (Figure 31), and falls in the LPF bandwidth. To correctly reject this band, we need a LPF with lower cut-off frequency (< 1.5 MHz). With the actual solution, we can correctly distinguish between the operators if there is a 10 MHz difference between their frequencies. Moving towards the center frequency of the fourth operator (910 MHz), a small signal level is observed, but it has sufficient rejection for it to be outside the power detector range.

To detect the third operator with a 5MHz frequency band (900 MHz – 905 MHz from Figure 30c), the low-pass filter is set to 3.5 MHz cut-off frequency (the minimum possible with the current available demoboard). This frequency does not reject sufficiently the signal at 5 MHz (about 15 dB of rejection). This means that if we want to detect an operator frequency with a frequency band of 5 MHz, we will have also some part of the adjacent operator. To solve this problem and to correctly detect the signals of the target operator, the following simple scheme is proposed.

The LEXNET dosimeter will be used to carry out measurements for the DL exposure essentially. Thus we will have a total of 8 frequency standards to measure defined in Table 17 below.

					Bouygues			SFR			Orange				Free	
	Centre	Start	End	BW (MHz)	Start	End	BW (MHz)	Start	End	BW (MHz)	Start	End	BW (MHz)	Start	End	BW (MHz)
LTE bande XX DL	806	791	821	30	791	801	10	801	811	10	811	821	10			
GSM 900 DL	947	925	960	35	925	935	10	950	960	10	935	945	10	945	950	5
DCS 1800 DL	1842	1805	1880	75	1853	1880	27	1805	1808	3	1808	1832	24			
DC3 1000 DL	1042	1003	1000	13	1033	1000	21	1832	1853	21	1000	1032	24			
UMTS DL	2140	2110	2170	60	2125	2140	15	2110	2125	15	2140	2145	5	2145	2150	5
OMITO DE	2140	2110	2110	00	2120	2140	13	2150	2155	5	2155	2170	15	2140	2130	9
Wifi	2450	2400	2483,5	83,5												
LTE bande VII DL	2650	2620	2690	70	2655	2670	15	2620	2635	15	2635	2655	20	2670	2690	20
Wimax	3600	3300	3900	600												
Wifi 5 G	5500	5150	5850	700												

Table 17 : DL exposure target frequency bands (e.g. France spectrum) for the LEXNET dosimeter

The first 6 bands will be measured through the DCR block. The last two bands (due to larger bandwidths) will be measured using fixed filters. Thus, this leaves us with only 6 frequency bands to be measured using the DCR block. These six bands are further divided among the service providers. The distribution in France is shown in Table 17 above among the four operators.



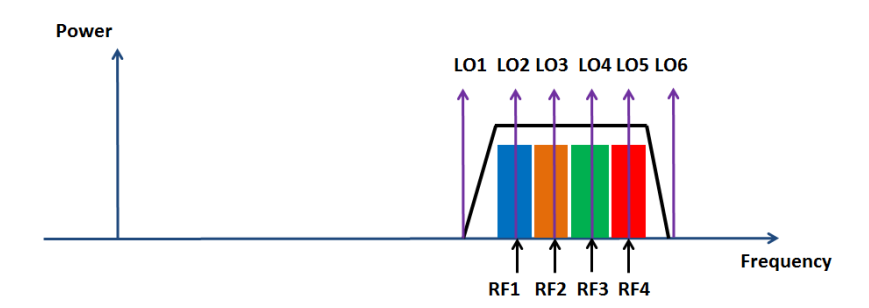


Figure 33 : Measurement scenarios with the DCR block and LO frequency positions for measurements.

Now looking at a typical scenario, we have four operators inside one frequency standard. To correctly detect each of the four operators, the LO frequency needs to be set at 6 different frequency points as shown in Figure 33. These positions will give us six measurements in base band. Knowing the rejection of the LPF, we can calibrate the measurements to correctly separate the response from each operator.

3.6 Microcontroller

After studying the control signals required for the whole dosimeter and characteristics requirements of each component, a suitable microcontroller component was identified. The ST microelectronics reference STM32F103 offers all the necessary driving system and connectivity, i.e. SPI bus, ADC, USB, GPIO, and UART.

This microcontroller is a 32 bit system with speeds up to 72 MHz for different calculations. The total size of the microcontroller depends on the total control signals that we will need. Two solutions are considered; either *i*) a single microcontroller chip will be used which will drive all the control signals (up to 80 control signals are available), or *ii*) an I/O expander will be used with a small size microcontroller for driving all controls.

3.7 Memory block

Two memory blocks will be used for the LEXNET dosimeter. One of them will be used for the storage of all the required parameters for driving the dosimeter for different configurations, and the other one for storage of the measurements.

Both memory slots will be of EEPROM type so that even when the power supply is disconnected, the data on is not erased. The memory chip size will be determined depending on the data necessary to store for the dosimeter configuration and for the measurements.

3.8 Bluetooth / USB connectivity block

The Bluetooth module identified for connectivity with the mobile devices is developed by Roving networks RN-42. This module requires very low power and is easily driven using an UART interface.

The connectivity block has a mini USB connector and the device reference identified for the LEXNET dosimeter is Molex 54819-0519.



3.9 Integration proposal for the LEXNET dosimeter

The integrated front end of the dosimeter is presented in detail in the form of an electrical diagram in Figure 34. The purpose is to show the different sub-components of the RF chain up to the power detector before the signal is sampled by the ADC in the microcontroller (Figure 4).

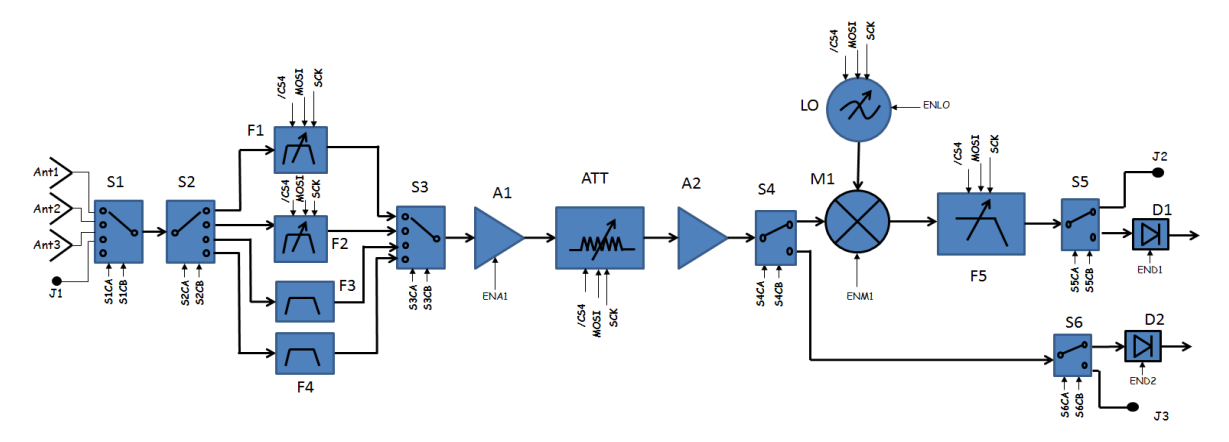


Figure 34: Electrical diagram of the RF front end of the dosimeter

Starting from the left side, first we have the three antenna probes along with an RF connector for calibration and debugging purposes. A four-way RF switch S1 allows us to select among the three antenna probes or the debugging switch J1. Then two four-way switches S2 and S3 select one of the four filters (F1 to F4). F1 and F2 are the tunable filters as presented in section 3.3. F3 and F4 are fixed filters for detection of the WiMAX and WLAN 5GHz frequency bands.

The amplification block consists of *A1*, *ATT* and *A2* as described in section 3.4. After that, a two-way switch *S4* separates the DCR block, used for measurements up to 3 GHz, from the measurements of the WiMAX and WLAN 5GHz frequency bands. The DCR block is composed of the mixer *M1*, the PLL-VCO designated as *LO*, and the tunable LPF *F5*. A two-way switch *S5* selects between the second debugging RF connector (*J2*) and the LPF output. Power detector *D1* is used for measurements up to the 3 GHz frequency bands. The RMS power detector *D2* is used for measurements for WiMAX and WLAN 5GHz frequency bands and is chosen using the two-way switches *S4* and *S6*. The debugging RF connector J3 is used for characterizing the RF chain for the two highest frequency bands. The output of *D1* and *D2* then goes through to the ADC of the microcontroller.

The characteristics of each of the sub-component of the dosimeter are summarized in the Table 18 below from individual component measurements and from datasheet specifications.



	Component func. & model	Refer ence	Operating bandwidth	Gain (dB) Typical	Voltage supply (typ) V	Current supply (typ) mA	Current supply (Max at startup) mA	Control circuit	Enable / disable voltage + current	On / Off time	Estimated size in mm (x * y * z)
1	SP4T HMC344LP3E	\$1,\$2, \$ 3,	DC-8GHz	-1,8	-5	3	6	OV off , -5V ON		150 ns	3x3x1
2	SPDT HMC536MS8G	S4,S5, S6	DC- 6,0 GHz	-0,8	+3,3	0,025	0,025	0V off, 3,3 Volts ON TTL	0,025	30 ns	5 x 3 x 1,3
3	Programmable band pass filter CEA-LETI	F1	700 MHz – 960 MHz	-7	+3,3	0.18	0.18	SPI	Standby 0.12mA	20 us	16*16*4
4	Programmable band pass filter CEA-LETI	F2	1,8 GHz - 2,7 GHz	-9	+3,3	0.84	0.84	SPI	Standby 0.15mA	70 us	16*16*4
5	WiMAX filter DEA203600BT	F3	3,3 GHz - 3,9 GHz	-1,4							2 x 1,25 x 0,95
6	WLAN 5GHz filter DEA205425BT 2028A4	F4	4,9 GHz - 5,95 GHz	-1,6							2 x 1,25 x 0,95
7	LNA VMMK2303	A1	0,5 GHz - 6 GHZ	14	1.8V	21mA	28mA	OV off, 1.8V ON	0V off 0.02mA, 1.8V on 21mA		1x0.5x0.25
8	Attenuator HMC624LP	ATT	DC- 6GHz	-2,8	0V & 5V	2mA	2mA	SPI	3	150ns	4x4x1
9	Driver PGA-1021+	A2	0.05-6GHz	12	3.3V	52mA	60mA	10	*	-	4.6x4.2x1.6
10	Mixer ADL5801	M1	10 MHz - 6 GHz	0	5 V & 3,8V	130 mA @ 5V 0mA @ 3,8V	200 mA		5V off, 0V ON 50 mA off current	182 ns / 28 ns	4 x4 x 1
11	PLL-VCO HMC833LP6GE	LO	0,025 - 6 GHz	-5	3,3 V & 5V	220 total 170 mA @ 5V 50 mA @ 3,3 V	250	SPI	0V off, 5V ON TTL	250 us	6x6x1
12	VGA + LPF HMC900LP5E	F5	3,5 MHz-50 MHz	10	5	70	150	SPI	Through SPI	250 us	5 x 5 x 1
13	Power detector HMC1020LP4E	D1	DC- 3,9 GHz		5	50	60	TTL	5V off, OV ON, 5mA off current	44 ns / 1 us	4 x 4 x1
14	Power detector ADL 5902	D2	DC- 9 GHz		5	73	90	ΠL	0V off, 5V ON, 0,3mA off current	5 us /3 us	4 x 4 x1
15	Microcontroller				3,3		100				

Table 18: Power consumption, size, and time delay estimation for the LEXNET dosimeter

3.10 Battery design

To identify a suitable battery size, the power consumption of all the components in the LEXNET dosimeter discussed above was evaluated. The required voltage levels, current consumption, time delays for different components were estimated from the Table 18 above. These values were evaluated from demo-board measurements and datasheet specifications.

From the above table, the total typical current consumption for the dosimeter is estimated to be between 650 mA (with D1) and 690 mA (with D2). The peak current of 890 mA can be expected. Voltage levels of +5V, -5V, and 3.3V will be required through regulators or battery supply. The voltage levels of 1.8V and 3.8V will be provided through resistive dividers as they do not draw large current levels.



Figure 35: Flat battery identified for the LEXNET dosimeter

The suitable battery with a flat profile and small size identified for the LEXNET dosimeter is presented in Figure 35 below. The reference number for this component is LPC884765 [15]. It has a capacity of 3000 mAh and provides a stable 3.7 V level. Version: V1.2



The size of this battery is 68 mm x 46 mm x 8.5 mm with a weight of 52 g. A battery with larger capacity (3700 mAh for example) is also available and will increase the operational time of the dosimeter, but it was not available with a demoboard at the time of the study.

3.11 Mechanical design proposal

A preliminary mechanical structure proposed to enclose the RF board, the battery, and the probe is proposed in the Figure 36.

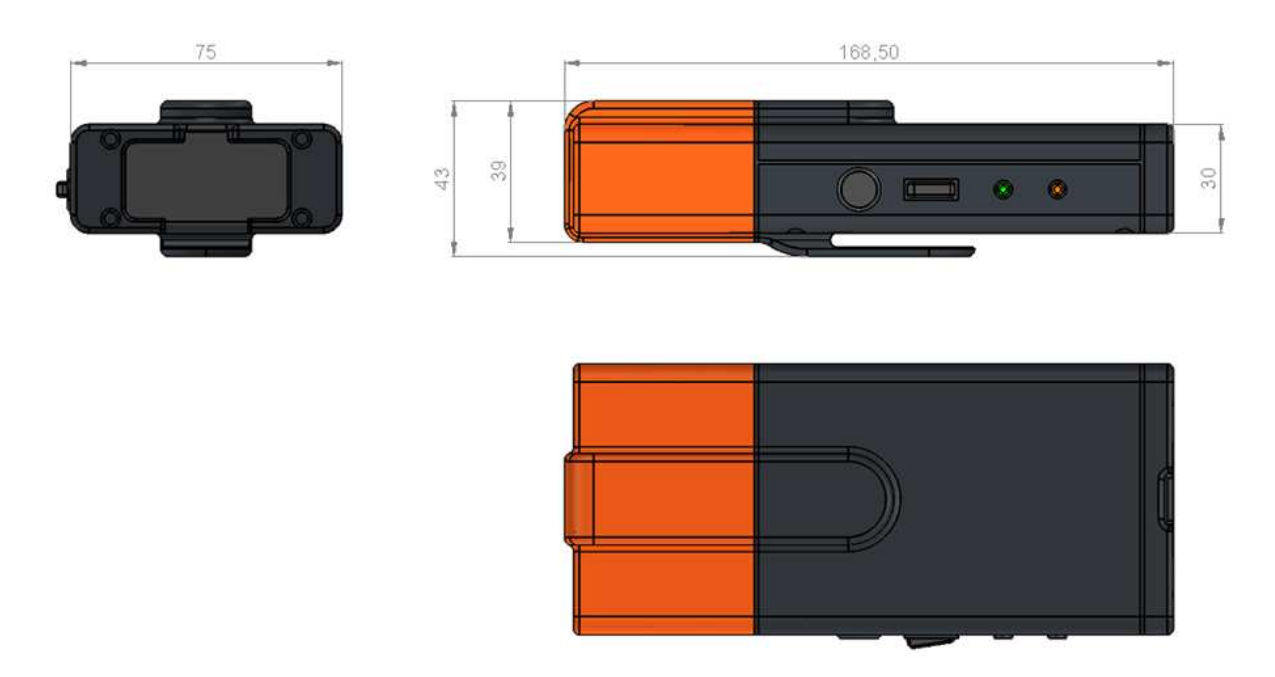


Figure 36: Proposal for the mechanical structure for the LEXNET wearable dosimeter

The dimensions of this preliminary design are 75 mm x 168.5 mm x 43 mm (including the belt clip). There are two buttons and two LEDs on the side of the dosimeter. The circular button is designed for starting or stopping the measurement cycle. The rectangular button is used for switching on/off the device. One of the LED shows the state of the battery charge and the other the measurement cycle.

The USB and charger connectors are at the bottom behind a protective cover in order to achieve the IP67 standard.



4 PRELIMINARY RESULTS ON WEARABLE DOSIMETER CHARACTERIZATION AND ENVIRONMENT IMPACT STUDY

4.1 Goals and approach description

The EMF exposure of the population due to wireless communications (2G, 3G, 4G and WLANs) originates both from DL emissions incoming from Base Stations (BS) and Access Points (AP), and from Up-Link ones produced by the terminals (cell phones, tablets and lap-tops). Although the main peak contribution comes generally from the last, the former must be considered as well, as contributions can be competitive for some cases for which both levels are low (e.g. in femtocells). Note however that in this case, the EMF levels are particularly low. In any case, DL emissions are continuous (and undergone by non-user as well) whereas UL ones are time limited.

This section addresses the issue of the field level assessment and more specifically its evaluation with dosimeters. The main technical challenge resides in the modelling of the measurement errors of body-worn sensors, induced by proximity effects, notably the shadowing effect of the body.

The section is organized as follows: first measurements of a triaxial sensor, both isolated and body-worn are analysed twofold, with a polarimetric approach on the one hand, and with a non-polarimetric one on the other hand; then, these analyses are carried on and deepened thanks to 3D electromagnetic simulations with realistic numerical anthropomorphic phantoms, which offer a greater flexibility regarding the possible "scenarios" (notably with regards to the "population variability" and the sensor positioning).

Simulations with simplified numerical models are addressed in order to reduce the simulation time and allow the opportunity to assess a large variability of different configurations. This task is still on-going and will be included in the second version of this deliverable.

Possible correction strategies are eventually rapidly drawn, but will be deepened in the second version.

4.2 **Preliminary measurements**

Measurements were carried out in an anechoic chamber with an EME Spy 140[®] dosimeter comprising a three-axial sensor, first isolated (Figure 37), and second placed near a whole body phantom (Figure 50). Various positions on the phantom were considered.

The analysis of the isotropy variance of both the isolated and worn sensor is presented in the following sections. For both cases, the polarimetric characteristics are first presented, followed by non-polarimetric approaches, "intrinsic" as a first step,

Version: V1.2 57



then including the characteristics of the propagation channel for various environments.

4.2.1 Isolated triaxial sensor

4.2.1.1 Polarimetric approach

The triaxial sensor provided by Satimo was characterized in reflection and transmission for each probe axis (Figure 38) over 0.5 – 6.5 GHz.

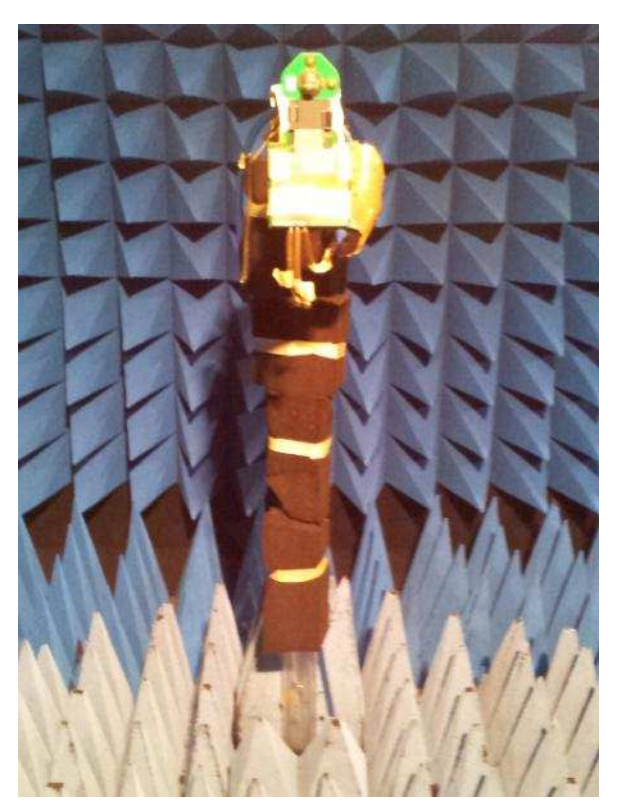




Figure 37 : Experimental setup for the measurement of the isolated sensor in anechoic chamber.

Although used in reception by essence, the sensor can be first characterized in emission. Indeed, the received signal at each probe port *n* can be written as [16]:

$$b_n(f,\hat{\mathbf{r}}) = e^{-j\mathbf{k}_i \cdot \mathbf{r}} \sqrt{\frac{4\pi}{\eta_0}} \mathcal{H}_n^R(f,\hat{\mathbf{r}}) \cdot \mathbf{E}_i(\mathbf{k}_i,\mathbf{r}) = -\frac{1}{2} j \sqrt{\frac{4\pi}{\eta_0}} \frac{c}{\omega} \mathcal{H}_n^T(f,\hat{\mathbf{r}}) \cdot \mathbf{E}_{i0}$$
(3.11.1)

where \mathcal{H}^{R} (resp. \mathcal{H}^{T}) are the antenna transfer functions in the receiving (resp. transmitting) modes, η_{0} the free space impedance, r the radial distance, $\hat{\mathbf{r}}$ the unit radial vector, $\mathbf{\omega} = 2\pi f$ the angular frequency, \mathbf{k}_{i} the wave vector of the incident plane wave \mathbf{E}_{i} and $\mathbf{E}_{i0} = \mathbf{E}_{i}$ (f,0) denotes the field at the origin chosen at the centre of the sensor spherical ground. Apart from a frequency scaling, the directional and polarization characteristics are the same in both modes.

The definition used for the Tx Antenna Transfer Function (ATF) is recalled hereafter for clarity:



$$\mathbf{E}_n^{\infty}(f,\hat{\mathbf{r}}) = \frac{e^{-jkr}}{r} \sqrt{\frac{\eta_0}{4\pi}} \boldsymbol{\mathcal{H}}_n^T(f,\hat{\mathbf{r}}) a_n$$
(3.11.2)

where a_n is the incident wave at the *n*-th probe port, k the wavenumber, and \mathbf{E}_n^{∞} the radiated Far Field (FF).

The radiation characteristics (polarimetric realized gain $G_r^{\theta,\varphi} = \left|\mathcal{H}_{\theta,\varphi}^T\right|^2$) are provided hereafter for each communication band of interest, i.e. the main current RATs: GSM 900, GSM 1800, UMTS (1.9 – 2.15 GHz), LTE 800 (0.7 – 0.8 GHz) & 2600 (2.6 – 2.7 GHz), and WiFi 2G (2.4 – 2.5 GHz) & 5G (5.15 – 5.85 GHz). The results are averaged over each frequency band, and normalized to the average of the realized gain in azimuth for each polarization, i.e.:

$$\hat{G}_r^{\theta,\varphi}(f_{RAT},\theta,\varphi) = \int_{\Delta f_{RAT}} G_r^{\theta,\varphi}(f,\theta,\varphi) df / \frac{1}{2\pi} \int_{\Delta f_{RAT}} \int_0^{2\pi} G_r^{\theta,\varphi}(f,\pi/2,\varphi) d\varphi df$$
(3.11.3)

This allows to focus on the isotropy variance considering polarization aspects.

The input matching is presented in Figure 38 and the realized gains in Figure 39. The antenna factors (AF) are shown in Figure 40; *AF* is defined as:

$$AF = \frac{E_{i0}}{V_r} = \left(\frac{4\pi\eta_0 f^2}{G_r Z_{ref} c^2}\right)^{1/2} = \frac{1}{\sqrt{4\pi}} \sqrt{\frac{\eta_0}{Z_{ref}}} \frac{1}{|\mathcal{H}^R|}$$
(3.11.4)

Radiation patterns (realized gain normalized to the mean in azimuth) are presented in Figure 41 and their variance in Figure 42.

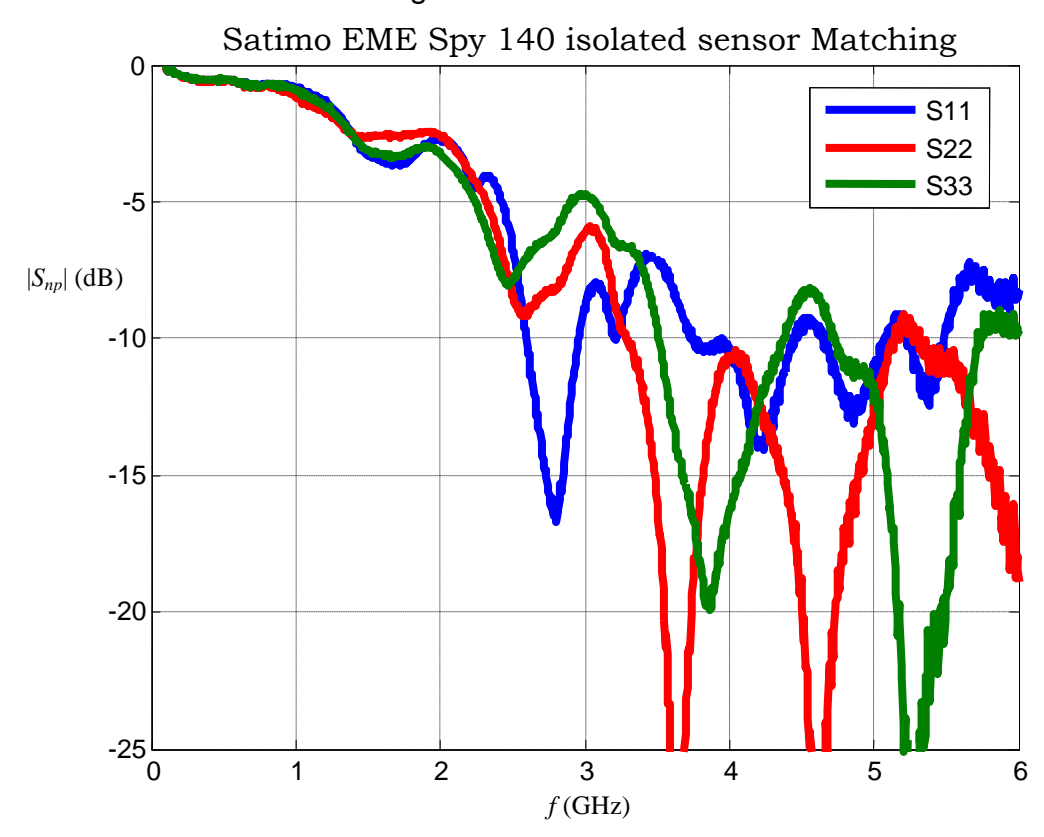




Figure 38: Reflection coefficient of each probe sensor.

Satimo EME Spy 140 isolated sensor realized gain measurement -5 -10 G_r (dB) -15 G_r (x'Ox probe, φ = 90°) G_r (y'Oy probe, $\varphi = 0$) -20 G_r (z'Oz probe, Φ = 0) G_{rmax} (x'Ox probe) -25 G_{rmax} (y'Oy probe) G_{rmax} (z'Oz probe) -30 1.5 2 3 3.5 4 4.5 2.5 5 5.5 6 f(Ghz)

Figure 39: Realized gains per probe.

Satimo EME Spy 140 isolated sensor antenna factor

AF (x'Ox probe)

AF (y'Oy probe)

AF (z'Oz probe)

1 2 3 4 5 6

f (Ghz)

Figure 40: Antenna Factor per probe.



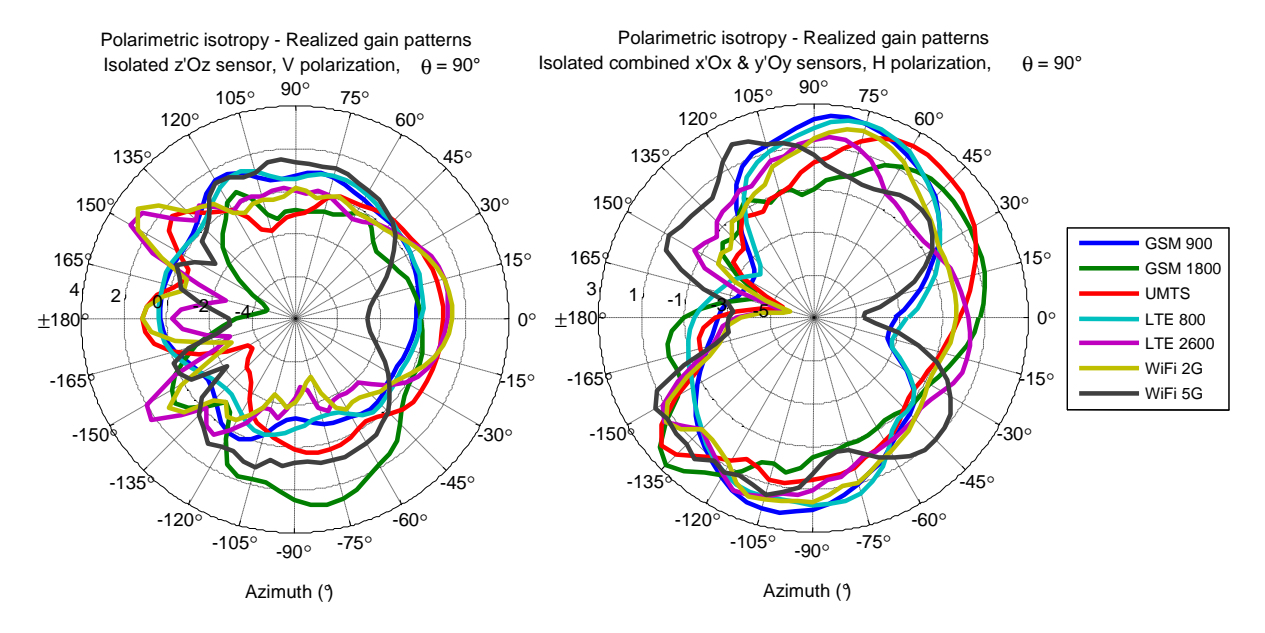


Figure 41 : Normalized realized gain patterns (averaged over each RAT band) of the "V"(z'Oz) probe and combined "H" probes (xOy) in the azimuthal plane, $\theta = 90^{\circ}$.

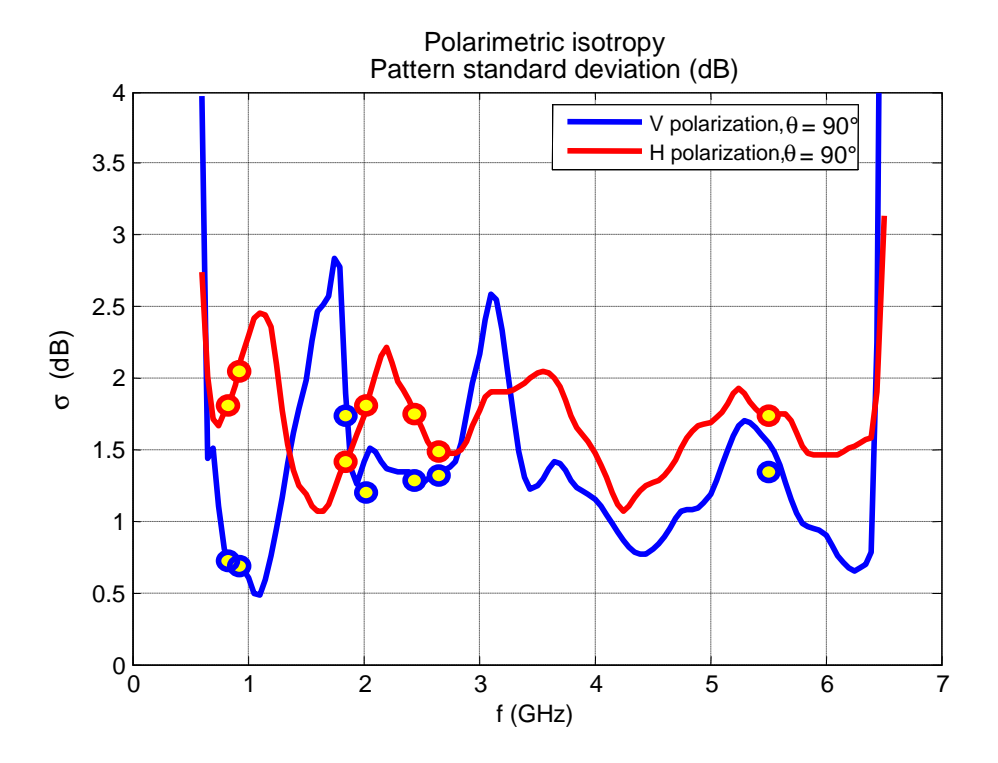


Figure 42 : Realized gain pattern standard deviation over azimuth (averaged over frequency for each RAT – yellow circles) of the "V"(z'Oz) probe and combined "H" probes (xOy), $\theta = 90^\circ$.

In the following tables, μ , σ and m are respectively the mean, the standard deviation and the median.

As can be observed in Figure 41 and in Table 18, the omni-directionality is very satisfactory (typ. $\sigma_G < 2$ dB), particularly for the "V" polarization.

Version: V1.2 61



T 11 40	Born Communication of the Comm		4 44 44	,		
Table 19:	Polarimetric	sisotropy	statistics	(over	azimuth). in dB

	GSM 900	GSM 1800	UMTS	LTE 800	LTE 2600	WiFi 2G	WiFi 5G
μ_{Gv}	-0.05	-0.32	-0.15	-0.06	-0.20	-0.18	-0.19
σ_{Gv}	0.68	1.7	1.2	0.72	1.3	1.3	1.35
m _{Gv}	0.02	-0.26	0.16	0.06	-0.01	-0.20	0.11
μ_{Gh}	-0.45	-0.22	-0.34	-0.36	-0.21	-0.30	-0.30
G _{Gh}	2.1	1.4	1.8	1.8	1.5	1.7	1.7
m _{Gh}	-0.30	-0.29	-0.22	-0.48	-0.09	-0.24	0.18

However, the polarization purity of the probes, although satisfactory for such small wideband sensor, is not very high, in particular for the "H" probes at low frequencies as can be observed in Figure 43 and Table 19 (the cross-polarization ratio (XPR) is defined as $XPR = G_r^{cx}/G_r^{co}$). For most of the cases, it is typically less than -10 dB for the vertical probe and less than -4 dB for the higher bands (LTE & WiFi) for the horizontal probes. However the XPR is high for the lower bands of the later. The XPR is even positive at low frequencies (up to +3 dB for the GSM900 and LTE800) in some directions. One of the first conclusions is hence that the polarization aspect should be considered cautiously for the calibration and next for the correction procedures in the wearable case.

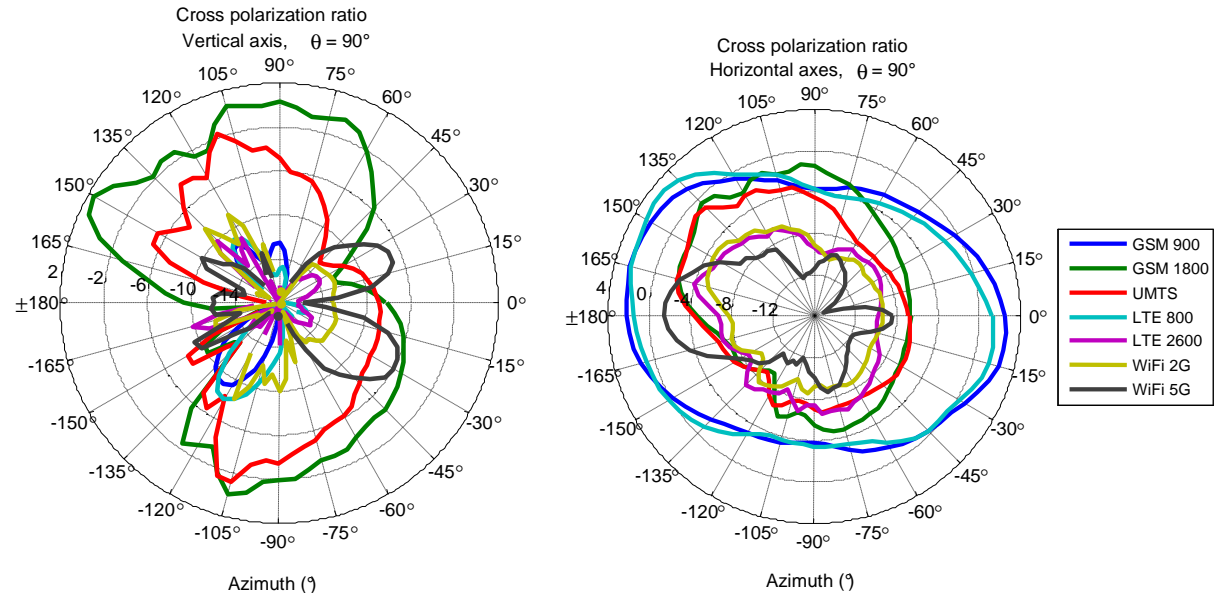


Figure 43 : XPR levels (averaged for each RAT) of the isolated "V"(z'Oz) probe and combined "H" probes (xOy) in the azimuthal plane, $\theta = 90^\circ$.

Version: V1.2 62



Table 20: Polarimetric sensor XPR statistics (over azimuth), in dB.

XPR	GSM 900	GSM 1800	UMTS	LTE 800	LTE 2600	WiFi 2G	WiFi 5G
$\mu_{_{XPRV}}$	–17.99	-5.10	-8.30	-17.86	–16.75	-14.42	-14.47
$\sigma_{_{XPRV}}$	5.20	4.69	4.53	5.49	3.71	3.44	5.35
μ _{XPRh}	-0.57	-4.99	-5.89	-0.83	-7.75	-8.41	-9.33
$\sigma_{\scriptscriptstyle XPRh}$	2.20	2.26	2.07	2.18	1.44	1.50	3.19

4.2.1.2 Non polarimetric approach

☐ INFLUENCE OF THE INCIDENT FIELD POLARIZATION

As the polarization of the incoming wave is a priori not known on the one hand, and, in the other hand, as the sensor XPR is not always low as shown in the previous section, a non polarimetric approach is presented hereafter. The influence of the incoming wave XPR is first considered. For simplicity, the analysis is restricted to linear polarization. To this end, the sensor is analysed in the receiving mode instead of in the transmitting mode as previously.

The XPR of the incident plane wave $\mathbf{E}_{i0} = E_{i0}^{V} \hat{\mathbf{\theta}} + E_{i0}^{H} \hat{\mathbf{\phi}}$ is defined as $xpr = \left| E_{i0}^{H} \right|^{2} / \left| E_{i0}^{V} \right|^{2}$ and the field strength is set to 1 V/m, so that:

$$E_{i0}^{V} = \pm \frac{1}{(1 + xpr)^{1/2}}$$
 (3.11.5)

$$E_{i0}^{H} = \pm \frac{xpr^{1/2}}{(1+xpr)^{1/2}}$$
 (3.11.6)

expressed in V/m.

Note that, besides the field component amplitude, the signs (i.e. the phase) of these components is important, as the field can be in any quadrant of any plane tangent to the sphere, and as the probes are not purely polarized, so that each projection must be added at the field level and not in power.

The XPR is expressed in dB in the sequel, i.e.: $XPR = 20 \log(xpr)$. Note that for this definition, the incoming field is horizontally polarized for large *positive* values of the XPR whereas it is vertically polarized for large *negative* values.

The received signal \bar{b} is computed as a normalized combination of the signals received at each probe port, i.e.:

$$\bar{b} = \left(\bar{b}_{\nu}^2 + \bar{b}_{h}^2\right)^{1/2} \tag{3.11.7}$$

with



$$\overline{b}_{v}^{2}(f_{RAT}, \boldsymbol{\varphi}, xpr) = \frac{\int_{\Delta f_{RAT}} \left| \boldsymbol{\mathcal{H}}_{z} \cdot \mathbf{E}_{i0} \right|^{2} df}{\int_{\Delta f_{RAT}} \left| \left| \boldsymbol{\mathcal{H}}_{z} \cdot \mathbf{E}_{i0} \right|^{2} \right|^{2} >_{\boldsymbol{\varphi}} df}$$

$$\overline{b}_{h}^{2}(f_{RAT}, \boldsymbol{\varphi}, xpr) = \frac{\int_{\Delta f_{RAT}} \left| \boldsymbol{\mathcal{H}}_{x} \cdot \mathbf{E}_{i0} \right|^{2} + \left| \boldsymbol{\mathcal{H}}_{y} \cdot \mathbf{E}_{i0} \right|^{2} df}{\int_{\Delta f_{RAT}} \left| \left| \boldsymbol{\mathcal{H}}_{x} \cdot \mathbf{E}_{i0} \right|^{2} + \left| \boldsymbol{\mathcal{H}}_{y} \cdot \mathbf{E}_{i0} \right|^{2} df}$$
(3.11.8)

where x, y (resp. z) refer to the "H" probes (resp. "V" probe), $< > \varphi$ denotes an averaging over variable φ , and the superscript "T" has been omitted in the ATF notation to ease the readability (actually any of the Tx or Rx ATF can be used in these expressions).

It is easy to show that $\overline{b}=1$ for an "ideal" sensor, i.e. perfectly matched, lossless and fully isotropic.

The following figures show the influence of the incoming wave XPR on the received signal \bar{b} for several RATs (some have been omitted because their behaviour is very similar to the presented ones, as the bands are very close, e.g. LTE 800 and GSM 900).

As can be observed in Figure 44, the deviation from isotropy depends on the field XPR and on the frequency bands. However, as compared to Figure 43 or Table 20, the deviation is lower (for the "V" polarization) or comparable. The main difference here is that the field polarization is not known a priori.

This shows actually, that we can take advantage of the polarimetric capabilities of the sensor to improve its isotropy using it as a non polarimetric probe. The improvement is rather low here, but as it depends on the probe isotropy and polarization purity on the one hand, and on the polarization and directional characteristics of the field (i.e. in practice on the channel characteristics, notably its depolarization effects) on the other hand, it is expected that the result will be more significant when the sensor will be placed near the body, because its presence induces a significant depolarization effect on both the incoming field and probe radiation characteristics.



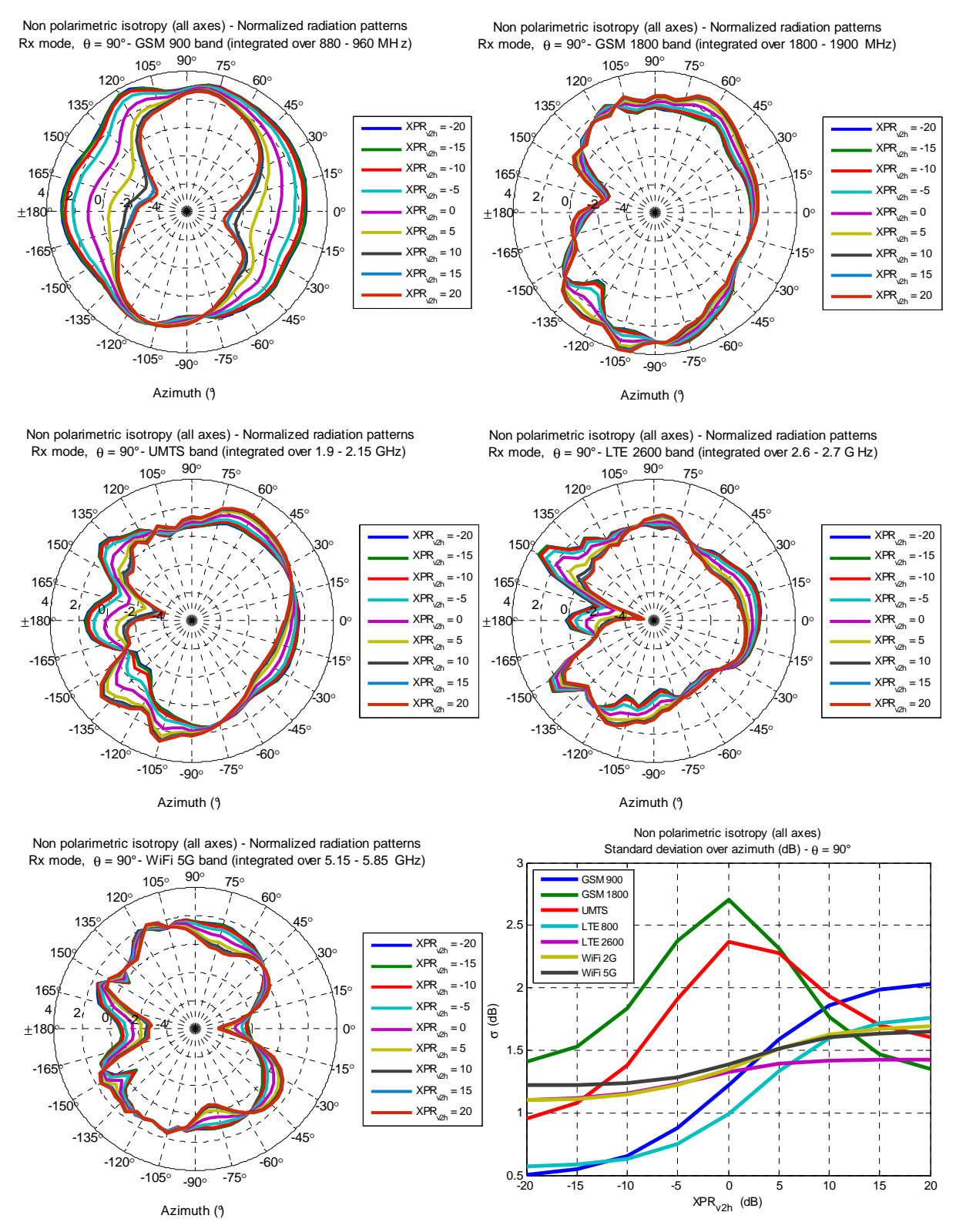


Figure 44 : Influence of the incoming wave XPR level on the isotropy (for various RATs), (a-e) received signal "patterns" in azimuth, (f) variance of the isotropy ($\theta = 90^{\circ}$).

Version: V1.2 65



☐ INFLUENCE OF THE CHANNEL CHARACTERISTICS

In order to extend the preceding analysis to take into account the channel characteristics, in particular its amplitude behaviour, angular spread and depolarization effect, a simplified version of the WINNER II / WINNER+ statistical channel model [19], [20], [21] for various scenarios is now introduced to assess the sensor performance.

The sensor probes are again considered in the Rx mode and the statistics of the received signal are analysed within this framework.

> Channel model

The received signal \bar{b} is computed in the same way as before, but the field obeys now to the statistical laws of the channel model. The total field level is still fixed to Ei_0 = 1 V/m, but its energy is angularly spread in several "clusters" considered here for simplification as simple MPCs (Multi Paths Components). More precisely, the "intracluster" MPC structure is "aggregated" here in a single path (the intra-cluster statistics, in particular the angular spreads are accounted for globally). The PL (Path Loss) modelling is irrelevant here as we are dealing with received waves and not radio link budgets. In the same way, the delay domain is not of concern as the signal is integrated at the receiver over durations which are far larger than the delay spread. The carrier phase aspect, and related small scale (or selective) fading is neither considered in order to simplify the approach, and also, more fundamentally, because in practice measurements are averaged over time and/or space. In the same way, the departure angular spectrum – related to the BS or AP antennas Tx characteristics - is not directly considered here. It is supposed that their effect (sectorised or omni, etc.) is included in the channel angular spread properties. The environment type ("scenarios" in WINNER models such as Indoor, Outdoor to Indoor (O2I), Urban Macrocells (UMa), in LOS or NLOS, etc.), the number of clusters ("multipaths"), the angular spectrum (Angle of Arrival, AoA) and polarization statistics (XPR) are however taken into account. In this part, only the azimuth spread is considered as the measurements were only performed over the azimuthal plane ($\theta = 90$ °).

In the simplified model which will be used, the number of paths, angular spectrum and XPR do not depend explicitly on the frequency, although they depend on the environment which is, for some, related to the RATs frequency bands (i.e. WLANs are mainly used in indoor environments and over WiFi bands). In other words any explicit frequency dependence of these parameters is neglected here. The channel model is briefly summarized below, and a detailed description is presented in appendix 3.

The model includes the statistics of: the number of paths N (normally distributed), the angle of arrival (AoA) and angular spread (AS) for both azimuth and elevation, the amplitude (Rayleigh or Rice distributed) and its dependence to the AS, and the XPR (lognormally distributed).

A summary of the characteristics of the four considered environments and their rough correspondence with WINNER scenarios is shown in Table 21: Radio channel parameters for the considered environments..



Table 21: Radio channel parameters for the considered environments.

Env. n°	Local environment	WINNER scenario	K factor Mean/Std (dB)	XPR Mean/Std (dB)	Azimuth Spread Mean/Std (°)	Nb clusters Mean/Std
1	Office/room indoor	A2, B4, C4		NLOS: 3.5/9.5	NLOS: 23/16	NLOS: 10.6/2.4
2	Urban (in street), LOS from BS	B1, C1	8.9/6.7	LOS: 12/4.5	LOS: 26/12	LOS: 6/3.5
3	Urban (in street), NLOS from BS	B1, C1-C3		NLOS: 7.5/3	NLOS: 34/17	NLOS: 14/3
4	Indoor small office / residential, LOS from AP	A1	8/3	LOS: 11.5/3.5	LOS: 44/9	LOS: 12/6

A typical example of 3D channel power, XPR and AoA spread in NLOS UMa scenario (Env. n°3) is shown in Figure 45.

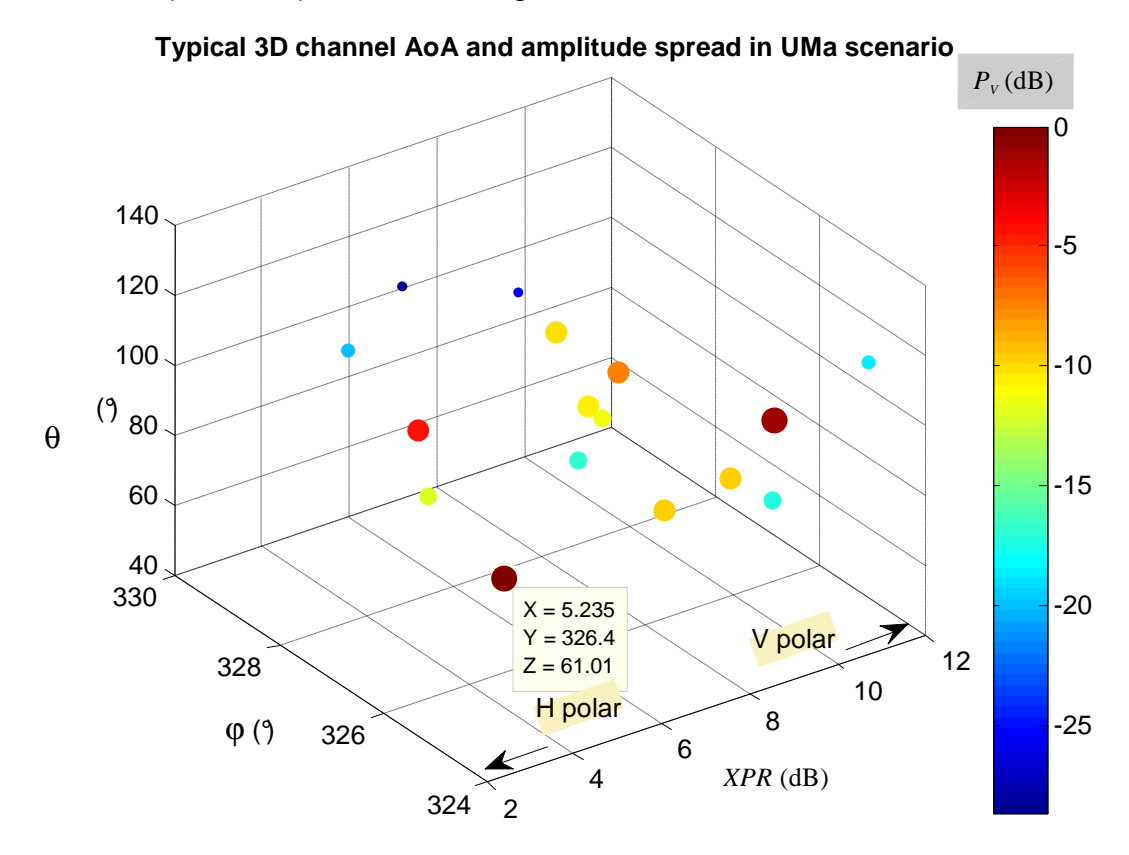


Figure 45: Typical WINNER+ based 3D channel example.

> Statistical results

The statistics of the isotropy deviation based on 5000 channel statistical samples for each environment are shown below.

Version: V1.2



The field is represented in linear scale in Figure 46 (to assess the field variance) and in dB in Figure 47 to be able to fairly compare the variance with the results of the previous sections.

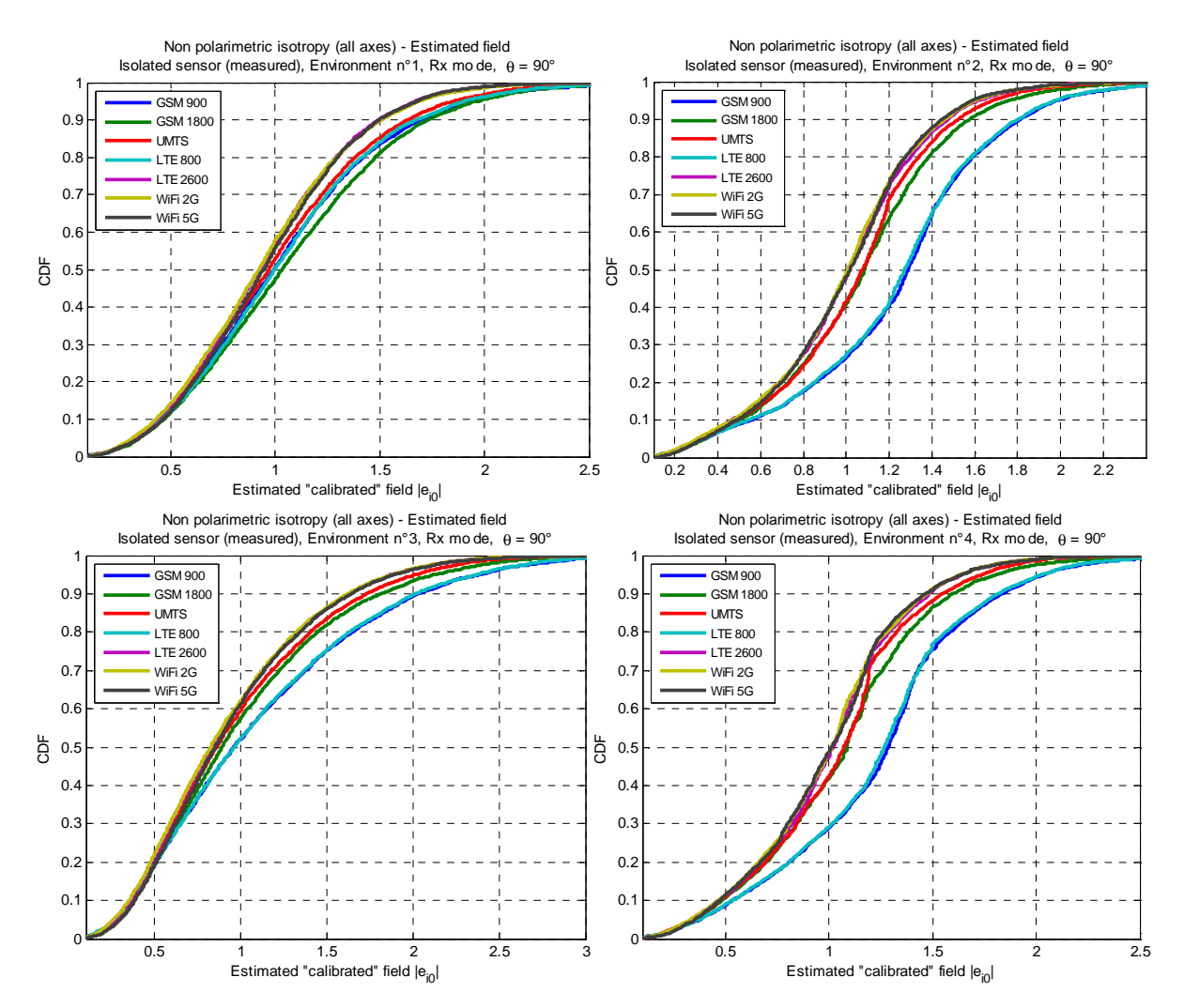


Figure 46 : Non polarimetric statistics (CDF) of isotropy deviation for 4 typical WINNER+ based 3D channel environments. The field strength ei0 is normalized to 1 V/m.

Version: V1.2



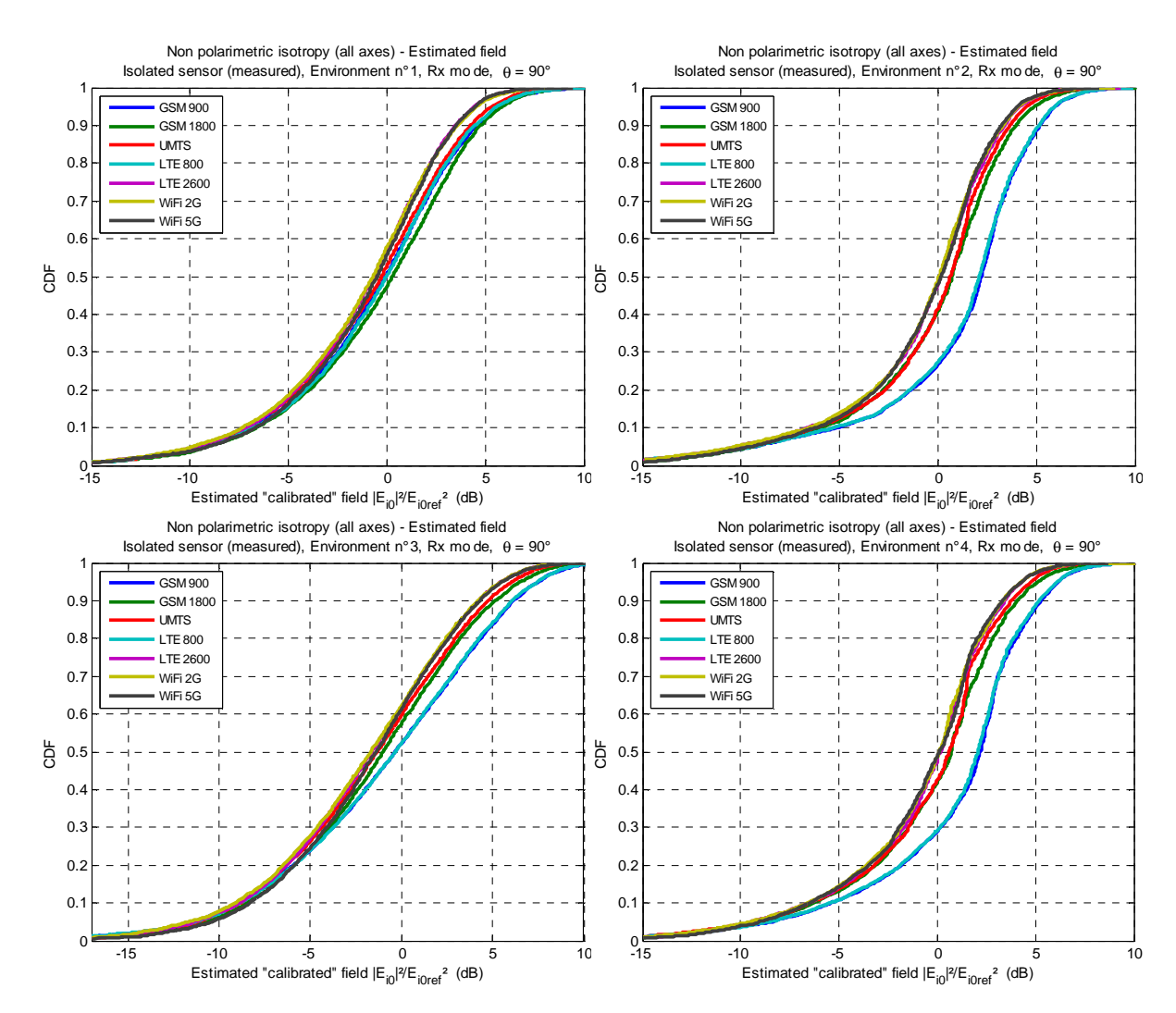


Figure 47: Non polarimetric statistics (CDF) of isotropy deviation for 4 typical WINNER+ based 3D channel environments. Normalized field expressed in dB.

Table 22: Non polarimetric sensor isotropy deviation statistics (over azimuth) for Env. n°1.

e _{i0norm}	GSM 900	GSM 1800	UMTS	LTE 800	LTE 2600	WiFi 2G	WiFi 5G
${\mu_{ei0}}^\dagger$	1.03	1.08	1.0	1.04	0.95	0.95	0.97
σ _{ei0} †	0.48	0.50	0.46	0.47	0.40	0.41	0.40
<i>т_{еі}</i> 0 (dВ)	-0.15	0.27	-0.34	-0.06	-0.64	-0.76	-0.45
σ _{εί0} (dB)	4.66	4.67	4.61	4.58	4.32	4.41	4.19

^T In linear scale. These quantities, "normalized" to a total incident field of 1 V/m, can hence be considered either in relative scale or in V/m.

Version: V1.2



Table 23: Non polarimetric sensor isotropy deviation statistics (over azimuth) for Env. n°2.

e _{i0norm}	GSM 900	GSM 1800	UMTS	LTE 800	LTE 2600	WiFi 2G	WiFi 5G
μ _{ei} ο	1.24	1.07	1.04	1.23	1.0	0.99	1.0
σ _{ei0}	0.46	0.41	0.38	0.46	0.37	0.37	0.36
<i>т_{еі}</i> 0 (dВ)	2.19	0.70	0.60	2.08	0.11	0.01	0.12
σ _{εί0} (dB)	4.36	4.11	4.03	4.34	4.04	4.07	3.83

Table 24: Non polarimetric sensor isotropy deviation statistics (over azimuth) for Env. n°3.

e _{i0norm}	GSM 900	GSM 1800	UMTS	LTE 800	LTE 2600	WiFi 2G	WiFi 5G
μ _{ei} ο	1.10	1.0	0.96	1.09	0.92	0.92	0.94
σ _{ei} 0	0.66	0.57	0.54	0.65	0.50	0.50	0.50
<i>т_{еі}</i> 0 (dВ)	-0.37	-1.02	-1.34	-0.33	-1.61	-1.66	-1.40
σ _{εί0} (dB)	5.92	5.35	5.33	5.89	5.22	5.28	4.95

As can be observed in Figure 46 or Figure 47 and Table 22 to Table 24, there is almost no bias in the field assessment for all the LOS scenarios (Environments n°2 and 4) and almost all NLOS scenarios (Environments n°1 and 3): means are very close to 1 V/m, although the medians are clearly shifted for the environment n°3 as the distribution is far from normality. Only 4 cases, for low frequency RATs (GSM 900 and LTE 800) in LOS situations (Env. n°2 & 4), pre sent such a bias of about 25 % (linear scale) or about 2 dB.

On the other hand, in all cases, the variance is significantly higher than previously (see Figure 42, Figure 44 and Table 18), ranging between 4 and 6 dB (instead of 0.7 – 2.7 dB). It is of course due to the fact that the channel characteristics were not previously taken into account: in particular, there is an interaction between the probes XPR and the channel depolarization effect, and above all, the signal received by each probe is a linear combination of signals proportional to the field of each MPC which consequently involves not only the directional amplitude variation of their transfer functions, but also their phase variation. This is probably why the variance is



larger for the 3rd environment: its angular spread and number of MPCs is larger, on average, than the first two.

Note that if the same computations are performed with a hypothetic channel characterized by a small number N of MPCs and a small angular spread, we find back results similar to the previous ones.

A partial conclusion here is that the real dispersion of the sensor measurement, i.e. in real environments, is higher than expected if the sensor accuracy is characterized regardless of the channel.

Some of the obtained statistics have been analysed in order to bring out some theoretical distribution fits. It appears that the Nakagami distribution is suitable for NLOS environments, whereas LOS ones are well fitted by truncated double exponential distributions ("asymmetric Laplace" distribution). All cases are significantly far-off normality. In LOS, the Ricean or gamma distributions are other possibilities, better than Gaussian, but worth than Nakagami. In NLOS, none of the previous distributions are suitable, only a truncated Laplacian type is satisfactory, the pure Laplace distribution being clearly less accurate than the double exponential. In complement to the CDF, probability plots are also shown in Figure 48, as the "goodness of fit" is better underlined.

Version: V1.2



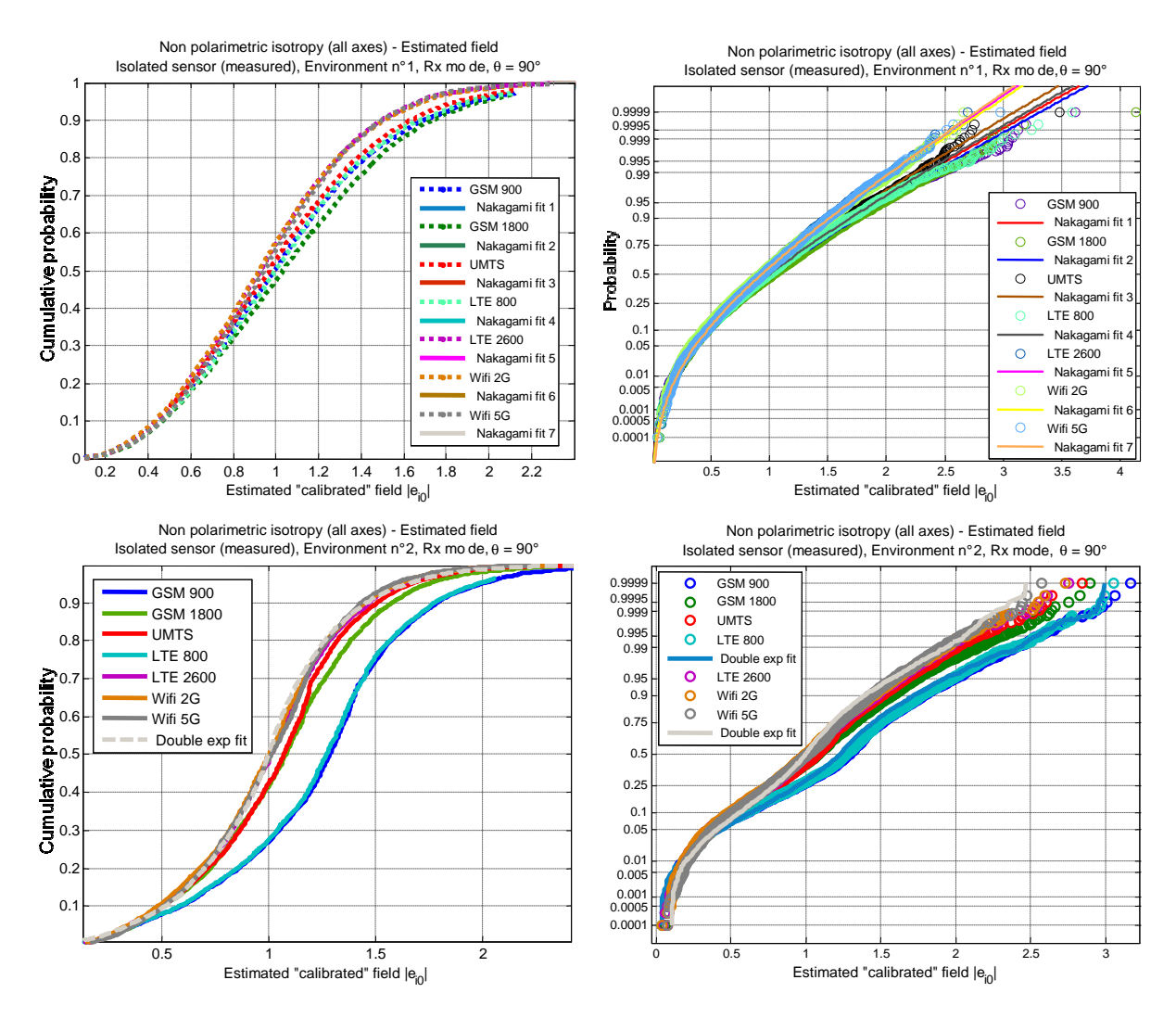


Figure 48 : Non polarimetric statistics (CDF) of isotropy deviation and examples of statistical fits for an NLOS and a LOS environments.

4.2.2 Sensor on whole body phantom

Measurements were carried out with a whole body phantom in an anechoic chamber, at IMT's premises, over an ultra wide band $(0.5-6.5~\mathrm{GHz})$. An EME Spy $140^{\$}$ dosimeter comprising a three-axial sensor was used to probe the far field, bypassing its internal electronics with coaxial cables directly connected to each of the three probes. Three positions on the phantom were considered: on the "left chest", on the "left hip" and at the level of the right back pocket of trousers. This positioning was chosen based on a criterion of realistic practical use, e.g. in the internal pocket of a jacket or in a pocket of a shirt for the first, and in a front pocket of trousers or attached to the belt for the second. For each location, three distances to the body were considered (about 0, 10 and 20 mm) in order to extend the practical relevance and test the spacing influence. For each configuration and axis, the antenna transfer function $\mathcal{H}(f,\theta,\varphi)$, was measured over the azimuthal plane for three elevations (0, 20° and -16°) and two orthogonal polarizations (ver tical, parallel to the rotation axis in azimuth, i.e. to the phantom, and horizontal). The reflection coefficients S_{11} were



also measured for each configuration. This constitutes a total measurement set of 11 691 frequency responses (comprising 162 conical cuts (3 probes x 3 sensor positions x 3 elevations x 2 polarizations) and 27 S_{11}). All relevant quantities, either in emission (realized gain G_r , power gain G) or in reception (e.g. (loaded) antenna factor AF), can be computed from the measured quantities, for each polarization. Any signal received at each probe port can be computed as well for a given incident power density or field strength.

4.2.2.1 Phantom characteristics

The whole body phantom used is 1.69 m tall (Figure 50). Its dielectric properties have been determined by T. Alves (University of Paris-Est Marne-la-Vallée) with an original experimental method [17]. They are illustrated in Figure 49. For comparison, the relative permittivity of the skin, fat and muscles (mainly based on Gabriel & Grabriel's work and provided by ITIS' Foundation [18]) are also shown in the Figure 49. The homogeneous phantom properties appear, at least for the $arepsilon_r$, as a weighted average of the skin, fat and possibly muscles ones. The ε_r seems however slightly larger than required for the frequencies of interest in the project. Nevertheless, this experimental model is globally really satisfactory.

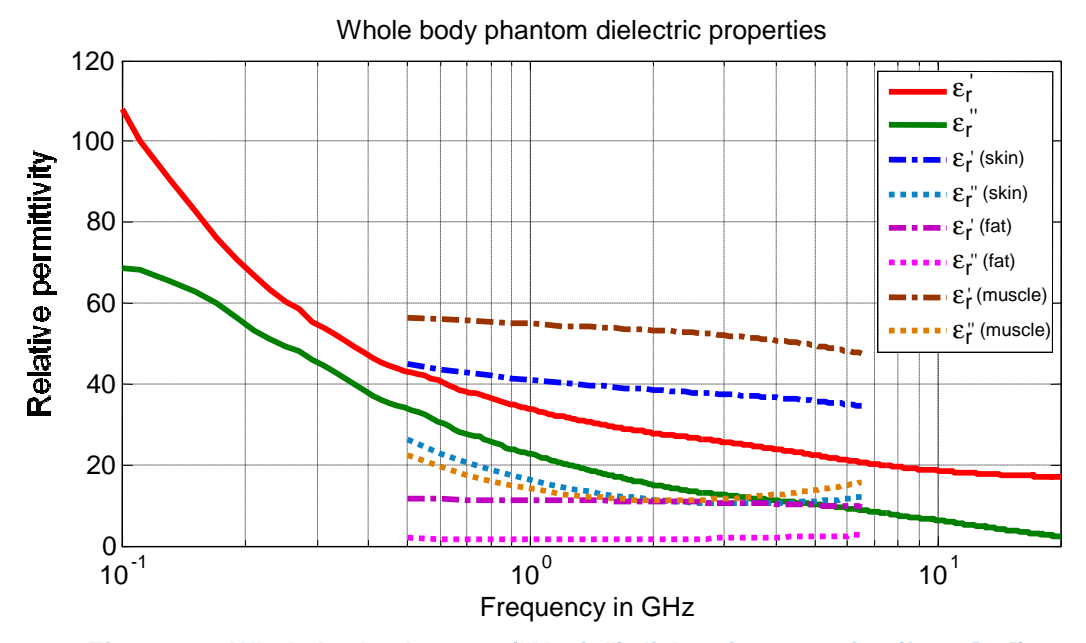


Figure 49: Whole body phantom ("Kevin") dielectric properties (from [17]).

4.2.2.2 Measurement setup

Measurements are carried out in an anechoic chamber. The phantom is placed at the rotation center of a positioning turntable (Figure 50), and transmission measurements for each of the three probes are performed in azimuth with a VNA (Vector Network Analyser R&S ZVA40), for three elevations (0, 20° and -16° from "horizon", i.e. $\theta = 90^{\circ}$, 70° and 106°, see Figure 54) and two orthogonal polarizations ("V" and "H").

Three sensor positions on the phantom are considered (Figure 50): on the "left chest" (Erreur! Source du renvoi introuvable.), on the "left hip" (Figure 53Erreur! Version: V1.2



Source du renvoi introuvable.) and at the level of the right back pocket of trousers (Figure 54). For each location, three distances to the body, thanks to foam spacers (Figure 52), are considered (about 0, 10 and 20 mm), in order to extend the practical relevance and test the spacing influence.

The measurement frequency band is 0.5-6.5 GHz, with a frequency step of $\delta f = 50$ MHz.

In the following, the retained approaches are similar to those presented in the previous section (polarimetric and non polarimetric, influence of the incoming field XPR and taking into account the channel). The notations are the same.





Figure 50: Phantom positioning in anechoic chamber.

Version: V1.2





Figure 51 : Sensor positioning on the phantom: left chest, left hip and right back.





Figure 52 : Sensor/phantom spacing: ~ 0, 10 and 20 mm (not shown here).

Version: V1.2 75







Figure 53 : Sensor positioning details: left chest,. ~12.5 cm from the saggital plane and ~ 23.5 cm from the top of the shoulder.

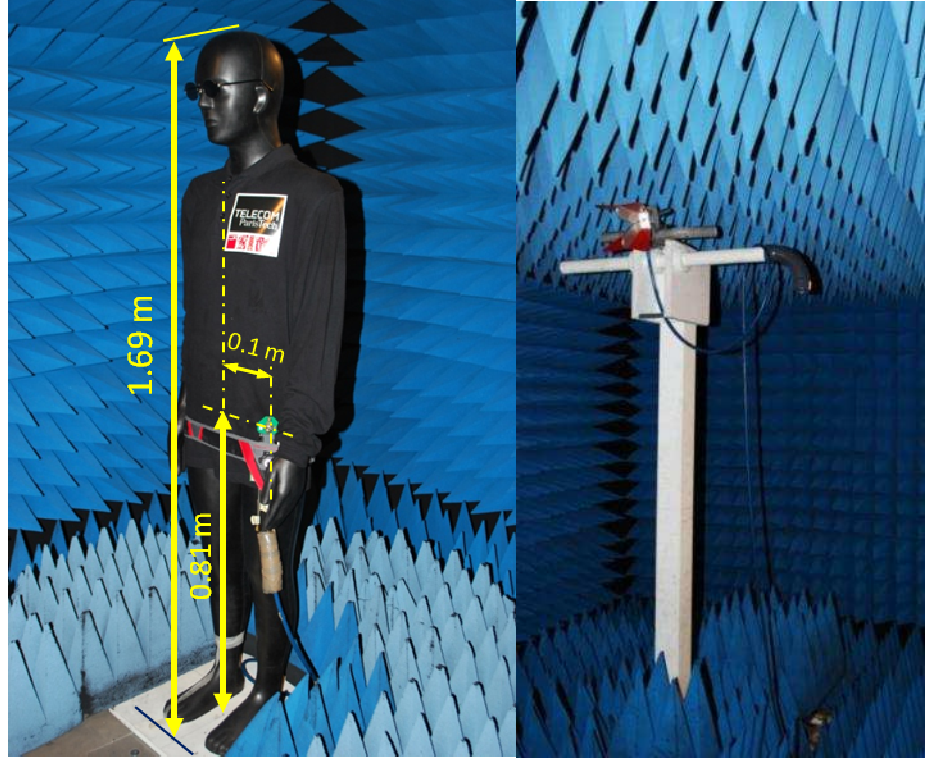


Figure 54: Left: Sensor positioning details on left hip,. ~10 cm from the saggital plane and ~81 cm from the ground; Right: reference antenna positioning for the conical cut at an elevation of 20° above horizon.

Version: V1.2 76



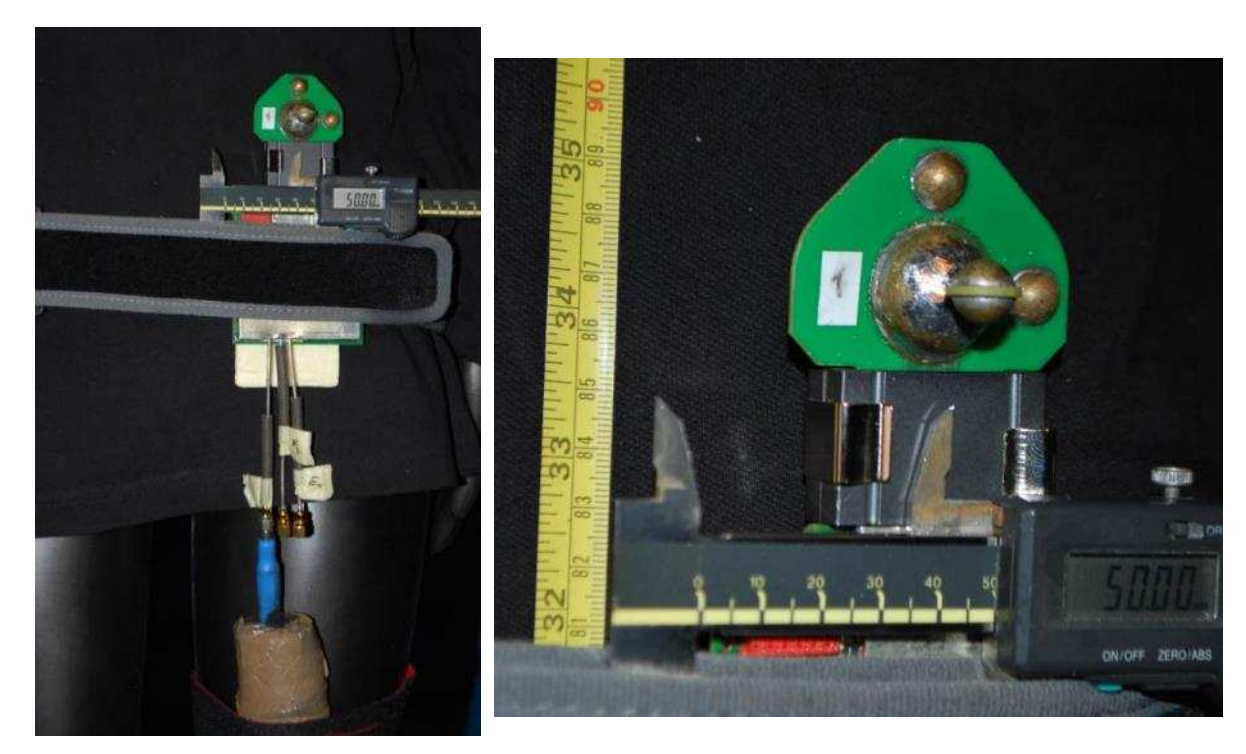


Figure 55 : Sensor positioning details: right back,. \sim 5 cm from the saggital plane and \sim 87 cm from the ground.

4.2.2.3 Measurement results - Elementary approach and global view

The input matching is presented in Figure 56 for the three sensor positions and the smallest spacing ($\delta \sim 0$). As can be observed, the body proximity effect on the $|S_{11}|$ is moderate even for the closest positioning.

Version: V1.2



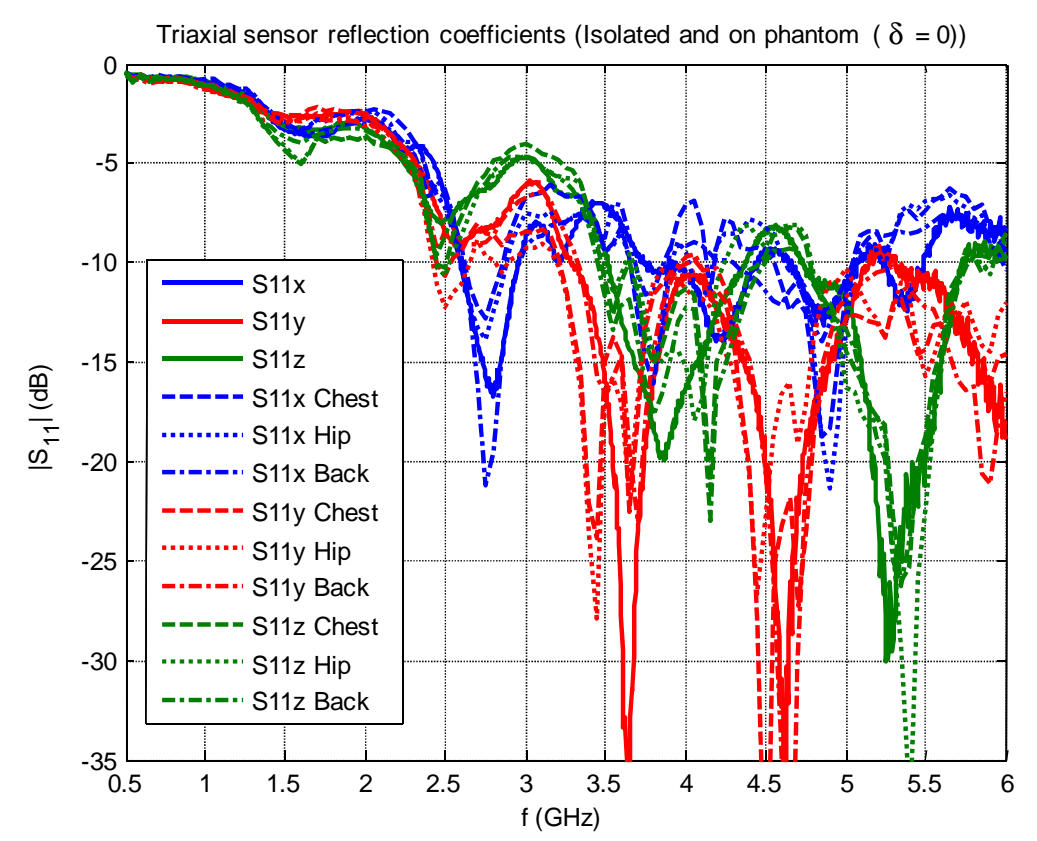


Figure 56: Reflection coefficient of each probe sensor and for all "scenarios" (compared to the isolated case).

An example of measurements offering a "global view" of the body shadowing effect is given in Figure 57: it shows the total (including all axes) Mean Realized Gain (MRG averaged over 0.7-6 GHz) in horizontal polarization, in the azimuthal plane ($\theta=90$ °). As expected, the body masking is the dominant effect, with FTBR of about 13 dB (resp. 15 dB) for the Chest (resp. for the Back). The Hip case is less "unidirectional", but the MRG is globally lower, both aspect being probably due to the effect of the hand. Such high FTBRs induce a high uncertainty of the exposimeter measurements, if it is used as is, without correction strategy. In addition, because of reflections or absorption and shadowing of the body, the exposimeter gain, hence the measured field, can be either higher or significantly lower than in the absence of the carrier.



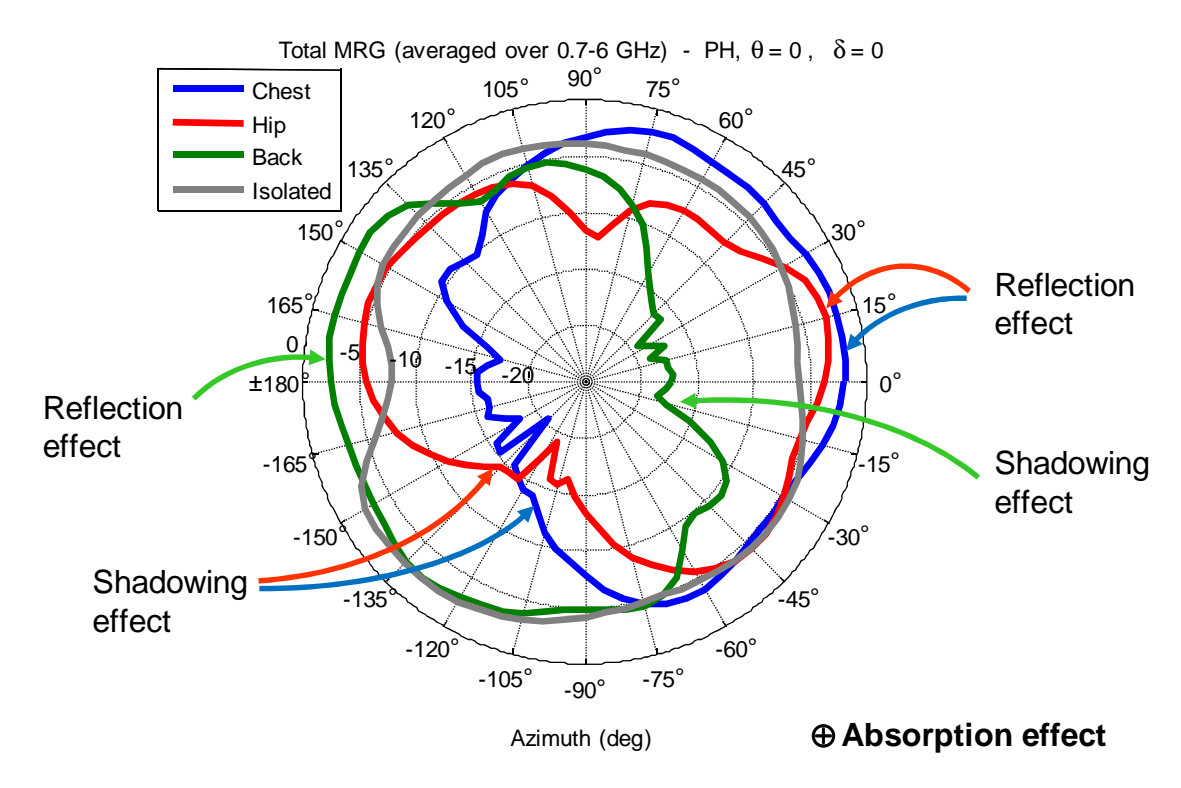


Figure 57: MRG of each probe sensor and for all "scenarios" (azimuthal cut).

4.2.2.4 Polarimetric approach

☐ POLARIMETRIC GAIN "ISOTROPY"

As previously, the radiation characteristics (polarimetric realized gain $G_r^{\theta,\varphi} = \left|\mathcal{H}_{\theta,\varphi}^T\right|^2$) are provided hereafter for each considered RAT. The results are as well averaged over each frequency band, but the normalization is now operated relative to the isolated sensor (i.e. its averaged realized gain over azimuth, in the azimuthal plane and for each polarization), instead of normalizing to its own mean, i.e.:

$$\hat{G}_{r,phant}^{\theta,\varphi}(f_{RAT},\theta,\varphi) = \int_{\Delta f_{RAT}} G_{r,phant}^{\theta,\varphi}(f,\theta,\varphi) df / \frac{1}{2\pi} \int_{\Delta f_{RAT}}^{2\pi} \int_{0}^{2\pi} G_{r,isol}^{\theta,\varphi}(f,\pi/2,\varphi) d\varphi df$$
(3.11.9)

This allows not only to focus on the isotropy variance considering polarization aspects, but also to underline the body effect, compared to the isolated case.

In addition, in practice, the radiation characteristics of the worn sensor won't be exactly known for each carrier user (but only statistically – this is the object of the simulation campaign carried out with various phantom models), whereas the isolated sensor is a priori known with precision.



"Chest scenario"

FP7 Contract n°318273

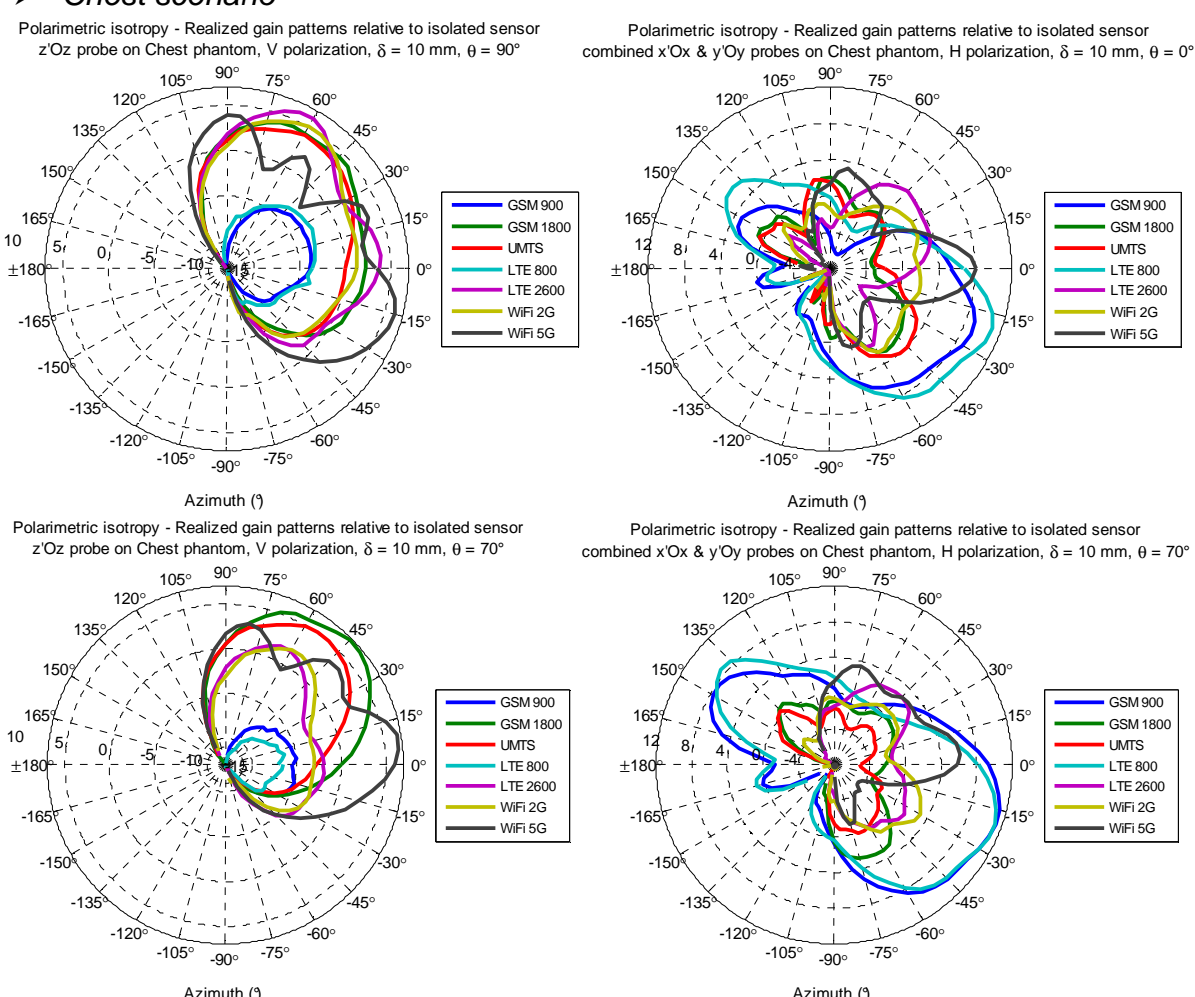


Figure 58 : Normalized (co-polar) realized gain patterns (averaged over each RAT band) of the "V"(z'Oz) probe and combined "H" probes (xOy) in the azimuthal plane for the "Chest scenario", $\theta = 90^\circ$ and 70° , $\phi = 10$ mm.

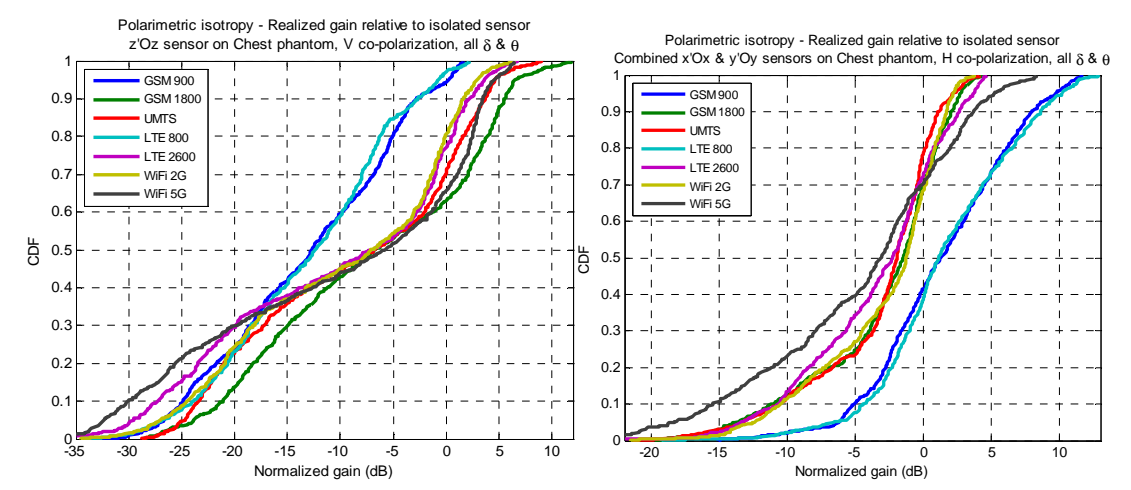


Figure 59 : Normalized (co-polar) realized gain CDF (averaged over each RAT band) of the "V"(z'Oz) probe and combined "H" probes (xOy) in the azimuthal plane for the "Chest scenario", all φ and θ .

Version: V1.2 80



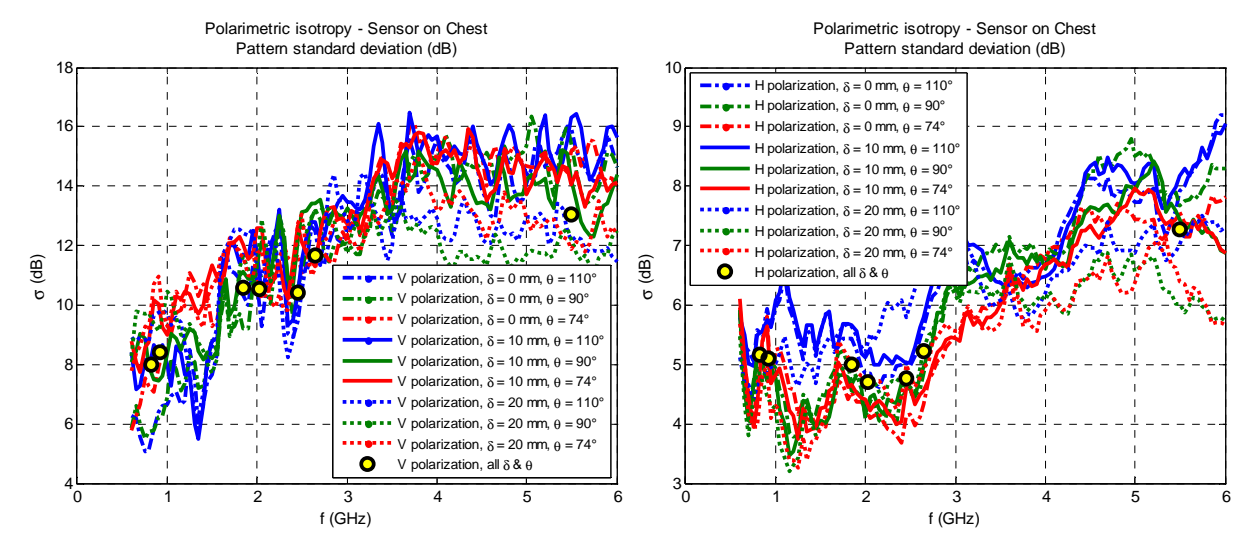


Figure 60 : Normalized (co-polar) realized gain patterns (averaged over each RAT band) of the "V"(z'Oz) probe and combined "H" probes (xOy) in the azimuthal plane for each "scenario", all φ and θ .

The significant reduction of the vertical probe gain at low frequency bands (GSM 900 & LTE 800) *in the visible region* (i.e. in the solid angle for which the sensor is not masked by the body, roughly a semi-space for the vertical probe; see e.g. the top left polar pattern of Figure 58) is probably due to a higher power absorption due to a deeper penetration of the waves in the tissues, related to the polarization which is tangent to the body. EM simulations show that the elevation plays also a non-negligible role.

Apart for the highest band (WiFi 5G), the "isotropy" variance depends only moderately on the elevation and on δ (Table 25).

The results are qualitatively similar for the "Back scenario".

Table 25 : Polarimetric isotropy statistics (over azimuth), Chest, all θ and ϕ (dB).

	GSM 900	GSM 1800	UMTS	LTE 800	LTE 2600	WiFi 2G	WiFi 5G
μ_{Gv}	-13.13	-7.05	-8.80	-13.14	-10.59	-9.89	-10.21
σ_{Gv}	8.40	10.58	10.55	7.99	11.65	10.40	13.06
m _{Gv}	-12.74	-6.64	-6.79	-12.35	-6.92	-7.13	-5.72
μ_{Gh}	1.37	-3.04	-3.29	1.61	-3.56	-3.02	-4.57
σ_{Gh}	5.10	5.00	4.71	5.16	5.22	4.76	7.27
m _{Gh}	1.30	-1.50	-1.97	1.12	-2.30	-1.28	-3.10

"Hip scenario"

The situation is significantly different for the "Hip scenario". As can be observed in Figure 61 and Figure 62, the power is spread both towards the front and toward the

Version: V1.2



back for both polarizations. This is partly attributed to the effect of the hand (and arm) which plays somehow a role of reflector. However, on average, the isotropy deviation is similar.

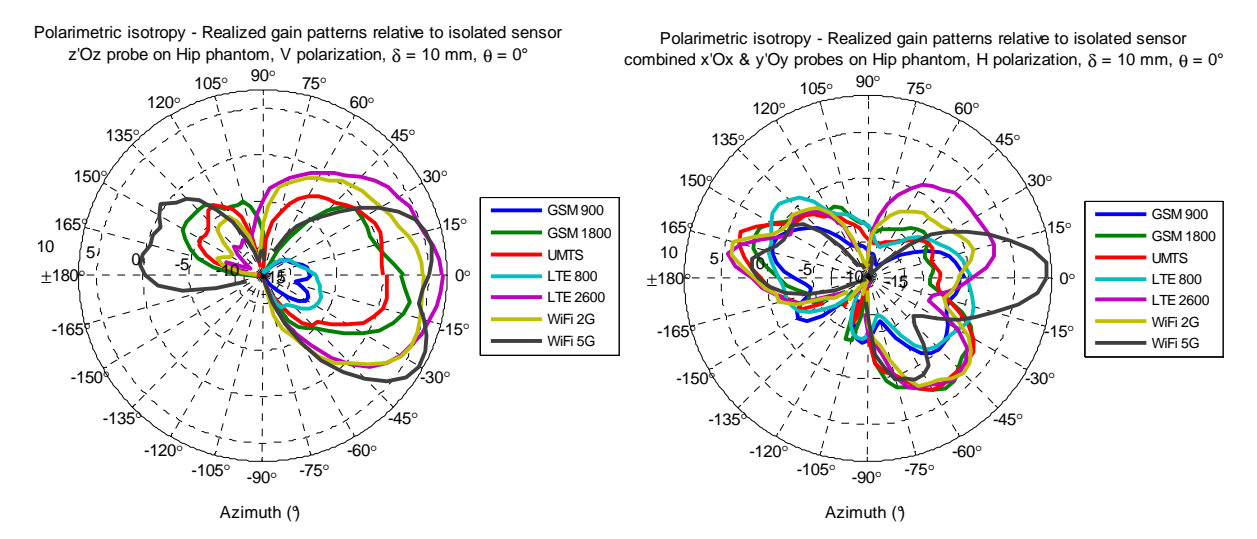


Figure 61 : Normalized (co-polar) realized gain patterns (averaged over each RAT band) of the "V"(z'Oz) probe and combined "H" probes (xOy) in the azimuthal plane for the "Hip scenario", θ = 90°, δ = 10 mm.

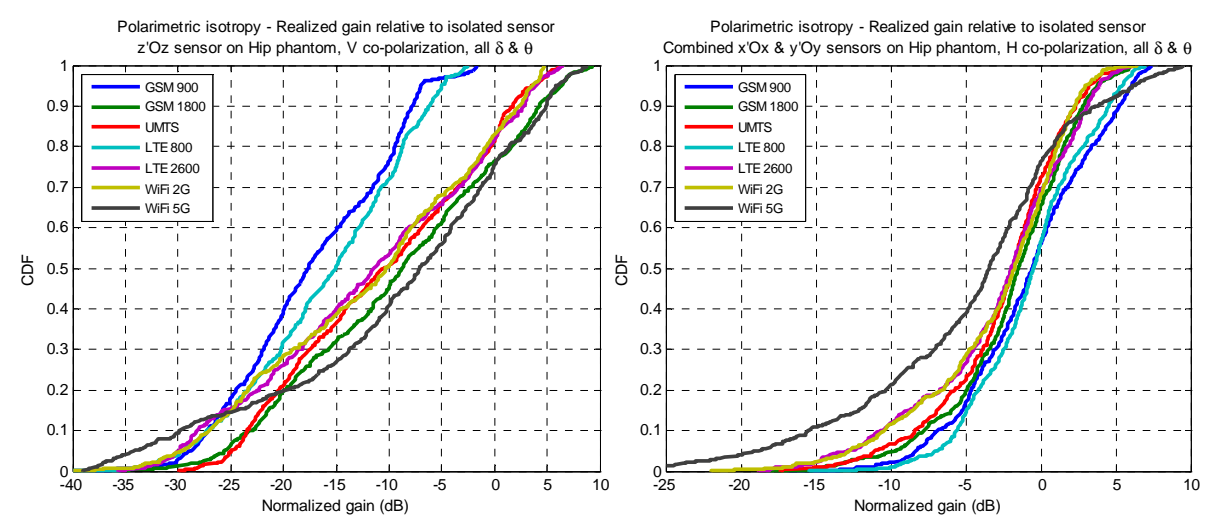


Figure 62 : Normalized (co-polar) realized gain CDF (averaged over each RAT band) of the "V"(z'Oz) probe and combined "H" probes (xOy) in the azimuthal plane for the "Hip scenario", all φ and θ .

Version: V1.2



Table 26 : Polarimetric isotropy	statistics (over azimuth), Hi	ρ , all θ and ϕ (dB).

	GSM 900	GSM 1800	UMTS	LTE 800	LTE 2600	WiFi 2G	WiFi 5G
μ_{Gv}	-17.21	-9.17	-10.55	-15.99	-11.77	-11.85	-9.37
σ_{Gv}	7.50	10.30	9.46	7.77	10.99	10.88	12.21
μ_{Gh}	-17.66	-8.73	-10.49	-15.03	-11.34	-10.28	−7.15
σ _{Gh}	4.40	4.18	4.19	3.81	5.11	4.91	7.30

□ POLARIMETRIC XPR

The XPR is still defined as: $XPR = G_r^{cx} / G_r^{co}$. The relative XPR is defined as the ratio of the "on-body XPR" and "isolated XPR":

$$. XPR_{rel} = \frac{XPR_{ph}}{XPR_{isol}} = \frac{G_{r,ph}^{cx} / G_{r,ph}^{co}}{G_{r,isol}^{cx} / G_{r,isol}^{co}} \quad \text{or} \quad XPR_{rel} = XPR_{ph} - XPR_{isol} \quad \text{in dB.} \quad (3.11.10)$$

For the sensor on the chest and the vertical probe, the XPR is typically increased, on average, by 2 – 15 dB (compared to the isolated case, Table 20), and up 35 dB for some directions and bands (comparing Figure 63 to Figure 43). This depolarization effect due to the presence of the body is less pronounced for the horizontal sensors. Results are comparable for the hip case. However, these high values occur in the shadow region (masked by the body). In the visible region, the XPR increase is less significant, ranging between –15 dB to 15 dB for the vertical probe (depending on directions and bands) and typically less than 8 dB for the horizontal ones.

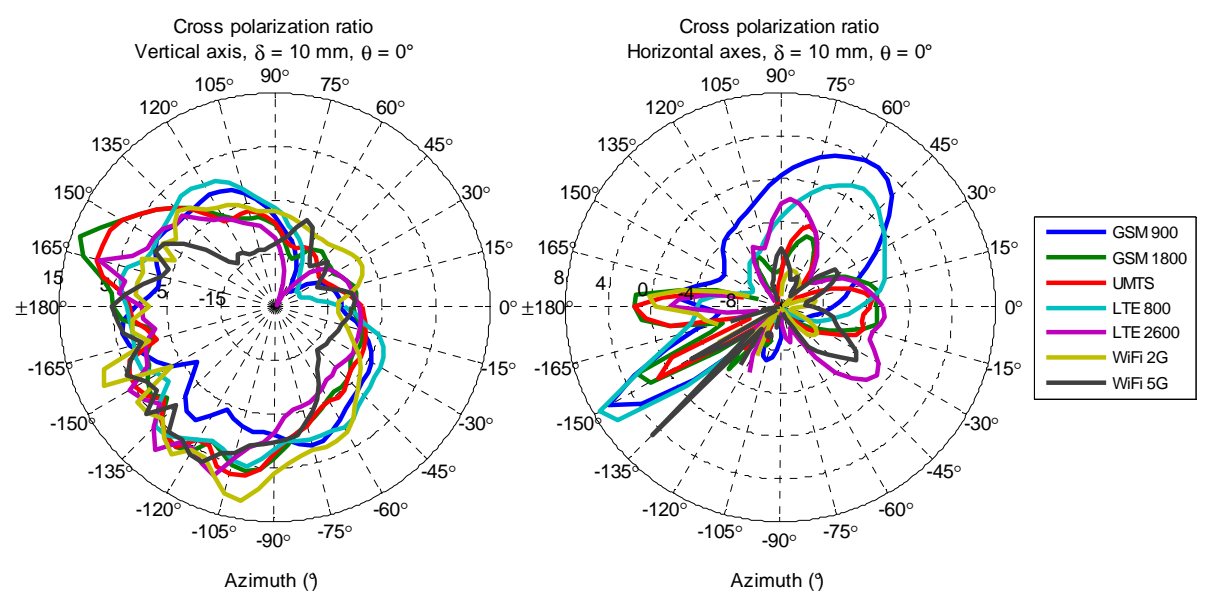


Figure 63 : XPR levels (averaged for each RAT) of the "V"(z'Oz) probe and combined "H" probes (xOy) in the azimuthal plane. Sensor on chest, $\delta = 10$ mm, $\theta = 90$ °.



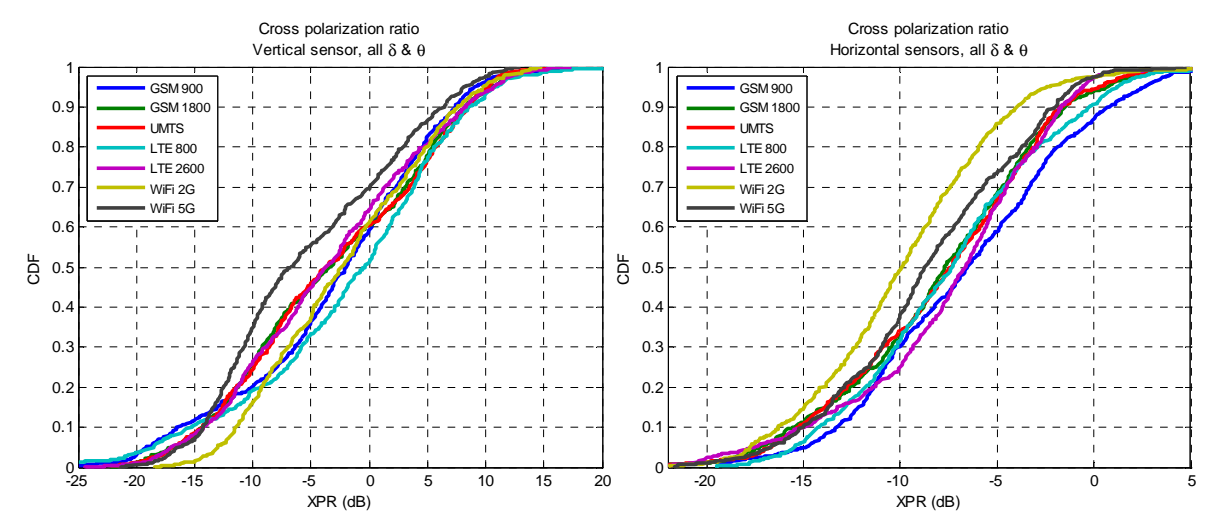


Figure 64 : XPR levels CDF (averaged for each RAT) of the "V"(z'Oz) probe and combined "H" probes (xOy) in the azimuthal plane. Sensor on chest, all θ and ϕ .

Table 27 : Polarimetric sensor XPR statistics (over azimuth) – Sensor on Chest (all θ and ϕ).

XPR	GSM 900	GSM 1800	UMTS	LTE 800	LTE 2600	WiFi 2G	WiFi 5G
$\mu_{\scriptscriptstyle XPRV}$	-2.94	-3.13	-3.07	-1.79	-3.40	-2.11	- 5.18
$\sigma_{_{XPRV}}$	8.54	8.65	8.65	9.10	8.41	7.22	7.87
μ _{xPRh}	- 6.57	- 7.90	- 7.86	- 7.33	- 7.44	-9.89	- 8.51
$\sigma_{\scriptscriptstyle XPRh}$	5.56	5.33	5.30	5.11	5.15	4.77	4.89
$\Delta\mu_{_{XPRV}}$	15.05	1.97	5.23	16.06	13.35	12.31	9.30
$\Delta\mu_{\mathit{XPRh}}$	-6.0	- 2.91	- 1.98	- 6.50	0.29	- 1.49	0.82

Regarding the "Back" scenario, the relative XPR is similar on average, but for the Hip case, the XPR is significantly increased (Figure 65), including in the visible region (around $\varphi = 0$, Figure 63).



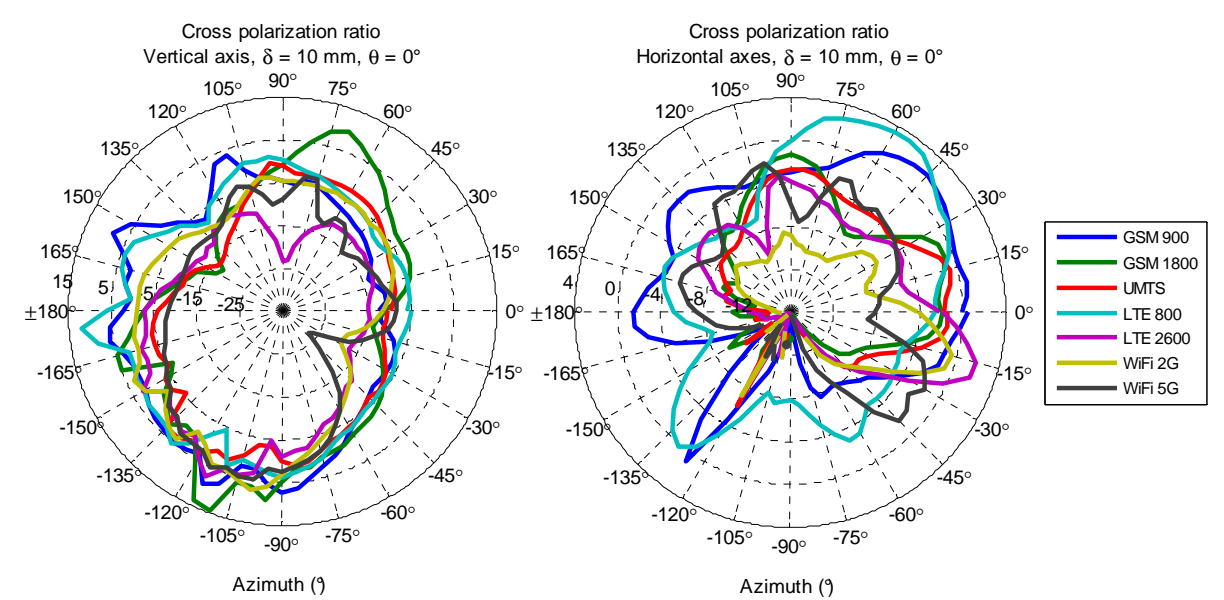


Figure 65 : XPR levels (averaged for each RAT) of the "V"(z'Oz) probe and combined "H" probes (xOy) in the azimuthal plane. Sensor on hip, δ = 10 mm, θ = 90°.

■ PARTIAL CONCLUSIONS

First partial conclusions regarding the worn sensor can be drawn here:

- First, as obviously expected, the isotropy variance is considerably increase compared to the isolated case, by typically 7 to 11 dB for the vertical probe and 2 to 6 dB for the horizontal ones, depending on the band.
- The XPR is clearly modified, significantly increased in many cases, which seriously compromise the perspective of performing reliable polarimetric measurements with the wearable triaxial sensor.
- Hence, resorting to non-polarimetric measurements is more promising.

This last point is considered in the following, based on 3D electromagnetic simulations.

4.3 **Simulations**

Electromagnetic simulations are based on various numerical phantoms, from simple canonical geometry based models to realistic fully non homogeneous anthropomorphic ones. The last are based on the Virtual Population suit from ITIS' Foundation (Table 28) [18].



Table 28 : Virtual	Population (ITIS)	Foundation)	anthropometric c	haracteristics.

Name	Sex	Age [year]	Height [m]	Weight [kg]	BMI† [kg/m²]	Number of Tissues
<u>Duke</u>	male	34	1.77	72.4	23.1	77
Ella	female	26	1.63	58.7	22.0	76
Louis	male	14	1.69	50.4	17.7	77
<u>Billie</u>	female	11	1.47	35.4	16.5	75
<u>Eartha</u>	female	8	1.36	30.7	16.7	75
Dizzy	male	8	1.40	26.0	13.4	66
<u>Thelonious</u>	male	6	1.17	19.3	14.0	76
Roberta	female	5	1.09	17.8	14.9	66

[†] Body Mass Index

4.3.1 Simplified model of isolated sensor

As a first approach, simulations of a simplified model (provided by Satimo®) of the sensor part of the EME Spy 140® dosimeter first isolated (Figure 66), then "worn" by a numerical phantom of the Virtual Population suit (from ITI'S foundation) are carried on.

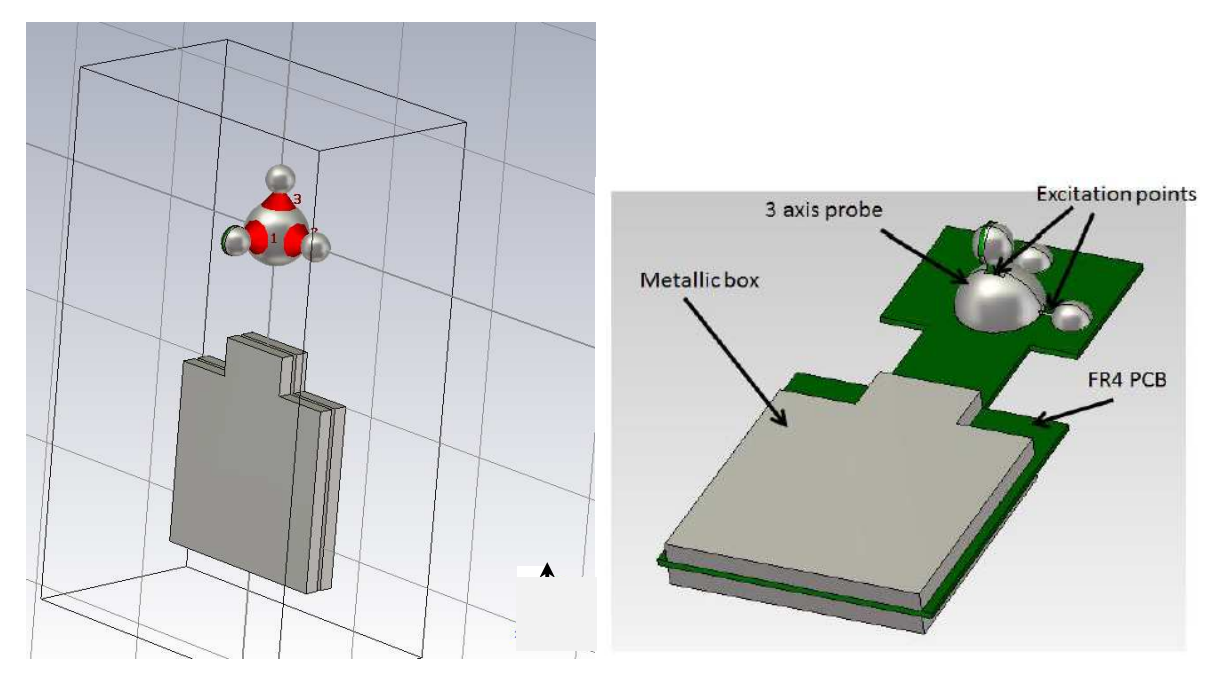


Figure 66: Sketch of the sensor simplified model (from Satimo).

As done in the measurements section, the main characteristics of the sensor are presented first in Figure 67 to Figure 71

Note that the fact that a high mismatch can be observed at low frequencies (with a significant deviation from the measured results), which is probably due to the model simplification, is not of primer importance as we are dealing with isotropy considering



87

normalized or relative quantities (i.e. the fact that the realized gain is particularly low at low frequencies is actually compensated in practice with an appropriate calibration, so that it only impacts the dosimeter sensitivity).

The quantities used in the following are the same as those defined in section 4.3.2.

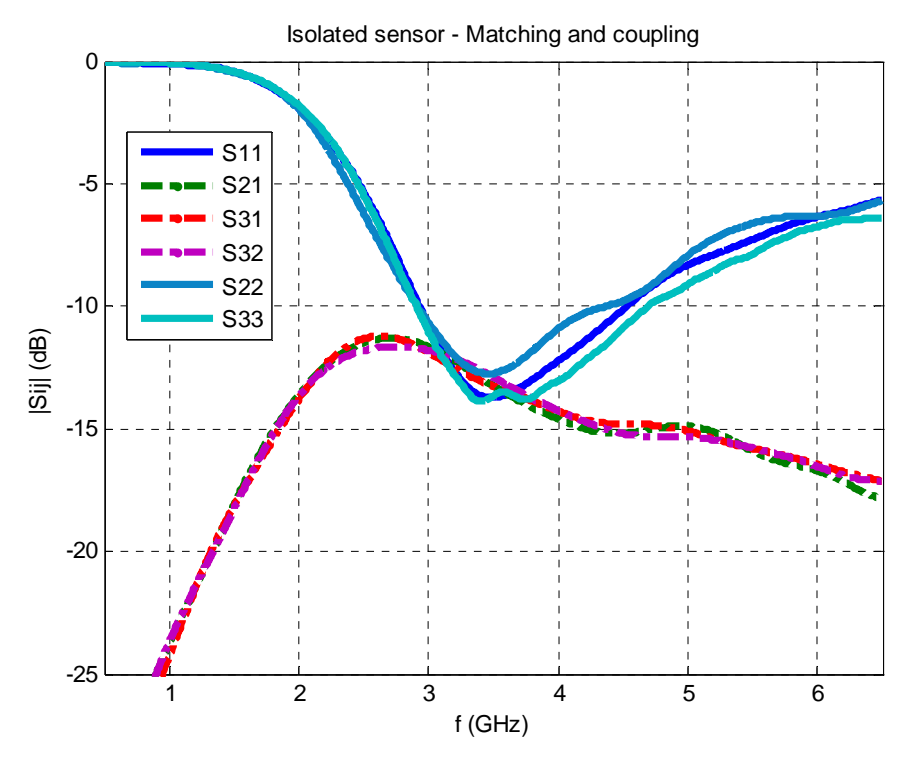


Figure 67: Simulated reflection coefficient of each probe sensor.

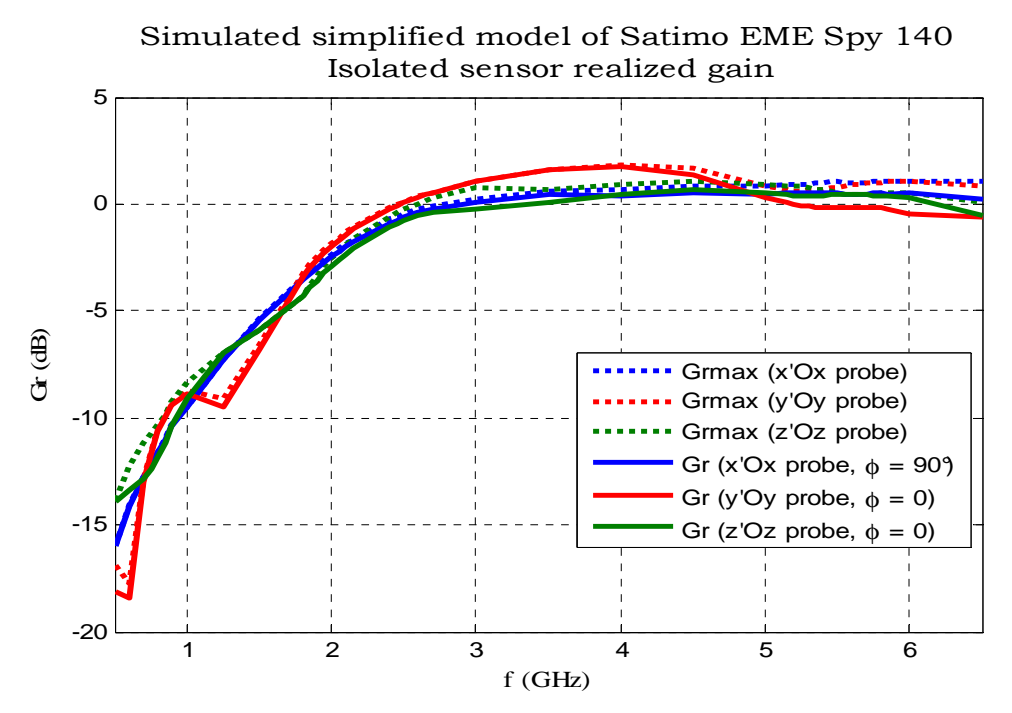


Figure 68: Simulated realized gains per probe.



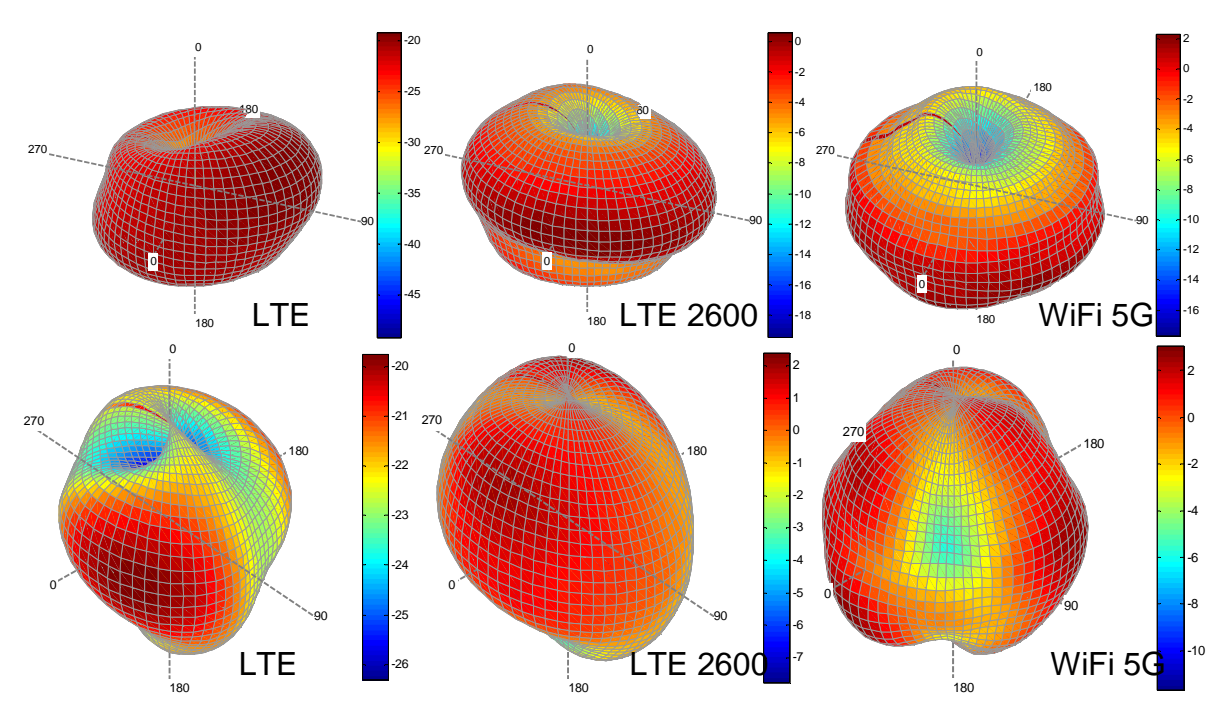


Figure 69: Simulated 3D co-polar realized gain patterns (averaged over each RAT band, LTE 800, LTE 2600 and WiFi 5G) of the "V"(z'Oz) probe (top) and combined "H" probes (xOy) in the azimuthal plane (bottom).

4.3.1.1 Polarimetric approach

We follow the same approach here as in section 4.2.1.1.

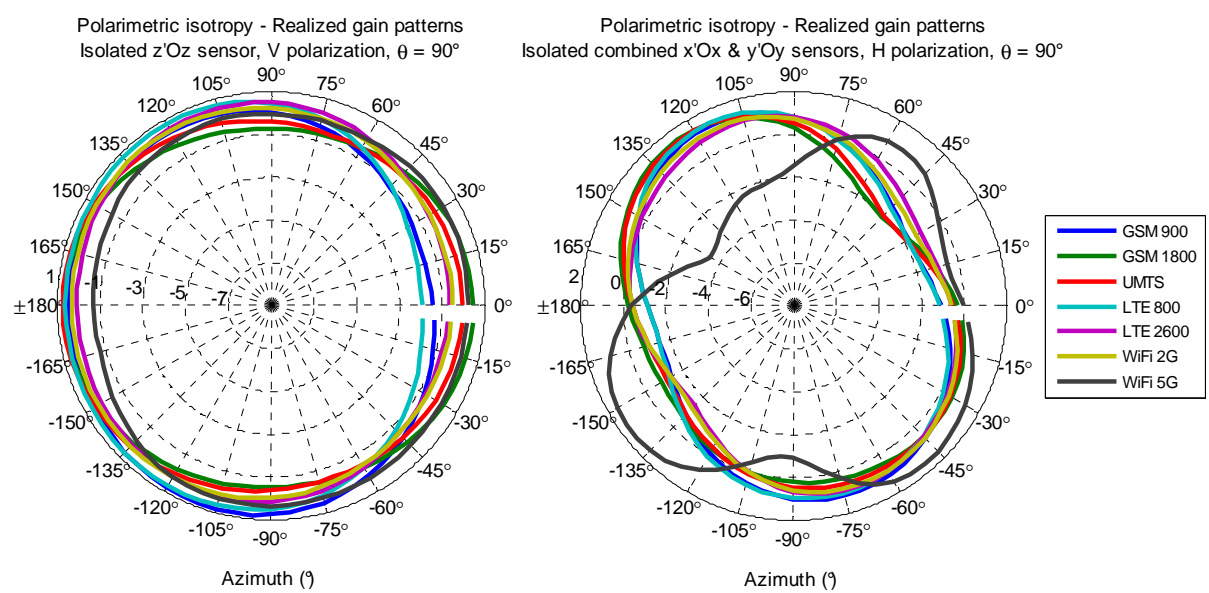


Figure 70 : Simulated normalized realized gain patterns (averaged over each RAT band) of the "V"(z'Oz) probe and combined "H" probes (xOy) in the azimuthal plane, $\theta = 90^\circ$.

Version: V1.2 88



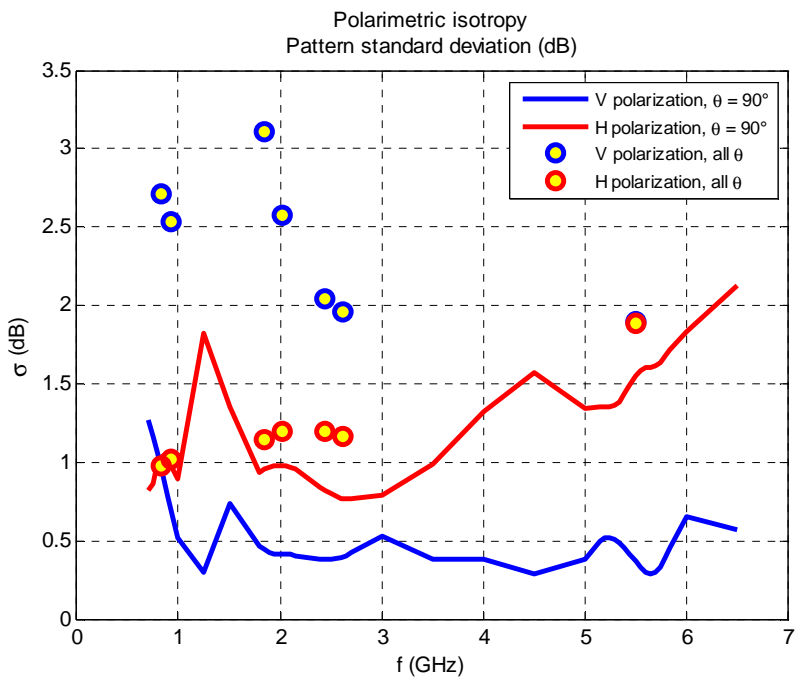


Figure 71 : Simulated normalized realized gain pattern standard deviation over azimuth (averaged over frequency for each RAT – yellow circles) of the "V"(z'Oz) probe and combined "H" probes (xOy), all θ (circles) and ϕ = 90°(plain).

Table 29: Polarimetric isotropy statistics (over azimuth and elevation), in dB

	GSM 900	GSM 1800	UMTS	LTE 800	LTE 2600	WiFi 2G	WiFi 5G
μ_{Gv}	-0.52	-0.75	-0.56	-0.59	-0.32	-0.35	-0.33
$\sigma_{\scriptscriptstyle Gv}$	2.53	3.10	2.57	2.71	1.96	2.04	1.89
μ_{Gh}	0.12	0.14	0.16	0.11	0.14	0.16	0.19
σ_{Gh}	1.02	1.14	1.19	0.98	1.16	1.20	1.89

As can be observed in Figure 70, Figure 71and in Table 29, the "isotropy" is very satisfactory (typ. $\sigma_{\rm G}$ < 3 dB), and similar to the measured one (Figure 41, Figure 42 and Table 19) in particular in H polarization. The variance is slightly higher in V polarization (by about 1.5 – 2 dB) because all θ are considered (whereas only the azimuthal plane was considered in the measurements).

The XPR is very satisfactory for the V probe over a wide solid angle around the horizon (typ. less than -10 dB). It is a little bit higher for the H probes in particular for the lower frequency bands (typ < -5 dB), in agreement with the measurements.



4.3.1.2 Non polarimetric approach

☐ INFLUENCE OF THE INCIDENT FIELD POLARIZATION

As expected, the isotropy is slightly improved when we resort to a non polarimetric received signal (combining all probe signals), as can be observed in the following figures.

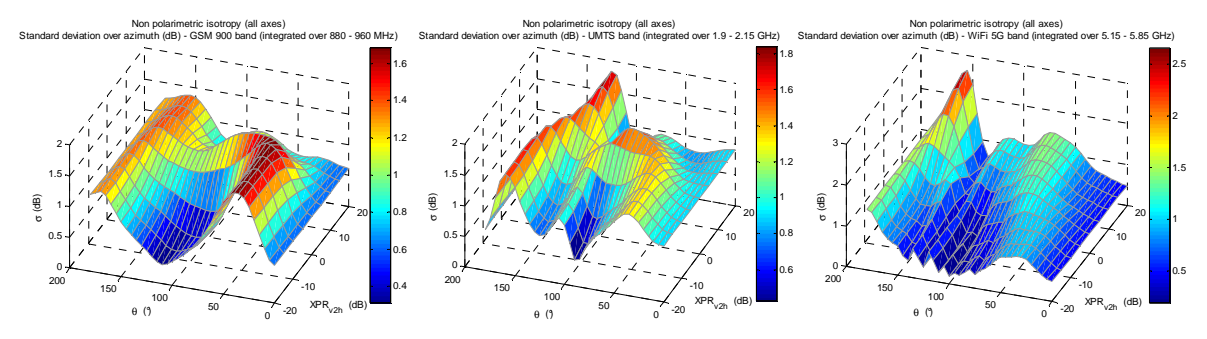


Figure 72 : Influence of the incoming wave XPR level on the isotropy (for various RATs): standard deviation of the received non polarimetric signal.

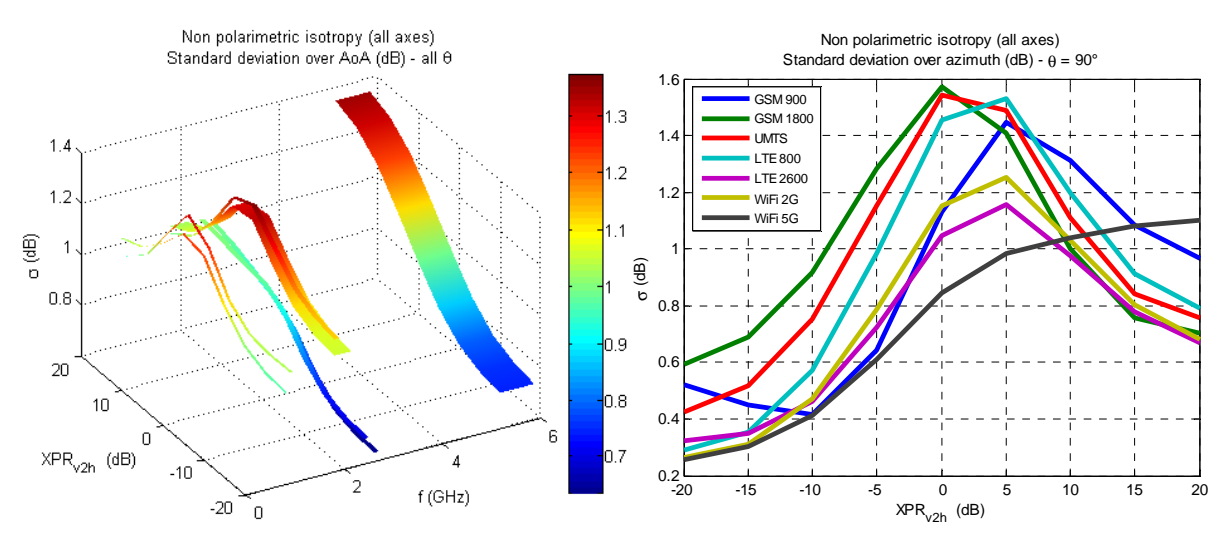


Figure 73 : Influence of the incoming wave XPR level on the isotropy (for each RATs): standard deviation of the received non polarimetric signal.

Version: V1.2



☐ INFLUENCE OF THE CHANNEL CHARACTERISTICS We give only a few results for Environments n°1 and 2 here, for sake of brevity.

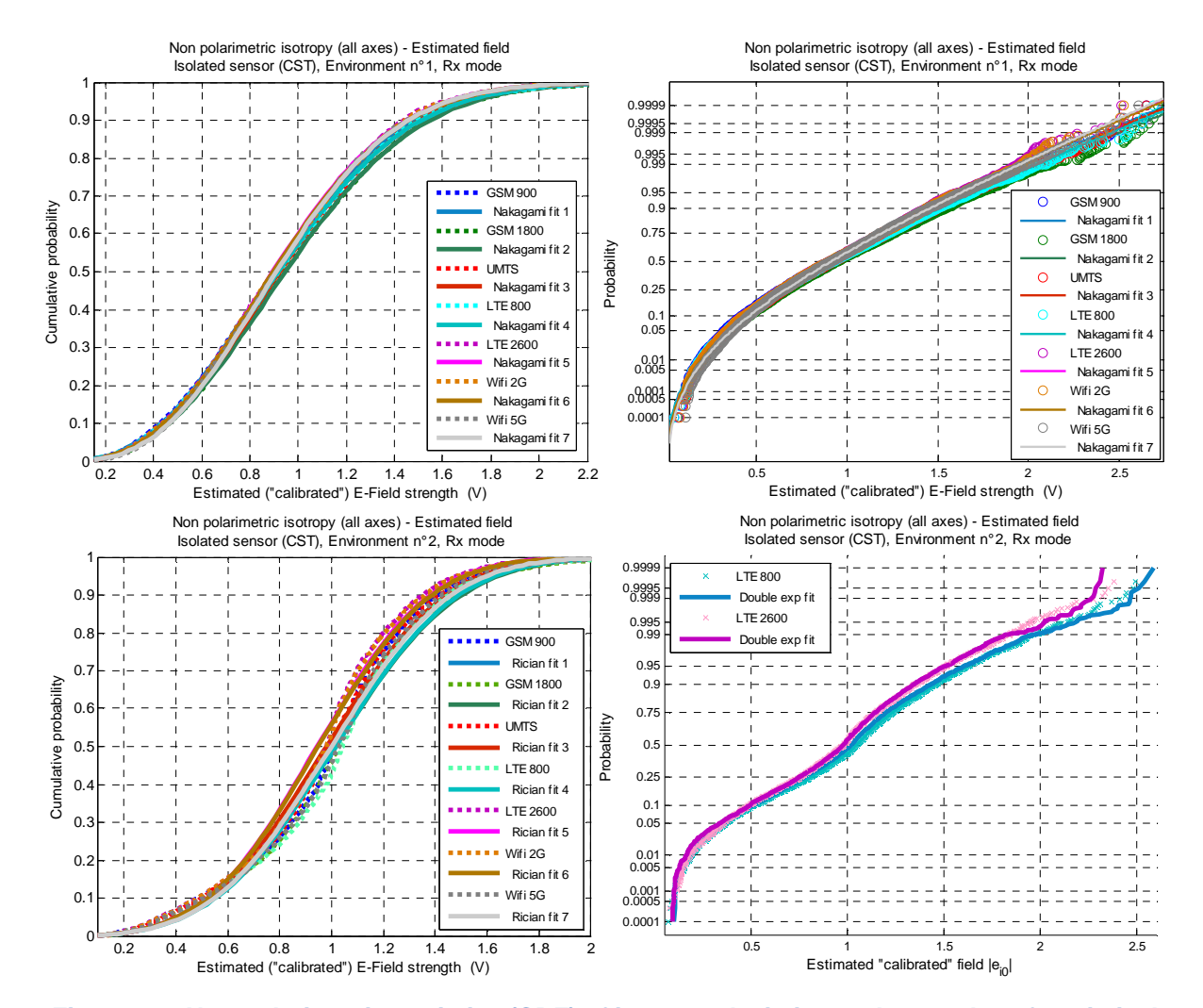


Figure 74: Non polarimetric statistics (CDF) of isotropy deviation and examples of statistical fits for an NLOS and a LOS environments (n°1 & 2, based on WINNER+ 3D channel models).

For Env. n° 1 (LOS), Nakagami fits are convenient, whereas for Env. n° 2 (NLOS) double exponential fits are clearly better than Rician (or Nakagami). All are rather far from normality.

Both for the "bias" (μ_{ei0}) and the isotropy deviation (σ_{Ei0}), results (Figure 74 and Table 30 and Table 31) are similar to the measured ones (Table 22 and Table 23), but all elevations are taken into account here whereas only the azimuthal plane was considered in the measurements. The same conclusion holds for both environments.

In addition, it must be underlined that these moments are almost independent on the frequency band.



Table 30: Non polarimetric sensor isotropy deviation statistics (over θ and φ) for Env. n°1.

e _{i0norm}	GSM 900	GSM 1800	UMTS	LTE 800	LTE 2600	WiFi 2G	WiFi 5G
μ _{ei0}	0.93	0.98	0.96	0.95	0.93	0.93	0.94
σ _{ei0}	0.41	0.42	0.41	0.41	0.39	0.39	0.
m_{Ei0} (dB)	-0.91	-0.55	-0.70	-0.73	-0.90	-0.88	-0.84
σ _{εί0} (dB)	4.34	4.22	4.21	4.33	4.18	4.19	3.98

Table 31: Non polarimetric sensor isotropy deviation statistics (over θ and φ) for Env. n°2.

e _{i0norm}	GSM 900	GSM 1800	UMTS	LTE 800	LTE 2600	WiFi 2G	WiFi 5G
μ _{ei0}	0.99	1.02	0.99	1.02	0.95	0.95	1.00
σ _{ei0}	0.35	0.37	0.35	0.36	0.33	0.34	0.35
m_{Ei0} (dB)	0.10	0.24	-0.02	0.35	-0.17	-0.16	0.25
σ _{εί0} (dB)	3.95	3.87	3.85	3.95	3.86	3.84	3.87

□ POLARIMETRIC XPR

For brevity, the detailed results are not presented here, but the trends are the same as for the measurements, i.e. a significant increase of the XPR notably for the "V" probe, including in the visible region.

4.3.2 Realistic body model simulations

4.3.2.1 Simulated body impact: dosimeter worn on the waist

The simulations have been performed in CST MWS[®], using time domain solver and the results contain the gain patterns of 3 dosimeter's probes for:

- isolated dosimeter (without the body),
- dosimeter on the body with given placement.

The results vary depending on:

- frequency.
- location of the dosimeter,
- distance from the dosimeter to the body.



In what follows, the proposal of the evaluation parameter describing the influence of the body on the performance of the dosimeter is presented. As example, the metric is evaluated for the dosimeter probes at 2.6 GHz. In Figure 75, the impact of the presence of the body on the probes' reflection coefficient, S_{11} , is presented.

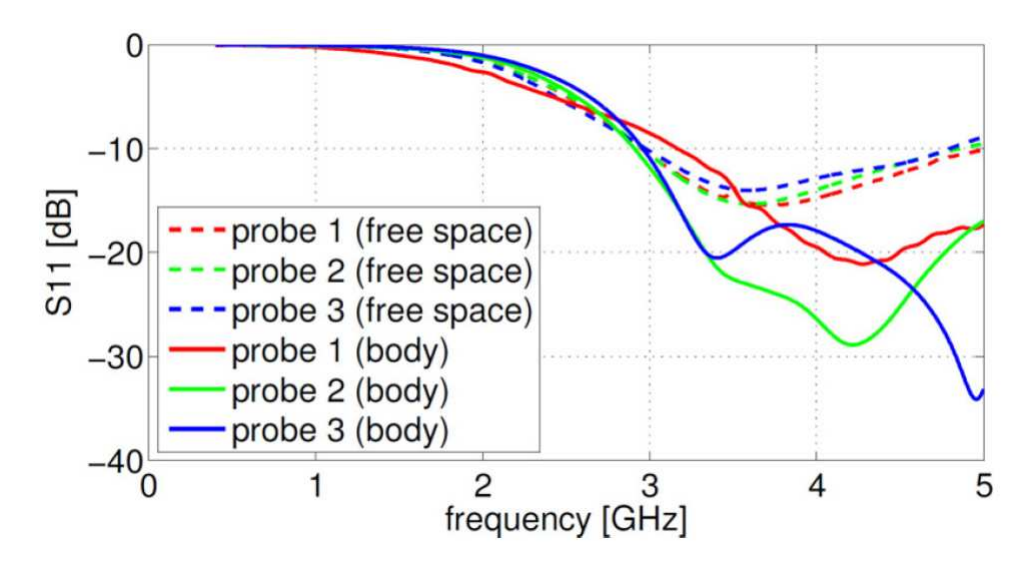


Figure 75: S11 for the dosimeter's probes

In Figure 76, the gain patterns of the dosimeter probes are presented for isolated case.

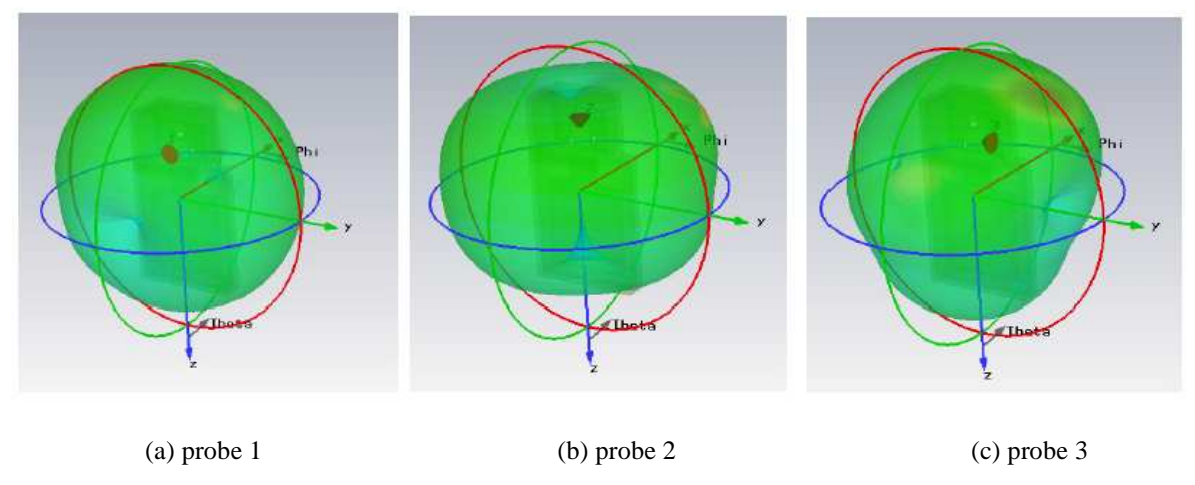


Figure 76: Radiation of the Isolated Dosimeter at 2.6 GHz

The gain patterns for the dosimeter located near to the body waist are presented in Figure 77.



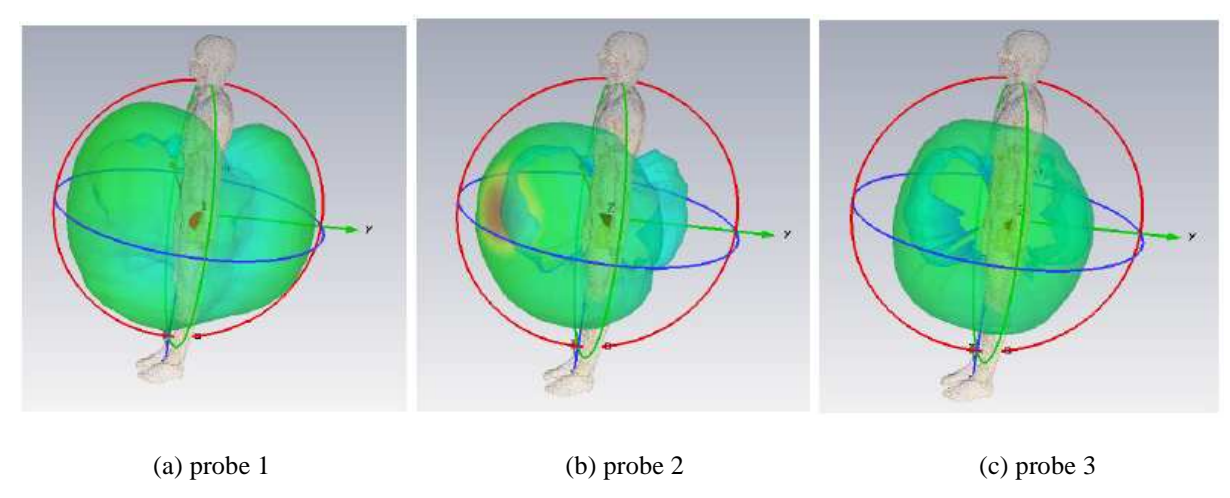


Figure 77: Radiation of the dosimeter on the Waist at 2.6 GHz

The Realized Gain is the gain of an antenna reduced by the losses due to the mismatch factor of the antenna input impedance to a specified impedance, [31]

$$G_R(\theta, \varphi) = \eta \times G(\theta, \varphi)$$

Where η is the impedance mismatch factor:

$$\eta = (1 - S_{11}^2)$$

The difference between the realised gain patterns, $G_R(\theta, \varphi)_{[d\mathbb{B}]}$, is calculated in all directions (i.e., horizontal and elevation angles):

$$\textit{G}_{\textit{R}}\left(\theta, \varphi\right)_{[\texttt{dB}]} = \textit{G}_{\textit{Rbody}}(\theta, \varphi)_{[\texttt{dB}i]} - \textit{G}_{\textit{Risolated}}\left(\theta, \varphi\right)_{[\texttt{dB}i]}$$

In Figure 78, the histograms representing the distribution of the difference for waist location and 2.6 GHz are presented.

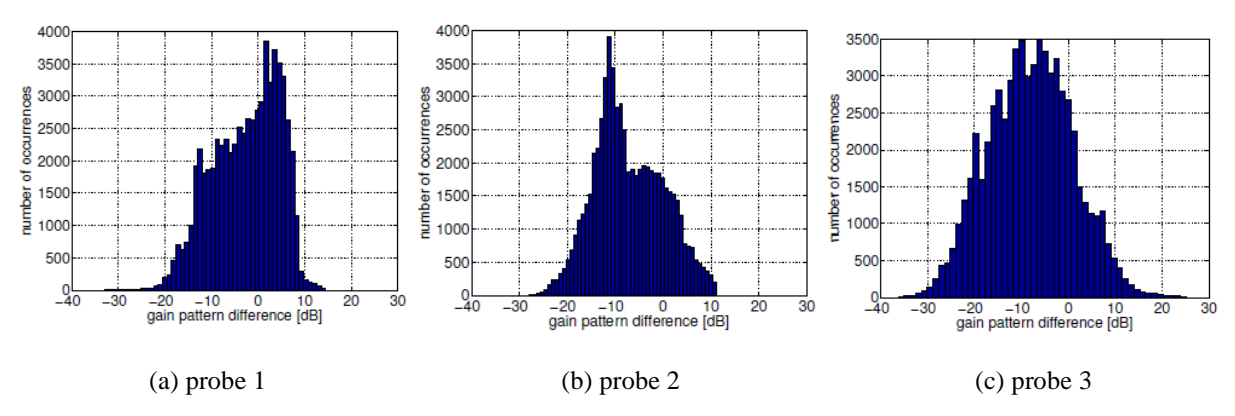


Figure 78: Realized Gain pattern difference distribution.

The statistics for 2.6 GHz, i.e., the average and the standard deviation, are gathered in Table 32.



Table 32 Realized gain pattern difference statistics for 2.6 GHz.

Probe	Av. Difference [dB]	STD [dB]
Probe 1	-2.61	7.15
Probe 2	-7.14	7.21
Probe 3	-8.06	9.04

The wideband study of the body influence on the dosimeter performance is presented in Figure 79. The distance between body and dosimeter goes from 0 cm (i.e., dosimeter attached to the body) to 5 cm (e.g., dosimeter attached to the clothe).

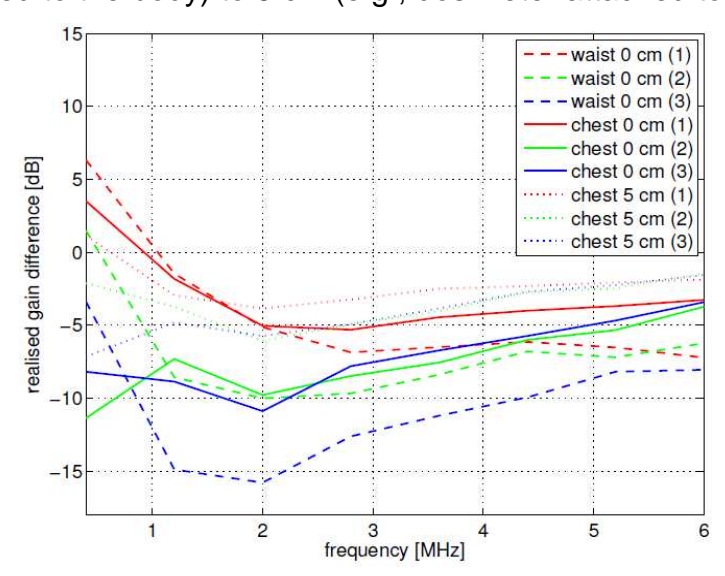


Figure 79: Realized Gain pattern difference vs. frequency (GHz

The values of the average Realized Gain difference are gathered in Table 33.

Table 33 The average Realized Gain difference in [0.4, 6] GHz.

Dosimeter Placement		$\overline{G_R(heta, arphi)_{ t [dB]}}$	
	Probe 1	Probe 2	Probe 3
Waist 0 cm	-4.19	-6.92	-10.51
Chest 0 cm	-3.01	-7.45	-7.04
Chest 5 cm	-2.21	-3.44	-4.12

4.3.2.2 Simulated body impact analysis: dosimeter worn on the chest

The purpose of this analysis is to identify trends through preliminary statistical assessments. A "small" phantom has been chosen to minimize the simulation time:

FP7 Contract n°318273



"Eartha", an 8-years old child girl (see Table 28). The sensor is placed at a few millimetres from her chest (Figure 80).

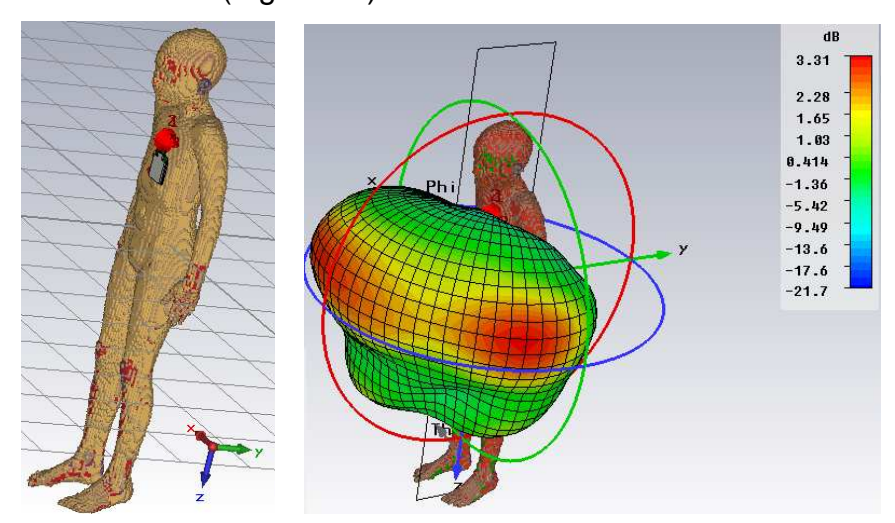


Figure 80 : (a) Sketch of the triaxial sensor placed on Eartha's phantom chest, (b) Example of realized gain pattern (2.5 GHz, □-polarization).

The Tx antenna transfer function (ATF) $\mathcal{H}(f,\theta,\varphi)$ [16] is computed from the Far Field calculated over 0.5-6 GHz by the time domain solver of CST Microwave Studio[®], for each axial probe.

The main characteristics of the body-worn sensor are shown below as before (Figure 81).

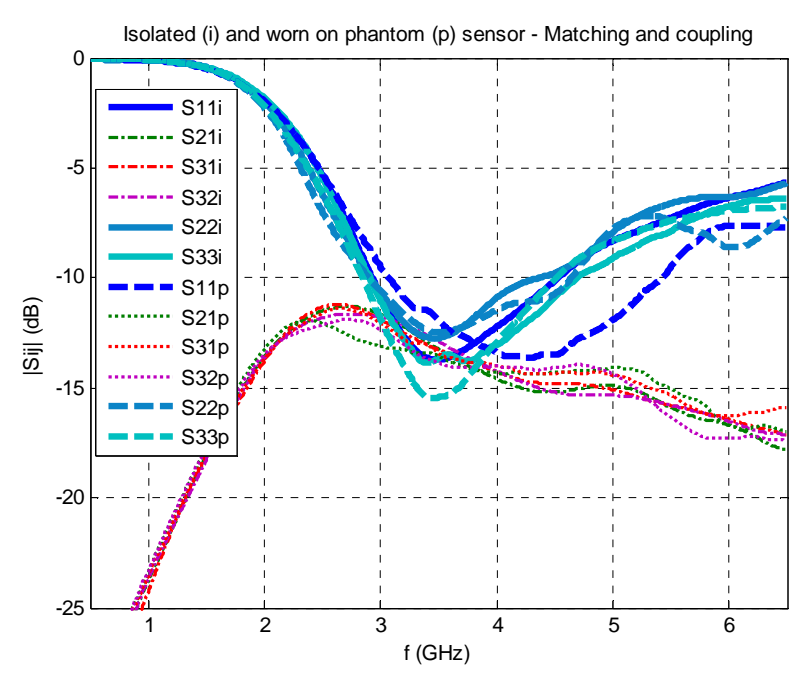


Figure 81 : Simulated reflection coefficient of each probe sensor – comparison between the worn and isolated cases.

As was observed in the measurement case, the body proximity has a moderate effect on the matching (it is even marginal here).



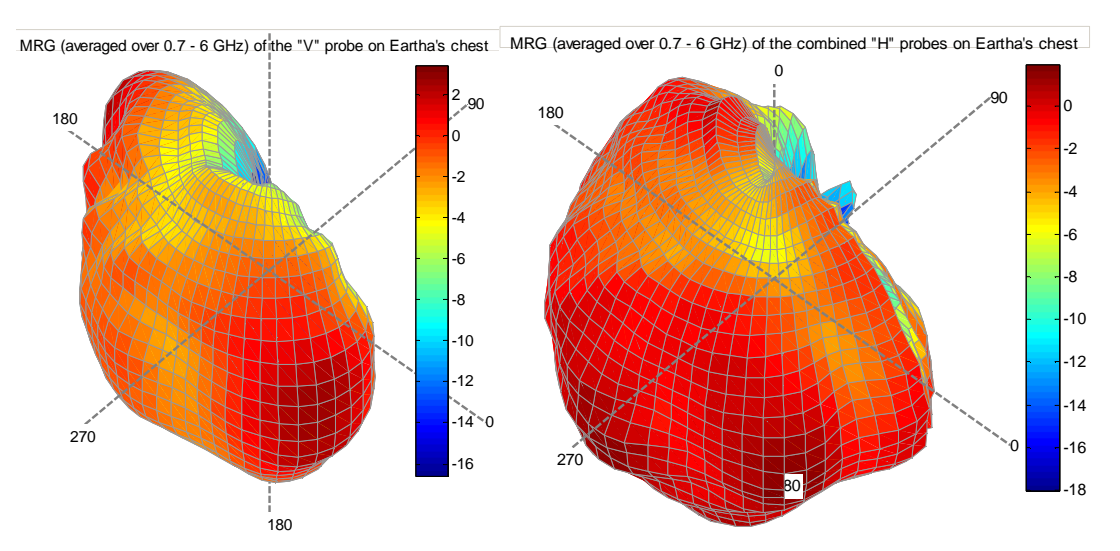


Figure 82 : MRG (co-polar components) of "V" and "H" probes on Eartha's chest averaged over 0.7 – 6 GHz (3D radiation patterns).

The (co-polar) MRG (averaged over 0.7-6 GHz) for the "V" probe and combined "H" probes are shown in Figure 82. This gives an overview of the masking effect of the phantom.



4.3.2.2.1 Polarimetric approach

Polarimetric gain "isotropy"

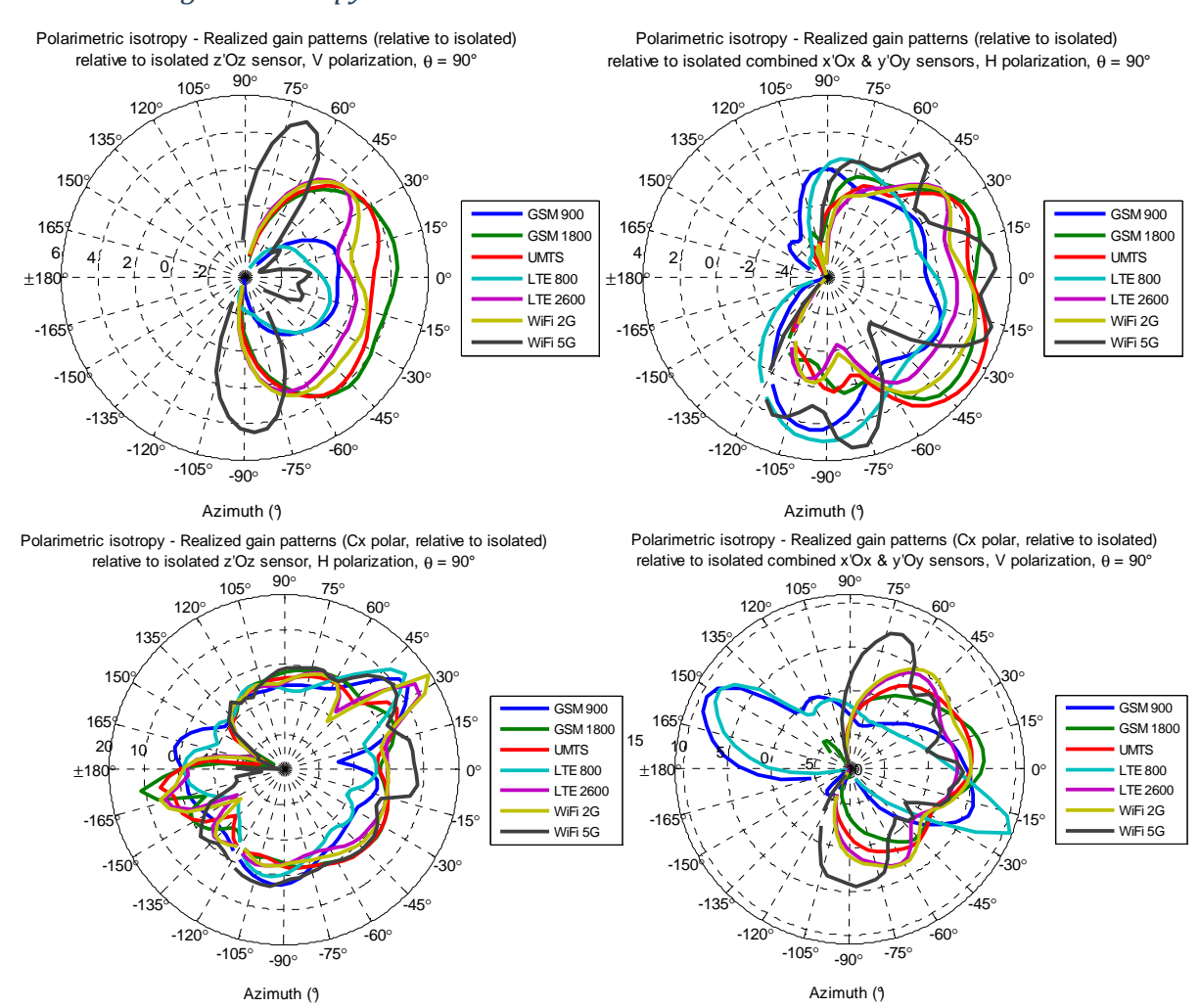


Figure 83 : Relative (to isolated) realized gain patterns (averaged over each RAT band) of the "V"(z'Oz) probe and combined "H" probes (xOy) in the azimuthal plane for the sensor worn on eartha's chest scenario, θ = 90°. Co-polar (top) and cross-polar (bottom).

Version: V1.2



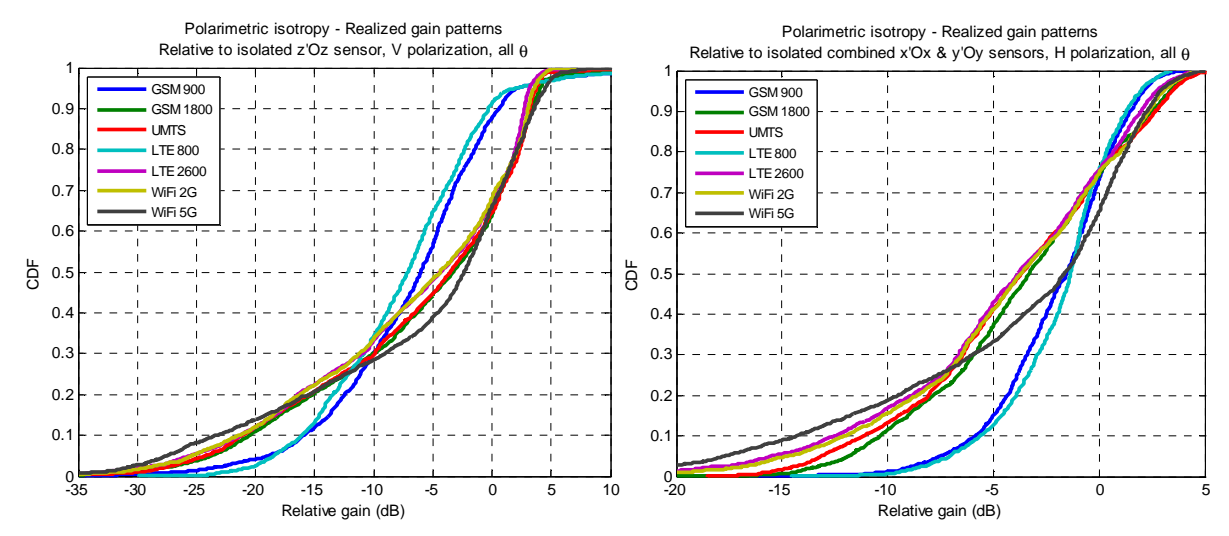


Figure 84 : Polarimetric "isotropy" (averaged over each RAT band) of the "V"(z'Oz) probe and combined "H" probes (xOy) for the sensor worn on Eartha's chest (relative to isolated), all φ.

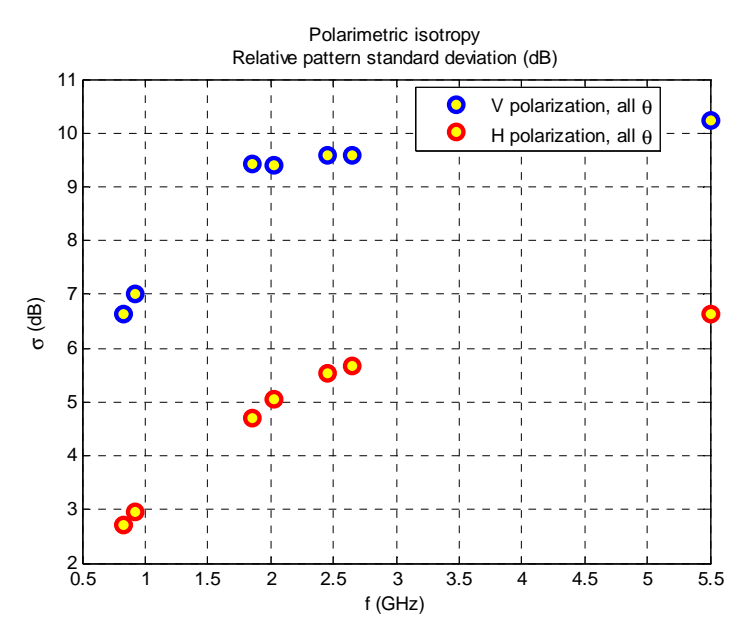


Figure 85 : Simulated realized gain pattern (relative to isolated) standard deviation over azimuth (averaged over frequency for each RAT – yellow circles) of the "V"(z'Oz) probe and combined "H" probes (xOy), all φ.

Table 34: Polarimetric isotropy statistics (over φ and θ), Eartha's chest (dB)

	GSM 900	GSM 1800	UMTS	LTE 800	LTE 2600	WiFi 2G	WiFi 5G
$\mu_{G v}$	-6.93	-6.03	-6.29	-7.52	-6.99	-6.97	-6.22
σ_{Gv}	7.02	9.42	9.40	6.62	9.58	9.59	10.22
μ_{Gh}	-2.02	-3.61	-3.90	-1.85	-4.51	-4.24	-4.07
σ_{Gh}	2.95	4.70	5.04	2.71	5.66	5.53	6.64

Version: V1.2



First, a significant "bias" can be observed (Figure 84 and Table 34) in particular for the "V" probe. This is due to the energy absorbed by the body. However, this effect is less pronounced (by about 1 to 5 dB) than for the measurements (see Table 25). The deviation compared to measurements is lower for the "H" probes (within about 1 to 3 dB). Note that the phantoms sizes are significantly different, precluding any strict comparisons: only the trends should be considered here, and they are globally similar.

Apart for a few cases, the isotropy variances are in better agreement: the standard deviations remain high in particular for the "V" probe ($\sim 7 - 10$ dB). This effect is significantly less pronounced for the "H" probes, in qualitative agreement with the measurements (see Figure 60 and Table 25).

4.3.2.2.2 Non polarimetric approach

Influence of the incident field polarization

In the following figures (Figure 86 to Figure 89), the realized gains are *relative* to the isolated case (see section 4.2.2.3).

The influence of the incoming wave XPR can be clearly seen. It is particularly significant for elevations around the horizon, which concentrate most of the energy for most typical environments studied in practice. This result again prompts to take into account the characteristics of the propagation channel.

Version: V1.2 100



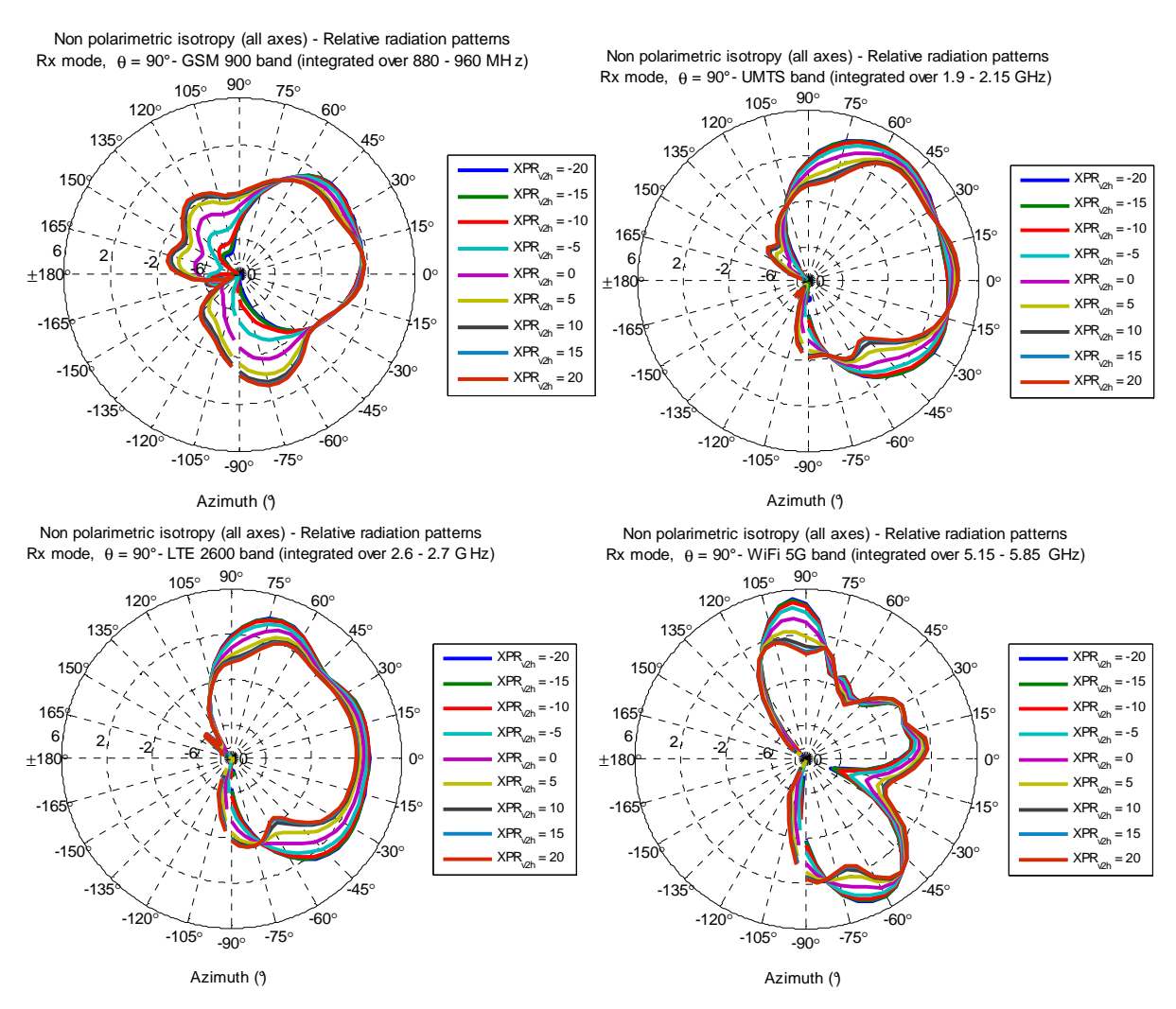


Figure 86 : Influence of the incoming wave XPR level on the isotropy (for various RATs), (a-e) received signal in azimuth (relative to isolated sensor), (f) variance of the isotropy ($\theta = 90^{\circ}$).

Version: V1.2



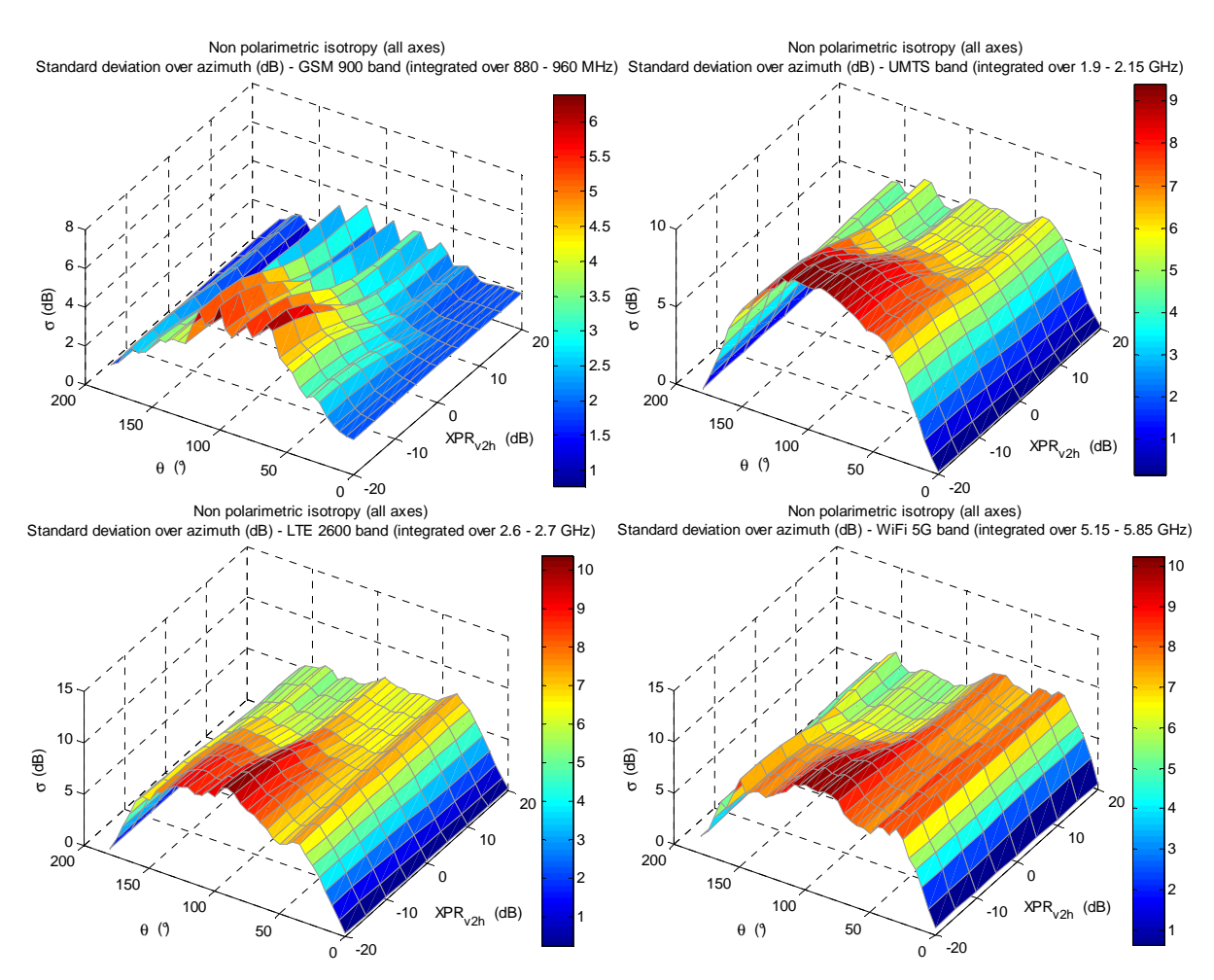


Figure 87: Influence of the incoming wave XPR level on the isotropy (for various RATs): standard deviation of the received non polarimetric signal (relative to isolated sensor).

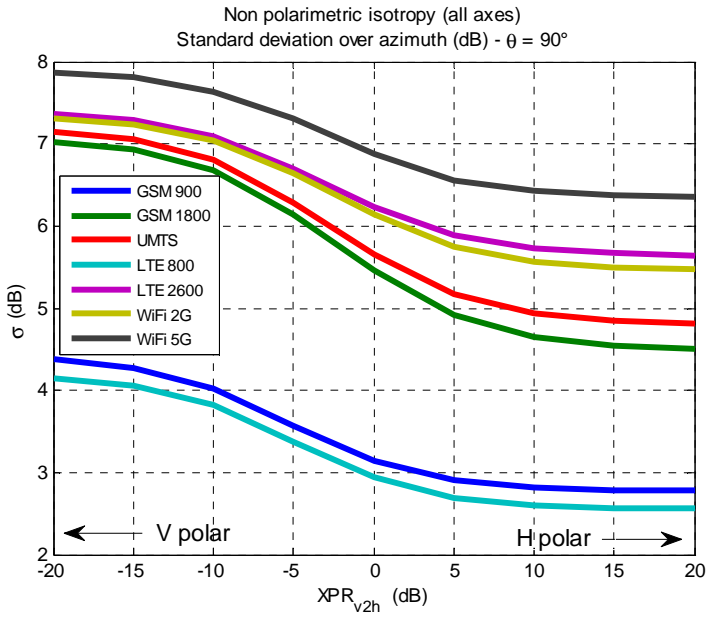


Figure 88 : Influence of the incoming wave XPR level on the isotropy (for all RATs): standard deviation of the received non polarimetric signal (relative to isolated sensor), θ =90°.

Version: V1.2 102



Influence of the channel characteristics

The analysis is restricted here to environments n° 1 (LOS) and 2 (NLOS) for brevity.

Both the "bias" (μ_{ei0}) and the isotropy deviation (σ_{Ei0}), results (Figure 89, Table 35, and Table 36) should be compared to those of the isolated case (Figure 42**Erreur! Source du renvoi introuvable.** and Table 19) on the one hand, and to the standard deviations obtained in the polarimetric analyses (Table 20).

The biases for both environments are non-negligible, the means (Tables 32 and 33) ranging typically between 0.6 and 0.85 V/m (instead of 1 V/m), but the main difficulty is of course the significant variances (up to almost 10 dB).

This should be of course corrected somehow.

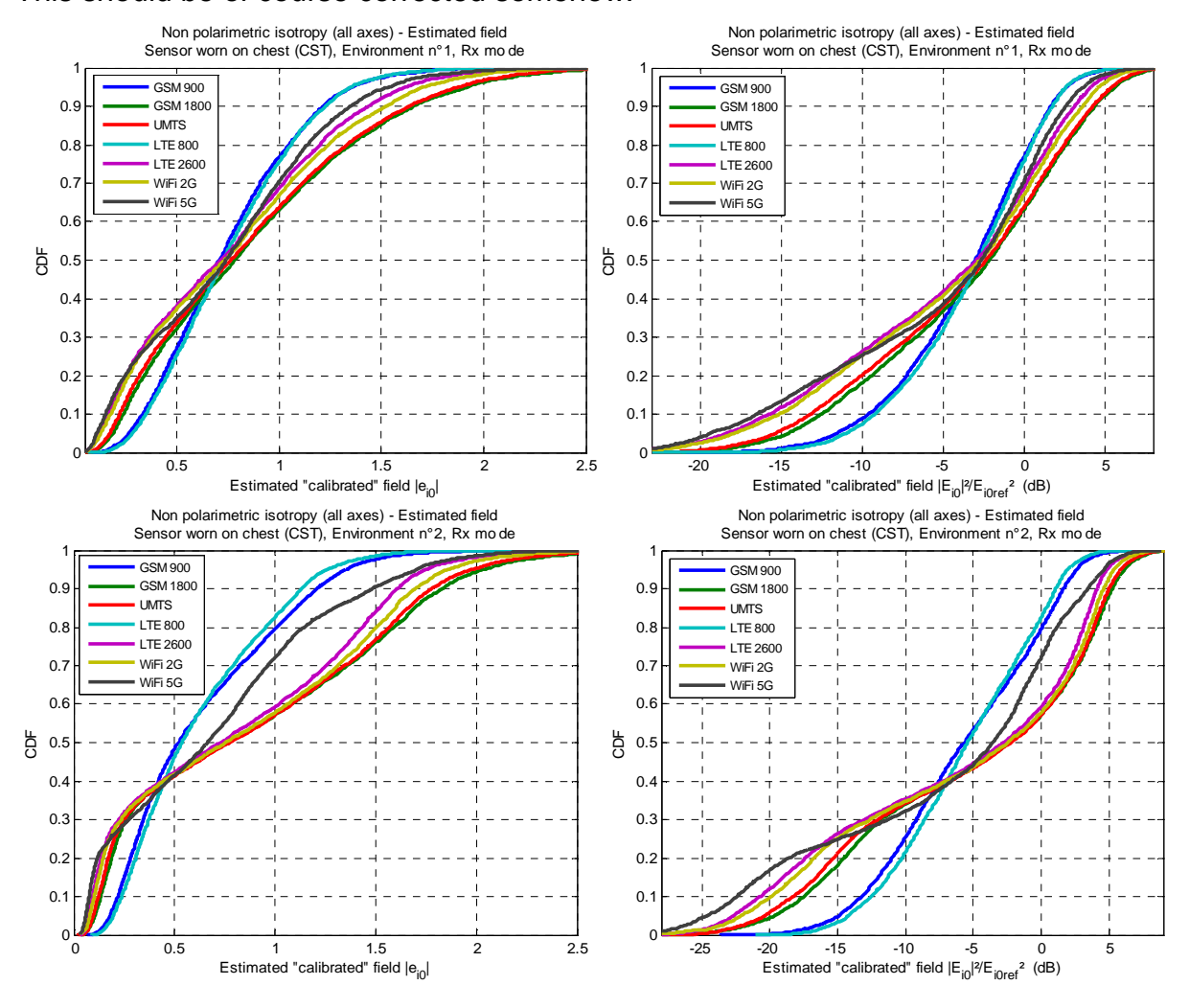


Figure 89: Non polarimetric statistics (CDF) of isotropy deviation for an NLOS (left) and a LOS (right) environments. Sensor worn by Eartha (signal relative to isolated case).

Version: V1.2 103



Table 35 : Non polarimetric sensor isotropy deviation statistics (over θ and ϕ) for Env. n°1.

e _{i0norm}	GSM 900	GSM 1800	UMTS	LTE 800	LTE 2600	WiFi 2G	WiFi 5G
μ _{ei0}	0.75	0.87	0.85	0.76	0.75	0.79	0.74
σ _{ei0}	0.44	0.57	0.57	0.41	0.56	0.57	0.53
m_{Ei0} (dB)	-3.00	-2.13	-2.33	-2.75	-2.90	-2.66	-2.62
σ _{εί0} (dB)	4.39	6.40	6.60	4.23	7.22	7.19	7.27

Table 36 : Non polarimetric sensor isotropy deviation statistics (over θ and ϕ) for Env. n°2.

e _{i0norm}	GSM 900	GSM 1800	UMTS	LTE 800	LTE 2600	WiFi 2G	WiFi 5G
μ _{ei0}	0.64	0.89	0.87	0.62	0.80	0.84	0.70
σ _{ei} 0	0.39	0.69	0.67	0.35	0.61	0.65	0.54
m_{Ei0} (dB)	-5.62	-2.38	-2.19	-5.43	-2.70	-2.42	-3.54
σ_{Ei0} (dB)	5.67	9.00	9.19	5.14	9.71	9.67	9.65

Version: V1.2 104





4.3.3 Intermediate results summary tables

Table 37: Measurement and simulation approaches summary: averages ("bias").

Detection bias		Isolated sensor										Body-worn sensor											
	Measurement						Simulation					Measurement (Chest/Hip) (Che						Sin		(Chest)			
De	$\mu_{Gv} \mu_{Gh}$	$\mu_{\overline{b}}^{V}$	$\mu_{\overline{b}}^{H}$	$ar{\mu}_{ar{b}}$	<i>m_{Ei}</i> 0 Env. 1/2	μ_{Gv}	μ_{Gh}	$\mu_{\overline{b}}^{V}$	$\mu_{\overline{b}}^{H}$	$ar{\mu}_{ar{b}}$	<i>m_{Ei}</i> 0 Env. 1/2	μ_{Gv}	μ_{Gh}	$\mu_{\overline{b}}^{V}$	$\mu_{ar{b}}^{H}$	$ar{\mu}_{ar{b}}$	<i>m_{Ei}</i> 0 Env. 1/2	$\mu_{Gv} \mu_{Gh}$	$\mu_{\overline{b}}^{V}$	$\mu_{\overline{b}}^{\underline{H}}$	$ar{\mu}_{ar{b}}$	<i>m_{Ei}</i> 0 Env. 1/2	
GSM 900	-0.1 -0.5	2.5	-0.3	1.2	-0.2/ 2.2	-0.5	-0.1	-0.2	-1.2	-0.7	-0.9/0.1	-13.1/-17.2	1.4/–17.7	-5.8/-8.8	-2.6/-5.1	-3.7	-5.3/-4.3	-6.9 -2.2	-5.7	-3.2	-4.3	-3.0/-5.6	
UMTS	-0.2 -0.4	0.9	0.7	0.8	-0.3/0.6	-0.6	-0.2	1.2	0.1	0.7	-0.7/-0.0	-8.8/-10.6	-3.3/-10.5	-6.3/-7.5	-5.8/-5.8	-5.5	-7.2/- 6.2	-6.3 -3.9	-4.7	-3.7	-4.0	-2.3/-2.2	
LTE 2600	-0.2 -0.2	0.5	-0.1	0.3	-0.6/0.1	-0.3	-0.1	-0.0	-0.5	-0.2	-0.9/-0.2	-10.6/-11.8	-3.6/-11.3	-7.2/-7.9	-6.0/-6.2	-6.0	-7.6/-6.5	−7.0 −4.5	-5.9	-4.9	-5.3	-2.9/-2.7	
WiFi 5G	-0.2 -0.3	0.4	-0.0	0.2	-0.5/0.1	-0.3	-0.3	-0.7	-1.3	-1.0	-0.8/0.3	-10.2/-9.4	-4.6/-7.2	-7.2/-6.2	-7.0/-6.6	-6.5	-5.5/-4.5	-6.2 -4.1	-6.1	-5.3	-5.5	-2.6/-3.5	

Table 38 : Measurement and simulation approaches summary: standard deviations.

Detection dispersion		Isolated sensor											Body-worn sensor											
	Measurement							Simulation						Measurement (Chest/Hip)						Simulation				(Chest)
Det	σ _G	σ _G	$\sigma_{\overline{b}}^{V}$	$\sigma_{ar{b}}^{H}$	$ar{\sigma}_{\!ar{b}}$	<i>σ_{Ei}</i> 0 Env. 1/2	σ _G	σ _G	$\sigma_{\overline{b}}^{V}$	$\sigma_{ar{b}}^H$	$ar{\sigma}_{\!\overline{b}}$	<i>σ_{Ei}</i> 0 Env. 1/2	σ_{Gv}	σ_{Gh}	$\sigma^{V}_{\overline{b}}$	$\sigma^H_{\overline{b}}$	$ar{\sigma}_{\!ar{b}}$	<i>σ_{Ei}</i> 0 Env. 1/2	σ _G	σ _G	$\sigma^{V}_{\overline{b}}$	$\sigma_{\overline{b}}^{H}$	$ar{\sigma}_{\!ar{b}}$	<i>σ_{Ei}</i> 0 Env. 1/2
GSM 900	0.7	2.1	0.5	2.0	1.25	4.7/4.4	2.5	1.0	1.4	1.3	1.35	4.3/4.0	8.4/7.5	5.1/4.4	6.6/6.0	6.7/5.7	6.7/5.8	6.3/5.3	7.0	3.0	4.4	2.8	3.4	4.4/5.7
UMTS	1.2	1.8	1.0	1.6	1.7	4.6/4.0	2.6	1.2	1.3	1.5	1.4	4.2/3.9	10.6/9.5	4.7/4.2	9.6/8.9	5.9/5.8	7.6/7.2	8.8/8.5	9.4	5.0	7.1	4.8	5.9	6.6/9.2
LTE 2600	1.3	1.5	1.1	1.4	1.3	4.3/4.0	2.0	1.2	0.9	1.6	1.2	4.2/3.9	11.7/11.0	5.2/5.1	10.2/10.0	6.3/6.5	8.1/8.0	9.8/9.8	9.6	5.7	7.4	5.6	6.4	7.2/9.7
WiFi 5G	1.4	1.7	1.2	1.6	1.4	4.2/3.8	1.9	1.9	1.5	2.1	1.7	4.0/3.9	13.1/12.2	7.3/7.3	12.0/10.6	7.7/6.9	9.7/8.6	10.5/10.5	10.2	6.6	7.9	6.3	7.0	7.3/9.7

PROPRIETARY RIGHTS STATEMENT

This document contains information, which is proprietary to the LEXNET Consortium. Neither this document nor the information contained herein shall be used, duplicated or communicated by any means to any third party, in whole or in parts, except with prior written consent of the LEXNET consortium.



Note that the programme giving the statistical results according to the channel characteristics has been validated (among other test) with a fictive environment corresponding to the analysis of the influence of the incoming field XPR (i.e. quasi deterministic, with no cluster azimuth spread, only one path and the same spread of the XPR). The values of σ_{E0} obtained in this case are comparable to those of $\bar{\sigma}_{\bar{b}}$ for all cases, in particular for the isolated case.

4.4 Strategies for body-worn field sensor correction

Recently, it has been proposed in [22] to resort to several exposimeters (in this case at 950 MHz) to compensate for the shadowing and reflection effects, and somehow "regain" omnidirectionality. The results improvement of this interesting approach is really significant. However, although the system uses textile antennas and wearable electronics, one wonder if it can be easily used on a large scale, in particular with regard to its user acceptability, or if it will be restricted to professionals.

CDF of the MRG (proportional to the total received power) for the considered scenarios are presented in Figure 90. As expected, the high variance observed by using only one sensor (notably in V polarization) can be drastically reduced when using two sensors (in particular on opposite sides of the body). Using all three does not bring any improvement (note however that, contrary to the strategy adopted in [22], no attempt was made here to optimize the sensors positioning).

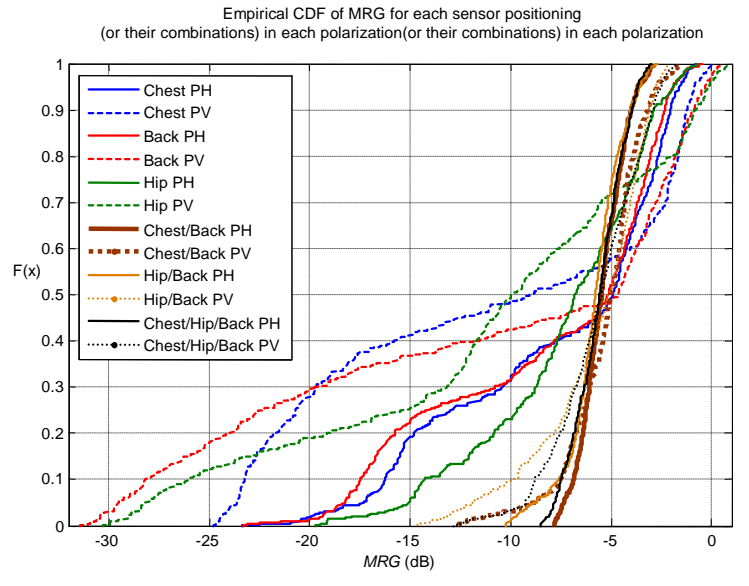


Figure 90 : Empirical CDF of the MRG for each sensor position and both polarizations, and results combining two or all positions.

Various approaches [21], [22], [23] and [24] have been proposed in the literature, in particular based on daily activity recording. Data fusion, resorting notably to GPS, accelerometers, gyrometers and magnetometers, are promising.

Some of these options will be studied in the second release of this deliverable.

PROPRIETARY RIGHTS STATEMENT

This document contains information, which is proprietary to the LEXNET Consortium. Neither this document nor the information contained herein shall be used, duplicated or communicated by any means to any third party, in whole or in parts, except with prior written consent of the LEXNET consortium.



5 NETWORK ENVIRONMENT IMPACT STUDIES

The dosimeter is developed for band-selective measurement of electric field strength in frequency range of LEXNET project. Measurement results from dosimeter are intended to be used for El calculation. In order to use these results in a proper way, variability of electric field strength should be analyzed. Guidelines which provide general rules for evaluating and expressing overall uncertainty in measurements carried out by LEXNET dosimeter are provided in appendix 3.

Besides the well-known short-term fading, which generally characterizes propagation of radio waves, several additional effects have also significant influence on the EMF strength in the mobile networks environment. The most important effects are [16]: traffic load, automatic transmitter power control and discontinuous transmission.

5.1 Traffic Load impact

The total BS Tx power directly depends on the number and troughputs of the active connections, i.e. its traffic load. In the case of GSM/DCS systems, depending on the traffic load, transmitters are turned on or off. On the other side, in the UMTS and LTE system, the increase in the traffic load forces transmitters to operate at higher power and vice-versa.

5.1.1 Description of the topic

BS traffic load varies during the day and depends on: the applied tariff profiles, the time of the day, the day of the week, the location of BS... As a rule, mobile operator configures the BS in such a way that under certain conditions it satisfies the traffic demands in the so-called busy hour (the sliding 60-minutes period during which the maximum total traffic load occurs in a given 24-hours period). It should be noted that even if the BS is operating with maximum traffic load, the number of active traffic channels is not constant because of the stochastic nature of call arrivals and call durations.

For each individual connection, the BS Tx power is automatically adjusted depending on the propagation conditions in which the mobile terminal resides. Automatic power control is implemented with a frequency of about 2 Hz in GSM/DCS system, with 1500 Hz in UMTS..

During an established call, when the user makes a normal pause in speech, the base station temporarily stops transmission (in GSM/DCS system transmitters are turned off, while the traffic channel is not transmitted in the UMTS and LTE systems)[26]. Typically, due to this functionality, for each voice connection, the BS transmitters are inactive approximately 40-50% of time.

All the previously mentioned effects lead to greater instability of the DL EMF strength at the measurement position. For this reason, an additional uncertainty stemming from telecommunications traffic must be taken into account. The value of



the uncertainty of this type is determined on the basis of daily traffic profiles obtained by measurements.

The dosimeter is intended to be used for band-selective measurements and it essentially measures a number of electric field components originating from distinct BS simultaneously. Variability of EMF strength originating from different BSs is different from each other, because the BSs are placed at different geographical locations, and carried different traffic loads. This leads to the necessity of analysis of band selective measurements variability with regards to network environment.

For this reason intensive measurements of electromagnetic field strength were carried out in Paris (France) and Belgrade (Serbia).

For sake of brevity, the set-up and detailed results of the two measurement campaigns in Paris and Belgrade are proposed in Appendix 2.

5.1.2 Discussions and conclusions

In this study, the variability of band selective measurements with regards to network environment is considered. Measurement results of the EMF strength for GSM, DCS and UMTS DL bands show that, with regards to field strength variations, day can be separated into two distinctive periods: "active hours" (9h-23h) with higher values and "night hours" (23h-9h) with lower ones. On the other side, as expected, seven day measurements show that two specific categories for 7-day week can be distinguished: working days (Monday to Friday) and weekends (Saturday to Sunday).

In order to use the results obtained with dosimeter band selective measurements for EI assessment, the variability of electric field strength is analysed. For this reason, an additional traffic uncertainty is calculated for 6 different categories regarding the days of the week and specific day periods. Having in mind that for the EI determination, the values of electric field strength (i.e. surface power density) averaged over the defined time periods are needed, the uncertainty caused by telecommunication traffic and transmitter functionalities is calculated for different time intervals of averaging: 10s, 30s, 1min, 6min, 15min, 30min, 1h, 3h, 6h and 10h. In this way, it can be determined how this type of variability of electric field strength affects the uncertainty of EI.

Comparing the uncertainty ranges corresponding to different systems it can be concluded that the highest values are for the UMTS, with range of uncertainties of 3.32 - 14.35 %. Range of uncertainties for the GSM is 4.08 - 10.24 %. The lowest values of uncertainties has DCS, the range is 3.85 - 8.65 %.

Besides the voice communications, UMTS system is often used for data communications, which causes higher variability of electric field strength and consequently higher uncertainty. On the other hand, GSM system provides service to broader user population, mostly for voice communications and lower for data communications. Finally, DCS part of the system has the lowest traffic share and mostly provides voice services for users. On the other hand, data communications are small portion of traffic in DCS.

The results show that uncertainty decreases with increasing of averaging interval. For example, in category "all days – all hours" for UMTS, the uncertainty is



decreasing from 14.35% calculated for 10s interval to 9.13% for 10h interval. In category "all days – all hours" for GSM, the uncertainty is decreasing from 10.24% for 10s interval to 6.59% calculated for 10h interval. For DCS, in category "all days – all hours", the uncertainty is decreasing from 7.99% for 10s interval to 5.54% calculated for 10h interval. For all other categories the similar behavior can be observed.

5.2 Extrapolation from mono-axial to isotropic EMF measurements

The main objective of this study is to find a way to extrapolate Mono-Axial Antenna (MAA) measurement results to isotropic (three-axial) electric field strength. Standards regulating the field of human exposure to EMF require isotropic measurements of EMF strength [28], [29], [30]. Similarly, for assessment of EI defined in LEXNET project isotropic measurements of DL power density are also required. This is very important issue since the simplified version of dosimeter is using MAA. Additionally, there are plans to employ user equipment (i.e. mobile phones) for measuring DL received power for the purpose of calculation of DL power density. It should be noted that most of user devices have a built-in MAA.

When MAA is used, additional extrapolation factor should be applied. Precisely, measurement readings should be multiplied by a scalar extrapolation factor. Consequently, the usage of MAA causes additional uncertainty in measurement readings and should be taken into account also.

The basic idea for determining additional extrapolation factor was to conduct simultaneous measurements of all three spatial components of electric field and try to develop empirically the model for the extrapolation of measurement results obtained with MAA to the isotropic case.

Due to the complex mechanisms of radio wave propagation, the uncertainty arising from the extrapolation from mono-axial to isotropic case is hard to analyze theoretically (or by simulations) and can be more easily determined by measurements in the field.

5.2.1 Measurement system and methodology

For the analysis, the calibrated measurement system composed of broadband field meter NARDA EMR300 and isotropic E-field measuring probe TYPE 18c (100 kHz to 3 GHz) is used. This equipment allows the measurements of overall electric field strength in the specified frequency range.

In order to collect a large number of measurement results, the measurement system was connected to a remote PC by using optical cable. For each sample, measurement system provides values for all three spatial components of electric field strength E_x , E_y and E_z . Total electric field strength E_{tot} is calculated using formula:

$$E_{\rm tot} = \sqrt{{E_{\rm X}}^2 + {E_{\rm Y}}^2 + {E_{\rm Z}}^2}$$

Measurements were performed in three different scenarios. Scenario 1 is representing indoor propagation environment with both LOS and NLOS conditions.



Propagation environment with indoor receiving area and outdoor transmitting antennas is represented in scenario 2. Scenario 3 is representing outdoor environment with outdoor receiving area and outdoor transmitting antennas. These three scenarios are representing environments where most of population is exposed. On the other hand, these environments are representing three different cases according to propagation and depolarization of RF EM waves.

Measurement system was mounted on a tripod, and it was placed on an industrial cart. E-field probe was placed at the angle of 45° with respect to a vertical axis. Industrial cart with measurement system were slowly moving in the chosen area and slowly rotating with respect to a vertical axis. In such a way equality among the axes was ensured. Measurements were done in 2 hours campaigns and 3600 samples were collected for each scenario. Sampling time was 2 sec.

5.2.2 Determination of extrapolation factor

For each sample value, estimates of extrapolation factors n_x , n_y and n_z were obtained using the following formulas:

$$n_X = \frac{E_{tot}}{E_X}$$

$$n_Y = \frac{E_{tot}}{E_Y}$$

$$n_Z = \frac{E_{tot}}{E_Z}$$

Based on the estimates n_{X} , n_{Y} and n_{Z} obtained for each scenario mean value, median value, standard deviation and uncertainty were determined. After that, all estimates of extrapolation factors n_{X} , n_{Y} and n_{Z} were grouped in one set n and for n mean value, median value, standard deviation and uncertainty were determined, also.

5.2.3 Uncertainty caused by the usage of mono-axial probe - u(MA)

The uncertainty caused by the usage of MAA was determined by statistical analysis of a series of measuring results [26][27]. In the first step, the mean value n_{meas} and the standard deviation $\sigma(n_{meas})$ were determined using:

$$n_{meas} = \frac{1}{N} \sum_{i=1}^{N} n_{meas\ i}$$

$$\sigma(n_{meas}) = \sqrt{\frac{1}{N-1} \sum_{i=1}^{N} (n_{meas\ i} - n_{meas})^2}$$

where $n_{meas\ i}$ denotes outcome of the *i*-th measurement and N is the total number of measurements.



The relative ratio of the standard deviation and the mean value defines the uncertainty caused by the usage of mono-axial probe u(MA):

$$u(MA) = \frac{\sigma(n_{meas})}{n_{meas}}$$

In the interests of brevity, the details of this extrapolation study measurements results) have been put in the Appendix 5

5.2.4 Discussions and conclusions

Results of this study show that it is possible to extrapolate MAA measurement results to isotropic (three-axial) E field strength. When mono-axial probe is used, additional extrapolation factor should be applied. Consequently, the MAA usage causes additional uncertainty in measurement results and should be taken into account. Measurement results show that the extrapolation factors are very similar for all three scenarios (Table 38). Namely, the mean value for overall extrapolation factor n is 1.94 for scenario 1, 1.87 for scenario 2 and 1.88 for scenario 3. In addition, the median has value 1.78 for scenario 1, 1.76 for scenario 2 and 1.77 for scenario 3. On the other hand, the uncertainty caused by the usage of MAA depends on the environment. The highest value of uncertainty is for scenario 1, and it is 32.61%. The lowest value, which is 25.86%, has the scenario 2. At the end, value of uncertainty for scenario 3 is 27.49%.

Regarding the mean values obtained for $n_{\textit{overall}}$, when MAA is used, additional multiplicative extrapolation factor value of 1.90 should be applied, and consequently additional uncertainty in measurement results of 28,65% should be taken into account.



6 CONCLUSIONS

This deliverable presents the detailed development of the wearable LEXNET dosimeter. First of all in chapter 2, an analysis explains the usages and the objectives of this E field measurement device which will assess the human exposure and particularly the LEXNET exposure global metric. The non-collaborative approach is selected. It means that the dosimeter, as a measurement tool stays independent from any data sharing with the transmitting sources. The innovative features of the LEXNET dosimeter are also given and compared with regard to the existing products.

Based on the IR3.1 specifications, the RF front-end architecture has been studied in chapter 3, by considering the trade-off between sensitivity, frequency selectivity, frequency range, and energy consumption. Two different configurations have been evaluated and the one with tunable pre-filter, variable gain LNA, and DCR receiver has been selected and developed. The two key advantages of the LEXNET wearable dosimeter are the unique frequency selectivity (able to isolate a 3 MHz service provider band from another) and the extreme hardware flexibility as regards current and future standards in the 0.7-6 GHz LEXNET frequency band. Each of the subcomponents evaluation has been individually detailed with their own performance indicators (frequency selectivity, loss, linearity, consumption, and occupied surface). Then each component from the antennas up to the microcontroller are integrated as a whole device and dimensions and total current consumption have been estimated in order to fix the mechanical design and the battery capacity.

Moreover an innovative study aims to analyze the impact of the body proximity on the E field measured level. Both amplitude and polarization impacts are quantified through measurement and simulation campaigns of an isolated and a body-worn dosimeter. Preliminary conclusions show the frequency dependent effect and the important depolarization of the fields do the presence of the body. These results drive the bias compensation strategies which will be based on a statistical approach to take into account the wide variability of the configurations.

By measuring the E field strength, when mono-axial probe is used instead of the three probes, additional extrapolation factor of 1.9 should be applied. Consequently, it causes up to 32% additional uncertainty in measurement results and should be taken into account. Moreover it has been determined how the variability of electric field strength due to the Network environment (throughput daily variation) affects the uncertainty of El. It is shown that the uncertainty is decreasing from 14.35% calculated for 10s interval to 9.13% for 10h interval.

The LEXNET wearable dosimeter is designed to fulfill the requirements of general public EM exposure on a larger deployment base. Thus the perspective at a longer term is to re-use the selected RF architecture study to transpose it on an integrated circuit in order to reach better performances and lower cost.

This February 2014 corresponds to the first release of deliverable D3.2. A second version will update it with consolidated results of the components characterization and the statistical approach to compensate the body impact bias.



7 REFERENCES

- [1]. EME-Guard broadband dosimeter developed by Satimo industries, [online] http://www.satimo.com/content/products/eme-guard
- [2]. Narda personal monitor, developed by Narda, [online] http://www.narda-sts.us/products-personal-nardalertxt.php
- [3]. EMEPY 140 dosimeter developed by satimo industries, [online] http://www.satimo.com/sites/www.satimo.com/files/EMESPY140_EN.pdf
- [4]. ESM-140 mobile phone dosimeter, [online] http://www.maschek.de/pdf/ESM-140-uk.pdf
- [5]. SEAWIND FP7 Project Deliverable D1.1: "Litterature review of exposure assessment and dosimetry of wireless networks", http://seawind-fp7.eu/uploads/Deliverable%20D1.1.pdf
- [6]. D. Picard, S. Chauvin, L. Fouquet, "Characterization of four different radio frequency dosimeters", 6th international workshop on biological effects of electromagnetic fields, Bodrum, Turkey, 2010.
- [7]. G. Neubauer, S. Cecil, W. Giczi, B. Petric, P. Preiner, J. Fröhlich, and M. Röösli, "Evaluation of the correlation between RF dosimeter reading and real human exposure", final report on the project C2006-07, 2008 [online] http://www.emf.ethz.ch/archive/var/SB_Neubaue_pre25f.pdf.
- [8]. J FB. Bolte, M. Pruppers, J. Kamer, G. Van der Zande, C. Schipper, S. Fleurke, T. Kluwer, H. Kromhout, and I van Kamp, "The Dutch exposimeter study: developing an activity exposure matrix", *ISEE 20th annual conference*, Passadena, California, 12-16 October, 2008.
- [9]. P. Juhasz, "Uncertainties in EMF antenna measurements", COST STSM scientific report, 2010, [online] http://www.cost-action-bm0704.org/doc/STSM_Report_Juhaszp.pdf
- [10]. http://www.avagotech.com/pages/home
- [11]. http://www.hittite.com/
- [12]. http://217.34.103.131/homepage/homepage.html



- [13]. http://www.rfmd.com/
- [14]. Wide band PLL- VCO from Hittite microwave corporation, [online] http://www.hittite.com/content/documents/data_sheet/hmc833lp6g.pdf
- [15]. http://www.ciblenergie.fr/fr/index.php
- [16]. C. Roblin, S. Bories, and A. Sibille, "Characterization tools of antennas in the Time Domain," IWUWBS, Oulu, June 2003.
- [17]. T. Alves, "UWB characterization of the dielectric properties of a phantom", Private communication, Feb. 2013.
- [18]. http://www.itis.ethz.ch/itis-for-health/virtual-population/human-models/
- [19]. J. Meinilä, T. Jämsä, P. Kyösti, D. Laselva, H. El-Sallabi, J. Salo, C. Schneider, D. Baum, "D5.2, Determination of Propagation Scenarios," IST-2003-507581 WINNER, 16/07/2004.
- [20]. Pekka Kyösti, Juha Meinilä, Lassi Hentilä, Xiongwen Zhao, Tommi, Jämsä, Christian Schneider, Milan Narandzić, Marko Milojević, Aihua Hong, Juha Ylitalo, Veli-Matti Holappa, Mikko Alatossava, Robert Bultitude, Yvo deJong, Terhi Rautiainen, "D1.1.1 V1.1, WINNER II interim channel models," IST-4-027756 WINNER II, 30/11/2006.
- [21]. Juha Meinilä, Pekka Kyösti, Lassi Hentilä, Tommi Jämsä, Essi Suikkanen, Esa Kunnari, Milan Narandžić, "D5.3: WINNER+ Final Channel Models," WINNER+, CELTIC / CP5-026, 30.6.2010.
- [22]. A. Thielens *et al*, "Design and Calibration of a Personal, Distributed Exposimeter for Radio Frequency Electromagnetic Field Assessment," COST IC1004, TD(13)08033, Ghent, Belgium, 25-27 Sept. 2013.
- [23]. J. Blas *et al*, "Potential exposure assessment errors associated with body-worn RF dosimeters," Bio Electro Magnetics, 28(7), 2007.
- [24]. S. Iskra *et al*, "Factors influencing uncertainty in measurement of electric fields close to the body in personal RF dosimetry," Radiation Protection Dosimetry, 140(1), 2010.
- [25]. Mishra A. R. (Editor). "Advanced cellular network planning and optimisation: 2G/2.5G/3G...evolution to 4G", John Wiley & Sons, West Sussex, England, (2007).
- [26]. Joint Committee for Guides in Metrology (BIPM, IEC, IFCC, ILAC, ISO, IUPAC, IUPAP and OIML), JCGM 100:2008, "Evaluation of measurement data Guide to the Expression of Uncertainty in Measurement".
- [27]. G.Basso, "Uncertainty in the measurement of electromagnetic field with isotropic broadband sensor and selective E&H field analyzer", NARDA Safety Solutions, 2009.
- [28]. European standard EN 50400:2006, "Basic standard to demonstrate the compliance of fixed equipment for radio transmission (110 MHz 40 GHz) intended for use in wireless telecommunication networks with the basic restrictions or the reference levels related to general public exposure to radio frequency electromagnetic fields, when put into service".



- [29]. European standard EN 50383:2010, "Basic standard for the calculation and measurement of electromagnetic field strength and SAR related to human exposure from radio base stations and fixed terminal stations for wireless telecommunication systems (110 MHz 40 GHz)".
- [30]. European standard EN 50492:2008, "Basic standard for the in-situ measurement of electromagnetic field strength related to human exposure in the vicinity of base stations".
- [31]. Antenna Standards Committee of the IEEE Antennas and Propagation Society, IEEE Standard Definitions of Terms for Antennas, IEEE Std 145-1993, IEEE Standards Board, New York, NY, USA, Mar. 1993.



APPENDIX 1: INTERNAL REVIEW

		Reviewer	1: Yoann Corre		Reviewer	2: Xavier Begaud					
		Answer	Comments	Type*	Answer	Comments	Type*				
1.	s the deliverable in	n accordan	ce with								
(i)	the Description of Work?	⊠ Yes □ No		□ M □ m □ a	⊠ Yes □ No		□ M □ m □ a				
(ii)	the international State of the Art?	⊠ Yes □ No	Yes regarding the wideband dosimeter	☐ M ⊠ m ☐ a	⊠Yes □ No		☐ M ☐ m ☐ a				
2.	2. Is the quality of the deliverable in a status										
(i)	that allows to send it to EC?	☐ Yes ☐ No		□ M □ m □ a	☐ Yes ☐ No		□ M □ m □ a				
(ii)	that needs improvement of the writing by the editor of the deliverable?	⊠ Yes □ No	The description of the wideband dosimeter subcomponents and of the integration is very clear. The characterization of the dosimeter is rich; and we can expect that the presented uncertainty analysis will help in the introduction of relevant corrections. Consider provided comments and corrections. Clarify the existence of a second release of this document (not mentioned in the DoW). Clarify complementarity between sections 4.1.3.3 and 4.1.3.4. Check the relevance of sections 4.3 and 4.4 for this deliverable.	M m □ a	⊠ Yes □ No	Report is well written and rich. As introduction, it will be interesting to remind the Lexnet index and after (for each part) explaining which term(s) of the index is(are) considered in the chapter. The content is maybe unbalanced. Part 2 is quick because it's seems that there is too few wearable dosimeters. Is-it the reality? The Sota only deals with only industrial products. No academic team is working on such a device? Part 3 is clearly presented but the justification of some choices are not realy explained.					

Version: V1.2

D3.2 Wideband dosimeter: design study & performances characterization FP7 Contract $n^{\circ}318273$



				Part 4 is difficult to assess because many results are presented. It's probably necessary to change the table of content or the organisation of this part to clearly see the contribution. Summary tables may help to synthetise with also tranfert of some results in the annexes.	
(iii) that needs further work by the partners responsible for the deliverable?	☐ Yes ☐ No	□ M □ m □ a	☐ Yes ☐ No		□ M □ m □ a

Version: V1.2

^{*} Type of comments: M = Major comment; m = minor comment; a = advice



APPENDIX 2: CHARACTERIZATION OF THE TRAFFIC IMPACT OF EMF MEASUREMENTS

Long-term variability of EMF strength - Paris measurements

A measurement campaign has been done with the aim to collect data about exposure level due to the mobile network Down-Link traffic in an indoor environment. The measurement campaign has been done in different environments as urban and rural areas. Information about the variability of the electromagnetic field can be extracted from this campaign.

The measurement system used for this campaign consisted of:

- 3-axis probe (SATIMO),
- a spectrum analyzer Agilent MXA 9020,
- a software (Xplora developed by Orange Labs) included in the analyzer which drives the measurements and saves the E field (E) values in V/m.

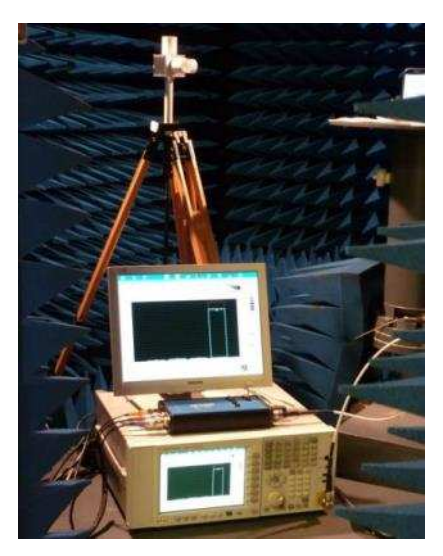


Figure 91: Frequency selective measurement system

The measured bands were selected in accordance with table 1.

Table 39Measured frequency bands

Band	Center frequency (MHz)	Span (MHz)		
GSM 900 DL	945	40		
DCS DL	1840	80		
UMTS DL	2150	80		

Version: V1.2



Twenty measurements were done in 9 different sites in urban zone and 6 measurements in 3 different sites in rural zone in Paris and around. For each site, and when it was possible, the system was installed at different places (bedroom, kitchen, and lounge) but was not moved during 24 hours.

The sampling rate was chosen in such a way to have a measurement of each band every 10 seconds during 24 hours.

In figure 2 is given an example of the signal obtained from the 24 hours measurements for the DCS in an urban configuration. The amplitude corresponds to the surface power density S in W/m² where $S = E^2 / 377$.

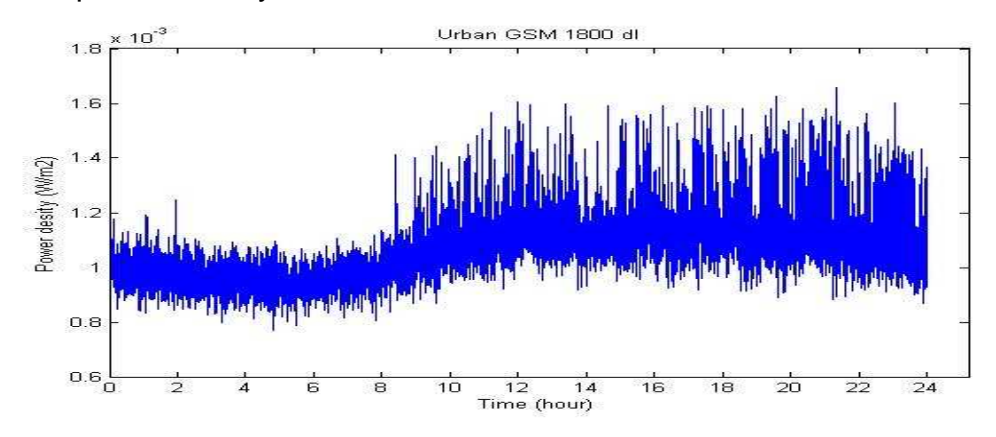


Figure 92 Example of the variation of the surface power density over 24 hours for the DCS

For each frequency band all the measurements have been normalized to their average value over 24 hour. A moving average and the standard deviation have been calculated for the signal at each hour.



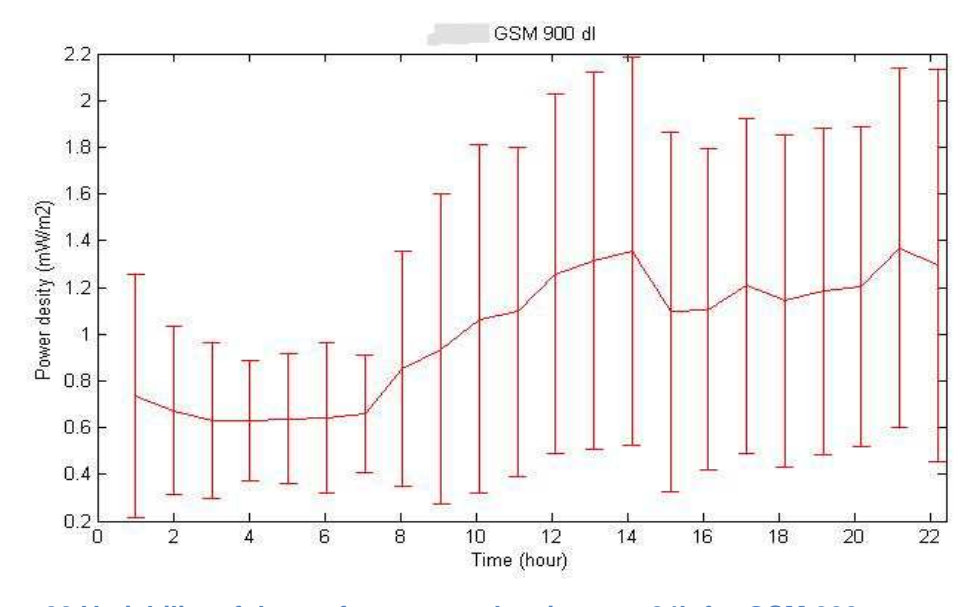


Figure 93 Variability of the surface power density over 24h for GSM 900



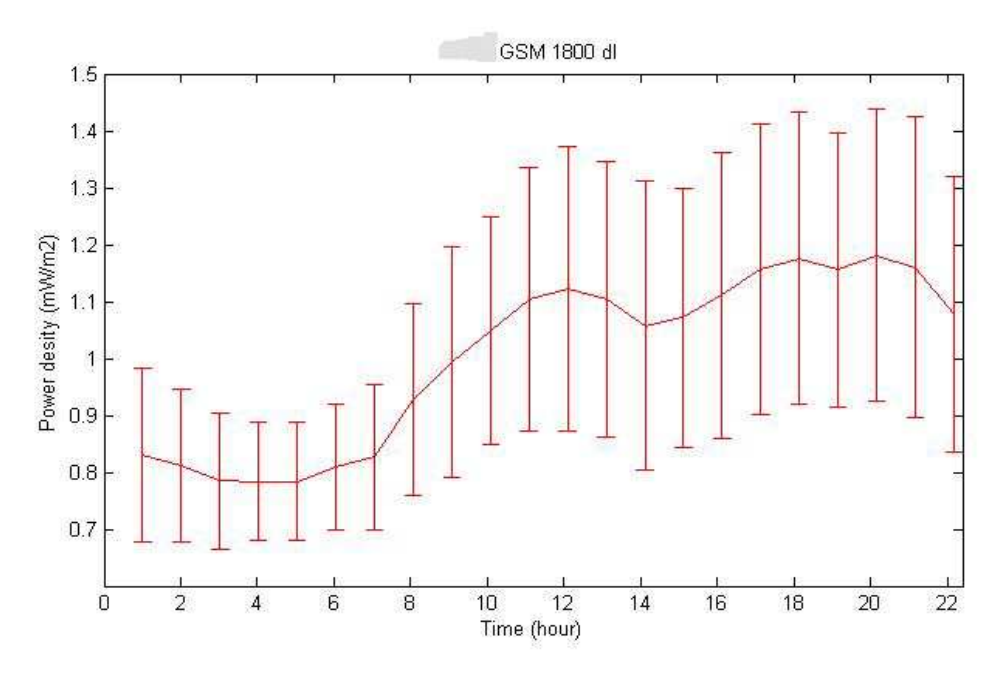


Figure 94 Variability of the surface power density over 24h for DCS

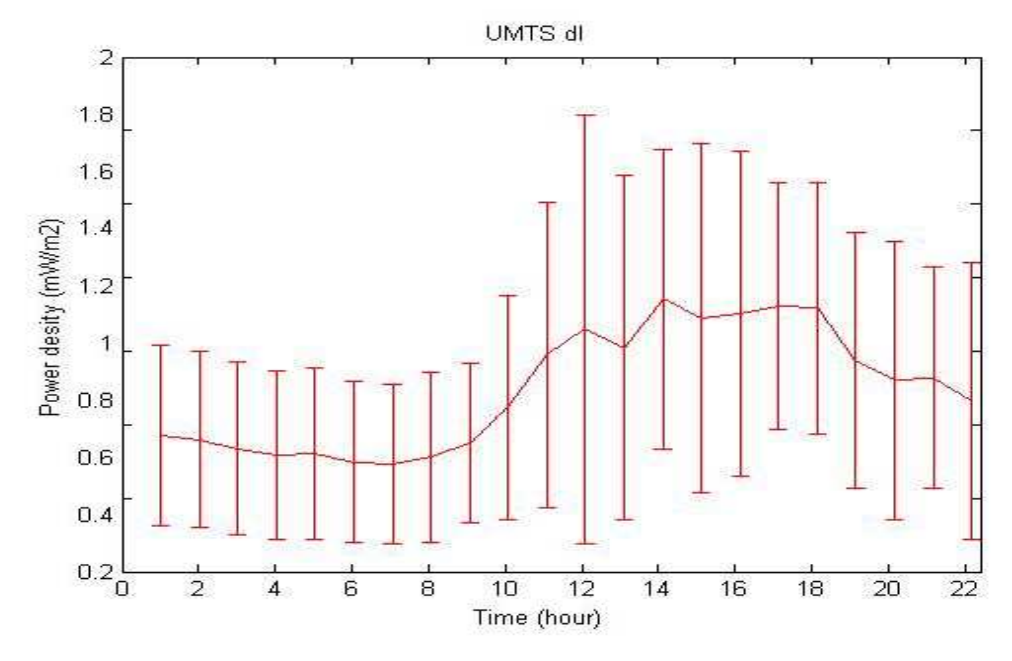


Figure 95 Variability of the surface power density over 24h for UMTS 2100

Long-term variability of electromagnetic field strength - Belgrade measurements

For the analysis which is the subject of the study, the calibrated Rohde&Schwarz portable EMF measurement system was used. Spectrum analyzer Rohde&Schwarz FSH6 and measuring antenna Rohde&Schwarz TS-EMF, in the form of an isotropic radiator, are the main measuring components of the system. This system is designed for frequency selective measurement of electric field strength in the frequency range Version: V1.2



from 30 MHz to 3 GHz. System is controlled with the softer module White Tigress Baby - Measurements, specially developed for the long-term measurements in Radio-communications Laboratory, School of Electrical Engineering, University of Belgrade for the purpose of LEXNET project.

Measurements were conducted with the sampling interval of 9.5 seconds and RMS detector was used. Following parameters were used for the measurements:

- Center frequency 947.5MHz and Channel bandwidth 25MHz (GSM band)
- Center frequency 2140MHz and Channel bandwidth 60MHz (DCS band) and
- Center frequency 1830.1MHz and Channel bandwidth 50.2MHz (UMTS band).

Intensive measurements of electromagnetic field strength in Belgrade were carried out at 3 different locations in urban area of Belgrade. Two locations were chosen as measurement locations in indoor environment and one in outdoor. Measurements were performed in time intervals of 7 days for each location. During the 7-day measurements the system was stationary with an antenna mounted on a tripod. In such a way measurement results for GSM, DCS and UMTS DL bands were obtained.

The examples of measurement results for one test location are shown in Figures 6-14. Specifically, figures 6, 9 and 12 represent electric field strength time variability for GSM, DCS and UMTS, respectively. Despite the fact that the measurement results are shown for only one test location, discussions and conclusions are based on results obtained for all three locations.

Time variability of electric field strength for all three systems clearly shows that for each day two different periods can be observed - one with high levels and one with low levels. Electric field strength for all three systems has very similar daily behaviour. At the beginning of the day (midnight), the strength of electric field decreases. After that there is a period approximately from 2:00 to 7:00 in which electric field strength has the lowest level. Beginning with the morning, the electric field strength starts to increase until approximately 9:00 when it reaches the level of the active part of a day. The active part of the day has the highest values of electric field strength and lasts until approximately 23:00. At the very end of the day, electric field strength starts to decrease. In accordance with the observed behaviour of electric field strength the day was separated in two distinctive periods: "active hours" (9h-23h) and "night hours" (23h-9h).

Measurement results show that the short-term variability during the "active hours" is higher than during the "night hours". On the other hand, when average value of this variability is considered, it is opposite case. Average values are fairly stable during the all period of "active hours" and have the highest levels. Some exceptions are detected for UMTS, where the distinctive periods with a significant increase of electric field strength during the "active hours" are observed.

As already stated, during the "night hours" the short-term variability of the electric field strength is lower than during the "active hours". As opposite to "active hours" the average values have significant changes for "night hours". At the beginning of "night hours" significant decrease of average values can be detected. Also, at the end of the "night hours" significant increase of average values can be obtained. On the other Version: V1.2



hand, period in middle of the "night hours" (approximately from 2:00 to 7:00) is time of inactivity in which the short-term variability, as well as average values of the electric field strength, have their lowest values.

Regarding the days of the week, it can be concluded that the weekend days are slightly different from the working days. These differences are manifested in the smaller differences between average values of the electric field strength of the "active hours" and "night hours" during the weekend, than for the working days.

For more detailed analysis two specific categories for 7-day week were distinguished: "working days" (Monday to Friday) and "all days" (Monday to Sunday). Also, the day was divided in two distinctive periods: "active hours" (9h-23h) and "night hours" (23h-9h). According to this, 6 different categories were analysed:

- "all days all hours",
- "working days all hours",
- "all days active hours",
- "working days active hours",
- "all days night hours" and
- "working days night hours".

Probability density function of the electric field strength for the previously defined 6 categories is presented on figures 7 and 8 for GSM, figures 10 and 11 for DCS, and figures 13 and 14 for UMTS.

In the case of GSM and DCS, probability density functions for "all hours" have behaviour which is similar to normal distribution (for "all days" category as well as for "working days" category). On the other hand, probability density function for UMTS has a behavior similar to log-normal distribution for "all days" category as well as for "working days" category.

Considering probability density functions for "active hours" and "night hours" separately, it can be concluded that both types of distributions have a similar behaviour than the "all hours" distributions, with the only difference in average values. The distributions for GSM and DCS have behavior similar to normal distribution, while the UMTS distribution behavior is again similar to log-normal distribution.



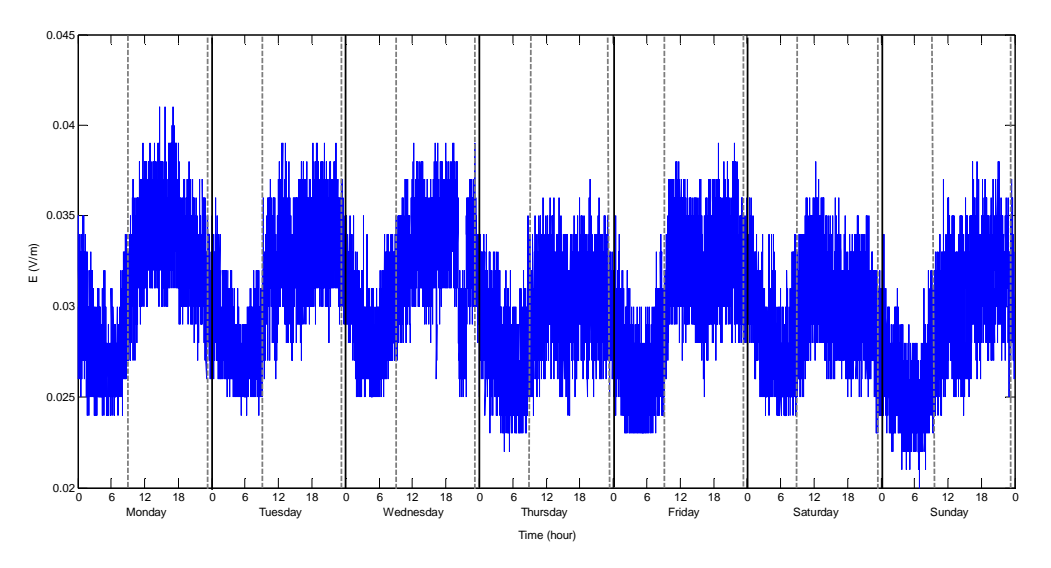


Figure 96 Time variability of electric field strength for GSM

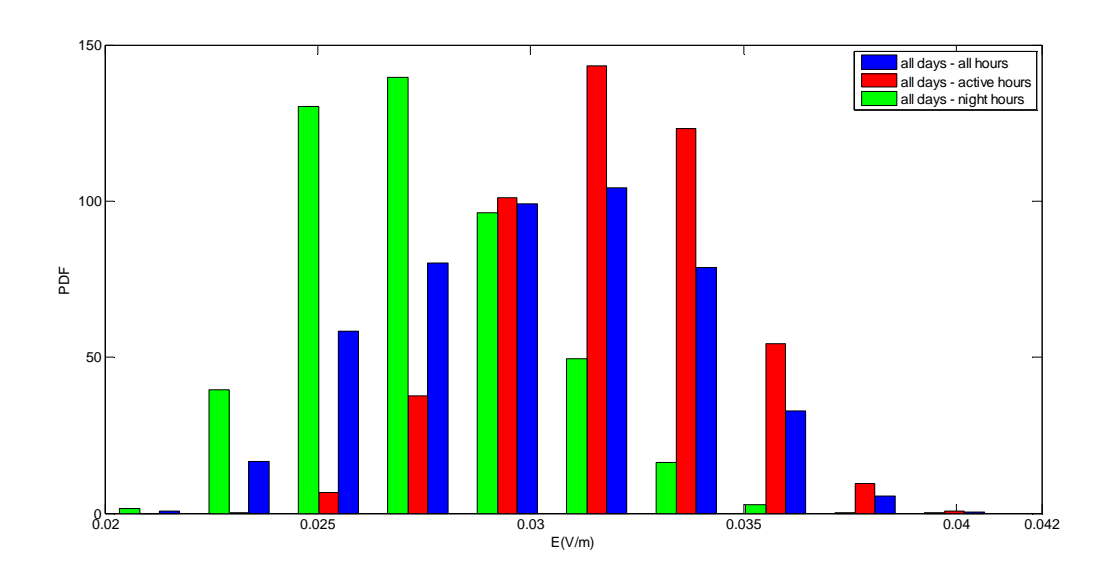


Figure 97 Probability density function of electric field strength for "all days" - GSM



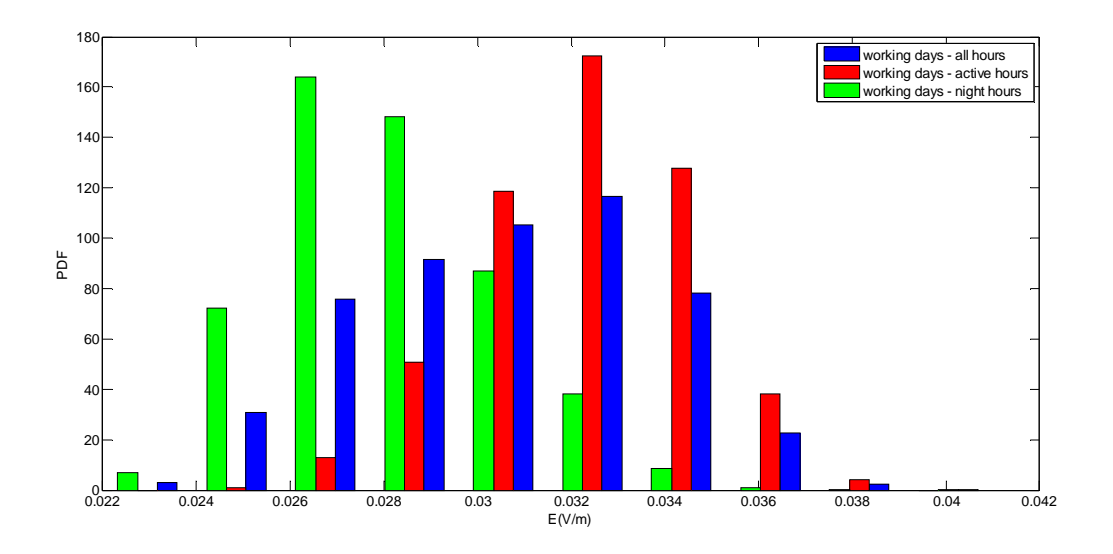


Figure 98 Probability density function of electric field strength for "working days" - GSM

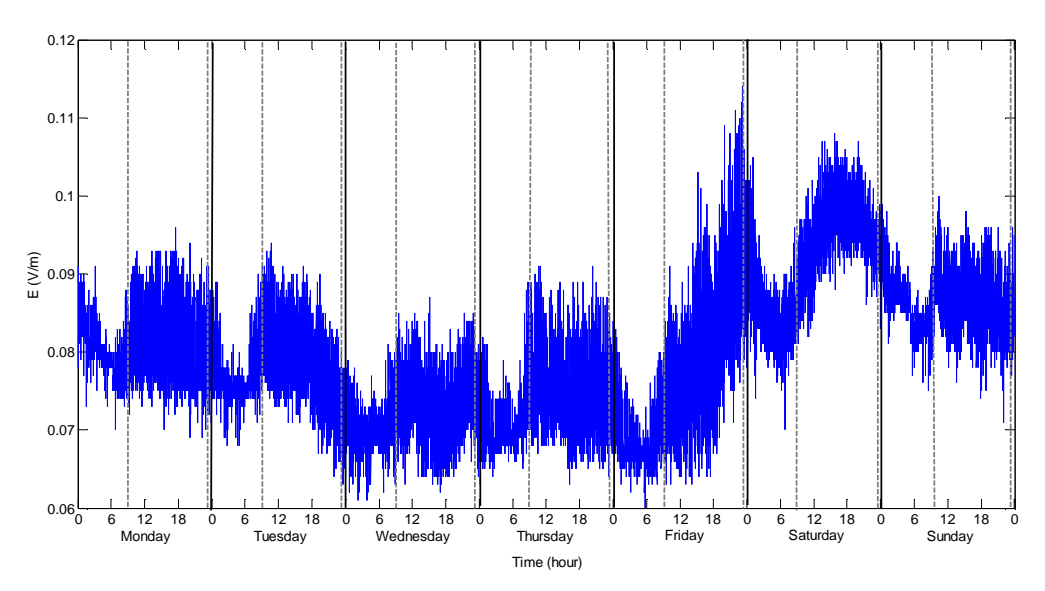


Figure 99 Time variability of electric field strength for DCS



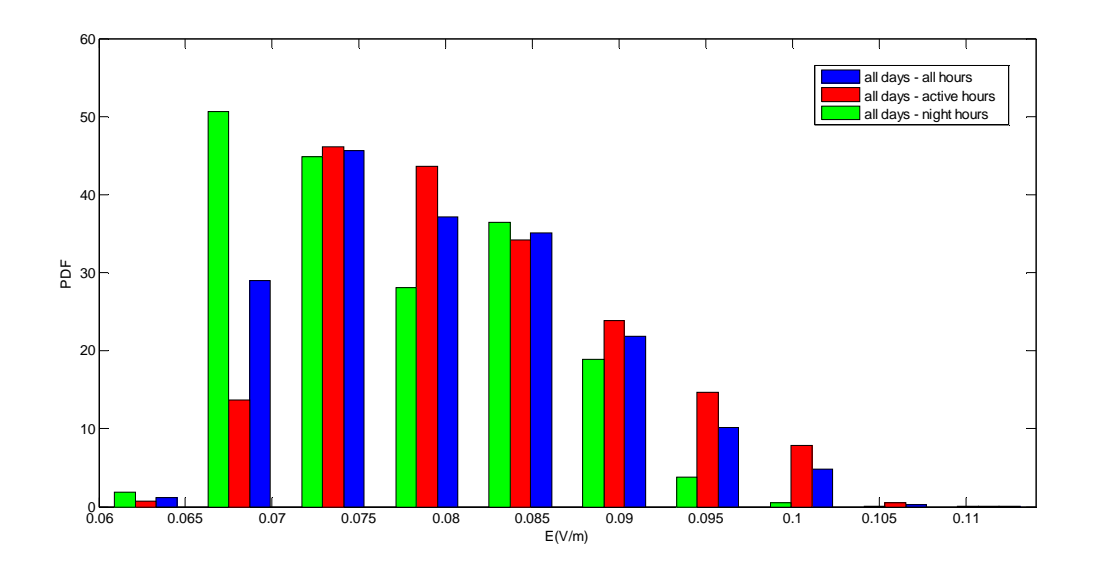


Figure 100 Probability density function of electric field strength for "all days" - DCS

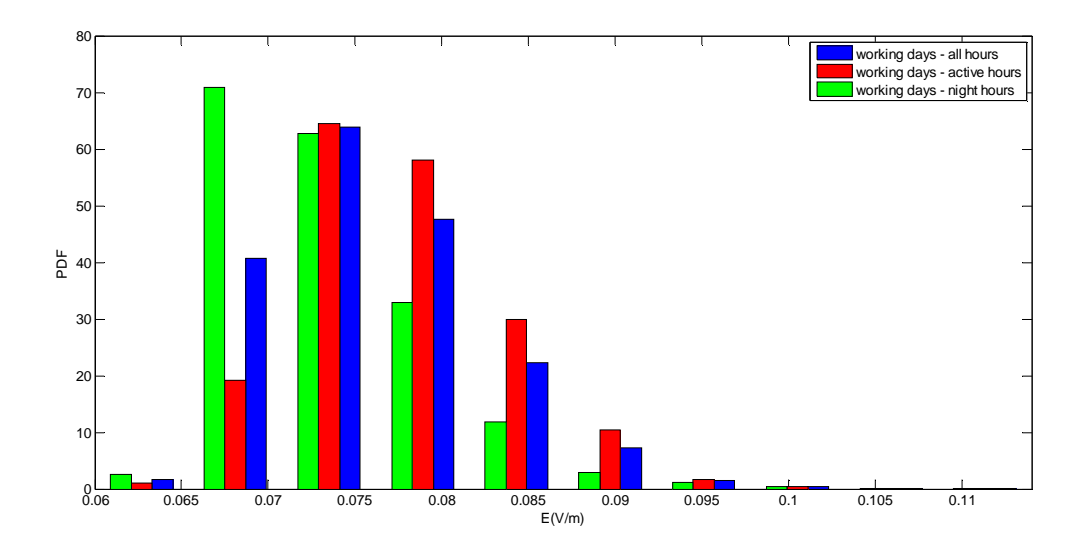


Figure 101 Probability density function of electric field strength for "working days" - DCS



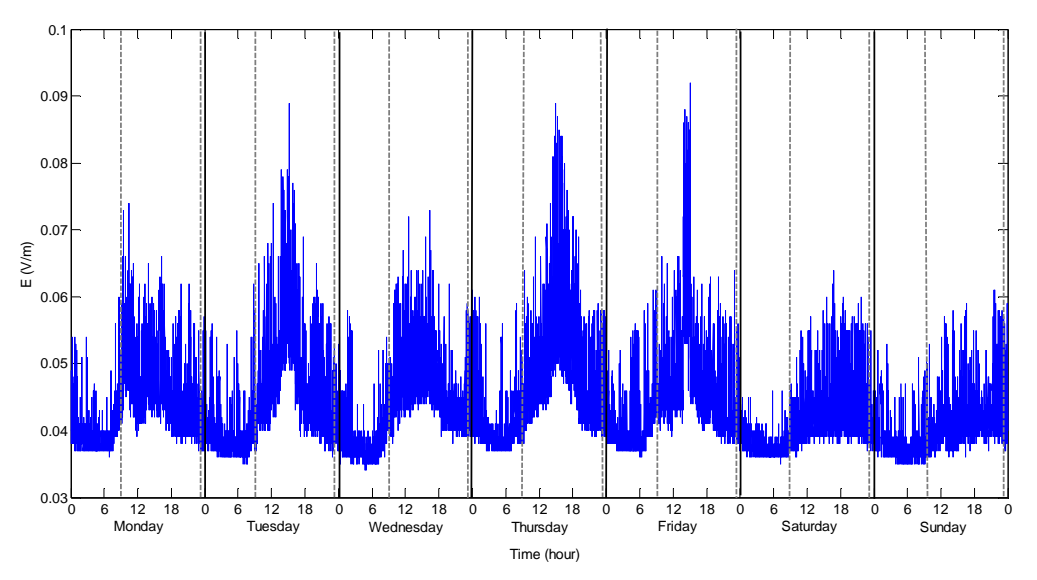


Figure 102 Time variability of electric field strength for UMTS

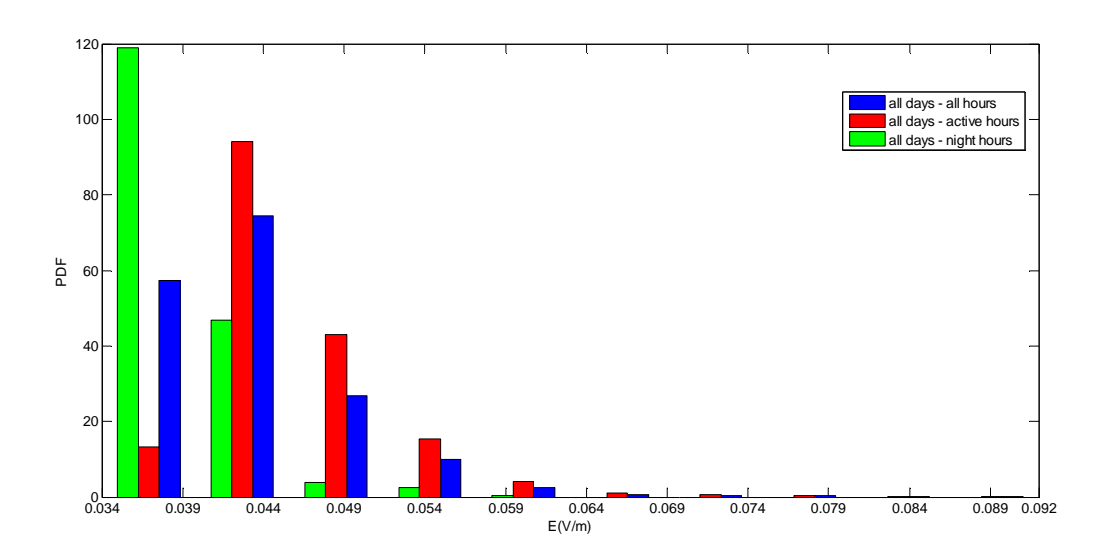


Figure 103 Probability density function of electric field strength for "all days" - UMTS



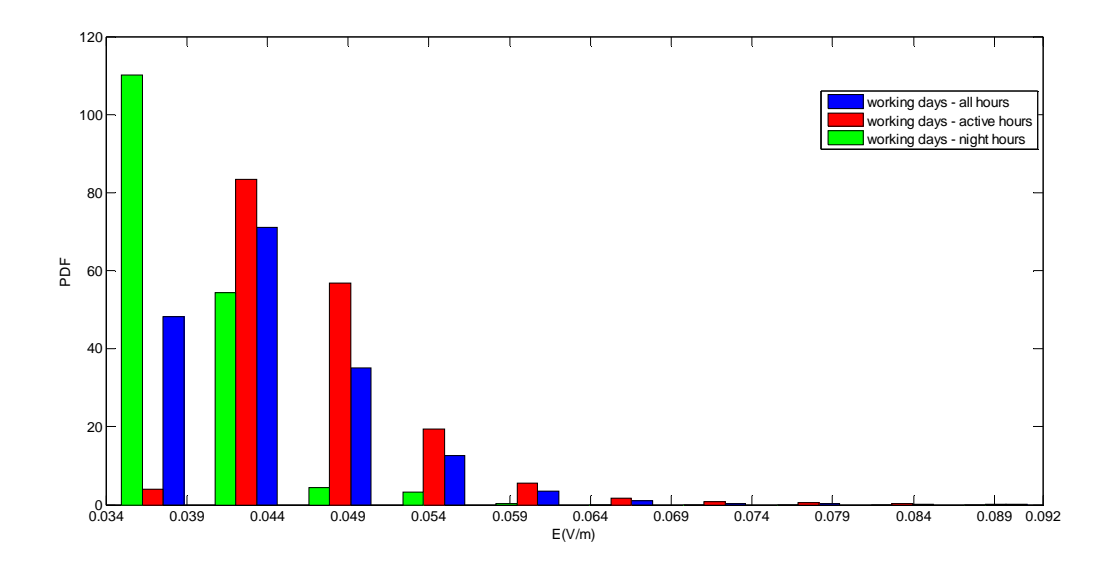


Figure 104 Probability density function of electric field strength for "working days" - UMTS

Uncertainty caused by telecommunication traffic and transmitter functionalities

With regards to the previously analyzed effects which lead to greater instability of the DL electromagnetic field strength, an additional uncertainty caused by telecommunications traffic and transmitter functionalities must be taken into account.

For each of previously defined categories, the uncertainty caused by telecommunications traffic and transmitter functionalities is analyzed for different time intervals of averaging: 10s, 30s, 1min, 6min, 15min, 30min, 1h, 3h, 6h and 10h. For the purpose of averaging, the total data set was divided in non-overlapping intervals of the defined duration. For each interval, a unique average value was determined with the exception of the intervals of 10s where no averaging were done. The maximum value of the averaging interval was 10h and it was determined according to the duration of "night hours".

The uncertainty caused by telecommunications traffic and transmitter functionalities can be determined by statistical analysis of a series of average values [26][27]. In the first step, the mean value E_{meas} and the standard deviation $\sigma(E_{meas})$ are determined using:

$$E_{meas} = \frac{1}{N} \sum_{i=1}^{N} E_{meas\ i} \tag{1}$$

$$\sigma(E_{meas}) = \sqrt{\frac{1}{N-1} \sum_{i=1}^{N} (E_{meas i} - E_{meas})^2}$$
 (2)



where $E_{\mathit{meas}\,i}$ denotes *i*-th averaged value and N is the total number of averaged values.

The relative ratio of the standard deviation and the mean value defines the traffic uncertainty *u(Traff)*:

$$u(Traff) := \frac{\sigma(E_{meas})}{E_{meas}} \tag{3}$$

Using equations 1-3, the traffic uncertainties for all 6 categories defined in previous section are determined.

Results of the uncertainty caused by telecommunication traffic and transmitter functionalities with regards to averaging interval, averaged over all 3 test locations are presented in tables 2, 3, and 4 for GSM, DCS and UMTS, respectively. Also, in these tables, the values of the uncertainties averaged over all 3 test locations are given. The obtained results are also presented graphically in Figures 15-20.

Table 40 Traffic uncertainty (%) with regards to time averaging intervals for GSM

Category	Averaging interval									
Category	10s	30s	1min	6min	15min	30min	1h	3h	6h	10h
"all days – all hours"	10.24	9.38	9.10	8.69	8.55	8.44	8.34	7.92	7.05	6.59
"working days - all hours"	10.48	9.59	9.30	8.87	8.75	8.65	8.53	8.14	7.17	6.75
"all days – active hours"	8.34	7.21	6.84	6.29	6.08	5.91	5.74	5.31	5.04	4.29
"working days – active hours"	8.55	7.00	6.61	6.02	5.80	5.62	5.46	4.88	4.59	4.08
"all days - night hours"	9.06	8.24	7.97	7.58	7.47	7.38	7.30	6.95	6.47	4.76
"working days - night hours"	9.04	8.18	7.89	7.48	7.36	7.28	7.17	6.84	5.07	4.31

Table 41 Traffic uncertainty (%) with regards to time averaging intervals for DCS

Category	Averaging interval									
Category	10s	30s	1min	6min	15min	30min	1h	3h	6h	10h
"all days – all hours"	7.99	7.59	7.46	7.27	7.18	7.10	7.01	6.56	6.07	5.54
"working days - all hours"	7.47	7.04	6.90	6.70	6.55	6.46	6.36	5.80	5.22	4.51
"all days – active hours"	8.65	8.19	8.04	7.82	7.73	7.63	7.49	7.29	6.63	5.77
"working days - active hours"	8.23	7.70	7.53	7.25	7.12	6.99	6.83	6.43	5.61	4.63
"all days - night hours"	6.26	5.90	5.79	5.65	5.60	5.59	5.51	5.56	5.42	5.50
"working days – night hours"	4.92	4.53	4.40	4.24	4.17	4.15	4.02	4.02	3.82	3.85

Version: V1.2 128



Table 42 Traffic uncertainty (%) with regards to time averaging intervals for UMTS

Category	Averaging interval									
Category	10s	30s	1min	6min	15min	30min	1h	3h	6h	10h
"all days - all hours"	14.35	13.18	12.76	12.12	11.91	11.73	11.54	11.02	10.07	9.13
"working days - all hours"	14.29	13.05	12.60	11.92	11.72	11.50	11.32	10.72	9.77	8.64
"all days – active hours"	13.37	11.84	11.29	10.41	10.09	9.81	9.53	9.05	7.96	5.64
"working days - active hours"	13.04	11.44	10.84	9.89	9.55	9.25	8.90	7.68	6.12	4.57
"all days – night hours"	11.15	10.09	9.70	9.15	8.96	8.82	8.70	8.17	5.59	3.46
"working days - night hours"	11.50	10.38	9.96	9.35	9.16	9.02	8.89	8.37	5.59	3.32

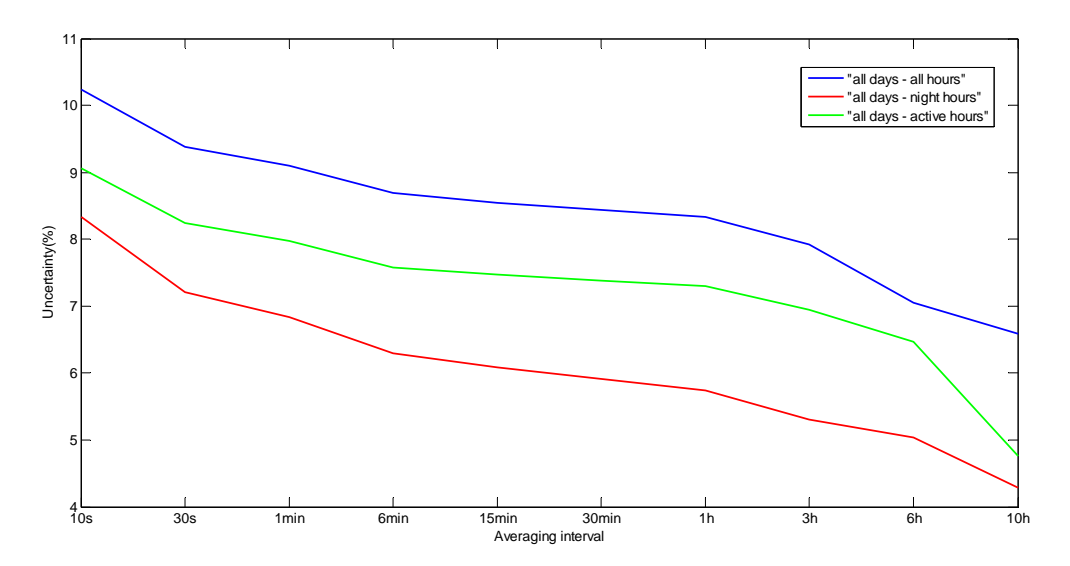


Figure 105: Traffic uncertainty with regards to time averaging intervals for "all days" - GSM



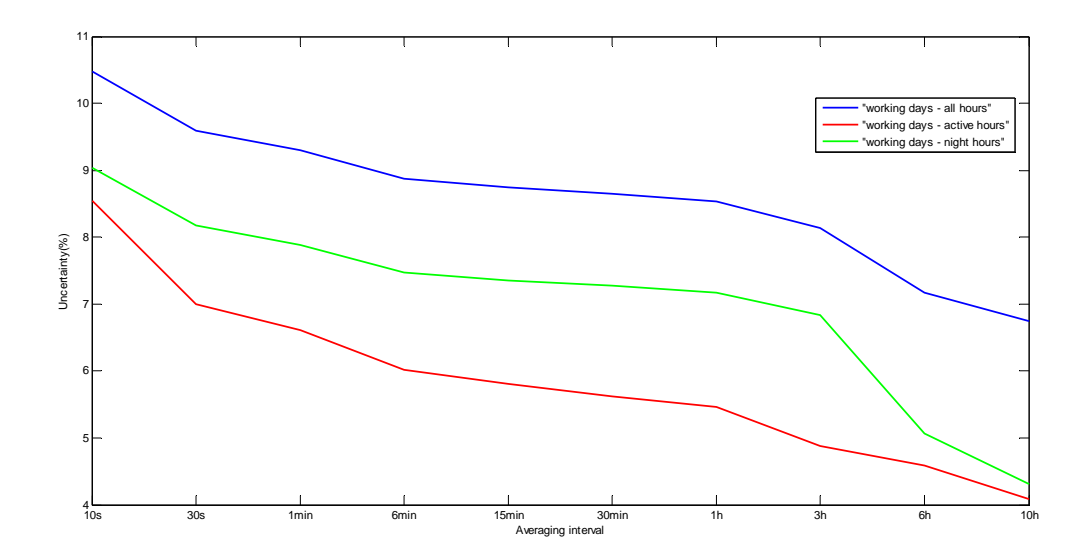


Figure 106: Traffic uncertainty with regards to time averaging intervals for "working days" - GSM

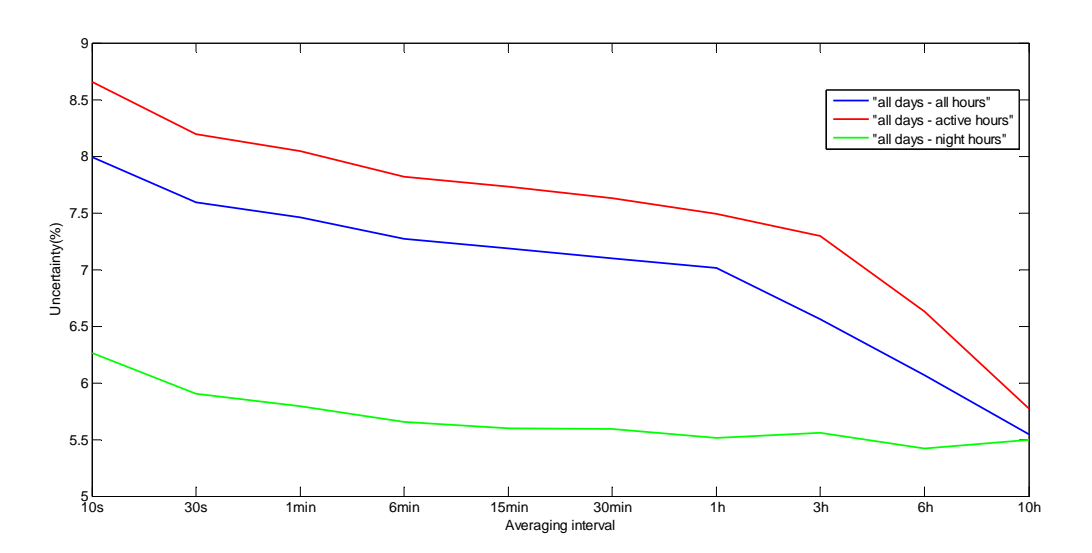


Figure 107 Traffic uncertainty with regards to time averaging intervals for "all days" - DCS



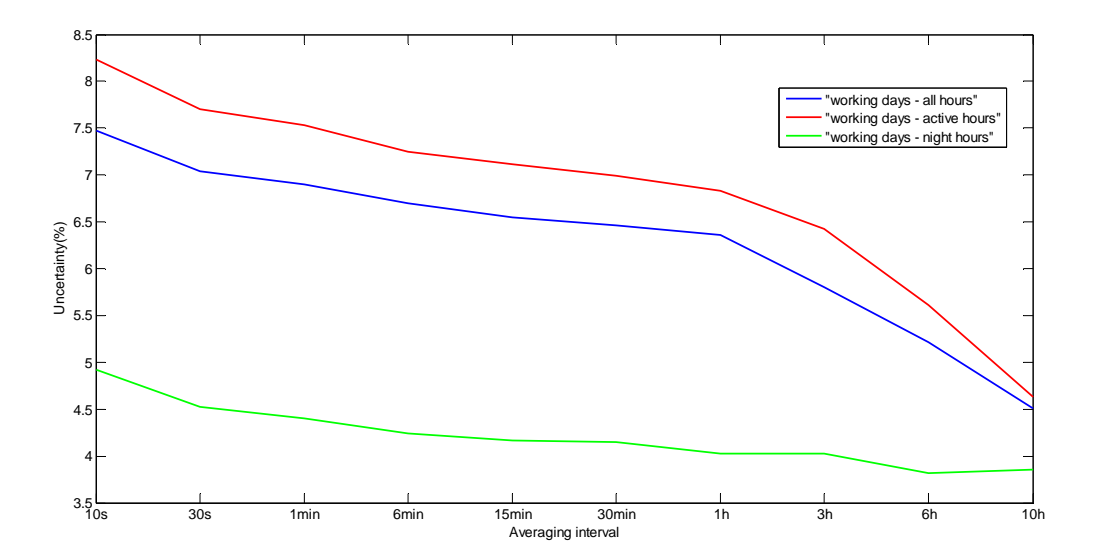


Figure 108 Traffic uncertainty with regards to time averaging intervals for "working days" - DCS

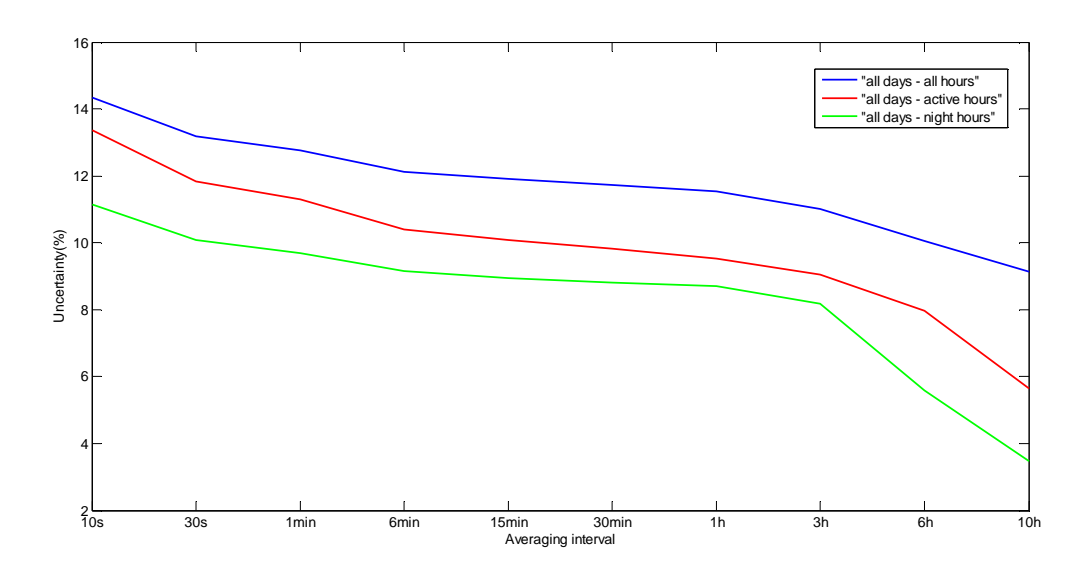


Figure 109 Traffic uncertainty with regards to time averaging intervals for "all days" - UMTS



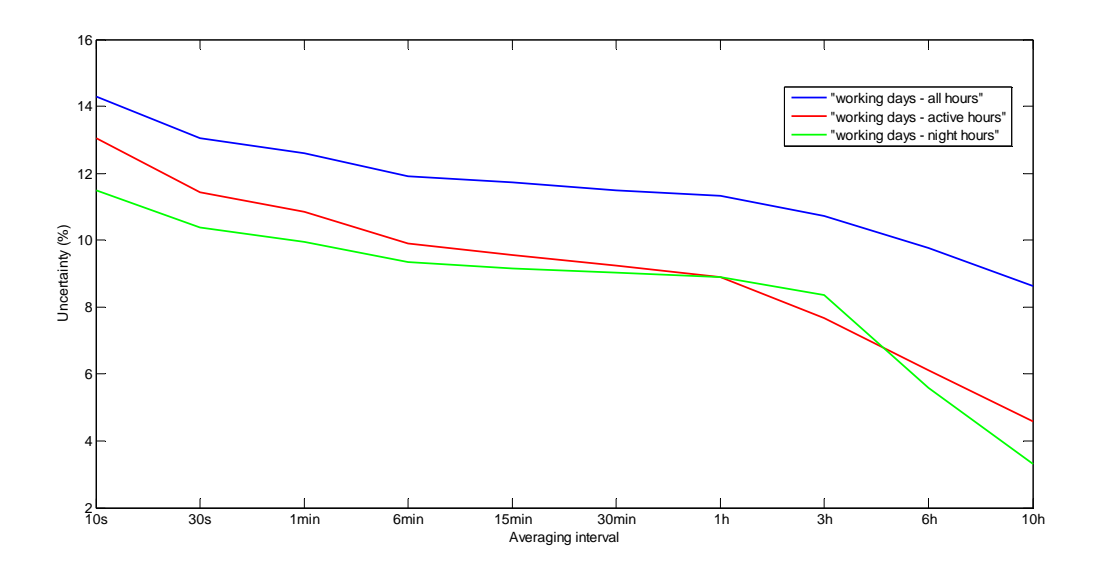


Figure 110 Traffic uncertainty with regards to time averaging intervals for "working days" – UMTS



APPENDIX 3: GUIDELINES ON THE EXPRESSION OF UNCERTAINTY IN LEXNET DOSIMETER MEASUREMENTS

This Guidelines provide general rules for evaluating and expressing uncertainty in measurements carried out by LEXNET dosimeter. According to [26], when reporting the result of a measurement of a physical quantity, it is obligatory that some quantitative indication of the quality of the result be given so that those who use it can assess its reliability. Without such an indication, measurement results cannot be compared, either among themselves or with reference values given in a specification or standard. Uncertainty of measurement is parameter, associated with the result of a measurement, that characterizes the dispersion of the values that could reasonably be attributed to the measurand.

Evaluation of uncertainty in measurements carried out by LEXNET Exposure Index (EI) dosimeter is based on the [26, 27, 28, 29, 30]. In order to estimate the uncertainty of measurement, it is generally necessary to know the "model" of the measuring system. In the considered case, the measurements are performed by an integrated system that directly shows the measured values. However, these measurements are considered "indirect". In this case the estimation of measurement uncertainty is carried out mainly on the basis of parameters that can be found in the technical specifications and certificates of calibration of the measuring system, based on the associated standard uncertainties.

In the following text, the assessment of the impact of significant parameters that contribute to the measurement uncertainty is discussed.

Uncertainity caused by Measurement device - u(Md)

Within the considered integrated measurement system (LEXNET Exposure Index dosimeter), as a measuring device a specific spectrum analyzer is used. The uncertainty caused by spectrum analyzer can be determined in two ways:

- based on the technical specifications of the manufacturer (provided that the relevant features of the analyzer are within the limits of the specified accuracy, which is evidenced by a certificate of calibration), or
- based on data from the calibration certificate for the individual parts (subsystems) of the device and based on the technical specifications of the manufacturer's knowledge of the "model" of the measuring device.

Using the second approach lower values of uncertainty are usually obtained, which provides the measurements of greater accuracy.

However, within this project the first approach will be applied. According to the manufacturer's specifications, probability density function for this type of uncertainty is rectangular.



Uncertainty of the calibration of the sensor - u(MS)

In the calibration phase, the sensor is immersed in a uniform electric field of a known constant intensity. Calibration process is obviously associated with an uncertainty depending strictly on the calibration chain: power meters, antennas, anechoic chamber, TEM cells, etc. These levels of uncertainty are the "best measurement capability" of the laboratory and they can vary depending on the calibration level and frequency. Calibration laboratories report this uncertainty values into Calibration Certificate. The probability distribution function for this type of uncertainty is considered to be Gaussian.

Uncertainty of the Antenna Factor Interpolation - u(FA)

During the calibration process, the antenna factors are determined for discrete operating frequencies. For frequencies that do not correspond to the frequencies for which the antenna factors are determined the interpolation should be done. However, interpolation process brings additional uncertainty. The uncertainty of this type can be determined on the basis of calibration certificate. It is considered that the probability density function for this type of uncertainty is of Gaussian type.

Uncertainty of the anisotropy - u(A)

Anisotropy is defined as the maximum deviation from the geometric mean of maximum and minimum value when the sensor is rotated around the ortho-axis (e.g., probe handle, rigid or flexible feed-line assembly, "virtual handle"). Anisotropy can be determined using the following expression:

$$A = 20 \cdot \log_{10} \left(\frac{S_{\text{max}}}{\sqrt{S_{\text{max}} \cdot S_{\text{min}}}} \right) dB$$

where S is the measured amplitude in the field strength units.

The probability distribution is considered to be rectangular. The uncertainty of the anisotropy should be taken into account when triaxal (isotropic) probe is used. Instead, when monoaxial probe is used the Uncertainty caused by the usage of monoaxial probe should be used (explained in the following text).

Uncertainty caused by the usage of monoaxial probe - u(MA)

When monoaxial probe is used, additional correction factor should be apllied (i.e., to be added to the measurement readings). In addition consequently the usage of monoaxial probe causes additional uncertainty in measurement readings and should be taken into account.

Due to the complex mechanisms of radio wave propagation, this type of uncertainty is hard to analyze theoreticaly (or by simulations) and can be determined by measuring in the field.



Uncertainty caused by mismatching - u(VSWR)

When two elements of the radio equipment are connected to each other, the mismatching occures to some extent. Due to this effect, a separate component of uncertainty is introduced. The upper limit of the uncertainty caused by mismatching can be determined as follows:

$$u(VSWR) = 100 \cdot \Gamma_e \Gamma_a$$
 %

where Γ_e denotes reflection coefficient of measuring device and Γ_a denotes the reflection coefficient of the antenna at the antenna feeding-point.

The exact values of VSWR factors (which are generally complex) are usually not known for the individual frequency components, but using the the worst-case principle the value of VSWR determined for the entire frequency range can be used. This approach will be applied as well for calculating the combined uncertainty. Of course, in this way, generally, the higher values of uncertainty are obtained than it is actually the case. It is considered that the corresponding probability distribution function is of U type.

Uncertainty caused by "electrical noise" - u(Noise)

Electrical noise is the signal detected by the measurement system even if the transmitters of the analyzed systems are not transmitting. The sources of these signals include RF noise (lighting systems, the scanning system, grounding of the laboratory power supply, etc.), electrostatic effects (movement of the probe, people walking, etc.) and other effects (light detecting effects, temperature, etc.). The electrical noise level shall be determined by three different coarse scans in the unused parts of the observed frequency range (essentially, the scans should be carried out with RF sources/transmitters switched off, what, of coarse, is impossible). None of the evaluated points shall exceed –30 dB of the highest incident field being measured. Within this constraint, the uncertainty due to noise shall be neglected.

Uncertainty caused by drift in the transmitting powers, measurement equipment, temperature and humidity - u(Drift)

The drift due to electronics of the transmitters and the measurement equipment, as well as temperature and humidity, are controlled by the first and last step of the measurement process defined in the measurement procedure and the resulting error should be less than \pm 5 % [30]. The uncertainty shall be evaluated assuming a rectangular probability distribution.

At this point, several important facts should be emphasized:

 uncertainty stemming from temperature variations of measuring equipment is taken into consideration through a separate factor of uncertainty (discussed within the uncertainty caused by measurement devices),

Version: V1.2



- according to the manufacturer's specification uncertainty stemming from the humidity can be ignored (if the prescribed operating conditions are observed),
- the sources of electromagnetic radiation belonging to the modern professional radio systems (GSM/UMTS/LTE base stations, TV and FM radio transmitters, etc.). Typically work under controlled environmental conditions (use of air conditioners, dehydrators, ...). The uncertainty which is caused by instability of base station transmitters is typically less than 2%. In all other cases, the value of 5% should be used as stipulated in the standard [28].

Uncertainty caused by human bodies - u(Body)

The presence of the human bodies during the measurements affects the measured results. However, when dosimeter is used at stationary positions (for example, lampposts), in all cases the minimum distance between the measurement probe and the bodies of the humans as well as any reflecting object shall be far enough so that the influence of the human bodies can be neglected. In all other cases uncertainty caused by human bodies [30] should be taken into consideration.

Uncertainty caused by small-scale fading - u(Fad)

In a wireless system, the characteristic that transmitted signal loses its deterministic properties and becomes incidental in time and space domain is described with the notion of fading. Essentially, the received signal is affected by both long-term (large-scale) fading and short-term (small-scale) fading. The long-term fading corresponds to the locally averaged electric field strength and is mainly caused by the environment profile between the transmitter and the receiver. On the other hand, the short-term fading is mainly caused by multi-path reflections. In practice, it is impossible to anticipate short-term signal fluctuations only on the basis of physical rules of signal propagation. Actually, it is only possible to talk about statistical characteristics of received electric field strength. According to the standard [30], to assess human exposure to electromagnetic fields, it is recommended to conduct multiple tests (on line or surface defined positions), and perform spatial averaging.

Uncertainty caused by small-scale fading (and which is dependant on the spatial averaging) can be determined based on the [30].

Uncertainty caused by telecommunication traffic and transmitter functionalities - u(Traff)

Besides the well-known short-term fading, which generally characterizes propagation of radio waves, several additional effects have also significant influence on the EMF strength in the mobile networks environment. The most important effects are [16]: traffic load, automatic transmitter power control and discontinuous transmission (section 4.2).

The total BS Tx power directly depends on the number and throughputs of the active connections, i.e. its traffic load. In the case of GSM/DCS systems, depending



on the traffic load, transmitters are turned on or off. On the other side, in the UMTS and LTE system, the increase in the traffic load forces transmitters to operate at higher power and vice-versa.

BS traffic load varies during the day and depends on: the applied tariff profiles, the time of the day, the day of the week, the location of BS... As a rule, mobile operator configures the BS in such a way that under certain conditions it satisfies the traffic demands in the so-called busy hour (the sliding 60-minutes period during which the maximum total traffic load occurs in a given 24-hours period). It should be noted that even if the BS is operating with maximum traffic load, the number of active traffic channels is not constant because of the stochastic nature of call arrivals and call durations.

For each individual connection, the BS Tx power is automatically adjusted depending on the propagation conditions in which the mobile terminal resides. Automatic power control is implemented with a frequency of about 2 Hz in GSM/DCS system, with 1500 Hz in UMTS..

During an established call, when the user makes a normal pause in speech, the base station temporarily stops transmission (in GSM/DCS system transmitters are turned off, while the traffic channel is not transmitted in the UMTS and LTE systems)[26]. Typically, due to this functionality, for each voice connection, the BS transmitters are inactive approximately 40-50% of time.

All the previously mentioned effects lead to greater instability of the DL EMF strength at the measurement position. For this reason, an additional uncertainty stemming from telecommunications traffic must be taken into account. The value of the uncertainty of this type is determined on the basis of daily traffic profiles obtained by measurements.

Total (combined) standard uncertainty

The uncertainty caused by the measurement system (data derived from calibration certificates and technical specifications), can be in principle determined in two ways:

- Adopting appropriate uncertainity values for the examined range of measured values (eg, considering only the data from the frequency range to be tested, the actual value of temperature, etc.). In this way the lower value for the total measurement uncertainty is obtained. However, determining the specific values of individual uncertainties caused by the measurement system is required for each test.
- Adopting the uncertainity values for the broader (or whole) range of the measuring device. In this way, the higher value for the total measurement uncertainty is obtained. However, determining the values of individual uncertainties caused by measurement system is carried out only once.

In practice, the second method is more often used.

Starting from the assumption that the individual uncertainties are mutually uncorrelated, the combined uncertainty shall then be evaluated according to the following equation:



$$u_c = \sqrt{\sum_{i=1}^m c_i^2 \cdot u_i^2}$$

where c_i is the weighting coefficient (sensitivity coefficient - usually equals 1).

Expanded uncertainty

As recommended by the standards, the expanded uncertainty shall be evaluated using a confidence interval of 95 % [26]. Formally, the expanded uncertainty is obtained by multiplying the total standard uncertainty with factor of k = 1.96.

EXAMPLE 1: Evaluation of measurement uncertainty when LEXNET dosimeter is at a fixed position (triaxial sensor)

cause of uncertainty	reference	specified uncertainty [%]	pdf	Scaling factor	Standard uncertainty
measuring device	datasheet	18.85	rectangle	1.73	10.90
calibration of the sensor	calibration certificate	23.00	normal (k=2)	2.00	11.50
antenna factor interpolation	calibration certificate	2.20	normal (k=2)	2.00	1.10
anisotropy	datasheet	27.00	rectangle	1.73	15.61
mismatching	datasheet	6.70 $(\Gamma_e$ =0.2, Γ_a =0.33 $(VSWR$ =2))	U- function	1.41	4.75

Combined standard uncertainty of measuring system [%]: 22.77

Expanding Factor: 1.96

Expanded uncertainty of measuring system [%]: 44.62

instability of transmitters	datasheet	2.00	rectangle	1.73	1.16
Telecommunication traffic	measurements	7.40	normal (k=1)	1.00	7.40
small-scale fading	standard	14.0	normal (k=1)	1.00	14.0

Combined standard measurement uncertainty of [%]: 27.76

Expanding Factor: 1.96

Expanded measurement uncertainty [%]: 54.40



EXAMPLE 2: Evaluation of measurement uncertainty when LEXNET dosimeter is at a fixed position (monoaxial sensor)

cause of uncertainty	reference	specified uncertainty [%]	pdf	Scaling factor	Standard uncertainty
measuring device	datasheet	18.85	rectangle	1.73	10.90
calibration of the sensor	calibration certificate	23.00	normal (k=2)	2.00	11.50
antenna factor interpolation	calibration certificate	2.20	normal (k=2)	2.00	1.10
monoaxial probe	literature	34.00	normal (k=2)	2.00	17.00
mismatching	datasheet	6.70 $(\Gamma_e$ =0.2, Γ_a =0.33 $(VSWR$ =2))	U-function	1.41	4.75

Combined standard uncertainty of measuring system [%]: 23.74

Expanding Factor: 1.96

Expanded uncertainty of measuring system [%]: 46.54

instability of transmitters	datasheet	2.00	rectangle	1.73	1.16
Traffic load	system characteristics	7.40	normal (k=1)	1.00	7.40
small-scale fading	standard	14.00	normal (k=1)	1.00	14.00

Combined standard measurement uncertainty of [%]: 28.56

Expanding Factor: 1.96

Expanded measurement uncertainty [%]: 55.98

Version: V1.2

APPENDIX 4: PRESENTATION OF THE CHANNEL MODEL USED IN SECTION 4.

The models used in section 4 are simplified versions of WINNER2/WINNER+ based models.

 The number of paths strongly depends on the environment and LOS or NLOS configuration. Its statistics is ("roughly") normally distributed with a lower threshold of one and as it is an integer, precisely:

$$N = \max \left[1, \mid N \mid (\mu_N, \sigma_N) \mid \right]$$

FP7 Contract n°318273

where $\mu_N(Env) = E[N]$, $\sigma_N(Env)$ is the standard deviation, all depending on the environment, N the normal distribution and $|\cdot|$ the integer part.

• The MPCs azimuths are normally distributed (and wrapped, modulo $[2\pi]$), i.e. : $\varphi_n = N \ (\Phi, \sigma_{\varphi})[360^{\circ}]$

where Φ is uniformly distributed over [0, 2π [(as the sensor orientation is random), and the RMS Azimuth Spread of Arrival (ASA) is also normally distributed, lower bounded by 1°, i.e., in [¶:

$$\sigma_{\varphi} = \max[1, N \ (\mu_{ASA}, \sigma_{ASA})]$$

where $\mu_{ASA}(Env) = \mathbb{E}\left[\sigma_{\varphi}\right]$, $\sigma_{ASA}\left(Env\right)$ is the spread standard deviation, all depending on the environment.

The LOS path (Env. 2 or 4) is treated specifically. Its DoA is taken to be the closest one to the mean angle Φ of the distribution, and its power relative to the power sum of the other paths is considered to be given by the Ricean K-factor. This K factor is generated by assuming it is lognormally distributed, with mean and variance given in Table 21. Following the renormalization of the path powers, the azimuth spread is not recomputed.

• The MPCs elevation are (truncated) Laplacian distributed, i.e., in [9:

$$\theta_n = L(\mu_{\theta}, \sigma_{\theta})$$

where $\mu_{\theta}(Env) = E[\theta_n]$, and the RMS Elevation Spread of Arrival (ESA) is lognormally distributed, lower bounded by 1°, i.e., in [¶:

$$\sigma_{\theta} = \max[1, LN \ (\mu_{ESA}, \sigma_{ESA})]$$

where $\mu_{ESA}(Env) = \mathbb{E}[\sigma_{\theta}]$, $\sigma_{ESA}(Env)$ is the spread standard deviation, all depending on the environment.

The elevation statistics, not used in this section, will be used in the following.

The vertical polarization path (field) amplitudes are Rayleigh distributed (NLOS scenarios), i.e.:

$$\left|E_{i0,n}^{V}\right| = R\left(\sigma_{n}\right)$$

where the variance of the Rayleigh distribution is a Laplacian function depending on the path azimuth:



$$\sigma_n^2 = \kappa \exp\left(-\sqrt{2}\left|\varphi_n - \Phi\right| / \sigma_{\varphi}\right)$$

Note that, for simplicity reasons, and because the amplitude statistics with respect to the elevation are not very well known (there's a lack of information in the literature regarding this point) the power spread does not depend here on the elevation spread.

 The horizontal polarization path amplitudes are derived from the vertical ones through the XPR; i.e.:

$$\left| E_{i0,n}^{H} \right|^{2} = xpr_{n}^{-1} \left| E_{i0,n}^{V} \right|^{2}$$

where the XPR is lognormally distributed, i.e.:

$$xpr = LN \ (\mu_{XPR}, \sigma_{XPR})$$

with the mean and standard deviation, indicated in Table 21 for the considered environments, are expressed in dB (i.e. $xpr = 10^{XPR/10}$),

and the κ constant is obtained through the normalization relation:

$$\sum_{n=1}^{N} \left| E_{i0,n}^{V} \right|^{2} (1 + xpr_{n}^{-1}) = 1$$

which means that the total field amplitude is always set to 1 V/m.

• For LOS scenarios, the total amplitude statistics are Ricean distributed. The LOS path (Env. 2 or 4) is treated specifically. Its DoA is taken to be the closest one to the mean angle Φ of the distribution, and its power relative to the power sum of the other paths is considered to be given by the Ricean K-factor. This K factor is generated by assuming it is lognormally distributed, with mean and variance given in Table 21. Following the renormalization of the path powers, the azimuth spread is not recomputed.



APPENDIX 5: DETAILS AND MEASUREMENTS OF THE EXTRAPOLATION FROM MONOAXIAL TO ISOTROPIQUE FIELD PROBE STUDY.

Unlike in chapter 4 (body-worn configuration), the current study considers the dosimeter isolated.

Measurements results

Having in mind that the propagation and depolarization of EM waves depend on the environment, measurements were conducted in 3 different scenarios.

In scenario 1, measurements were performed in an indoor environment into an urban area. Transmitting antennas of the nearest BSs were installed indoor. The route of measurement system comprised measurement points in which LOS (visibility with at least one of transmitting antennas) and NLOS conditions were approximately equally represented. Measurement results of electric field strength for all three spatial components E_X , E_Y , and E_Z , and total electric field strength E_{tot} are presented in Figure 111. Accompanying extrapolation factors n_X , n_Y , n_Z and n are shown in Figure 112, while the corresponding statistical values are given in Table 43.

For scenario 2, measurements were performed as well in indoor environment into an urban area. Transmitting antennas of the nearest BSs were not installed indoor. The route of measurement system comprised measurement points where NLOS conditions were fulfilled. Measurement results of electric field strength for all three spatial components E_X , E_Y , and E_Z , and total electric field strength E_{tot} are presented in Figure 113 and . Statistical values for accompanying extrapolation factors n_X , n_Y , n_Z and n are given in Table 44.

In scenario 3, measurements were performed in an urban area and in outdoor environment. Transmitting antennas of the nearest BSs were installed outdoor. The route of measurement system comprised the measurement points where LOS conditions with at least one of BS antennas were satisfied. Measurement results of electric field strength for all three spatial components E_x , E_y and E_z , and total electric field strength E_{tot} are presented in Figure 114. Accompanying statistical values of extrapolation factors n_x , n_y , n_z and n given in Table 45

For comparison of all three scenarios mean values, medians, standard deviations and uncertainties for extrapolation factor n are shown in Table 46. Using these values, mean values for $n_{Overall}$ are determined.

Version: V1.2 142



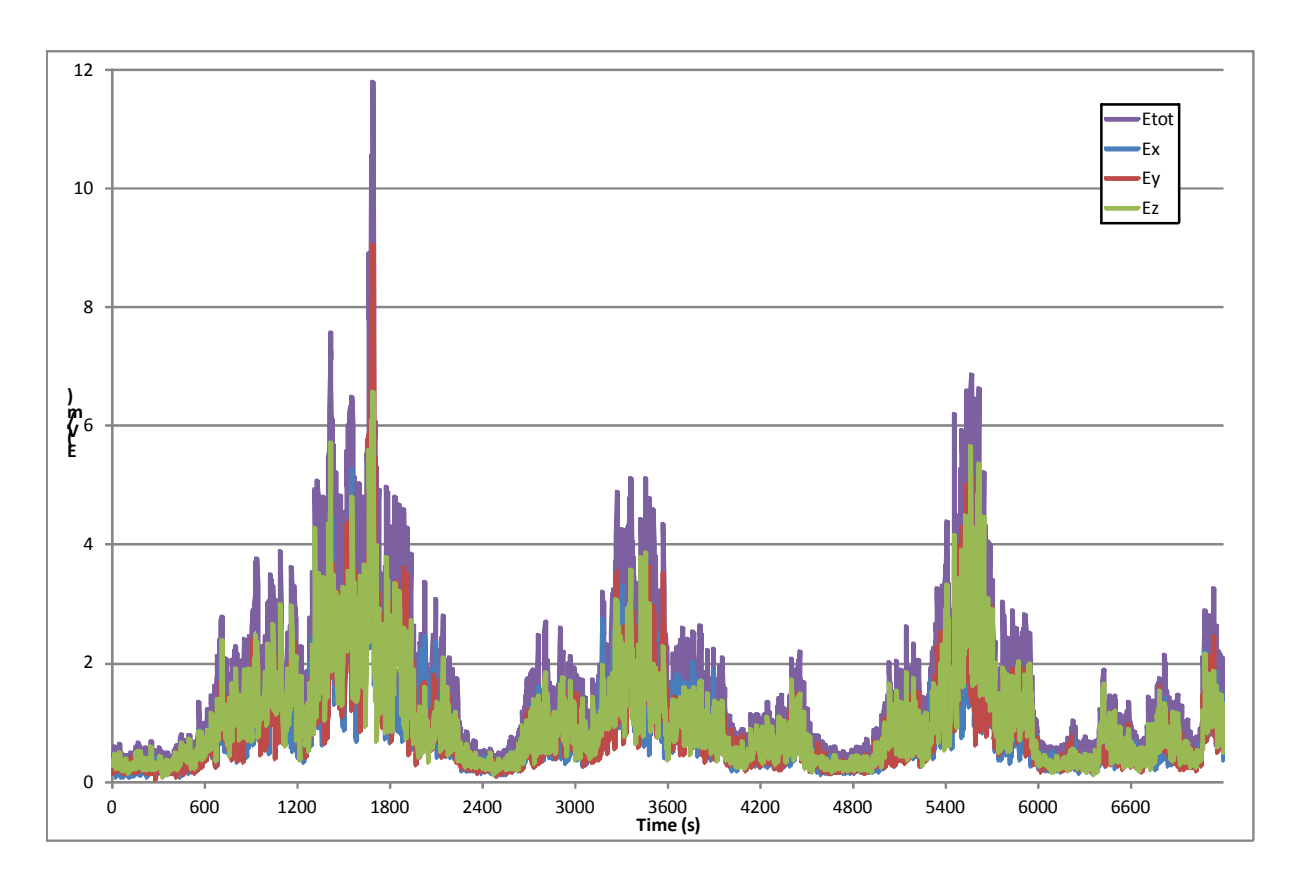


Figure 111 Electric field strength (mV/m) with regards to time for scenario 1

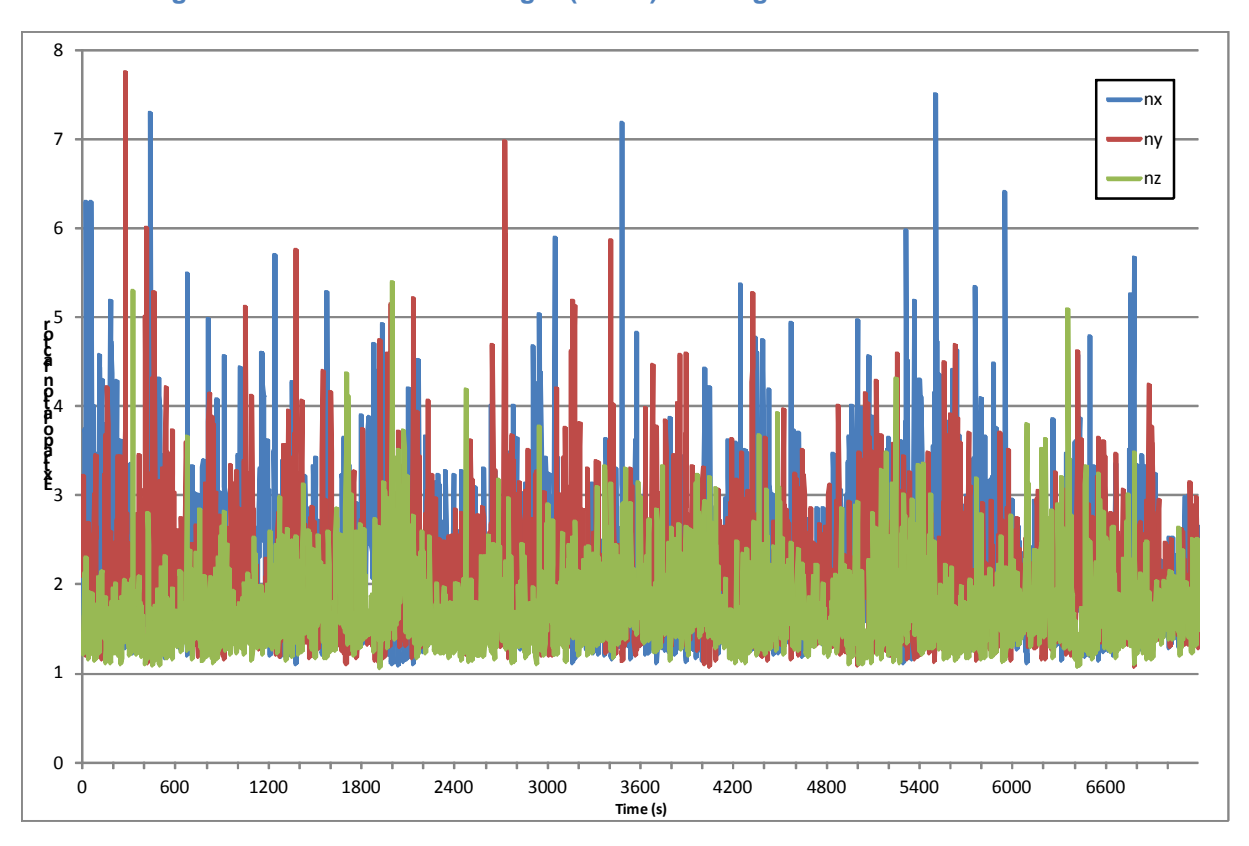


Figure 112 Extrapolation factors with regards to time for scenario 1



Table 43: Mean values, medians, standard deviations and uncertainties for scenario 1

	n_{X}	n_Y	n_Z	n
Mean	2.08	2.03	1.70	1.94
Median	1.91	1.89	1.60	1.78
Standard deviation	0.71	0.65	0.44	0.63
Uncertainty (%)	33.99	31.94	25.78	32.61

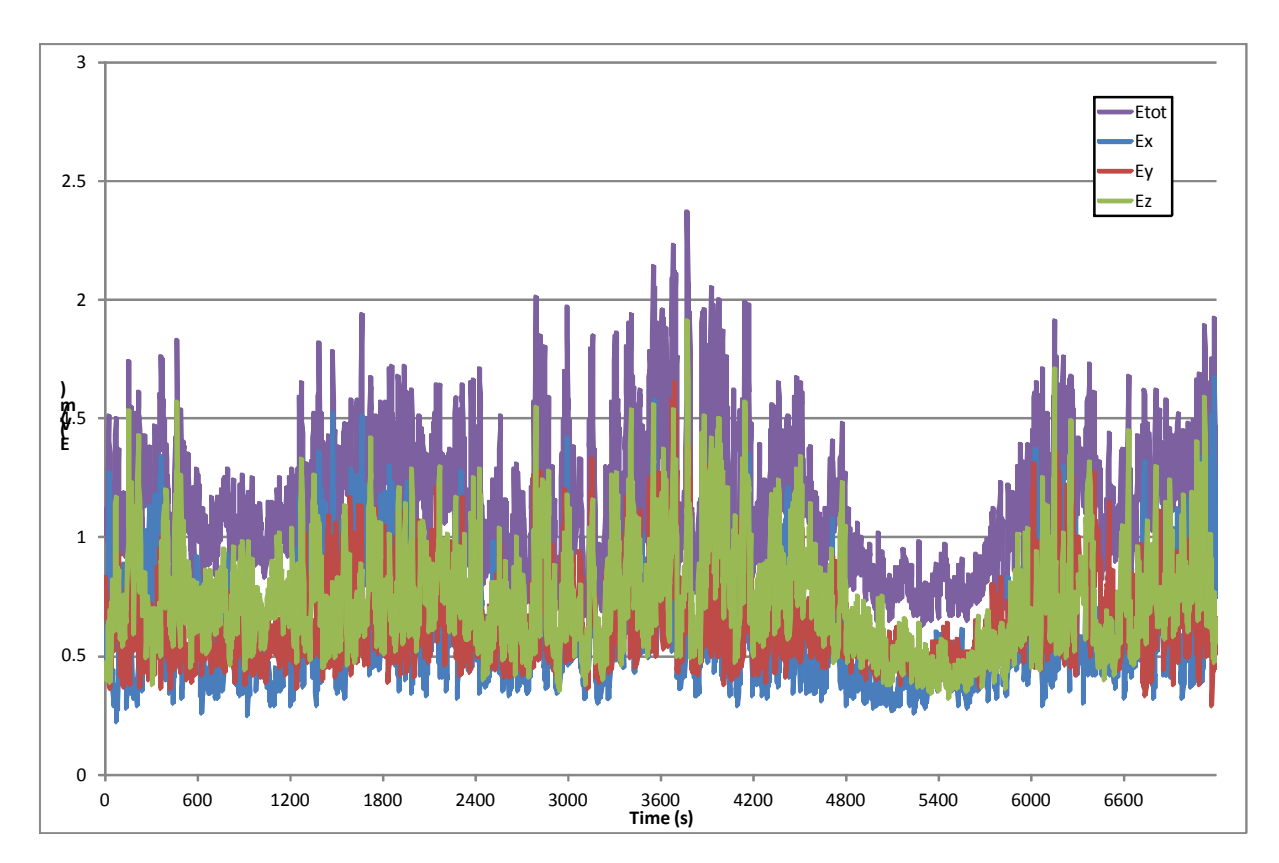


Figure 113 Electric field strength (mV/m) with regards to time for scenario 2

Table 44: Mean values, medians, standard deviations and uncertainties for scenario 2

	n_{X}	n_Y	n_Z	n
Mean	2.10	1.87	1.65	1.87
Median	2.02	1.76	1.59	1.76
Standard deviation	0.56	0.43	0.31	0.48
Uncertainty (%)	26.75	23.17	18.71	25.86



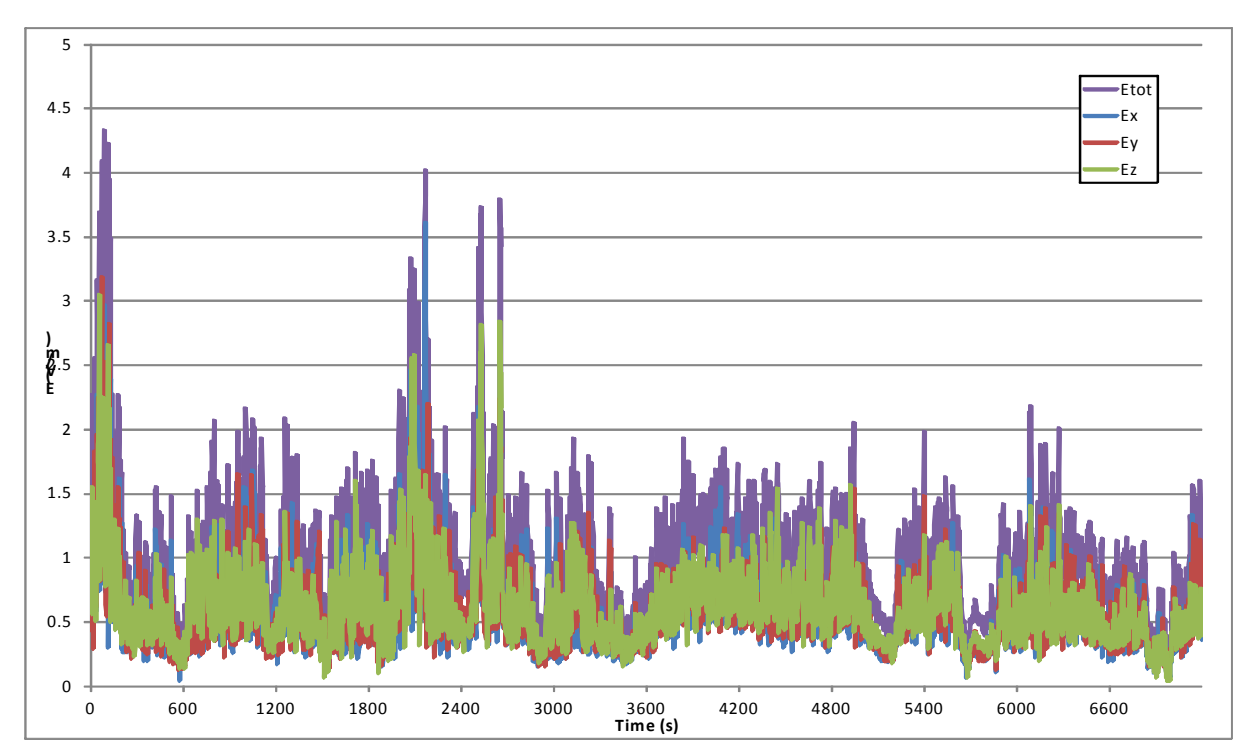


Figure 114 Electric field strength (mV/m) with regards to time for scenario 3

Table 45 Mean values, medians, standard deviations and uncertainties for scenario 3

	n_{X}	n_{Y}	n_Z	n
Mean	2.00	1.89	1.76	1.88
Median	1.90	1.78	1.67	1.77
Standard deviation	0.58	0.49	0.45	0.52
Uncertainty (%)	28.81	26.22	25.33	27.49

Table 46 Comparison of mean values, medians, standard deviations and uncertainties for all three scenarios

	n _{Scenario} 1	n _{Scenario} 2	n _{Scenario} 3	$n_{Overall}$
Mean	1.94	1.87	1.88	1.90
Median	1.78	1.76	1.77	1.77
Standard deviation	0.63	0.48	0.52	0.54
Uncertainty (%)	32.61	25.86	27.49	28.65